

Szabolcs BEREZVAI, Constitutive modelling of compressible solids including viscoelastic-viscoplastic effects, PhD Dissertation, Budapest, 2020

Corrections

version: 2020.07.09.

The officially submitted version of the dissertation contains some typesetting errors, which cannot be corrected after the successful PhD defense due to the regulations of *Géza Pattantyús-Ábrahám Doctoral School of Mechanical Engineering Sciences, Budapest University of Technology and Economics*.

The present PDF is the “**unofficial**” corrected version of my dissertation, which is **published only on my personal webpage**. This document is the exclusive property of the Author and protected by copyright laws. Please cite the dissertation as:

Berezvai, Szabolcs, Constitutive modelling of compressible solids including viscoelastic-viscoplastic effects, PhD Dissertation, Budapest University of Technology and Economics, Budapest, Hungary, 2020.

Copyright © Szabolcs Berezvai, 2020.

Budapest, 2020.07.09.

Dr. Szabolcs Berezvai, PhD
berezvai@mm.bme.hu

List of Corrections

Location	Original	Corrected
Nomenclature, Greek letters (pg. 5-6.)	-	$\alpha(t), \alpha(\omega)$ Acceleration signal and its FFT
Nomenclature, Greek letters (pg. 5-6.)	δ_{rel} Relative error	$\delta_{\text{abs}}, \delta_{\text{rel}}$ Absolute and relative error
Nomenclature, Greek letters (pg. 5-6.)	-	ω Angular frequency
Nomenclature, Abbreviations (pg. 6)	UN Uniaxial	UN, UA Uniaxial
pg. 9. below Eq. (2.5)	Kelvin-Voight	Kelvin-Voigt
pg. 15. below Eq. (2.47)	$W(\boldsymbol{\varepsilon}) =$	$W(\boldsymbol{\varepsilon}) = (\boldsymbol{\varepsilon} : \boldsymbol{\mathcal{D}}^e : \boldsymbol{\varepsilon})/2$
in Eq. (2.82), (2.84) and (2.85)	$\dot{\lambda}$	$\dot{\lambda}_p$
pg. 19 after Eq. (2.82)	yield that $\dot{\Phi}_p = 0,$	yield that $\dot{\Phi} = 0,$
pg. 28, above Eq. (3.45)	stain increment	strain increment
pg. 29, above Fig. 3.2	nature of its characteristic	nature of its characteristics
Caption of Fig. 3.2	The layour of	The layout of
pg. 30 above Eq. (3.53)	the fist Piola--Kirchhoff stress	the first Piola--Kirchhoff stress
Eq. (3.53)	$\lambda_1^{\text{UNexp}} = 1 + \frac{u}{L_0}$	$\lambda^{\text{UNexp}} = 1 - \frac{u}{L_0}$
Eq. (3.55)	$\lambda_1^{\text{EBexp}} = 1 - \frac{u}{\sqrt{2}L_0}$	$\lambda^{\text{EBexp}} = 1 - \frac{u}{\sqrt{2}L_0}$
pg. 36. Thesis Statement 1/B	$\lambda_T^{\text{EB}} = 2\lambda_T^{\text{UN}} + 1.$	$\lambda_T^{\text{EB}} = 2\lambda_T^{\text{UN}} - 1.$
pg. 39-41	missing brackets in citations for equations are replaced at 6 places.	
pg. 40.	A possible formulation of (..) materials are provided	A possible formulation of (..) materials is provided
pg. 42. Eqs (4.16)-(4.19) and above Eq. (4.18)	SYMM	SYM
Eq. (4.54)	$\sigma_i^{\text{long}} = \frac{\sigma_{i,\text{max}}^{\text{up}} + \xi\sigma_{i,\text{min}}^{\text{un}}}{1 + \xi}.$	$\sigma_i^{\text{long}} = \frac{\sigma_{i,\text{max}}^{\text{up}} + \xi_i\sigma_{i,\text{min}}^{\text{un}}}{1 + \xi_i}.$
pg. 53. above Eq. (4.58)	small strain formulation	small strain formulation is
pg. 67, above Section 5.4	accordingly to Section 2.79.	accordingly (2.79).
Fig. 5.17 axis labels on	σ_{Y0} and f	σ_{y0} and f_e
Fig. 6.4	$\mu = 0.5$	$\mu = 0.3$
Appendix C	SYMM	SYM

SZABOLCS BEREZVAI
PHD DISSERTATION

BUDAPEST UNIVERSITY OF TECHNOLOGY AND ECONOMICS
FACULTY OF MECHANICAL ENGINEERING
DEPARTMENT OF APPLIED MECHANICS





M Ű E G Y E T E M 1 7 8 2

BUDAPEST UNIVERSITY OF TECHNOLOGY AND ECONOMICS
FACULTY OF MECHANICAL ENGINEERING
DEPARTMENT OF APPLIED MECHANICS

Constitutive modelling of compressible solids including viscoelastic-viscoplastic effects

PhD Dissertation

Author:

Szabolcs BEREZVAI

Supervisor:

Dr. Attila KOSSA, associate professor

Submitted to

Géza Pattantyús-Ábrahám Doctoral School of Mechanical Engineering Sciences,
Budapest University of Technology and Economics

Budapest, 2020

Copyright © Szabolcs Berezvai, 2020

To My Family

Acknowledgements

First of all, I would like to express my deepest thanks to my supervisor, *Attila Kossa*, for his outstanding guidance and leadership during our seven years of collaboration. I am indebted for all the invaluable professional and personal support, inspiration and encouragement he gave me during our common work.

I would also like to thank *Prof. Gábor Stépán* and *Prof. Tamás Insperger* for providing a comfortable, calm and motivating work environment. I am thankful to all of my colleagues, especially fellow PhD students, at the Department of Applied Mechanics, for their help and for all conversations. In particular, I would like to mention *Dávid Hajdu*, *Henrik Sykora* and the entire *MeMento Team*, who always stood by me in overcoming the critical periods.

I am thankful to *Imre Bojtár* and *Gábor Hénap* for their thorough review and for their useful suggestions to improve the quality of the thesis. I also thank *László Szabó*, *Máté Vizi* and *Dávid Hajdu* for proofreading the dissertation.

I also would like to express my appreciation to *Brigitta Szilágyi* for introducing me the methodology and innovations of university education.

The MC-PET foam specimens and the heat chamber measurement facility were provided by Furukawa Electric Institute of Technology (FETI) Ltd., Hungary, which support is gratefully acknowledged.

Last but not least, I would like to thank my *friends* from high-school and from the university, my *family* and my *love*, *Zsófi* for their patience and unwavering support during my studies, and who I could always count on indeed. Especially to my *Mum*, who always supported my dreams and goals.

This work has been supported by the ÚNKP-16-3-I, ÚNKP-17-3-I and ÚNKP-18-3-I. New National Excellence Program and the NTP-NFTÖ-19-B National Talent Program of the Ministry of Human Capacities, Hungary.

The research leading to these results has received funding from the European Research Council under the European Union's Seventh Framework Programme (FP/2007-2013)/ERC Advanced Grant Agreement n. 340889. and the European Union's Horizon 2020 research and innovation programme (Grant agreement No. 862308).

This research has been supported by the Hungarian Scientific Research Fund, Hungary (PD 108691), the Hungarian National Research, Development and Innovation Office (NKFI FK 128662) and the János Bolyai Research Scholarship of the Hungarian Academy of Sciences. The research reported in this paper was supported by the Higher Education Excellence Program of the Ministry of Human Capacities in the frame of Nanotechnology research area of Budapest University of Technology and Economics (BME FIKP-NANO).

Contents

1	Introduction	1
1.1	Layout	3
1.2	Nomenclature	4
2	Theoretical background	7
2.1	Rheological models	7
2.1.1	Viscoelastic behaviour	8
2.2	Description of finite strain deformations	10
2.2.1	Strain measures	11
2.2.2	Velocity and time-derivatives	12
2.2.3	Concept of stress	13
2.2.4	Objectivity	14
2.3	Theory of Hyperelasticity	14
2.3.1	Isotropic hyperelasticity	16
2.4	Theory of small strain plasticity	17
2.4.1	Associative flow rule with von Mises criterion	18
2.4.2	Isotropic hardening	18
2.4.3	Elastic-plastic constitutive model	19
3	Elastic deformation of polymer foams	21
3.1	Overview and goals	21
3.2	Hyperfoam model for compressible foams	23
3.2.1	Development of Hyperfoam model	23
3.2.2	Open-cell foams	24
3.2.3	Stress solutions	24
3.2.3.1	Uniaxial extension (UN)	25
3.2.3.2	Confined uniaxial extension (CU)	25
3.2.3.3	Equibiaxial extension (EB)	26
3.2.3.4	Confined biaxial extension (CB)	26
3.2.3.5	Volumetric deformation (VOL)	26
3.2.3.6	Simple shear (SS)	27
3.2.4	Material stability	27
3.2.4.1	Simplified stability criteria for open-cell foams	29
3.3	Mechanical tests	29
3.3.1	Uniaxial test with video processing	30
3.3.2	Equibiaxial test	30
3.4	Parameter-fitting strategies	31
3.4.1	Strategy A	32
3.4.2	Strategy B	32

3.4.3	Strategy C	33
3.4.4	Evaluation of strategies	34
3.5	Main results	36
4	Viscoelastic characterisation of memory foams	37
4.1	Literature overview and objectives	38
4.2	Finite strain visco-hyperelastic model for foams	39
4.2.1	Solution of the generalized Standard Linear Solid model	39
4.2.2	Finite strain viscoelasticity	40
4.2.3	Numerical solution	42
4.3	Closed-form stress solutions	42
4.3.1	Homogeneous confined compression	43
4.3.2	Homogeneous compression with $\beta_i = 0$	46
4.3.3	Comparison with numerical integration (FEA)	47
4.3.3.1	Material parameters	47
4.3.3.2	Comparison of results	48
4.4	Case-study: Polyurethane memory foam	49
4.4.1	Measurement results	49
4.4.1.1	Relaxation test	50
4.4.1.2	Cyclic test	50
4.4.1.3	Summary of results	51
4.4.2	Parameter-fitting	51
4.4.2.1	Separated fitting - Hyperfoam parameters	52
4.4.2.2	Separated fitting - Prony parameters	53
4.4.2.3	Closed-form parameter fitting	55
4.4.3	Evaluation of results	55
4.5	Main results	57
5	Viscoelastic-viscoplastic model for microcellular foams	59
5.1	Literature overview and objectives	59
5.2	Mechanical behaviour of micro-cellular PET foam	60
5.2.1	Preliminary material tests	61
5.2.2	Uniaxial tensile tests	62
5.3	Parallel viscoelastic-viscoplastic constitutive models	64
5.3.1	Elastic behaviour	64
5.3.2	Nonlinear creep laws	65
5.3.3	Yielding behaviour	66
5.4	Fitting strategy and results	67
5.4.1	Numerical optimization scheme	67
5.4.2	Fitting results: strain-hardening creep law	69
5.4.3	Fitting results: time-hardening creep law	70
5.4.4	Comparison of models	71
5.4.5	Sensitivity of parameters	72
5.5	Temperature-dependency of parameters	74
5.5.1	Analytical parameter functions	75
5.5.2	Improved fitting with analytical functions	77
5.6	Punch-test based validation procedure	79
5.6.1	Punch-tests	79
5.6.2	Laser scanning	80

5.6.3	Simulation of punch-test	81
5.6.4	Validation results	81
5.7	Main results	83
6	Pellet impacts for impulse excitation	85
6.1	Impulse excitation of high-speed rotating machine tools	86
6.2	Material characterisation	87
6.2.1	Compression tests	87
6.2.2	Constitutive model and fitting	87
6.2.3	Elastic-plastic boundary models	88
6.3	FE simulation of pellet impacts	89
6.3.1	FE model	89
6.3.2	Impact characteristics	90
6.3.3	Relevant excitation frequency bandwidth	90
6.3.4	Prediction of the contact characteristics	92
6.4	Experimental validation	92
6.4.1	Experimental results	93
6.4.2	Modal parameters	94
6.5	Main results	97
	Appendices	99
A	Linearization of Hyperfoam model and its relation to Hooke's law	101
B	Incomplete Gamma-function	103
B.1	The (complete) gamma function	103
B.2	The upper incomplete gamma function	104
B.3	Special cases	104
C	Numerical integration scheme for finite strain viscoelastic model	105
C.1	Integration of the hydrostatic stress	105
C.2	Integration of the deviatoric stress	106
C.3	Total stress solution	107
D	Biaxial compression fixture	109
	References	121

1

Introduction

Understanding the mechanical behaviour of materials is an essential part of everyday engineering work in order to accurately determine and predict the deformation and stress state of structures and parts subjected to external effects including mechanical loading. In order to relate the deformation of a general three-dimensional body to the applied external effects, the local behaviour of the material at every point should be characterised by a suitably chosen constitutive equation. In continuum mechanics approach, the simplest constitutive model is the isotropic Hooke's law, that describes accurately the deformation of metals in the small-strain regime, where the material behaves in a linear elastic manner. In the linearised theory of deformation, the advanced constitutive models may also include several complex phenomena such as permanent (yielding or plastic) and rate-dependent (viscous) deformations [1, 2, 3, 4].

The mechanical behaviour of modern polymer materials exhibits different types of phenomena when exposed to normal loading such as creep, stress relaxation, yielding, plastic flow, fracture or fatigue [5]. The goal of the material characterisation (or constitutive modelling) process is to mathematically describe these phenomena and predict the material behaviour for complex load cases. There are two main modelling approaches that aim to capture the material response to external effects: microstructural and phenomenological approaches [5, 6].

Microstructural (or micromechanical) models estimate the global mechanical behaviour using the knowledge about the local behaviour including interactions and deformation mechanisms from the atomic level in a monomer to the interaction of molecular chains in molecular level [5, 7, 8]. These models are always more reliable than phenomenological models; however, due to the complexity of micromechanical interactions (also including electrostatic, thermodynamical and chemical effects), it becomes complicated to derive a constitutive model based solely on micromechanical considerations. Therefore, such models are rarely applied in computational solid mechanics [4, 6, 9].

The phenomenological modelling approach is mainly concerned with finding suitable mathematical relations between measurable macroscopic quantities (e.g. stress, strain, temperature, load-rate) based on experimental investigation focusing on the phenomena to be characterised. Although, these models are not capable of describing the microstructural deformation mechanisms underlying the macroscopic structure of the material [6]. Due to the fact, that phenomenological models are fitted to certain load cases, they are only strictly applicable for the exact loading conditions for which the constitutive modelling was performed or for which the model was val-

idated. The steps of the complete phenomenological characterisation process are illustrated in Fig. 1.1 [5]. The material characterisation process is usually based on simple experimental work that highlights all the phenomena to be modelled in the simplest possible manner (e.g. using homogeneous deformations), which are then applied during the development of constitutive models. The constitutive modelling part ends with a validation step where the prediction of the proposed model are compared with the results of the simple mechanical tests. As a next step, the material model should also be validated for complex load cases using, e.g. finite element simulations for obtaining the model prediction for the load case. In this dissertation, this modelling approach is applied and investigated.

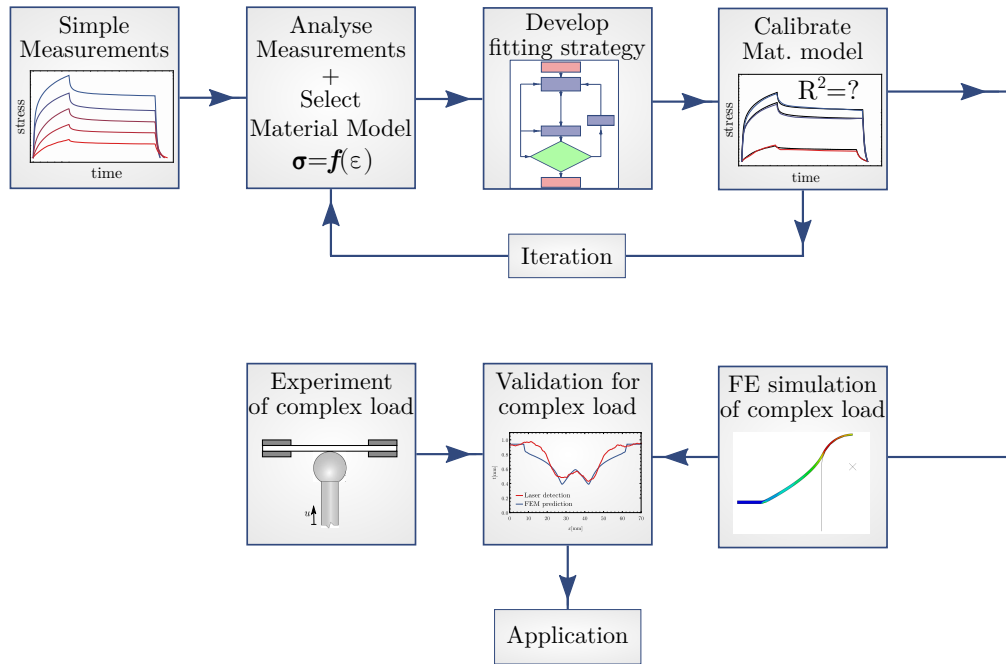


Figure 1.1: Schematics of complete material modelling using phenomenological approach (based on [5])

The mechanical behaviour of polymers usually exhibits large strains and large deformations with highly nonlinear effects. Therefore, in general, finite strain (or large-strain) continuum mechanics description is required for the adoption of such behaviours. In addition to the nonlinear elastic contribution, the deformation may also show linear/nonlinear viscous and linear/nonlinear yielding properties [10, 11, 12, 13, 14]. The available constitutive models (elastic, viscoelastic, viscoplastic) implemented in a commercial finite element (FE) software (such as ABAQUS [15], ANSYS [16], MSC MARC [17]) can be effectively used to obtain very accurate numerical results for the deformation of metals even with finite strain formulation. These models certainly have limitations, but those are still widely accepted and applied by the engineering and academic community. However, it should be emphasised that general, accurate constitutive models for polymers with finite strain deformations in combination with viscoelastic and viscoplastic effects are not available, and hence, researchers usually develop their own models for the particular material under investigation.

The commonly applied method for modelling the nonlinear viscoelastic-viscoplastic behaviour of polymers is the combination of a so-called hyperelastic constitutive equation with a suitably selected network of basic elements characterising nonlinear viscous and yielding behaviours. The hyperelastic modelling approach (which is described in detail in Section 2.3), was firstly developed for rubber-like materials, which are considered to be incompressible (or nearly-incompressible), and since then several incompressible hyperelastic models were published [18, 19]. However,

several polymers show significant volumetric deformation, for which usually an additional term is introduced in the strain-energy potential [6, 20, 21]. In the literature and in the commercial finite element software, the number of large-strain compressible hyperelastic material models are limited, while in the industry, there is significant need to model such material behaviour accurately.

According to the highly-cited flowchart of Hughes [22], the material modelling process takes at least 6–10% of the total engineering hours during a complete FE simulation process. However, the choice of material models fundamentally determines the result of the simulation and its validity. In industry, the design and manufacturing time can be significantly reduced, and process parameters can be optimised when the entire production process (e.g. thermoforming) is investigated with accurate FE simulations [23, 24, 25]. This requires a complete understanding of the behaviour of large-strain compressible materials with viscoelastic and viscoplastic effects and to develop the corresponding material models and parameter fitting strategies.

This thesis is dedicated to the mechanical modelling of polymer materials where different aspects of viscoelastic and viscoplastic properties occur under finite strain deformations. Three fundamental constitutive modelling approaches are investigated and combined: compressible hyperelastic, viscoelastic and viscoplastic. The hyperelastic constitutive models are applied when the deformations are elastic but in a nonlinear manner with large strains. Viscoelastic approach is assumed when explicit time-dependence occurs in the governing equations and the material has strain-rate dependent behaviour or “memory effect” without permanent deformations. Finally, viscoplastic models are adopted for those materials where the yielding behaviour is also rate-dependent. In this thesis, all three kinds of modelling approaches are considered through examples related to real engineering application.

The thesis contributes to the state-of-the-art literature by developing material characterisation process including experimental, analytical, and numerical methods as well as by providing advanced constitutive models for open- and closed-cell foams, microcellular thermoplastic foams and polymer airsoft pellets. The mechanical characterisation of such materials is an actively researched field due to their widespread use and industrial importance. The primary motivation of the thesis was to develop such phenomenological models, parameter fitting algorithms and strategies that can efficiently be utilised in real engineering problems and forms also the basis for further research. A further aim of the thesis was analysing the applicability of the proposed phenomenological models and investigating the model prediction on complex load cases. With this aim, experimental validation methods were also developed and proposed.

1.1 Layout

The present dissertation contains six chapters and is structured as follows. Chapter 1 summarises the background of the thesis, the motivation and goals of the Author. Then, the goals and the structure of the thesis are reviewed, and finally, the most important notations are summarised.

The chapters of the thesis discuss various engineering problems with large-strain compressible material behaviour; therefore, the literature overview is given at the beginning of each chapter. However, a general overview of the necessary theoretical background is provided in Chapter 2. After a brief introduction to the fundamentals of phenomenological modelling and material network models with small-strain formulation, the large-strain continuum mechanics formulation and the description of large-strain deformations and stresses are presented, including the theory of hyperelasticity as well. The summary of the small-strain elastoplasticity and viscoelasticity is also an essential part of this Chapter.

Chapter 3 considers the first engineering application, which is the pure elastic modelling of open- and closed-cell polymer foams using the Ogden–Hill compressible hyperelastic (or Hyperfoam¹) model. This model is well-known for foams and also implemented in ABAQUS, although, the material characterisation strongly depends on the transversal behaviour. In this Chapter, experimental investigations are presented, including mechanical tests and image processing techniques, whereas constitutive modelling strategies are compared and analysed.

In Chapter 4, the rate-dependent behaviour of open-cell foams (so-called “memory foams”) are investigated, for which a large-strain visco-hyperelastic constitutive model is proposed based on the previously applied Hyperfoam model. For this material model analytical stress solutions are derived, that can be utilised in the parameter-fitting procedure, which significantly improves the fitting accuracy compared to the separated fitting approach. The benefits of the closed-form fitting method are also illustrated via a case study on memory foams applied in mattresses.

Chapter 5 is dedicated to the modelling of thermoplastic microcellular polyethylene-terephthalate foam material (MC-PET), which is applied in lighting applications and manufactured using thermoforming. In this case, the material behaviour, in addition to its elastic behaviour, also exhibits viscous properties, and the permanent deformation is also significant. Here, a parallel viscoelastic-viscoplastic model was proposed for characterising the material response on the entire temperature domain that is relevant from the thermoforming aspect. For the parameter-fitting task, a FE-based numerical algorithm was implemented, whereas, for the validation, a punch-test based laser scanning method was proposed.

Finally, Chapter 6 presents the simulation of airsoft pellet impacts and its applicability as an impulse excitation method. This topic was motivated by the lack of proper excitation methods for rotating machine tools due to the posed safety-risks and the infeasibility of excitation by a modal hammer. In the ERC² funded research SIREN and ProExcer, a pneumatic ball excitation method was developed. However, the estimation of the relevant excitation frequency domain should be determined based on numerical simulations. According to the mechanical tests, similar material behaviour was detected as in case of the MC-PET material. Thus the similar modelling approach was extended, and the applicability of pellet impacts was also demonstrated via an experimental case study and numerical simulations.

1.2 Nomenclature

Latin letters

A, n, m	Creep law parameters
A_0, a	Initial and current cross section
\mathbf{A}, \mathbf{a}	Surface element vectors in the reference and in the current configuration
\mathbf{b}	Left Cauchy–Green deformation tensor
\mathbf{C}	Right Cauchy–Green deformation tensor
D	Damping factor
\mathbf{d}	Rate of deformation tensor
\mathbf{E}	Green–Lagrange strain tensor
E	Elastic modulus (Young’s modulus)
E_0, E_∞	Instantaneous and long-term elastic moduli
e_k	Relative elastic modulus
$\mathbf{E}_1, \mathbf{E}_2, \mathbf{E}_3$	Unit basis vectors in the reference configuration
$\mathbf{e}_1, \mathbf{e}_2, \mathbf{e}_3$	Unit basis vectors in the spatial configuration

¹The name of Ogden–Hill’s hyperelastic model in ABAQUS

²www.siren.mm.bme.hu

\mathbf{F}	Deformation gradient
f	Frequency
f_E	Fraction of elasticity (or elastic-ratio)
F	Load, force
G	Shear modulus
g_i	Relative shear modulus
\mathbf{H}	Right logarithmic (Hencky) strain tensor
\mathbf{h}	Left logarithmic (Hencky) strain tensor
H	Linear hardening modulus
H_0	Initial separation
\mathbf{I}	Second-order identity tensor
I_1, I_2, I_3	Principal scalar invariants of \mathbf{C} and \mathbf{b}
J	Volume ratio ($J = \det \mathbf{F}$)
K	Bulk modulus
k_i	Relative bulk modulus
\mathbf{l}	Eulerian velocity gradient
L_0, L	Initial and actual heights of the specimen
\mathbf{n}_i	Unit eigenvectors of \mathbf{b}
\mathbf{N}_i	Unit eigenvectors of \mathbf{C}
\mathbf{N}_Φ	Outward normal of the yield surface
N	Order of the hyperelastic material model
P	Order of the Prony-series
\mathbf{R}	Rotation tensor (proper orthogonal)
S	Standard error of regression
\mathbf{P}	First Piola–Kirchhoff stress tensor
\mathbf{S}	Second Piola–Kirchhoff stress tensor
\mathbf{s}	Deviatoric Cauchy stress tensor
t	Time
\mathbf{t}	Traction vector
t_r	Relaxation time
T	Temperature
T_g	Glass-transition temperature
u, U	Displacements
\mathbf{U}	Right stretch tensor
\mathbf{V}	Left stretch tensor
\mathbf{v}	Eulerian velocity field
\mathbf{v}_{Ω_0}	Lagrangian velocity field
W	Strain energy potential
\mathbf{w}	Spin tensor

Greek letters

$\alpha(t), \alpha(\omega)$	Acceleration signal and its FFT
α_i, β_i, μ_i	Material parameters in the Ogden–Hill’s hyperelastic material model
$\Gamma(\nu, x)$	Upper incomplete gamma function
$\delta_{\text{abs}}, \delta_{\text{rel}}$	Absolute and relative error
$\boldsymbol{\varepsilon}$	Small-strain tensor
ε^{eng}	Engineering strain
$\varepsilon^{\text{true}}$	True (or logarithmic) strain

ε^{cr}	Creep strain
$\boldsymbol{\varepsilon}^e, \varepsilon^e$	Elastic strain tensor, elastic strain
$\boldsymbol{\varepsilon}^p, \varepsilon^p$	Plastic strain tensor, plastic strain
$\bar{\varepsilon}^p$	Accumulated plastic strain
$\dot{\varepsilon}$	Engineering strain rate
η	Dynamic viscosity
Φ	Yield function
λ	Stretch
$\lambda_1, \lambda_2, \lambda_3$	Principal stretches
λ_p	Plastic multiplier
λ_T	Transversal stretch
ν	Poisson's ratio
σ	Cauchy stress
$\boldsymbol{\sigma}$	Cauchy stress tensor
σ_{y0}, σ_y	Initial and actual yield stress
τ	Kirchhoff stress
$\boldsymbol{\tau}$	Kirchhoff stress tensor
τ_i	Prony parameters
τ_r	Relaxation or retardation time
ω	Angular frequency

Calligraphic letters

\mathcal{D}^e	Elastic tangent modulus
\mathcal{D}^{ep}	Elastic-plastic tangent modulus
\mathcal{T}	Deviatoric projection tensor

Abbreviations

CU	Confined uniaxial
CB	Confined biaxial
D	Deviatoric
EB	Equibiaxial
H	Hydrostatic
inst	Instantaneous
long	Long-term
SS	Simple shear
UN, UA	Uniaxial
VOL	Volumetric

2

Theoretical background

This thesis focuses on the phenomenological modelling of polymers with large strain deformation in combination with viscoelastic and viscoplastic effects. In order to thoroughly understand the applied models and to analyse their performance and applicability, the theoretical background is summarised briefly.

2.1 Rheological models

In solid mechanics, the structure of complex three-dimensional constitutive models are often represented as one-dimensional networks of basic rheological elements (see Fig. 2.1), where the state variables are the $\sigma(t)$ Cauchy-stress and $\varepsilon(t)$ strain [5, 10, 26, 7, 8]. The elastic behaviour is usually illustrated by springs and in small-strain formulation characterised by the Hooke's law:

$$\sigma = E\varepsilon, \quad (2.1)$$

where E is the elastic (or Young's) modulus. The nonlinear elastic behaviour can be modelled with a nonlinear spring (see Nonlinear Hooke-element in Fig. 2.1/b), which is characterised formally by $\sigma = f_\sigma(\varepsilon)$. However, the exact formulation of such nonlinear springs is based on continuum mechanics formulation and the theory of hyperelasticity, which is discussed in Section 2.3 [6, 2, 1].

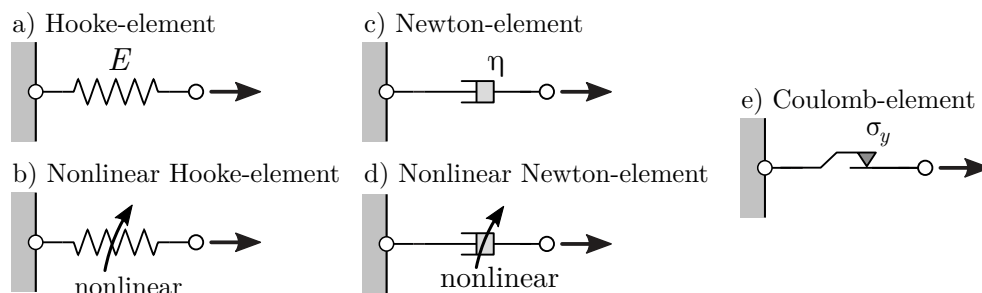


Figure 2.1: The basic rheological elements: a) Hooke-element, b) Nonlinear Hooke-element, c) Newton-element d) Nonlinear Newton-element and d) Coulomb-element

The viscous properties can be modelled with the Newton-element, illustrated as dashpots in Fig. 2.1/c, which provide a one-to-one connection between the stress $\sigma(t)$ and the strain rate $\dot{\varepsilon}(t)$.

If linear relation is assumed, the Newton-law holds, namely

$$\sigma = \eta \dot{\epsilon}, \tag{2.2}$$

where η is the (dynamic) viscosity. Of course, similarly to nonlinear springs, nonlinear Newton-elements can also be defined formally as $\sigma = f_\eta(\dot{\epsilon})$, for which several possible relations are proposed in the literature, see for example Anand, Norton–Hoff, Power-law, Hyberbolic-Sine or Eyring nonlinear viscous models [10, 14, 27].

Finally, the so-called Coulomb-element is applied to describe yielding properties, where (plastic) strain occurs only above a certain stress limit (e.g. yield stress). Therefore, the stress-strain relation can be summarised as [28]

$$\dot{\epsilon} = 0 \quad \text{if} \quad |\sigma| < \sigma_y, \quad \text{and} \quad \sigma = \begin{cases} \sigma_y & \rightarrow \dot{\epsilon} > 0 \\ -\sigma_y & \rightarrow \dot{\epsilon} < 0 \end{cases}. \tag{2.3}$$

This element is usually represented as a slider in Fig. 2.1/e. The detailed theory and the corresponding governing equations of small strain elastoplasticity are summarised in Section 2.4.

2.1.1 Viscoelastic behaviour

Elastic materials are capable of storing the potential energy during the loading process, and when the load is removed, the original shape is retrieved immediately. Compared to this, viscoelastic materials have viscous properties as well, which means that some energy is dissipated during loading, while the original shape is retrieved only in "infinite" time after the unloading. Viscoelastic behaviour also means that in case of cyclic loading a hysteresis can be observed in the stress-strain characteristic ($\sigma - \epsilon$), while the strain rate ($\dot{\epsilon}$) also influences the material response causing significant hardening, these properties are illustrated in Fig. 2.2/a-b [5, 10, 29, 1].

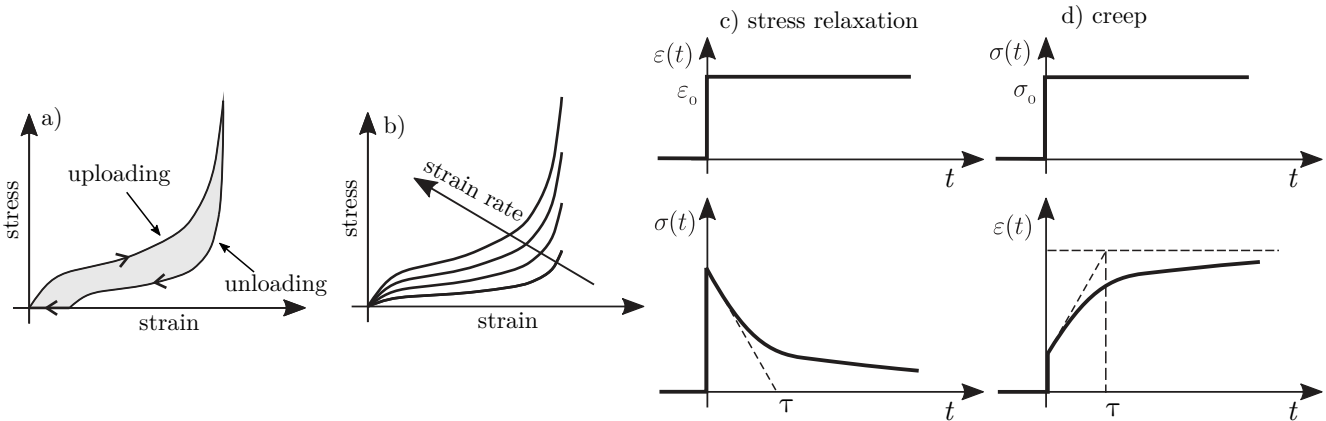


Figure 2.2: The main viscoelastic properties: a) hysteresis during cyclic loading with stress control, b) strain-rate dependence, and the illustration of a possible type of c) stress-relaxation and d) creep phenomena

The two most significant phenomena of the viscoelastic material behaviour are the stress-relaxation and the creep. In case of stress relaxation the stress decays exponential-likely, when the strain is kept constant $\epsilon(t) = \epsilon_0$, while in case of creep the stress is kept constant $\sigma(t) = \sigma_0$, which cause monotonously increasing strains (see Fig. 2.2/c-d).

Using the previously introduced linear spring and dashpot elements, the basic rheological models characterising viscoelastic behaviour can be constructed. The Maxwell-model (Fig. 2.3/a)

is the series connection of the spring and dashpot elements, where the total strain can be split between the spring and the dashpot elements as

$$\varepsilon(t) = \varepsilon_e(t) + \varepsilon_v(t), \quad \text{while} \quad \sigma(t) = \sigma_v(t) = \sigma_e(t), \quad (2.4)$$

where indices e and v refers to elastic and viscous contributions, respectively. Thus, applying (2.1) and (2.2), the governing equation for the total strain-rate becomes

$$\dot{\varepsilon}(t) = \frac{\sigma(t)}{\eta} + \frac{\dot{\sigma}(t)}{E}. \quad (2.5)$$

On the other hand, the parallel connection of the spring and the dashpot (Fig. 2.3/b) is called Kelvin–Voigt-model, where the total stress is decomposed additively and governing equations are expressed as

$$\sigma(t) = \sigma_v(t) + \sigma_e(t), \quad \varepsilon(t) = \varepsilon_e(t) = \varepsilon_v(t), \quad \text{and} \quad \sigma(t) = E\varepsilon(t) + \eta\dot{\varepsilon}(t). \quad (2.6)$$

The mechanical characterisation process of viscoelastic materials is usually based on stress-relaxation and displacement-driven mechanical tests. Connecting a spring in parallel with the Maxwell-element (see Fig. 2.3/c) gives the so-called Standard Linear Solid element (SLS), which is commonly applied for describing stress-relaxation. Combining the relations in (2.1)-(2.6), the governing differential equation of SLS becomes

$$\sigma(t) + \frac{\eta}{E}\dot{\sigma}(t) = E_\infty\varepsilon(t) + \left(1 + \frac{E_\infty}{E}\right)\eta\dot{\varepsilon}(t), \quad (2.7)$$

which can also be expressed in the form of a hereditary (or convolution) integral of the strain-rate as

$$\sigma(t) = \int_0^t E(t-s)\dot{\varepsilon}(s)ds, \quad (2.8)$$

where $E(t)$ is the relaxation modulus, which is defined as

$$E(t) = E_\infty + Ee^{-t/\tau_r}, \quad (2.9)$$

while E_∞ is the long-term elastic modulus. A significant parameter of the system is the time constant $\tau_r = \eta/E$, which is also commonly referred as relaxation or retardation time, respectively. Note, that SLS model forms the basis of the most-commonly applied finite-strain viscoelastic models (see Chapter 4).

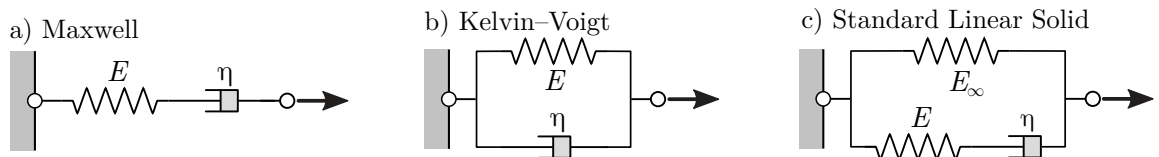


Figure 2.3: The basic models of linear viscoelasticity: a) Maxwell-model, b) Kelvin–Voigt-model and c) Standard Linear Solid model

2.2 Description of finite strain deformations

In solid mechanics, finite strain deformations and nonlinear material behaviour can effectively be described using the phenomenological approach of continuum mechanics. The fundamental assumption of continuum theory states that the material body is imagined as a continuous set of material points and has a continuous distribution of matter both in space and time, which can be characterised by continuous field variables on macroscopic level [1, 2, 6, 20, 21].

The general motion of a deformable body is shown in Fig. 2.4. At their initial position at $t = 0$, the material particles (occupying the region Ω_0) are identified with their \mathbf{X} coordinates with respect to Cartesian basis \mathbf{E}_i , which is referred as initial, reference or undeformed configuration. After deformation, the current position of particles at time instance t is described by coordinates \mathbf{x} in basis \mathbf{e}_i in the region Ω , which is also called current, spatial or deformed configuration [6, 20]. Furthermore, it is widely accepted simplification that the origin of the coordinate systems corresponding to initial and current configurations coincides. It should be noted, that there exists a more general description, where non-orthogonal curvilinear coordinates are applied for both configurations [30, 31, 32, 33]. However, from the material constitutive modelling point of view [5, 9], this representation has minor benefits, and thus the simplified, orthogonal Cartesian coordinates are applied.

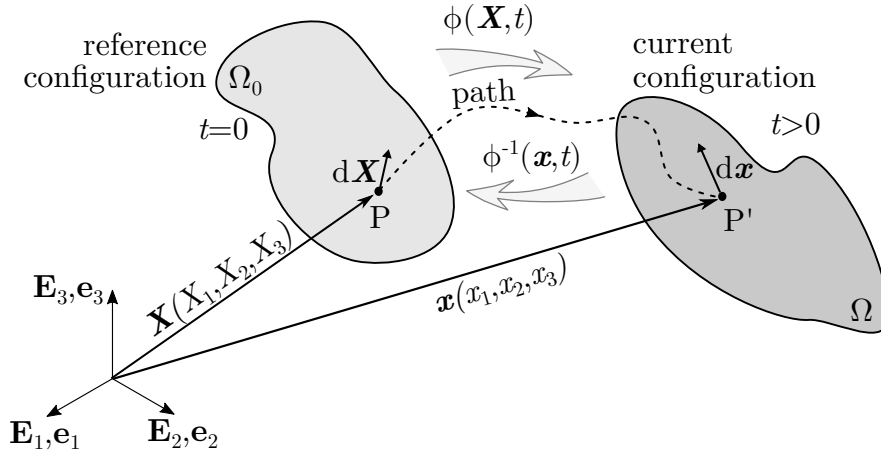


Figure 2.4: Representation of deformable solid in reference and current configurations

The mathematical description of the motion is given as a unique mapping ϕ between the initial and the reference configurations, namely

$$\mathbf{x} = \phi(\mathbf{X}, t). \quad (2.10)$$

Since, motion is assumed to be uniquely invertible, its inverse can be expressed as

$$\mathbf{X} = \phi^{-1}(\mathbf{x}, t). \quad (2.11)$$

In continuum mechanics, a careful distinction should be made between the description of quantities corresponding to the body under motion. The so-called material (or Lagrangian) description is applied to characterise quantities in the reference configuration, as a function of coordinates \mathbf{X} and time t . Whereas, the spatial (or Eulerian) description uses coordinates \mathbf{x} and time t corresponding to the deformed configuration.

The local deformation is characterised primarily by the deformation gradient \mathbf{F} defined as

$$\mathbf{F}(\mathbf{X}, t) = \frac{\partial \phi(\mathbf{X}, t)}{\partial \mathbf{X}} = F_{aB} \mathbf{e}_a \otimes \mathbf{E}_B, \quad (2.12)$$

which relates the infinitesimal line elements as $d\mathbf{x} = \mathbf{F}(\mathbf{X}, t)d\mathbf{X}$. To ensure non-singular motion, the deformation gradient should satisfy $\det(\mathbf{F}) > 0$. Using the inverse motion, the inverse deformation gradient can be expressed as

$$\mathbf{F}^{-1}(\mathbf{x}, t) = \frac{\partial \phi^{-1}(\mathbf{x}, t)}{\partial \mathbf{x}} = F_{Ab} \mathbf{E}_A \otimes \mathbf{e}_b. \quad (2.13)$$

The motion is considered to be homogeneous, if the deformation gradient does not depend on the material coordinates, namely $\mathbf{F}(\mathbf{X}, t) = \mathbf{F}(t)$ or $\mathbf{F}^{-1}(\mathbf{x}, t) = \mathbf{F}^{-1}(t)$.

2.2.1 Strain measures

Using the deformation gradient several deformation and strain measures can be introduced [2, 6, 20]. The symmetric and positive definite left and right Cauchy–Green deformation tensors are defined as:

$$\text{right Cauchy–Green deformation tensor: } \mathbf{C}(\mathbf{X}, t) = \mathbf{F}^T \mathbf{F}, \quad (2.14)$$

$$\text{left Cauchy–Green deformation tensor: } \mathbf{b}(\mathbf{x}, t) = \mathbf{F} \mathbf{F}^T, \quad (2.15)$$

from, which the Green–Lagrange strain tensor can be introduced as

$$\mathbf{E}(\mathbf{X}, t) = \frac{1}{2} (\mathbf{C} - \mathbf{I}). \quad (2.16)$$

The non-singular deformation gradient can be decomposed uniquely using the so-called polar decomposition theorem [6, 20] as

$$\mathbf{F} = \mathbf{R} \mathbf{U} = \mathbf{V} \mathbf{R} \quad (2.17)$$

where $\mathbf{U}(\mathbf{X}, t)$ and $\mathbf{V}(\mathbf{x}, t)$ are the right and left stretch tensors, respectively, while \mathbf{R} is a proper orthogonal rotation tensor. Using the polar decomposition, the deformation is split to stretching (given by \mathbf{U} and \mathbf{V}) and a superimposed rigid-body rotation given by \mathbf{R} . The stretch tensors are related to the strain tensors as

$$\mathbf{U} = \sqrt{\mathbf{C}}, \quad \text{and} \quad \mathbf{V} = \sqrt{\mathbf{b}}. \quad (2.18)$$

The λ_i eigenvalues of \mathbf{U} and \mathbf{V} are called principal stretches, while the corresponding normalized eigenvectors \mathbf{N}_i and $\mathbf{n}_i = \mathbf{R} \mathbf{N}_i$ define the principal directions. The principal stretches give the ratio between current and initial lengths of a line element in the principal directions. Consequently, \mathbf{C} and \mathbf{U} can be expressed with their spectral decomposition as

$$\mathbf{U} = \sum_{i=1}^3 \lambda_i \mathbf{N}_i \otimes \mathbf{N}_i, \quad \text{and} \quad \mathbf{C} = \sum_{i=1}^3 \lambda_i^2 \mathbf{N}_i \otimes \mathbf{N}_i. \quad (2.19)$$

Similarly, the corresponding Eulerian quantities can also be expressed as

$$\mathbf{V} = \sum_{i=1}^3 \lambda_i \mathbf{n}_i \otimes \mathbf{n}_i, \quad \text{and} \quad \mathbf{b} = \sum_{i=1}^3 \lambda_i^2 \mathbf{n}_i \otimes \mathbf{n}_i. \quad (2.20)$$

Using \mathbf{U} and \mathbf{V} the material and spatial logarithmic strain tensors can also be introduced as

$$\mathbf{H}(\mathbf{X}, t) = \sum_{i=1}^3 \ln \lambda_i \mathbf{N}_i \otimes \mathbf{N}_i = \ln \mathbf{U}, \quad \text{and} \quad \mathbf{h}(\mathbf{x}, t) = \sum_{i=1}^3 \ln \lambda_i \mathbf{n}_i \otimes \mathbf{n}_i = \ln \mathbf{V}. \quad (2.21)$$

Finally, the volume change of an infinitesimal volume element is given by the volume ratio J as

$$J = \det \mathbf{F}, \quad (2.22)$$

for which $J > 0$ should hold in order ensure physically admissible deformation [6, 20].

2.2.2 Velocity and time-derivatives

Obviously, the deformation is in many cases rate-dependent and thus, the velocity and other time-derivatives should be obtained [2, 6, 20]. The Lagrangian velocity field can be introduced as

$$\mathbf{v}_{\Omega_0}(\mathbf{X}, t) = \frac{\partial \phi(\mathbf{X}, t)}{\partial t}, \quad (2.23)$$

while the Eulerian velocity field can be obtained as

$$\mathbf{v}(\mathbf{x}, t) = \mathbf{v}_{\Omega_0}(\phi^{-1}(\mathbf{x}, t), t). \quad (2.24)$$

From the velocity field, the Eulerian velocity gradient \mathbf{l} can be defined as

$$\mathbf{l}(\mathbf{x}, t) = \frac{\partial \mathbf{v}(\mathbf{x}, t)}{\partial \mathbf{x}} = \dot{\mathbf{F}} \mathbf{F}^{-1}, \quad (2.25)$$

which can be additively decomposed to the symmetric rate of deformation tensor \mathbf{d} and the skew-symmetric spin tensor \mathbf{w} using

$$\mathbf{l}(\mathbf{x}, t) = \mathbf{d}(\mathbf{x}, t) + \mathbf{w}(\mathbf{x}, t), \quad (2.26)$$

where

$$\mathbf{d} = \frac{1}{2} (\mathbf{l} + \mathbf{l}^T), \quad \text{and} \quad \mathbf{w} = \frac{1}{2} (\mathbf{l} - \mathbf{l}^T). \quad (2.27)$$

Similarly, the time-derivative of other quantities can be introduced. However, different derivation rules apply for Lagrangian and Eulerian fields. In continuum mechanics, material time derivative (total time derivative) represents the rate of change seen by an observer following the path of a certain material particle. Let us consider a general Lagrangian scalar or tensor field $\mathcal{F}_{\Omega_0}(\mathbf{X}, t)$ and an Eulerian one $f_{\Omega}(\mathbf{x}, t)$. The material time derivative of such quantities can be expressed as

$$\dot{\mathcal{F}}_{\Omega_0}(\mathbf{X}, t) = \frac{D\mathcal{F}_{\Omega_0}(\mathbf{X}, t)}{Dt} = \left(\frac{\partial \mathcal{F}_{\Omega_0}(\mathbf{X}, t)}{\partial t} \right)_{\mathbf{X}}, \quad (2.28)$$

$$\dot{f}_{\Omega}(\mathbf{x}, t) = \frac{Df_{\Omega}(\mathbf{x}, t)}{Dt} = \frac{\partial f_{\Omega}(\mathbf{x}, t)}{\partial t} + \text{grad}(f_{\Omega}(\mathbf{x}, t)) \cdot \mathbf{v}(\mathbf{x}, t). \quad (2.29)$$

In case of the material time derivative of spatial fields, the first term in (2.29) is called local (or spatial) time derivative, while the second term is the convective derivative. Using the derivation rules, most important time derivatives of the previously introduced strain and stress measures become

$$\dot{\mathbf{F}} = \mathbf{lF}, \quad (2.30)$$

$$\dot{\mathbf{C}} = 2\mathbf{F}^T \mathbf{dF}, \quad (2.31)$$

$$\dot{\mathbf{b}} = \mathbf{lb} + \mathbf{bl}^T, \quad (2.32)$$

$$\dot{\mathbf{E}} = \mathbf{F}^T \mathbf{dF}, \quad (2.33)$$

$$\dot{J} = J \text{tr}(\mathbf{d}). \quad (2.34)$$

2.2.3 Concept of stress

During the deformation of a solid body, interaction occurs in between the neighbouring regions of the body. Let us cut virtually the body into two parts and investigate the resultant spatial force $\Delta \mathbf{f}$ acting on the element area Δa corresponding to the normal vector \mathbf{n} (see Fig. 2.5) [2, 6, 20]. Then, the traction field can be defined as

$$\mathbf{t}(\mathbf{n}) = \lim_{\Delta a \rightarrow 0} \frac{\Delta \mathbf{f}}{\Delta a} = \frac{d\mathbf{f}}{da}, \quad (2.35)$$

for, which according to Newton's third law $\mathbf{t}(\mathbf{n}) = -\mathbf{t}(-\mathbf{n})$ holds. For each material point \mathbf{x} in the current configuration, there exists a second-order tensor field $\boldsymbol{\sigma}(\mathbf{x}, t)$ such that

$$\mathbf{t}(\mathbf{n}, \mathbf{x}, t) = \boldsymbol{\sigma}(\mathbf{x}, t)\mathbf{n}, \quad \text{and} \quad d\mathbf{f} = \boldsymbol{\sigma}\mathbf{n}da = \boldsymbol{\sigma}d\mathbf{a} \quad (2.36)$$

which is called the Cauchy-stress tensor, which is a symmetric tensor, thus $\boldsymbol{\sigma} = \boldsymbol{\sigma}^T$. In the derivation of the Cauchy-stress tensor both the area element $\Delta \mathbf{a} = \Delta a \mathbf{n}$ and the force vector $\Delta \mathbf{f}$ were given in the current configuration.

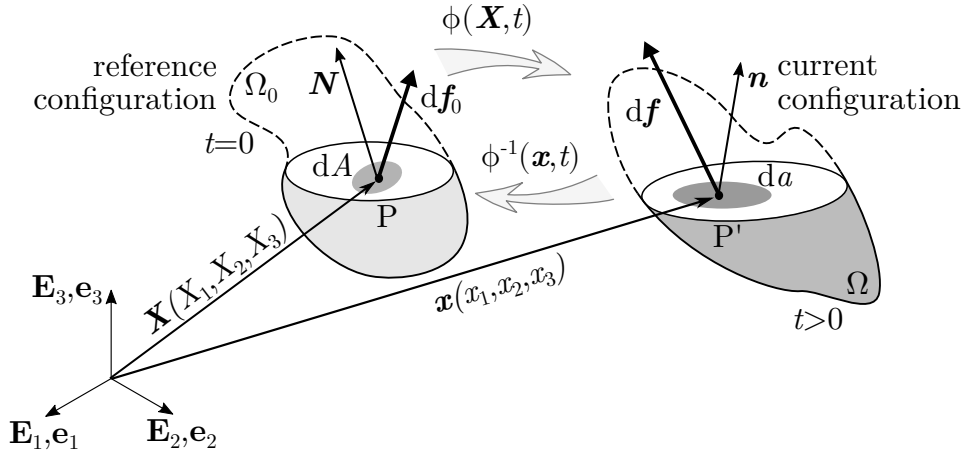


Figure 2.5: Representation of surface traction

The first Piola–Kirchhoff stress tensor is a two-point tensor that relates $d\mathbf{f}$ with the area element $d\mathbf{A}$ in the reference configuration. Therefore, using Nanson's formula $d\mathbf{a} = J\mathbf{F}^{-T}d\mathbf{A}$, the non-symmetric, two-point Piola–Kirchhoff stress tensor becomes

$$d\mathbf{f} = \mathbf{P}N dA = \mathbf{P}d\mathbf{A}, \quad \text{and} \quad \mathbf{P} = J\boldsymbol{\sigma}\mathbf{F}^{-T}. \quad (2.37)$$

Similarly, the infinitesimal force vector $d\mathbf{f}$ can also be expressed in the reference configuration with $d\mathbf{f}_0$ using $d\mathbf{f} = \mathbf{F}d\mathbf{f}_0$. Substituting, this back into (2.37), the second Piola–Kirchhoff stress tensor \mathbf{S} can be introduced as

$$d\mathbf{f}_0 = \mathbf{S}N dA = \mathbf{S}d\mathbf{A}, \quad \text{and} \quad \mathbf{S} = J\mathbf{F}^{-1}\boldsymbol{\sigma}\mathbf{F}^{-T}. \quad (2.38)$$

Finally, the spatial, Kirchhoff stress tensor can also be introduced by

$$\boldsymbol{\tau} = J\boldsymbol{\sigma}. \quad (2.39)$$

The relation of the stress tensors are summarised in Table 2.1.

Table 2.1: The relation of stress tensors

	$\boldsymbol{\sigma}$	\boldsymbol{P}	\boldsymbol{S}	$\boldsymbol{\tau}$
$\boldsymbol{\sigma}$	-	$\boldsymbol{\sigma} = J^{-1} \boldsymbol{P} \boldsymbol{F}^T$	$\boldsymbol{\sigma} = J^{-1} \boldsymbol{F} \boldsymbol{S} \boldsymbol{F}^T$	$\boldsymbol{\sigma} = J^{-1} \boldsymbol{\tau}$
\boldsymbol{P}	$\boldsymbol{P} = J \boldsymbol{\sigma} \boldsymbol{F}^{-T}$	-	$\boldsymbol{P} = \boldsymbol{F} \boldsymbol{S}$	$\boldsymbol{P} = \boldsymbol{\tau} \boldsymbol{F}^{-T}$
\boldsymbol{S}	$\boldsymbol{S} = J \boldsymbol{F}^{-1} \boldsymbol{\sigma} \boldsymbol{F}^{-T}$	$\boldsymbol{S} = \boldsymbol{F}^{-1} \boldsymbol{P}$	-	$\boldsymbol{S} = \boldsymbol{F}^{-1} \boldsymbol{\tau} \boldsymbol{F}^{-T}$
$\boldsymbol{\tau}$	$\boldsymbol{\tau} = J \boldsymbol{\sigma}$	$\boldsymbol{\tau} = \boldsymbol{P} \boldsymbol{F}^T$	$\boldsymbol{\tau} = \boldsymbol{F} \boldsymbol{S} \boldsymbol{F}^T$	-

2.2.4 Objectivity

An important concept in solid mechanics is the notion of objectivity [20]. The main concept of objectivity is that the material response should remain invariant for the change of equivalent observers, which are related through the Euclidean transformation expressed as $\tilde{\boldsymbol{x}} = \boldsymbol{c}(t) + \boldsymbol{Q}(t)\boldsymbol{x}$ and $\tilde{t} = t - \alpha$. This can equivalently be viewed as a rigid-body motion superimposed on the current configuration. The requirement of objectivity is fulfilled, if the different spatial field variables transform under the change of observer according to the following rules [6]:

$$\text{Second-order tensor fields: } \tilde{\boldsymbol{A}}(\tilde{\boldsymbol{x}}, \tilde{t}) = \boldsymbol{Q}(t) \boldsymbol{A}(\boldsymbol{x}, t) \boldsymbol{Q}^T(t), \quad (2.40)$$

$$\text{Vector fields: } \tilde{\boldsymbol{u}}(\tilde{\boldsymbol{x}}, \tilde{t}) = \boldsymbol{Q}(t) \boldsymbol{u}(\boldsymbol{x}, t), \quad (2.41)$$

$$\text{Scalar fields: } \tilde{\phi}(\tilde{\boldsymbol{x}}, \tilde{t}) = \phi(\boldsymbol{x}, t). \quad (2.42)$$

Note that the transformation of two-point tensors (e.g. \boldsymbol{F} , or \boldsymbol{P} follow the rule of vectors. Among the previously introduced fields $J, \boldsymbol{F}, \boldsymbol{C}, \boldsymbol{b}, \boldsymbol{E}, \boldsymbol{R}, \boldsymbol{U}, \boldsymbol{V}, \boldsymbol{d}$ and $\boldsymbol{\sigma}$ are objective, whereas $\boldsymbol{v}, \boldsymbol{l}$ and $\dot{\boldsymbol{\sigma}}$ are not objective [2, 6, 20]. This latter one causes severe problem since constitutive models are usually formulated in rate form. A possible solution is to introduce so-called objective rates, which are modified material time derivatives in order to ensure objectivity. The two most commonly applied objective rates in FE implementations: the Jaumann- and the Green-Naghdi rates [6, 15, 16, 17]. The general form of such co-rotational rate is expressed as

$$\dot{\boldsymbol{M}}^* = \dot{\boldsymbol{M}} - \boldsymbol{Q}^* \boldsymbol{M} + \boldsymbol{M} \boldsymbol{Q}^*, \quad (2.43)$$

where the corresponding skew-symmetric spin tensor \boldsymbol{Q}^* is defined for Jaumann-rate as $\boldsymbol{Q}^J = \boldsymbol{w}$, while for the Green-Naghdi rate $\boldsymbol{Q}^{\text{GN}} = \dot{\boldsymbol{R}} \boldsymbol{R}^T$.

2.3 Theory of Hyperelasticity

In linear isotropic elasticity the stress and the strain are related by the Hooke's law as

$$\boldsymbol{\sigma} = \frac{E}{1+\nu} \left[\boldsymbol{\varepsilon} + \frac{\nu}{1-2\nu} \varepsilon_I \boldsymbol{I} \right]. \quad (2.44)$$

For simplicity, let us introduce the 4th-order elasticity tensor $\boldsymbol{\mathcal{D}}^e$ (also called as Hooke's operator), which is defined as

$$\boldsymbol{\mathcal{D}}^e = \frac{E}{1+\nu} \boldsymbol{\mathcal{T}} + \frac{E}{3(1-2\nu)} \boldsymbol{I} \otimes \boldsymbol{I}, \quad (2.45)$$

where $\boldsymbol{\mathcal{T}}$ is the 4th-order deviatoric projection tensor. Therefore, the Hooke's law can be rewritten in a simplified form using the Hooke's operator as [1, 2]

$$\boldsymbol{\sigma} = \boldsymbol{\mathcal{D}}^e : \boldsymbol{\varepsilon}. \quad (2.46)$$

Alternatively, one can also express the linear stress-strain relation (i.e. the Hooke's law) as

$$\boldsymbol{\sigma} = \mathcal{D}^e : \boldsymbol{\varepsilon} = \frac{\partial}{\partial \boldsymbol{\varepsilon}} \left(\frac{1}{2} \boldsymbol{\varepsilon} : \mathcal{D}^e : \boldsymbol{\varepsilon} \right), \quad (2.47)$$

where the scalar-valued function $W(\boldsymbol{\varepsilon}) = (\boldsymbol{\varepsilon} : \mathcal{D}^e : \boldsymbol{\varepsilon})/2$ is the stored elastic (or strain) energy per unit volume.

Similarly, when the mechanical behaviour cannot be described using small-strain theory and one consider finite-strain material formulation, the so-called hyperelastic constitutive equations can also be derived from a polyconvex scalar function $W(\mathbf{F})$, which expresses the stored strain energy per unit reference volume as the function of deformation gradient \mathbf{F} [2, 6].

The existence of such a function $W(\mathbf{F})$ for a hyperelastic material leads that the stress power per unit reference volume is equal to the time derivative of W i.e. \dot{W} . The stress power \dot{W} can also be related to the stress tensors as

$$\dot{W} = J \boldsymbol{\sigma} : \mathbf{d} = \boldsymbol{\tau} : \mathbf{d} = \mathbf{P} : \dot{\mathbf{F}}. \quad (2.48)$$

Simultaneously, \dot{W} can be expressed as the time derivative of the strain energy function $W(\mathbf{F})$ by applying the chain rule of derivation, therefore

$$\dot{W} = \frac{\partial W(\mathbf{F})}{\partial \mathbf{F}} : \dot{\mathbf{F}}. \quad (2.49)$$

Comparing the formulations of \dot{W} in (2.48) and (2.49) gives that the first Piola–Kirchhoff stress tensor (\mathbf{P}) can be directly derived from the strain energy function as

$$\mathbf{P} = \frac{\partial W(\mathbf{F})}{\partial \mathbf{F}}. \quad (2.50)$$

When an additional rigid body rotation (\mathbf{Q}) added to the deformation, the deformation gradient satisfies the material objectivity, thus the deformation gradient in the rotated coordinate system becomes $\tilde{\mathbf{F}} = \mathbf{Q}\mathbf{F}$. This yields that the strain energy function can be rewritten as

$$W(\mathbf{F}) = W(\mathbf{Q}\mathbf{F}), \quad (2.51)$$

because the stored strain energy does not change when an additional rigid body rotation is applied on the body. If the rigid body rotation tensor is chosen as $\mathbf{Q} = \mathbf{R}^T$ based on the polar decomposition theorem in (2.17), then W can be expressed as

$$W(\mathbf{F}) = W(\mathbf{Q}\mathbf{R}\mathbf{U}) = W(\mathbf{R}^T \mathbf{R}\mathbf{U}) = W(\mathbf{U}), \quad (2.52)$$

which is a necessary and sufficient condition for an objective strain energy function [6]. Consequently, using the relation in (2.18) the strain energy function W is also the function of the right Cauchy–Green deformation tensor \mathbf{C} , therefore

$$W(\mathbf{F}) = \tilde{W}(\mathbf{C}), \quad (2.53)$$

from which the stress power can be expressed as

$$\dot{W} = \frac{\partial W(\mathbf{F})}{\partial \mathbf{F}} : \dot{\mathbf{F}} = \frac{\partial \tilde{W}(\mathbf{C})}{\partial \mathbf{C}} \frac{\partial \mathbf{C}}{\partial \mathbf{F}} : \dot{\mathbf{F}}. \quad (2.54)$$

According to (2.14), the partial derivative in (2.54) can be simplified as

$$\frac{\partial \mathbf{C}}{\partial \mathbf{F}} = 2\mathbf{F}. \quad (2.55)$$

Consequently, when the strain energy function W is related to the right Cauchy–Green deformation tensor as $W = W(\mathbf{C})$, the first Piola–Kirchhoff stress tensor becomes

$$\mathbf{P} = 2\mathbf{F} \frac{\partial W(\mathbf{C})}{\partial \mathbf{C}}. \quad (2.56)$$

Therefore, applying the relations of the stress tensors in Table 2.1 leads to

$$\mathbf{S} = 2 \frac{\partial W(\mathbf{C})}{\partial \mathbf{C}}, \quad \boldsymbol{\tau} = 2\mathbf{F} \frac{\partial W(\mathbf{C})}{\partial \mathbf{C}} \mathbf{F}^T, \quad \text{and} \quad \boldsymbol{\sigma} = \frac{2}{J} \mathbf{F} \frac{\partial W(\mathbf{C})}{\partial \mathbf{C}} \mathbf{F}^T. \quad (2.57)$$

2.3.1 Isotropic hyperelasticity

In case of isotropic material the strain energy function satisfies $W(\mathbf{C}) = W(\mathbf{C}\mathbf{Q})$ for any arbitrary proper orthogonal tensor \mathbf{Q} , and consequently it can be expressed by either the function of the principal invariants of \mathbf{C} (I_1, I_2 and I_3) or the principal stretches (λ_1, λ_2 and λ_3) [6]. Therefore

$$W = W(I_1, I_2, I_3) \quad \text{or} \quad W = W(\lambda_1, \lambda_2, \lambda_3), \quad (2.58)$$

where the scalar invariants of \mathbf{C} are defined as

$$I_1 = \text{tr}(\mathbf{C}), \quad I_2 = \frac{1}{2}(I_1^2 - \text{tr}(\mathbf{C}^2)), \quad I_3 = \det \mathbf{C} = J^2. \quad (2.59)$$

Since the $(\lambda_i)^2$ are the eigenvalues of tensor \mathbf{C} , the scalar invariants can be expressed using the principal stretches (λ_1, λ_2 and λ_3) as

$$I_1 = \lambda_1^2 + \lambda_2^2 + \lambda_3^2, \quad I_2 = (\lambda_1\lambda_2)^2 + (\lambda_1\lambda_3)^2 + (\lambda_2\lambda_3)^2, \quad I_3 = (\lambda_1\lambda_2\lambda_3)^2. \quad (2.60)$$

Let us consider the case when the strain energy function is defined using the principal stretches, i.e. $W = W(\lambda_1, \lambda_2, \lambda_3)$. Then the chain-rule for derivation gives that

$$\mathbf{S} = 2 \frac{\partial W(\lambda_1, \lambda_2, \lambda_3)}{\partial \mathbf{C}} = 2 \sum_{k=1}^3 \frac{\partial W(\lambda_1, \lambda_2, \lambda_3)}{\partial \lambda_k} \frac{\partial \lambda_k}{\partial \mathbf{C}}, \quad (2.61)$$

where the corresponding derivation rule is

$$\frac{\partial \lambda_k}{\partial \mathbf{C}} = \frac{1}{2\lambda_k} \mathbf{N}_k \otimes \mathbf{N}_k, \quad (2.62)$$

in which \mathbf{N}_k are the unit eigenvectors of \mathbf{C} . Then substituting (2.62) back into (2.61), the second Piola–Kirchhoff stress tensor \mathbf{S} becomes

$$\mathbf{S} = \sum_{k=1}^3 \frac{1}{\lambda_k} \frac{\partial W}{\partial \lambda_k} \mathbf{N}_k \otimes \mathbf{N}_k. \quad (2.63)$$

Therefore, applying the relation of the stress tensors in Table 2.1, they can be expressed as

$$\boldsymbol{\sigma} = \sum_{k=1}^3 \frac{\lambda_k}{J} \frac{\partial W}{\partial \lambda_k} \mathbf{n}_k \otimes \mathbf{n}_k, \quad (2.64)$$

$$\boldsymbol{\tau} = \sum_{k=1}^3 \lambda_k \frac{\partial W}{\partial \lambda_k} \mathbf{n}_k \otimes \mathbf{n}_k, \quad (2.65)$$

$$\mathbf{P} = \sum_{k=1}^3 \frac{\partial W}{\partial \lambda_k} \mathbf{n}_k \otimes \mathbf{N}_k, \quad (2.66)$$

where \mathbf{n}_k are the unit eigenvectors of the left Cauchy–Green deformation tensor (\mathbf{b}), for which $\mathbf{N}_k = \lambda_k \mathbf{F}^{-1} \mathbf{n}_k$ holds. Based on equations (2.63) - (2.66) the principal stresses can be expressed as

$$S_k = \frac{1}{\lambda_k} \frac{\partial W}{\partial \lambda_k}, \quad \sigma_k = \frac{\lambda_k}{J} \frac{\partial W}{\partial \lambda_k}, \quad \tau_k = \lambda_k \frac{\partial W}{\partial \lambda_k}, \quad P_k = \frac{\partial W}{\partial \lambda_k}, \quad k = 1, 2, 3. \quad (2.67)$$

2.4 Theory of small strain plasticity

The mathematical theory of plasticity gives a general framework for the phenomenological description of materials that sustain permanent deformation after complete unloading. The basic assumption for plastic behaviour is the existence of an elastic domain within the material behaviour is considered as purely elastic without any permanent strain occurring. This elastic domain, however, is limited by the so-called yield stress, above which the evolution of permanent (or plastic) strains take place, which might be accompanied by the evolution of yield stress when hardening is assumed [2, 11, 12, 13, 34, 35]. In the following, the introduction of basic equations of plasticity is restricted to infinitesimal deformations and thus small strain formulation is applied, which can be generalized to finite strains according to [1, 11].

The fundamental assumption in the theory of incremental plasticity is the additive decomposition of the total strain increment $d\boldsymbol{\varepsilon}$ into elastic and plastic contributions as

$$d\boldsymbol{\varepsilon} = d\boldsymbol{\varepsilon}^e + d\boldsymbol{\varepsilon}^p, \quad (2.68)$$

where $d\boldsymbol{\varepsilon}^e$ and $d\boldsymbol{\varepsilon}^p$ stand for elastic and plastic strain increments, respectively. The additive split of the total strain for one-dimensional case is illustrated in Fig. 2.6, which shows an ideal uniaxial stress-strain response of an elastic-plastic material. Close to the origin, the material response is purely elastic, until the initial yield stress σ_{y0} is reached. Above that point, the material yields and the deformation shows elastic-plastic properties. Note, that for this simplified case the additive split in (2.68) also holds for the total strains, letting $\boldsymbol{\varepsilon} = \boldsymbol{\varepsilon}^e + \boldsymbol{\varepsilon}^p$.

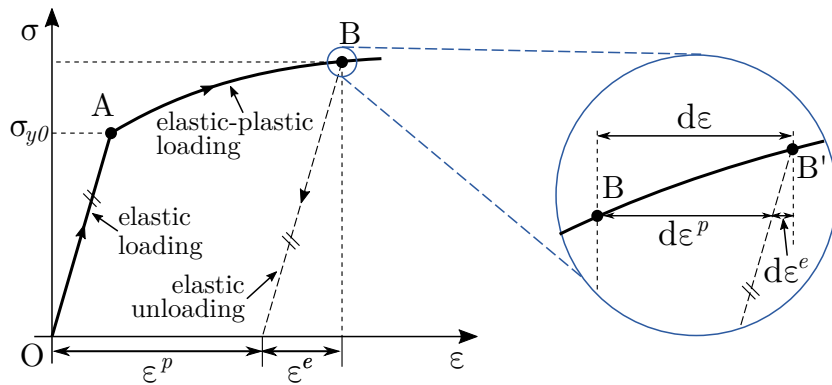


Figure 2.6: Elastic-plastic material response for uniaxial loading

The elastic domain is limited by the yield function $\Phi(\boldsymbol{\sigma}, \sigma_y)$, which defines a yield surface in the Haigh-Westergaard stress-space [36, 37] by

$$\Phi(\boldsymbol{\sigma}, \sigma_y) = 0, \quad (2.69)$$

where σ_y is the actual yield stress. The elastic domain is defined as

$$\Phi(\boldsymbol{\sigma}, \sigma_y) < 0, \quad (2.70)$$

while in case of yielding or plastic deformation $\Phi = 0$ holds. Therefore, the physically admissible stress states are defined by the criterion $\Phi \leq 0$ [2, 11].

2.4.1 Associative flow rule with von Mises criterion

In this thesis, the associative von Mises elastoplasticity model is applied in combination with linear isotropic hardening. According to the von Mises yield criterion [38], plastic yielding begins when $J_2 = \text{tr}(\mathbf{s}^2)/2$ stress deviator invariant reaches a critical value, where \mathbf{s} is the deviatoric part of the Cauchy stress, namely

$$\mathbf{s} = \boldsymbol{\sigma} - \frac{1}{3} \text{tr}(\boldsymbol{\sigma}) \mathbf{I}. \quad (2.71)$$

Therefore, the yield function for the von Mises criterion, which defines a cylinder in the Haigh–Westergaard stress space can be expressed as

$$\Phi(\boldsymbol{\sigma}, \sigma_y) = \sqrt{\frac{3}{2} \mathbf{s} : \mathbf{s}} - \sigma_y. \quad (2.72)$$

As the yield stress is reached, further loading initiates plastic flow, which is governed by the associative plastic flow rule as

$$\dot{\boldsymbol{\epsilon}}^p = \dot{\lambda}_p \frac{\partial \Phi}{\partial \boldsymbol{\sigma}} = \dot{\lambda}_p \sqrt{\frac{3}{2}} \frac{\mathbf{s}}{\|\mathbf{s}\|}, \quad (2.73)$$

where $\dot{\lambda}_p$ is the plastic multiplier, while the direction of the plastic strain rate is defined by the surface gradient $\partial \Phi / \partial \boldsymbol{\sigma} = \mathbf{N}_\Phi$, yielding that the strain rate is perpendicular to the yield surface. Note, that the associative von Mises perfectly plastic constitutive model is commonly referred to as Prandtl–Reuss equations [12, 39, 40].

During plastic flow, the plastic strain accumulates in the material, while during elastic loading the accumulated strain is conserved, thus for the plastic multiplier, the consistency criterion of

$$\dot{\lambda}_p \geq 0 \quad (2.74)$$

should hold [2, 11, 12, 13, 34]. Together, with the criterion corresponding to the yield function, the Kuhn–Tucker conditions [11, 12] can be formulated as

$$\dot{\Phi} \leq 0, \quad \dot{\lambda}_p \geq 0, \quad \text{and} \quad \Phi \dot{\lambda}_p = 0. \quad (2.75)$$

2.4.2 Isotropic hardening

During plastic deformation, the yield stress might also increase during loading, which can be characterised by the so-called hardening laws. A hardening law is said to be isotropic when the yield surface expands uniformly without translation. In such case, the elastic region expands equally in tension and compression during plastic flow, which can also be imagined as an increase in the radius of the von Mises cylinder [2, 11, 12, 13, 34, 36, 37].

Firstly, let us introduce the accumulated plastic strain as

$$\bar{\varepsilon}^p = \int_0^t \sqrt{\frac{2}{3} \dot{\varepsilon}^p : \dot{\varepsilon}^p} dt, \quad (2.76)$$

which after comparison with (2.73) yields

$$\dot{\varepsilon}^p = \dot{\lambda}_p. \quad (2.77)$$

In isotropic hardening the yield stress is assumed to be a function of the accumulated plastic strain, letting

$$\sigma_y = \sigma_y(\bar{\varepsilon}^p). \quad (2.78)$$

In case of linear isotropic hardening, the hardening rule simplifies to

$$\sigma_y(\bar{\varepsilon}^p) = \sigma_{y0} + H\bar{\varepsilon}^p, \quad (2.79)$$

where H is the plastic hardening modulus. Of course, if necessary, nonlinear hardening characteristics can also be introduced [2], like

$$\sigma_y(\bar{\varepsilon}^p) = \sigma_{y0} + H(\bar{\varepsilon}^p)^m \quad \text{or} \quad \sigma_y(\bar{\varepsilon}^p) = \sigma_{y0} + H(1 - e^{-m\bar{\varepsilon}^p}), \quad (2.80)$$

whereas in the FE software any arbitrary hardening function can be prescribed in tabular form [15, 16, 17].

2.4.3 Elastic-plastic constitutive model

In this section the constitutive model for the associative von Mises elastoplastic model with linear isotropic hardening is derived. In the 3D-theory of plasticity, the Cauchy stress and the elastic strain is always related via the Hooke's law [2, 11, 12, 36], namely

$$\boldsymbol{\sigma} = \mathcal{D}^e : \boldsymbol{\varepsilon}^e \quad \text{or in rate-form} \quad \dot{\boldsymbol{\sigma}} = \mathcal{D}^e : \dot{\boldsymbol{\varepsilon}}^e. \quad (2.81)$$

Substituting the additive split of strain rates according to (2.68) yields

$$\dot{\boldsymbol{\sigma}} = \mathcal{D}^e : \dot{\boldsymbol{\varepsilon}} - \mathcal{D}^e : \dot{\boldsymbol{\varepsilon}}^p = \mathcal{D}^e : (\dot{\boldsymbol{\varepsilon}} - \dot{\lambda}_p \mathbf{N}_\Phi). \quad (2.82)$$

In case of plastic flow, $\dot{\lambda}_p > 0$, which yields that $\dot{\Phi} = 0$, c.f. (2.75). Using the chain rule of derivation in combination with (2.72) and (2.78) gives

$$\dot{\Phi} = \frac{\partial \Phi}{\partial \boldsymbol{\sigma}} : \dot{\boldsymbol{\sigma}} + \frac{\partial \Phi}{\partial \sigma_y} \frac{\partial \sigma_y}{\partial \bar{\varepsilon}^p} \dot{\bar{\varepsilon}}^p = 0, \quad (2.83)$$

where $\partial \Phi / \partial \boldsymbol{\sigma} = \mathbf{N}_\Phi$, while $\partial \Phi / \partial \sigma_y = -1$ and $\partial \sigma_y / \partial \bar{\varepsilon}^p = H$. Substituting (2.77) back into (2.83) and using (2.82) yields

$$\dot{\Phi} = \mathbf{N}_\Phi : \dot{\boldsymbol{\sigma}} - H\dot{\lambda}_p = \mathbf{N}_\Phi : \mathcal{D}^e : (\dot{\boldsymbol{\varepsilon}} - \dot{\lambda}_p \mathbf{N}_\Phi) - H\dot{\lambda}_p = 0, \quad (2.84)$$

from which the plastic multiplier can be expressed as

$$\dot{\lambda}_p = \frac{\mathbf{N}_\Phi : \mathcal{D}^e : \dot{\boldsymbol{\varepsilon}}}{\mathbf{N}_\Phi : \mathcal{D}^e : \mathbf{N}_\Phi + H}. \quad (2.85)$$

After substituting this back into (2.82) the constitutive model becomes

$$\dot{\boldsymbol{\sigma}} = \mathcal{D}^e : \left(\dot{\boldsymbol{\varepsilon}} - \frac{\mathbf{N}_\Phi : \mathcal{D}^e : \dot{\boldsymbol{\varepsilon}}}{\mathbf{N}_\Phi : \mathcal{D}^e : \mathbf{N}_\Phi + H} \mathbf{N}_\Phi \right), \quad (2.86)$$

which can be written in simplified form as

$$\dot{\boldsymbol{\sigma}} = \left(\mathcal{D}^e - \frac{\mathcal{D}^e : \mathbf{N}_\Phi \otimes \mathbf{N}_\Phi : \mathcal{D}^e}{\mathbf{N}_\Phi : \mathcal{D}^e : \mathbf{N}_\Phi + H} \right) : \dot{\boldsymbol{\varepsilon}} = \mathcal{D}^{ep} : \dot{\boldsymbol{\varepsilon}}, \quad (2.87)$$

where \mathcal{D}^{ep} is the elastic-plastic tangent modulus [2, 11, 12, 13, 34, 36, 37].

3

Elastic deformation of polymer foams

The elastic behaviour of polymer foams attracts substantial attention, thanks to their favourable mechanical and production properties. The production of polymer foams is low-cost and simple, whereas polymer foam shows excellent energy absorption properties, chemical resistance and thermal conductivity [3, 41, 42, 43, 44]. Due to their cellular structure, polymer foams are light-weight with low overall density ρ^* since they are typically 90% cavity. Additionally, the mechanical behaviour is characterised by low moduli, such as the elastic modulus, the shear modulus and the bulk modulus. The utilization of polymer foams covers a broad spectrum of industrial and everyday applications that range from core materials for sports equipment, seat cushions, thermal insulations, electromagnetic shielding, filtrations, tissue scaffolds, flexible sensors to growth of cells and artificial organs or implant materials for endovascular procedures [42, 45, 46, 47, 48].

Therefore, there is a significant need to accurately model the mechanical behaviour of foams, to develop suitable material models and to improve the parameter fitting procedures of such models. In order to accurately describe the mechanical characteristics of polymer foams, accurate prediction of their large strain elastic behaviour is crucial. This chapter is devoted to the analysis of the constitutive modelling of elastic foams, based on compressible hyperelastic constitutive models using finite strain formulation.

3.1 Overview and goals

From the mechanical point of view, the behaviour of polymer foams is highly nonlinear with significant volumetric strains due to their special cellular microstructure. In the literature, two main groups of polymer foams are distinguished: (i) open-cell and (ii) closed-cell foams (see Fig. 3.1). In open-cell foams, the neighbouring cells are not encapsulated and thus, air can pass freely between them, whereas closed-cell foams cell are separated by connected cell-faces, in which substantial fraction of solid can be found [3, 41, 42].

The general stress-strain curve for both types of foams is illustrated in Fig. 3.1. During compression, the stress-strain characteristic shows linear elasticity at low stresses, which is followed by a long collapse plateau and finally by the regime of densification. Whereas, in tension, the behaviour is monotonous in a highly nonlinear manner [41].

Such material behaviour can be described based on microstructural mechanisms, which were discussed in details by Gibson and Ashby [41, 43, 49]. In their approach, the representative volume element of the cells are modelled as cubic arrays (see Fig. 3.1), while the overall behaviour is derived using homogenisation approach. According to their model, the linear elastic regime is related to cell-wall bending and additional cell-face stretching in case of closed-cell foams. The plateau is associated with the collapse of cells, i.e. elastic buckling. At the densification, due to the collapse, cell walls touch each other, and the cell-edge solid itself starts to compress. During tension, the stiffness change caused by the rotation of cell edges towards the tensile axis leads to a nonlinear stress-strain characteristic. In the case of closed-cell foams, the membrane stretching and internal gas pressure also have a significant effect on the overall behaviour.

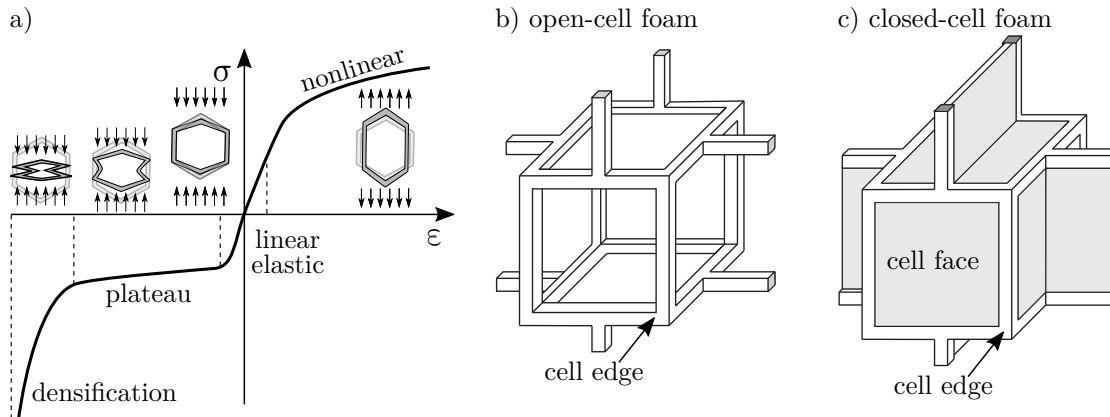


Figure 3.1: The a) stress-strain characteristic of foams and the micromechanical model for b) open- and c) closed-cell foams [41]

Moreover, open- and closed-cell foams also differ in their lateral behaviour. As it has been demonstrated in several studies, the transversal deformation of open-cell foams shows nonlinear characteristics [50, 51, 52], which is close-to-zero at moderate strains and often shows auxetic effects (i.e. negative Poisson’s ratio [53, 54, 55]) at higher strains due to the significant buckling of cell edges. This property is commonly approximated by neglecting the transversal effects [9, 29, 42, 56, 57], yielding

$$\nu_{\text{open}} \approx 0. \tag{3.1}$$

Compared to this, in closed-cell foams, gas cannot escape from the cells, yielding small, but not negligible transversal deformations. Therefore $\nu_{\text{closed}} > 0$ applies [41, 43, 45, 58]. However, several studies also use the zero Poisson’s ratio condition¹ in order to eliminate the transversal stretches [15, 41, 50, 59], which is difficult to measure accurately.

The finite strain elastic behaviour of polymer foams can also be accurately captured using isotropic hyperelastic material models with the assumption that the material is homogeneous [9, 42]. The development of hyperelastic material models was originally indicated by the need for modelling rubber-like materials, which exhibit large deformations, while the volume change is approximately zero. Compared to rubber-like materials, the deformation of polymer foams shows large volumetric strains. Therefore, the hyperelastic material models developed for rubber-like materials cannot be applied for polymer foams. In the recent years, several authors proposed hyperelastic constitutive models for compressible foams [60, 45, 61, 62].

¹The zero Poisson’s ratio condition is also commonly applied for *cork* materials, which also has negligible transverse effects in compression

However, in the literature, there is only one widely applied model, which is also implemented in all commercial finite element software. The model is referred to as Hyperfoam in ABAQUS [15], Ogden foam in ANSYS [16] and Rubber foam in MSC MARC [17]. The material model is named differently in the literature as well, since its introduction can be related to three different authors, but mostly cited as Ogden–Hill’s hyperelastic or simply Hyperfoam model.

The parameter fitting of Hyperfoam model is more complicated than in case of other hyperelastic models proposed for incompressible materials. In the incompressible case, the transverse stretches can be easily calculated from the incompressibility constraint $J \equiv 1$ in uniaxial compression/tension or other homogeneous deformations [63]. However, for the Hyperfoam model the transverse stretch, in general, cannot be obtained from the zero transverse stress constraint, even in uniaxial compression since the constraint-equations are highly-nonlinear. Therefore, the parameter fitting procedure is not so trivial for this material model [64, 65]. Moreover, it is well-known, that the hyperelastic characterisation may also lead to unwanted material instabilities and difficulties. If only uniaxial test data is used to obtain the material parameters of the applied particular hyperelastic model, then the simulated biaxial response may have very poor accuracy or even physically nonrealistic response [66, 67].

This chapter is devoted to the investigation of the constitutive modelling of elastic polymer foams using Hyperfoam model including also material stability and approximation of the transversal strains via the case study of a particular closed-cell polyethylene foam material using uniaxial and biaxial test data. The chapter also aims to propose and compare different optimization strategies for the hyperelastic material characterisation procedure.

3.2 Hyperfoam model for compressible foams

3.2.1 Development of Hyperfoam model

Ogden [68] investigated the hyperelastic modelling of compressible materials and provided a hyperelastic material model, in which a former compressible hyperelastic material model for rubber-like materials was extended with an additional unknown function $f(\lambda_1, \lambda_2, \lambda_3)$, which describes the strain energy corresponding to the volumetric strain. In his formulation, the strain energy function of the compressible materials is written as

$$W = \sum_{i=1}^N \frac{\bar{\mu}_i}{\alpha_i} (\lambda_1^{\alpha_i} + \lambda_2^{\alpha_i} + \lambda_3^{\alpha_i} - 3) + f(\lambda_1, \lambda_2, \lambda_3), \quad (3.2)$$

where N denotes the order of the hyperelastic model, α_i and $\bar{\mu}_i$ are material parameters. Later, Hill [69] proposed a volumetric part for the Ogden model (3.2) as

$$f(\lambda_1, \lambda_2, \lambda_3) = \sum_{i=1}^N \frac{\bar{\mu}_i}{\alpha_i} \frac{1 - 2\nu}{\nu} \left(J^{-\frac{\nu}{1-2\nu}\alpha_i} - 1 \right), \quad (3.3)$$

which can be substituted back into (3.2) resulting

$$W = \sum_{i=1}^N \frac{\bar{\mu}_i}{\alpha_i} \left(\lambda_1^{\alpha_i} + \lambda_2^{\alpha_i} + \lambda_3^{\alpha_i} - 3 + \frac{1 - 2\nu}{\nu} \left(J^{-\frac{\nu}{1-2\nu}\alpha_i} - 1 \right) \right). \quad (3.4)$$

In the above formulation, material parameters α_i , $\bar{\mu}_i$ and ν are included, therefore the model contains $2N + 1$ material parameters. Storåkers [70] proposed the following alternative form for this model:

$$W = \sum_{i=1}^N \frac{\bar{\mu}_i}{\alpha_i} \left(\lambda_1^{\alpha_i} + \lambda_2^{\alpha_i} + \lambda_3^{\alpha_i} - 3 + \frac{1}{n} \left(J^{-n\alpha_i} - 1 \right) \right), \quad (3.5)$$

where the new parameter n is related directly to the ground-state Poisson's ratio as

$$n = \frac{\nu}{1 - 2\nu}. \quad (3.6)$$

The formulation of the model in ABAQUS is based on the formulation of Storåkers (3.5), but the parameters are defined in a different way [44], namely

$$W = \sum_{i=1}^N \frac{2\mu_i}{\alpha_i^2} \left(\lambda_1^{\alpha_i} + \lambda_2^{\alpha_i} + \lambda_3^{\alpha_i} - 3 + \frac{1}{\beta_i} (J^{-\alpha_i\beta_i} - 1) \right). \quad (3.7)$$

It should be noted that the μ_i parameters in the ABAQUS formulation are not equal with the $\bar{\mu}_i$ parameters used in (3.5). Furthermore, ABAQUS allows to use multiple β_i parameters not just a single n parameter. Therefore, $3N$ material parameters are included in the model. The μ_i and β_i parameters in this formulation can be directly related to the initial (ground-state) shear (μ_0) and bulk (K_0) moduli as

$$\mu_0 = \sum_{i=1}^N \mu_i > 0, \quad K_0 = \sum_{i=1}^N 2\mu_i \left(\frac{1}{3} + \beta_i \right) > 0, \quad (3.8)$$

which also define criteria for the possible values of the material parameters μ_i and β_i [18, 71]. The detailed derivation is provided in Appendix A. During the further calculations the ABAQUS formulation of the Ogden–Hill's (or Hyperfoam) hyperelastic model in (3.7) will be applied.

3.2.2 Open-cell foams

As it was discussed in Chapter 3.1, the ground-state Poisson's ratio of open-cell foams $\nu_{\text{open}} \approx 0$. This means, that the original parameter n in (3.5) and the β_i parameters in the ABAQUS notation can be approximated as

$$n \approx 0 \quad \text{and} \quad \beta_i \approx 0. \quad (3.9)$$

3.2.3 Stress solutions

The stress solutions of the rate-independent Hyperfoam model can be obtained by substituting the previously defined strain energy function (3.7) into (2.67). Therefore, the principal stresses become

$$\tau_k = \sum_{i=1}^N \frac{2\mu_i}{\alpha_i} \left(\lambda_k^{\alpha_i} - J^{-\alpha_i\beta_i} \right), \quad (3.10)$$

$$\sigma_k = \frac{1}{J} \sum_{i=1}^N \frac{2\mu_i}{\alpha_i} \left(\lambda_k^{\alpha_i} - J^{-\alpha_i\beta_i} \right), \quad (3.11)$$

$$S_k = \sum_{i=1}^N \frac{1}{\lambda_k^2} \frac{2\mu_i}{\alpha_i} \left(\lambda_k^{\alpha_i} - J^{-\alpha_i\beta_i} \right), \quad (3.12)$$

$$P_k = \sum_{i=1}^N \frac{1}{\lambda_k} \frac{2\mu_i}{\alpha_i} \left(\lambda_k^{\alpha_i} - J^{-\alpha_i\beta_i} \right), \quad (3.13)$$

where the load is characterised by the principal stretches λ_k .

In the following, the stress solutions will be derived for homogeneous deformations using the first Piola–Kirchhoff stress tensor.

3.2.3.1 Uniaxial extension (UN)

In case of uniaxial extension, the stretch in the longitudinal direction is prescribed, whereas in the other two principal directions, which are referred as transversal (lateral) directions, no load is applied and the transversal stretches are identical $\lambda_2 = \lambda_3$. For simplicity, let $\lambda := \lambda_1$ and $\lambda_T := \lambda_2 = \lambda_3$, where subscript T refers to the transverse direction. The deformation gradient \mathbf{F} and the volume ratio can be written as

$$\mathbf{F}^{\text{UN}} = \begin{bmatrix} \lambda & 0 & 0 \\ 0 & \lambda_T & 0 \\ 0 & 0 & \lambda_T \end{bmatrix}, \quad \mathbf{P}^{\text{UN}} = \begin{bmatrix} P_1^{\text{UN}} & 0 & 0 \\ 0 & 0 & 0 \\ 0 & 0 & 0 \end{bmatrix}, \quad J^{\text{UN}} = \lambda \lambda_T^2. \quad (3.14)$$

Consequently, the principal first Piola–Kirchhoff stresses, after substituting (3.14) into (3.13), can be expressed as

$$P_1^{\text{UN}}(\lambda, \lambda_T) = \sum_{i=1}^N \frac{1}{\lambda} \frac{2\mu_i}{\alpha_i} \left(\lambda^{\alpha_i} - (\lambda \lambda_T^2)^{-\alpha_i \beta_i} \right), \quad (3.15)$$

$$P_2^{\text{UN}}(\lambda, \lambda_T) = P_3^{\text{UN}}(\lambda, \lambda_T) = 0 = \sum_{i=1}^N \frac{1}{\lambda_T} \frac{2\mu_i}{\alpha_i} \left(\lambda_T^{\alpha_i} - (\lambda \lambda_T^2)^{-\alpha_i \beta_i} \right). \quad (3.16)$$

For the first-order case $N = 1$, the transverse stretch can be expressed from the zero transverse stress constraint (3.16) as

$$\lambda_T = \lambda^{-\frac{\beta}{1+2\beta}} = \lambda^{-\nu}, \quad (3.17)$$

and thus, the nominal stress along the loading direction can be written as the function of λ as

$$P_1^{\text{UN}}(\lambda) = \frac{2\mu}{\alpha} \left(\lambda^{\alpha-1} - \lambda^{-\frac{\alpha\beta}{1+2\beta}-1} \right). \quad (3.18)$$

However, for higher-order models ($N > 1$), the relation (3.16) cannot be solved for λ_T in closed-form. Consequently, the stress along the loading direction cannot be expressed solely as a function of the longitudinal stretch λ .

3.2.3.2 Confined uniaxial extension (CU)

During confined uniaxial extension, the transversal deformation is fixed, therefore $\lambda_T \equiv 1$ and the deformation gradient and the volume ratio reduce to

$$\mathbf{F}^{\text{CU}} = \begin{bmatrix} \lambda & 0 & 0 \\ 0 & 1 & 0 \\ 0 & 0 & 1 \end{bmatrix}, \quad \mathbf{P}^{\text{CU}} = \begin{bmatrix} P_1^{\text{CU}} & 0 & 0 \\ 0 & P_2^{\text{CU}} & 0 \\ 0 & 0 & P_3^{\text{CU}} \end{bmatrix}, \quad J^{\text{CU}} = \lambda. \quad (3.19)$$

Whereas, stress will also occur in the transverse direction, letting

$$P_1^{\text{CU}}(\lambda) = \sum_{i=1}^N \frac{1}{\lambda} \frac{2\mu_i}{\alpha_i} \left(\lambda^{\alpha_i} - \lambda^{-\alpha_i \beta_i} \right), \quad (3.20)$$

$$P_2^{\text{CU}}(\lambda) = P_3^{\text{CU}}(\lambda) = \sum_{i=1}^N \frac{2\mu_i}{\alpha_i} \left(1 - \lambda^{-\alpha_i \beta_i} \right) \neq 0. \quad (3.21)$$

Note that when $\beta_i = 0$ and the transversal effects are neglected, the load does not affect the transversal directions i.e. the uniaxial extension (UN) has the same kinematic description as the confined uniaxial extension (CU) and thus the same stress state.

3.2.3.3 Equibiaxial extension (EB)

In equibiaxial extension, the same stretch is prescribed in two principal directions, while in the third, transverse direction, the material deforms freely. Therefore, using the same notation as for UN case,

$$\mathbf{F}^{\text{EB}} = \begin{bmatrix} \lambda & 0 & 0 \\ 0 & \lambda & 0 \\ 0 & 0 & \lambda_T \end{bmatrix}, \quad \mathbf{P}^{\text{EB}} = \begin{bmatrix} P_1^{\text{EB}} & 0 & 0 \\ 0 & P_1^{\text{EB}} & 0 \\ 0 & 0 & 0 \end{bmatrix}, \quad J^{\text{EB}} = \lambda^2 \lambda_T. \quad (3.22)$$

Consequently, the stresses can be obtained as

$$P_1^{\text{EB}}(\lambda, \lambda_T) = P_2^{\text{EB}}(\lambda, \lambda_T) = \sum_{i=1}^N \frac{1}{\lambda} \frac{2\mu_i}{\alpha_i} \left(\lambda^{\alpha_i} - (\lambda^2 \lambda_T)^{-\alpha_i \beta_i} \right), \quad (3.23)$$

$$P_3^{\text{EB}}(\lambda, \lambda_T) = \sum_{i=1}^N \frac{1}{\lambda_T} \frac{2\mu_i}{\alpha_i} \left(\lambda_T^{\alpha_i} - (\lambda^2 \lambda_T)^{-\alpha_i \beta_i} \right) = 0. \quad (3.24)$$

Assuming first-order model ($N = 1$), the transverse stretch can be written as

$$\lambda_T = \lambda^{-\frac{\beta}{1+\beta}}, \quad (3.25)$$

and thus, the nominal stress becomes

$$P_1^{\text{EB}}(\lambda) = \frac{2\mu}{\alpha} \left(\lambda^{\alpha-1} - \lambda^{-\frac{2\alpha\beta}{1+\beta}-1} \right). \quad (3.26)$$

Similarly to the UN case, for $N > 1$, the closed-form solution cannot be expressed analytically.

3.2.3.4 Confined biaxial extension (CB)

In confined biaxial extension, the transversal deformation is fixed, yielding

$$\mathbf{F}^{\text{CB}} = \begin{bmatrix} \lambda & 0 & 0 \\ 0 & \lambda & 0 \\ 0 & 0 & 1 \end{bmatrix}, \quad \mathbf{P}^{\text{CB}} = \begin{bmatrix} P_1^{\text{CB}} & 0 & 0 \\ 0 & P_1^{\text{CB}} & 0 \\ 0 & 0 & P_2^{\text{CB}} \end{bmatrix}, \quad J^{\text{CB}} = \lambda^2. \quad (3.27)$$

Whereas, the principal stresses read

$$P_1^{\text{CB}}(\lambda) = P_2^{\text{CB}}(\lambda) = \sum_{i=1}^N \frac{1}{\lambda} \frac{2\mu_i}{\alpha_i} \left(\lambda^{\alpha_i} - \lambda^{-2\alpha_i \beta_i} \right), \quad (3.28)$$

$$P_3^{\text{CB}}(\lambda) = \sum_{i=1}^N \frac{2\mu_i}{\alpha_i} \left(1 - \lambda^{-2\alpha_i \beta_i} \right) \neq 0. \quad (3.29)$$

Similarly to CU load case, for $\beta_i = 0$, the kinematics and stresses for EB and CB are identical. Furthermore, the longitudinal principal stresses $[\mathbf{P}^{\text{CB}}]_{11}$ and $[\mathbf{P}^{\text{CB}}]_{22}$ are also equal with the uniaxial principal stress $[\mathbf{P}^{\text{CU}}]_{11}$ for $\beta_i = 0$.

3.2.3.5 Volumetric deformation (VOL)

In this deformation mode, all the principal stretches are prescribed equally, namely $\lambda_k = \lambda$ with $k = 1, 2, 3$; letting

$$\mathbf{F}^{\text{VOL}} = \begin{bmatrix} \lambda & 0 & 0 \\ 0 & \lambda & 0 \\ 0 & 0 & \lambda \end{bmatrix}, \quad \mathbf{P}^{\text{VOL}} = \begin{bmatrix} P_1^{\text{VOL}} & 0 & 0 \\ 0 & P_1^{\text{VOL}} & 0 \\ 0 & 0 & P_1^{\text{VOL}} \end{bmatrix}, \quad J^{\text{VOL}} = \lambda^3. \quad (3.30)$$

The principal stresses are equal in all the three principal directions, thus

$$P_1^{\text{VOL}}(\lambda) = P_2^{\text{VOL}}(\lambda) = P_3^{\text{VOL}}(\lambda) = \sum_{i=1}^N \frac{1}{\lambda} \frac{2\mu_i}{\alpha_i} \left(\lambda^{\alpha_i} - \lambda^{-3\alpha_i\beta_i} \right). \quad (3.31)$$

In this case, $\beta_i = 0$ condition leads to $P_1^{\text{VOL}} = P_1^{\text{CU}}$.

3.2.3.6 Simple shear (SS)

For simple shear case, the deformation gradient is given by

$$\mathbf{F}^{\text{EB}} = \begin{bmatrix} 1 & \gamma & 0 \\ 0 & 1 & 0 \\ 0 & 0 & 1 \end{bmatrix}, \quad J^{\text{SS}} = 1, \quad (3.32)$$

where the corresponding principal stretches are

$$\lambda_1 = \frac{1}{2} \left(\gamma + \sqrt{\gamma^2 + 4} \right), \quad \lambda_2 = \frac{1}{2} \left(-\gamma + \sqrt{\gamma^2 + 4} \right), \quad \text{and} \quad \lambda_3 = 1. \quad (3.33)$$

Substitution into (3.13) gives

$$P_1^{\text{SS}}(\gamma) = \sum_{i=1}^N \frac{2\mu_i}{\alpha_i} \left(\left(\frac{\gamma}{2} + \frac{1}{2}\sqrt{\gamma^2 + 4} \right)^{\alpha_i - 1} - \left(\frac{\gamma}{2} + \frac{1}{2}\sqrt{\gamma^2 + 4} \right)^{-1} \right), \quad (3.34)$$

$$P_2^{\text{SS}}(\gamma) = \sum_{i=1}^N \frac{2\mu_i}{\alpha_i} \left(\left(-\frac{\gamma}{2} + \frac{1}{2}\sqrt{\gamma^2 + 4} \right)^{\alpha_i - 1} - \left(-\frac{\gamma}{2} + \frac{1}{2}\sqrt{\gamma^2 + 4} \right)^{-1} \right), \quad (3.35)$$

$$P_3^{\text{SS}}(\lambda) = 0. \quad (3.36)$$

3.2.4 Material stability

The material parameters in the Ogden–Hill’s compressible hyperelastic material model cannot be chosen freely. Some criteria have already been formulated in (3.8), but in order to receive physically acceptable results, the material model should be stable for all strains or at least in the strain regime used in the application. Otherwise, the numerical simulation will be inaccurate or may not converge. This defines new criteria for the material parameters, which has to be checked after the parameter fitting process. The most widely used method to check material stability is the application of Drucker-stability criteria.

The Drucker-stability [72] criteria states, that the strain energy has to increase for any increment in the strain. The criteria can be expressed as [9, 15]

$$d\boldsymbol{\tau} : d\mathbf{h} > 0, \quad (3.37)$$

where \mathbf{h} is the spatial logarithmic strain tensor introduced in (2.21). In case of isotropic material the relation can be expressed using the principal values as

$$\sum_{k=1}^3 d\tau_k dh_k = d\tau_1 dh_1 + d\tau_2 dh_2 + d\tau_3 dh_3 > 0, \quad (3.38)$$

where dh_k are the logarithmic strain increments and $d\tau_k$ are the corresponding principal Kirchhoff stress increments. Applying the chain rule of derivation and the definition in (2.21), we obtain

$$dh_k = \frac{\partial h_k}{\partial \lambda_k} d\lambda_k = \frac{\partial(\ln \lambda_k)}{\partial \lambda_k} d\lambda_k = \frac{1}{\lambda_k} d\lambda_k, \quad (3.39)$$

furthermore

$$dJ = \frac{\partial J}{\partial \lambda_1} d\lambda_1 + \frac{\partial J}{\partial \lambda_2} d\lambda_2 + \frac{\partial J}{\partial \lambda_3} d\lambda_3 = \frac{J}{\lambda_1} d\lambda_1 + \frac{J}{\lambda_2} d\lambda_2 + \frac{J}{\lambda_3} d\lambda_3 = \quad (3.40)$$

$$= J \sum_{k=1}^3 \frac{d\lambda_k}{\lambda_k} = J \sum_{k=1}^3 dh_k. \quad (3.41)$$

The incremental $d\tau_k$ can be obtained [9] as

$$d\tau_k = \frac{\partial \tau_k}{\partial \lambda_k} d\lambda_k + \frac{\partial \tau_k}{\partial J} dJ. \quad (3.42)$$

After substituting (3.13), (3.39) and (3.41) into (3.43)

$$d\tau_k = \left(\sum_{i=1}^N 2\mu_i \lambda_k^{\alpha_i} \right) dh_k + \left(\sum_{i=1}^N 2\mu_i \beta_i J^{-\alpha_i \beta_i} \right) \sum_{k=1}^3 dh_k. \quad (3.43)$$

According to Silber [9], let us introduce $A_i = \beta_i J^{-\alpha_i \beta_i}$ and the matrix notation of

$$d\boldsymbol{\tau}_k = \begin{bmatrix} d\tau_1 \\ d\tau_2 \\ d\tau_3 \end{bmatrix}, \quad d\mathbf{h}_k = \begin{bmatrix} dh_1 \\ dh_2 \\ dh_3 \end{bmatrix}. \quad (3.44)$$

Using the notation above, the stress and the strain increment vectors can be related as

$$d\boldsymbol{\tau}_k = \mathbf{D} d\mathbf{h}_k, \quad (3.45)$$

where the \mathbf{D} matrix is defined from principal stresses in (3.13) as

$$\mathbf{D} = \begin{bmatrix} D_{11} & D_{12} & D_{13} \\ D_{21} & D_{22} & D_{23} \\ D_{31} & D_{32} & D_{33} \end{bmatrix} = \sum_{i=1}^N 2\mu_i \begin{bmatrix} \lambda_1^{\alpha_i} + A_i & A_i & A_i \\ A_i & \lambda_2^{\alpha_i} + A_i & A_i \\ A_i & A_i & \lambda_3^{\alpha_i} + A_i \end{bmatrix}, \quad (3.46)$$

After substituting back (3.45) into the stability criterion (3.37), it yields

$$d\mathbf{h}_k \mathbf{D} d\mathbf{h}_k > 0. \quad (3.47)$$

The criterion is satisfied, when \mathbf{D} is positive definite, thus its scalar invariants should be positive. Therefore, the criteria for \mathbf{D} and its eigenvalues (D_1 , D_2 and D_3) can be expressed as

$$I_{\mathbf{D}} = \text{tr} \mathbf{D} = D_1 + D_2 + D_3 > 0, \quad (3.48)$$

$$II_{\mathbf{D}} = \frac{1}{2} ((\text{tr} \mathbf{D})^2 - \text{tr} \mathbf{D}^2) = D_1 D_2 + D_1 D_3 + D_2 D_3 > 0, \quad (3.49)$$

$$III_{\mathbf{D}} = \det \mathbf{D} = D_1 D_2 D_3 > 0. \quad (3.50)$$

It should be noted that \mathbf{D} contains the principal stretches (λ_k), therefore the stability depends on the load as well. In order to assume, that the fitted material model is stable, the Drucker-stability should be checked for all homogeneous deformations, namely uniaxial tension/compression, biaxial tension/compression, volumetric tension/compression, simple shear and pure shear [15]. This stability check, however, requires transversal stretches, which cannot be solved analytically for $N > 1$. Therefore a numerical root finding algorithm (e.g. Newton–Raphson) should be applied [9, 15].

3.2.4.1 Simplified stability criteria for open-cell foams

However, in the case of open-cell foams, the assumption $\beta_i = 0$ holds [SzB1], and thus the Drucker-stability matrix simplifies to

$$\mathbf{D}^{\text{open}} = \begin{bmatrix} D_{11}^{\text{open}} & 0 & 0 \\ 0 & D_{22}^{\text{open}} & 0 \\ 0 & 0 & D_{33}^{\text{open}} \end{bmatrix} = \sum_{i=1}^N 2\mu_i \begin{bmatrix} \lambda_1^{\alpha_i} & 0 & 0 \\ 0 & \lambda_2^{\alpha_i} & 0 \\ 0 & 0 & \lambda_3^{\alpha_i} \end{bmatrix}, \quad (3.51)$$

which is a diagonal matrix. It is known, that a diagonal matrix is positive definite if and only if all the diagonal elements are positive. Therefore, for open-cell foams the Drucker-stability criterion in (3.47) can be simplified by the novel expression of

$$\sum_{i=1}^N \mu_i \lambda_k^{\alpha_i} > 0, \quad k = 1, 2, 3. \quad (3.52)$$

This means that using the closed-form solution, the Drucker-stability could efficiently be evaluated for a given parameter set.

3.3 Mechanical tests

A possible way to find the material parameters of a certain hyperelastic model is to fit the model responses of particular homogeneous deformations to experimental data. For the mechanical tests a particular closed-cell polyethylene foam sheet was chosen ($\rho_{\text{PE}} = 922 \text{ kg/m}^3$, $\rho^* = 40.5 \text{ kg/m}^3$), on which the transversal strains are not negligible. The microstructure of the foam is illustrated in Fig. 3.2, in which significant surface-skin layer is observable. The effect of the surface skin layer has also been investigated experimentally, which revealed that the existence of such a layer with increased density cause hardening in the stress-strain curve, whereas the nature of its characteristics (i.e. the three regimes in Fig. 3.1) is not affected [SzB2].

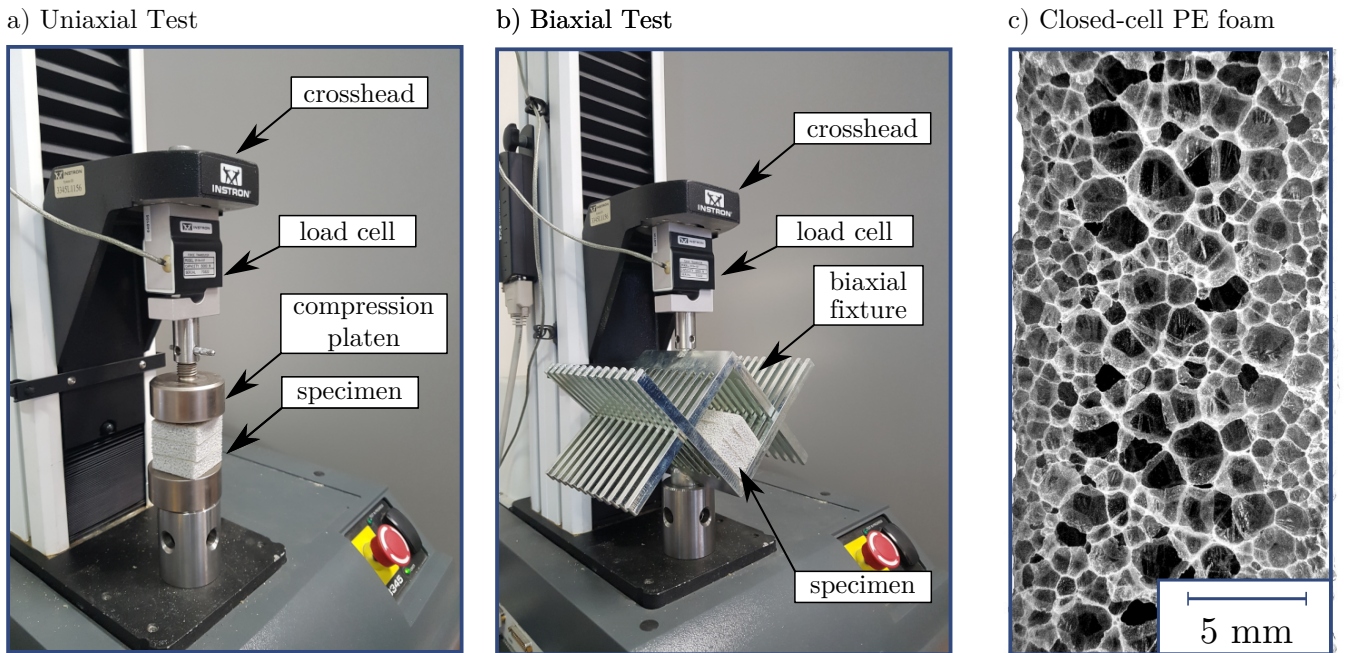


Figure 3.2: The layout of a) uniaxial and b) biaxial measurement; and c) the microstructure of the investigated closed-cell PE foam

3.3.1 Uniaxial test with video processing

The geometry of specimens used in compression test is based on the recommendation of ISO 3386 standard [73], which recommends the specimens to be right parallelepiped with a minimum width/thickness ratio of 2:1. Therefore, the three 40×40 mm specimens with thickness were piled together. The measurements were performed with an Instron 3345 Single Column Universal Testing System, while the load was measured by an Instron model 2519-107 5kN load cell. The compression test was performed with engineering strain rate of $\dot{\varepsilon} = 10^{-5}$ 1/s, while the maximal displacement was $u_{\max} = 30$ mm. The captured data points corresponding to the loading and unloading phases cannot be distinguished, hence the viscoelastic effect was eliminated. Thus, the experimental data can be considered as the long-term pure hyperelastic response of the material. During the measurement, in every sampling point the load (F) and the displacement (u) values were recorded, from which the longitudinal stretch and the first Piola–Kirchhoff stress data can be obtained as

$$\lambda^{\text{UNexp}} = 1 - \frac{u}{L_0}, \quad P_1^{\text{UNexp}} = \frac{F}{L_0^2}, \quad (3.53)$$

where $L_0 = 40$ mm is the compression length (edge length) and $A_0 = L_0^2 = 1600$ mm².

The transverse deformation of the specimen was recorded using optical measurement and image processing, that is illustrated in Fig. 3.3/b [SzB2]. In the image processing a slice of the video recording was cut and binarized, while the lateral stretch at the i^{th} frame was obtained as

$$\lambda_{T,i}^{\text{UNexp}} = \frac{A_{\text{Wh},i}}{A_{\text{Wh},0}}, \quad (3.54)$$

where $A_{\text{Wh},i}$ and $A_{\text{Wh},0}$ is the area of white pixels corresponding to the i^{th} and the first frame, respectively [SzB2]. The measurement results are summarised in Fig. 3.3/b.

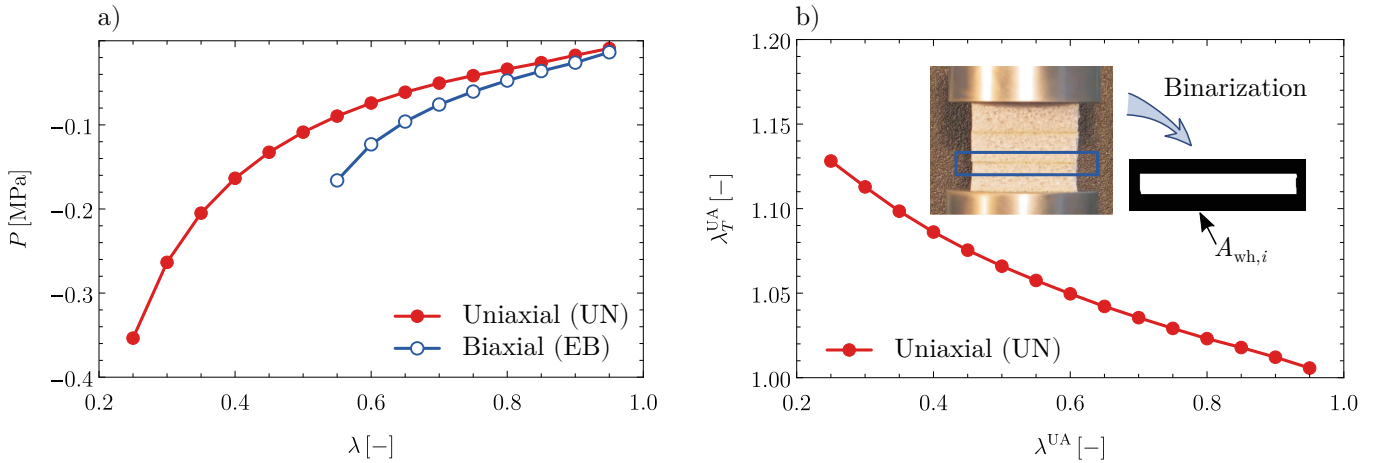


Figure 3.3: The measured a) engineering stress - stretch characteristics in uniaxial and equibiaxial load case, b) the measured lateral stretch characteristics and the steps of video processing

3.3.2 Equibiaxial test

For the equibiaxial compression test, the test fixture developed by Kossa [66] was used. for further details see Appendix D). The specimen was a cube material having $L_0 = 100$ mm edge dimensions, while the applied engineering strain rate was the same as in the uniaxial compression. For the biaxial test, the stress and stretch values were obtained using

$$\lambda^{\text{EBexp}} = 1 - \frac{u}{\sqrt{2}L_0}, \quad P_1^{\text{EBexp}} = \frac{F}{\sqrt{2}L_0^2}. \quad (3.55)$$

The measured engineering stress-stretch characteristics are presented in Fig. 3.3/a. Since the biaxial compression fixture hid the specimen, it was not possible to measure the transverse stretch using side-view optical measurement [SzB3].

3.4 Parameter-fitting strategies

Hereafter, the Hyperfoam model will be fitted to the uniaxial and the equibiaxial compression experimental data, including the corresponding measured and estimated transverse stretch data. The parameter fitting algorithm of the first-order ($N = 1$) model is relatively simple compared to higher-order models because closed-form solution is available for the stresses in terms of the primary stretches as in (3.18) and (3.26). In addition, transverse stretches can also be expressed in terms of the primary stretch (see (3.17) and (3.25)). Therefore, the quality (or error) function to be minimized can be easily constructed by summing the errors between the experimental data and the model responses. However, the first-order model may serve an inaccurate result and higher-order model ($N > 1$) should be used for the characterisation. As discussed in Section 3.2.3, for the higher-order models, the transverse stretch cannot be eliminated and cannot be fitted separately as in the case of using a first-order model. Consequently, another strategy has to be deployed.

If the transverse stretch is significant, one can use the method proposed by Schrodtt et al. [74]. In the proposed method, each iteration step of the parameter fitting procedure is divided into two parts: 1) solving the zero transverse stress constraint (3.16) and (3.24) for the transverse stretch λ_T and 2) calculating the model response after substitution of the obtained λ_T value into (3.15) and (3.23). The drawback of this method is that there is no guarantee that (3.16) and (3.24) can be solved for any value of the primary stretch. Besides, the predicted transverse stretch value may be very inaccurate. However, the method can be improved by modifying the quality function in the optimization routine, including the fitting of the transverse stretch prediction to the experimental data. The main drawback is that an optimization code should be applied alongside the numerical solution scheme. In the following, three different fitting strategies are proposed and analysed: i) using only uniaxial data, ii) using uniaxial data with analytic transversal stretch function and iii) using uniaxial and biaxial data, which are illustrated in Fig. 3.4.

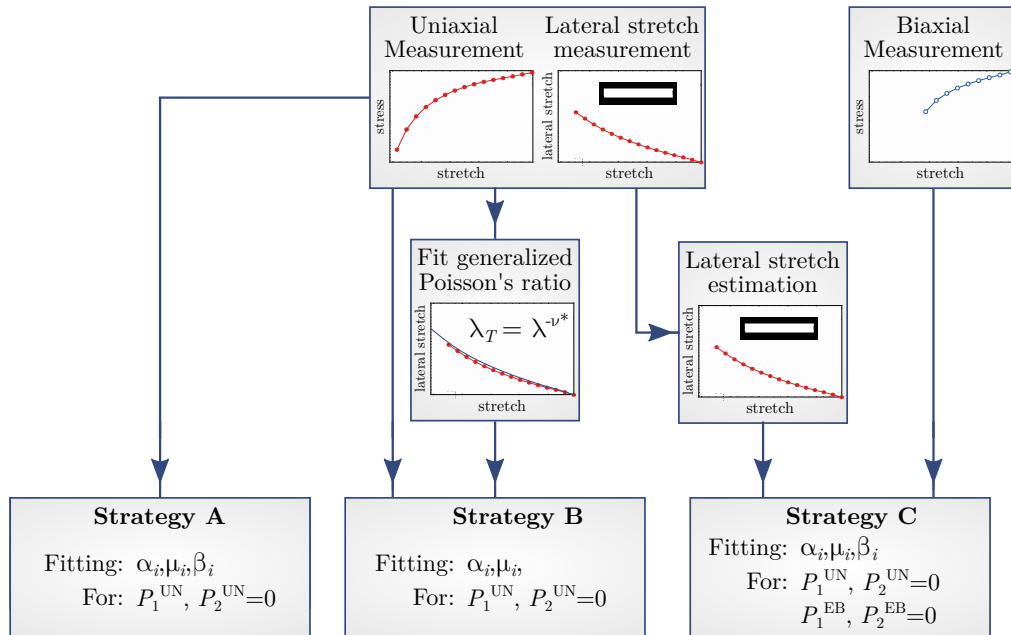


Figure 3.4: The summary of the proposed parameter fitting strategies

3.4.1 Strategy A

In the simplest approach, only the uniaxial measurement data is used in the fitting process. In the corresponding quality function not only the error between the uniaxial principal stress $P_1^{\text{UN}}(\lambda, \lambda_T)$ and the measurement data $P_1^{\text{UNexp}}(\lambda, \lambda_T)$ is minimized, but also the zero transverse stress is also enforced by adding an extra term to the quality function. Therefore, the novel quality function reads

$$Q^{\text{A}} = Q_1^{\text{UN}} + Q_T^{\text{UN}}, \quad (3.56)$$

where

$$Q_1^{\text{UN}} = \sum_{r=1}^R \left(\frac{P_r^{\text{UNexp}} - P_1^{\text{UN}}(\lambda_r^{\text{UNexp}}, \lambda_{T,r}^{\text{UNexp}})}{P_r^{\text{UNexp}}} \right)^2, \quad (3.57)$$

$$Q_T^{\text{UN}} = \sum_{r=1}^R \left(\frac{P_2^{\text{UN}}(\lambda_r^{\text{UNexp}}, \lambda_{T,r}^{\text{UNexp}})}{P_r^{\text{UNexp}}} \right)^2, \quad (3.58)$$

where R is the number of captured data points in uniaxial tests [SzB3].

The experimental data for the transverse stress is obviously zero; therefore, in the normalized error expressions (3.58), the stress values corresponding to the loading directions are applied. Minimizing the quality function Q^{A} in (3.56) serves a parameter set which tries to enforce the zero transverse stress constraint in addition to the fitting of the transverse stretches to the experimental data. It should be noted that the transverse stretch is not fitted explicitly; however, it is fitted implicitly via the zero transverse stress constraint. The main benefit of this method is that there is no need to solve the highly nonlinear expression in (3.16) for the transverse stretch.

3.4.2 Strategy B

In this new strategy the transversal stretch behaviour is modelled using the generalized Poisson's ratio, which reduced the number of parameters in the fitting process. According to the model proposed by Blatz and Ko [53, 75], the relation of the lateral and longitudinal stretches for uniaxial deformation can be expressed using the generalized Poisson's ratio. According to their ad hoc assumption,

$$\lambda_T = \lambda^{-\nu^*}, \quad (3.59)$$

which also means that by taking the natural logarithm of both sides

$$\ln \lambda_T = \ln(\lambda^{-\nu^*}), \quad (3.60)$$

where $\ln \lambda_T = \varepsilon_T^{\text{true}}$ and $\ln \lambda = \varepsilon^{\text{true}}$ are the logarithmic strains or true strains. Therefore, their model simplifies to

$$\varepsilon_T^{\text{true}} = -\nu^* \varepsilon^{\text{true}}, \quad (3.61)$$

which can also be interpreted as the finite strain generalization of the 1D Hooke's law.

Following this assumption, the parameter fitting can be separated to a) fitting the generalized Poisson's ratio based on the measured uniaxial transverse stretch characteristics and then b) fitting the Hyperfoam model using only a single β parameter [SzB3], which is defined as

$$\beta_i = \beta^{\text{B}} = \frac{\nu^*}{1 - 2\nu^*}. \quad (3.62)$$

After performing the fitting to the uniaxial transverse stretch data $\nu^* = 0.0899$ and thus, $\beta^B = 0.10964$ were obtained. The accuracy of the fitting is presented in Fig. 3.5. This yields that during the hyperelastic fitting only α_i and μ_i parameters should be fitted, which significantly reduces the parameter-space where the global minima are searched.

3.4.3 Strategy C

In order to include the biaxial measurement data in the parameter fitting, the equibiaxial transverse stretch values λ_T^{EBexp} should also be obtained. Due to the measurement layout, such data is not available, therefore an estimation should be applied. This approach assumes that the linear Hooke's law can also be generalized for biaxial load case [SzB3], letting

$$\varepsilon_T^{\text{EB,true}} = -2\nu^* \varepsilon^{\text{EB,true}}. \quad (3.63)$$

After combining with (3.61) and using the relation $\varepsilon^{\text{true}} = \ln \lambda$ the lateral stretches could be obtained as

$$\lambda_T^{\text{EBexp}}(\lambda) = 2 \left(\lambda_T^{\text{UAexp}}(\lambda) - 1 \right) + 1 = 2\lambda_T^{\text{UAexp}}(\lambda) - 1. \quad (3.64)$$

Using this method, the transverse stretch characteristic corresponding to the biaxial test was obtained, which is presented in Fig. 3.5.

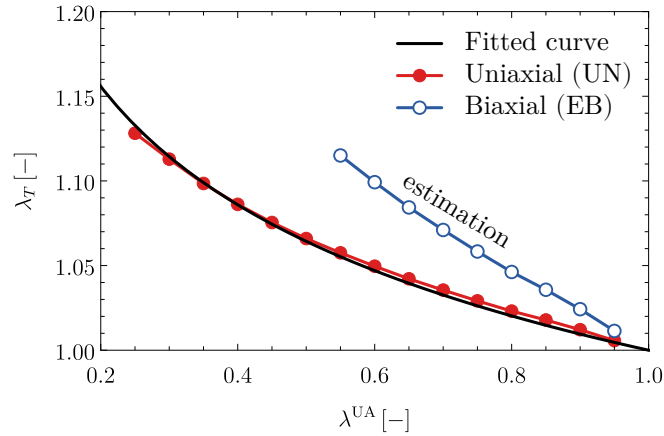


Figure 3.5: The fitted transversal stretch characteristics using the generalized Poisson's ratio and the estimated transverse stretches for biaxial measurement

Using the proposed transverse stretch data, the optimization criteria in (3.56) can be extended for biaxial case [SzB3], letting

$$Q^C = Q_1^{\text{UN}} + Q_T^{\text{UN}} + Q_1^{\text{EB}} + Q_T^{\text{EB}}, \quad (3.65)$$

where

$$Q_1^{\text{EB}} = \sum_{l=1}^L \left(\frac{P_l^{\text{EBexp}} - P_1^{\text{EB}} \left(\lambda_l^{\text{EBexp}}, 2\lambda_T^{\text{UAexp}}(\lambda_l^{\text{EBexp}}) - 1 \right)}{P_l^{\text{EBexp}}} \right)^2, \quad (3.66)$$

$$Q_T^{\text{EB}} = \sum_{l=1}^L \left(\frac{P_2^{\text{EB}} \left(\lambda_l^{\text{EBexp}}, 2\lambda_T^{\text{UAexp}}(\lambda_l^{\text{EBexp}}) - 1 \right)}{P_l^{\text{EBexp}}} \right)^2, \quad (3.67)$$

where L is the number of captured data points in biaxial tests.

3.4.4 Evaluation of strategies

The global minimization of the quality functions using all three methods was performed in Wolfram Mathematica using the built-in “NMinimize” algorithm with Random Search method. The parameter fitting for Strategy C was also performed using the built-in fitting procedure of ABAQUS [15]. The fitted parameters for $N = 1, 2, 3$ cases are listed in Table 3.1. It should be noted, that the ABAQUS fitting for $N = 3$ resulted in physically inadmissible results, since $\sum \beta_i^{\text{Aba}, N=2} < -1/3$. Furthermore, the stability analysis was also performed based on Section 3.2.4, which revealed that the Hyperfoam model with all fitted parameter sets satisfy the Drucker-stability criterion.

Table 3.1: The fitted Hyperfoam parameters using Strategy A, B, C and ABAQUS

		μ_1 [MPa]	α_1 [-]	β_1 [-]	μ_2 [MPa]	α_2 [-]	β_2 [-]	μ_3 [MPa]	α_3 [-]	β_3 [-]
Strategy A	N=1	0.0806	4.361	0.162						
	N=2	0.0163	0.187	0.670	0.0712	7.655	0.0164			
	N=3	-0.673	3.514	0.377	0.1829	1.961	0.4180	0.5770	4.368	0.329
Strategy B	N=1	0.0724	2.596	0.109						
	N=2	0.0679	7.621	0.109	0.0206	0.6789	0.1096			
	N=3	22.864	12.56	0.109	0.0168	-0.221	0.1096	-22.798	12.59	0.109
Strategy C	N=1	0.1048	7.108	0.135						
	N=2	0.0582	4.266	0.220	0.0508	20.98	0.0448			
	N=3	-1.460	37.64	-0.013	0.0588	4.835	-0.3248	1.517	37.28	0.011
ABAQUS	N=1	0.1012	6.578	0.1378						
	N=2	0.0756	15.84	0.0569	0.0361	2.829	0.3044			
	N=3									No data

Table 3.2: The quality and time of fitting using different strategies and ABAQUS

		P_1^{UN}		P_1^{EB}		λ_T^{UN}		Fitting time [s] (3.1 GHz CPU)
		R^2 [%]	S [kPa]	R^2 [%]	S [kPa]	R^2 [%]	S [kPa]	
Strategy A	$N = 1$	96.54	16.72	69.93	23.56	79.36	27.69	0.76
	$N = 2$	99.94	0.808	70.84	22.72	99.64	22.57	15.41
	$N = 3$	99.99	0.549	70.54	22.92	99.89	12.85	169.45
Strategy B	$N = 1$	96.62	16.56	69.51	23.48	99.59	26.26	0.45
	$N = 2$	99.98	0.667	79.62	18.78	99.59	26.26	4.51
	$N = 3$	99.99	0.521	80.01	17.93	99.59	26.26	99.98
Strategy C	$N = 1$	98.70	10.19	97.15	8.05	92.02	14.19	1.23
	$N = 2$	99.34	8.533	99.59	3.34	99.22	3.21	55.44
	$N = 3$	99.82	3.381	99.19	4.61	98.68	4.12	193.82
ABAQUS	$N = 1$	98.26	12.37	96.02	9.38	90.85	15.51	No data
	$N = 2$	99.35	8.889	99.24	4.46	99.78	1.82	
	$N = 3$				Failed			

Using the fitted parameters, the numerical solution of the uniaxial and biaxial load cases were calculated, in which the transversal stretches were obtained numerically from the zero transverse stress condition in (3.16) and (3.24). The accuracy of the models could be quantified by the

coefficient of determination R^2 and the standard error of regression S , which are defined as

$$R^2 = 1 - \frac{\sum_{i=1}^M (f_i^{\text{meas}} - f_i^{\text{fit}})^2}{\sum_{i=1}^M (f_i^{\text{meas}} - \bar{f})^2}, \quad \text{and} \quad S = \sqrt{\frac{\sum_{i=1}^M (f_i^{\text{meas}} - f_i^{\text{fit}})^2}{M - 2}}, \quad (3.68)$$

where f stands for the quantity to be compared, while \bar{f} is its average value. The value of R^2 should satisfy $0 < R^2 \leq 1$, where $R^2 = 1$ represents the perfect fit.

The variation of goodness quantities for P_1^{UN} , λ_T^{UN} and P_1^{EB} curves are presented in Table 3.2 and in Fig. 3.6. The results show that the second-order models are very accurate and introducing an additional term in the strain energy potential results only in a slight improvement. It could also be stated, that Strategy C performed the best, even better than the fitting of ABAQUS, whereas Strategy B where β_i were obtained separately using ν^* become significantly faster than the original Strategy A.

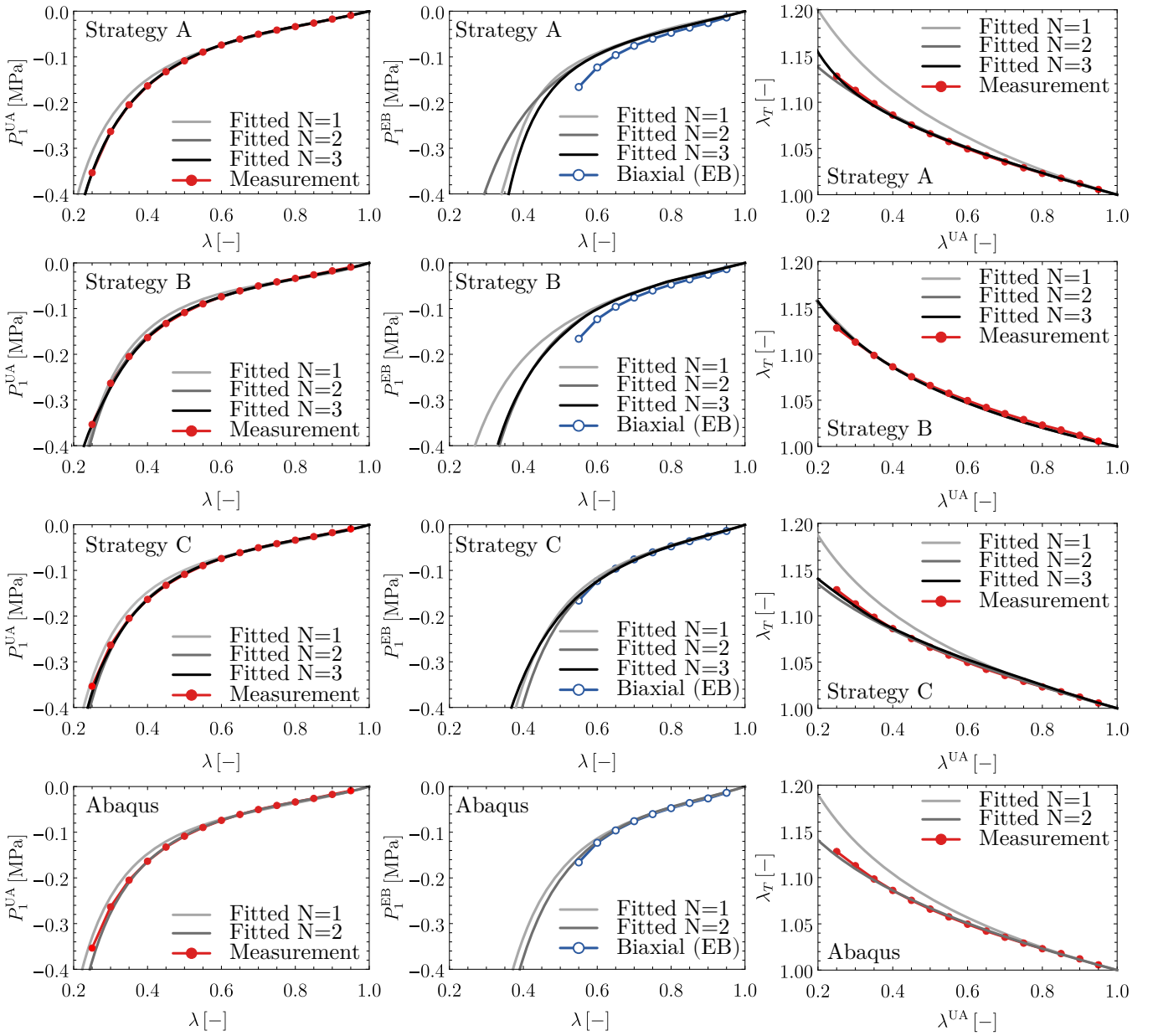


Figure 3.6: Comparison of measurement and fitted Hyperfoam model by Strategy A, B, C and ABAQUS

3.5 Main results

I have analysed the purely elastic behaviour of polymer foams using the Ogden–Hill’s compressible hyperelastic material model with particular interest on the lateral deformations. I have proposed an analytical Drucker-stability criterion for open-cell foams and I have performed detailed experimental analysis on a particular closed-cell polyethylene foam material including uniaxial, biaxial tests, and image processing. I have proposed two novel parameter-fitting strategies to simplify the uniaxial and to estimate the transverse biaxial stretches. By means of comparative analysis with the fitting procedure in ABAQUS, I have drawn the following conclusions.

Thesis statement 1

A) Consider the N -th order Ogden–Hill’s hyperelastic (Hyperfoam) constitutive model for a material (e.g. open-cell polymer foam) where the transverse deformations are negligibly small. Then, the assumption for the hyperelastic parameter $\beta_i = 0$ leads that the material meets the Drucker-stability criterion of $d\boldsymbol{\tau} : d\mathbf{h} > 0$, if and only if, the hyperelastic parameters μ_i and α_i satisfy

$$\sum_{i=1}^N \mu_i \lambda_k^{\alpha_i} > 0, \quad k = 1, 2, 3$$

for all λ_k principal stretches corresponding to any arbitrary deformation.

B) During the parameter fitting of the Ogden–Hill’s hyperelastic (Hyperfoam) model for closed-cell polymer foams with non-negligible transversal effects, let the approximation of λ_T^{UN} uniaxial transversal stretch characteristic be

$$\lambda_T^{\text{UN}} = \lambda^{-\nu^*},$$

where ν^* is the generalized Poisson’s ratio for finite strains, while λ is the longitudinal stretch. In this case, the unmeasured biaxial stretch characteristic (λ_T^{EB}) can be estimated from the uniaxial transverse stretch characteristic as

$$\lambda_T^{\text{EB}} = 2\lambda_T^{\text{UN}} - 1.$$

With this estimation, the accuracy of the parameter fitting can be significantly improved, when the optimization criterion is prescribed for both uniaxial and biaxial test data as

$$Q = Q_1^{\text{UN}} + Q_T^{\text{UN}} + Q_1^{\text{EB}} + Q_T^{\text{EB}},$$

in which Q_1^{UN} and Q_1^{EB} are the errors of the longitudinal stress predictions, while Q_T^{UN} and Q_T^{EB} ensure zero transverse stresses.

Related publications: [SzB1],[SzB2], [SzB3]

4

Viscoelastic characterisation of memory foams

Besides the previously introduced large strain, nonlinear stress-strain characteristic in compression, the mechanical behaviour of several polymer foams also show significant viscoelastic properties [3, 9, 29, 76]. Among the typical viscoelastic properties (summarised in Section 2.1.1), large energy absorption property has the greatest significance from the industrial point of view. Thanks to the properties mentioned above, polymer foams are applied mostly in the industrial field of impact protecting and packaging. The primary goal here is to protect the products from impacts and damages during transportation, storage and delivery, and additionally to damp the environmental vibrations and insulate the product. Besides the industrial applications, viscoelastic polymer foams can also be familiar from everyday life like sport shoe treads, car seats or helmets [9, 77, 78, 42].

These rate-dependent properties are also presented in the memory foam layers of mattresses, where the duration of the loading, caused by the human body during the sleep, is several hours [79, 80]. Originally, the memory foams were developed by NASA [81] for spaceship seats. After the first experiments, the results were published for the public domain. The memory foam was initially referred to as “slow spring back foam”; most called it “temper foam” [81]. The Swedish Fagerdala World Foams released the first commercial memory foam mattress in 1991 [82]. Since then, several manufacturers have joined into production and development. Memory foam mattresses are able to follow the body shape, thus supporting the body uniformly (see Fig. 4.1). Therefore, the pressure on the backbone and the body decreases, which increases the comfort during sleep [79, 80].



Figure 4.1: The commercial a) memory foams and b) the horizontal spine and c) the body shape following the support of memory foam mattresses Sources: cardo.hu, matracguru.hu, www.topmattress.com

4.1 Literature overview and objectives

The behaviour of finite strain viscoelastic materials can be described with adequate precision using the so-called visco-hyperelastic constitutive equation. In this approach, the rate-dependent stress-relaxation phenomenon is modelled with a properly chosen viscoelastic model [10, 27], while for the long-term rate-independent behaviour, a hyperelastic material model is adopted, which can be derived from the corresponding strain energy function.

The characterisation of the rate-dependent properties has been provided in several discussions in the literature. In the work of Weber et al. [83], the rate-dependent material moduli and Poisson’s ratio were determined based on uniaxial compression tests, while Bekkour et al. [84] investigated the rate-dependent and flow properties of polymeric foams experimentally. In some studies, creep and stress-relaxation behaviour were discussed, including the superposition of the temperature and the rate-dependent principles [85, 86]. There are also several recent studies regarding the mechanical modelling approaches, in which different strain energy functions (e.g. extended Ogden, extended Yeoh, Mooney–Rivlin or Exp-Lin) were applied to model the pure hyperelastic behaviour [87, 88, 89]. However, novel strain energy functions can also be applied, like the model by Yang [90] and Elfarhani [91]. Recently, an enhanced KHL-model was proposed by Lee for characterising polymeric foams over a wide range of strain rates [92, 93]. However, the most common method is to combine the previously introduced Hyperfoam model (see Section 3.2) with a Maxwell-type viscoelastic model using the Prony-series representation [9, 80, 94, 95, 96, 97].

The most critical part of material modelling in the latter case to determine all the parameters in the constitutive equation, which should be obtained directly from experimental data using parameter-fitting algorithm. However, the visco-hyperelastic material law is defined in the form of a hereditary integral, therefore the general stress response function cannot be defined. The usually adopted algorithm to find the material parameters for a particular visco-hyperelastic material is to separate the fitting of Prony’s and pure hyperelastic parameters using idealised stress-relaxation and long-term elastic test data [74, 76]. This approach may involve significant errors into the fitting process, consequently, the fitted material parameters cannot describe the overall visco-hyperelastic behaviour accurately, and the solution will be inaccurate (see Fig. 4.2), which is a well-known phenomenon [93, 98]. Using the analytically derived stress-response functions for the stress-relaxation loading case, which have not been provided in the literature yet, the entire visco-hyperelastic material model could be fitted to the measurement data directly as it was provided for the Mooney–Rivlin incompressible hyperelastic material model by [99].

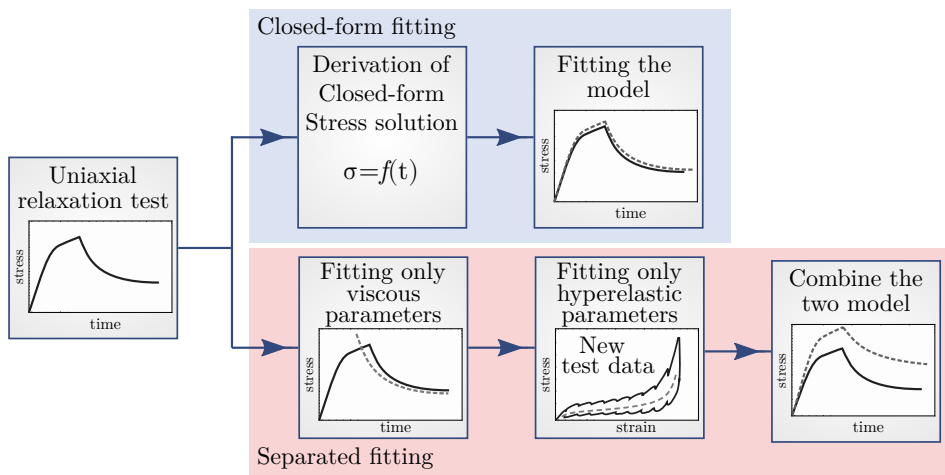


Figure 4.2: Closed-form and separated fitting strategies

The lack of the closed-form stress solution for the visco-hyperelastic constitutive equation based on the Hyperfoam model and the development of the parameter-fitting process was the primary motivation to investigate the material behaviour of compressible polymer foams with rate-dependent properties analytically.

4.2 Finite strain visco-hyperelastic model for foams

The proposed constitutive model for memory foams can be represented as a generalized Standard Linear Solid model, in which P piece of Maxwell-elements and a single Hooke-element are assembled in parallel (see Fig. 4.3/a). Unfortunately, the model name is not uniform in the literature; it is also commonly cited as generalized Maxwell model [15]. Due to the parallel Maxwell-branches, this model characterises the stress relaxation phenomena with improved accuracy compared to the Standard Linear Solid model, introduced in (2.7) [5].

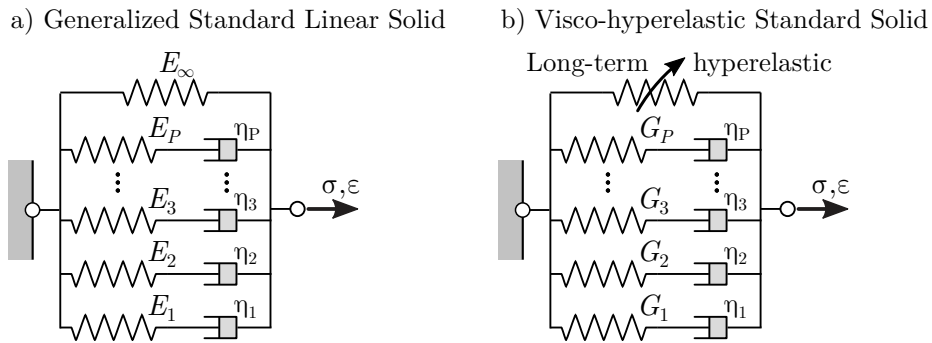


Figure 4.3: Schematics of a) Standard Linear Solid model and b) the proposed large-strain visco-hyperelastic model for memory foams

4.2.1 Solution of the generalized Standard Linear Solid model

In order to develop the general large strain constitutive model, firstly, the stress-strain relation of the generalized Standard Linear Solid model should be derived. In this approach the Hooke-element captures the long-term elastic behaviour, where E_∞ is the long-term elastic modulus, while η_k and E_k denotes the parameters in the Maxwell-elements, respectively [9, 27]. According to (2.9) the relaxation time for each branches can be introduced, namely $\tau_k = \eta_k/E_k$. Thus, similarly to (2.9) the rate-dependent elastic modulus $E(t)$ can be expressed as

$$E(t) = E_\infty + \sum_{k=1}^P E_k e^{-t/\tau_k}. \quad (4.1)$$

This series representation of exponential function is also called as Prony-series [5, 100], which is a widely applied function in the characterisation of even more complex viscoelastic behaviour e.g. using fractional derivatives [101, 102]. The model defines the stress solution in 1D as a hereditary integral as in (2.8), which can be rewritten in an alternative, but equivalent form, which is based on the instantaneous elastic response, instead. In this form, the instantaneous elastic and the viscoelastic contributions can be separated as

$$\sigma(t) = \sigma_0(t) - \sum_{k=1}^P \frac{e_k}{\tau_k} \int_0^t \sigma_0(t-s) e^{-s/\tau_k} ds, \quad (4.2)$$

where the instantaneous stress response $\sigma_0(t)$ can be obtained from $\sigma_0(t) = E_0\varepsilon(t)$ and

$$E_0 = E(0) = E_\infty + \sum_{k=1}^P E_k. \quad (4.3)$$

The above introduced model also contains the so-called relative elastic moduli e_k , which are defined as $e_k = E_k/E_0$ [9, 5].

4.2.2 Finite strain viscoelasticity

The visco-hyperelastic material model can be obtained by reformulating the linear viscoelastic material model using finite strain theory. The resulting model is a finite-strain visco-hyperelastic model, where the long term behaviour is modelled using a hyperelastic model (see Fig. 4.3/b). A possible formulation of such visco-hyperelastic materials is provided by ABAQUS [15]. It should be noted, that in ABAQUS version 6.9, the material model was updated and reformulated [103, 104], but for the Hyperfoam model the implementation remained the previous (as in ABAQUS version 6.8). Therefore, in the present calculations the original formulation is applied. According to this formalism, the constitutive equation is defined for the Kirchhoff stress tensor ($\boldsymbol{\tau}$). For compressible materials the instantaneous Kirchhoff stress tensor $\boldsymbol{\tau}_0$ can be split into hydrostatic and deviatoric parts as

$$\boldsymbol{\tau}_0(t) = \boldsymbol{\tau}_0^D(\bar{\mathbf{F}}(t)) + \boldsymbol{\tau}_0^H(J(t)), \quad (4.4)$$

where the hydrostatic part is the function of the volume ratio J , while the deviatoric part is related to the so-called distortional deformation gradient $\bar{\mathbf{F}}$. The distortional deformation gradient can be directly obtained from the deformation gradient \mathbf{F} , as

$$\bar{\mathbf{F}} = \mathbf{F}J^{-1/3}. \quad (4.5)$$

The visco-hyperelastic constitutive equation corresponding to finite strain materials can be obtained by the following convolution integrals [15]:

$$\boldsymbol{\tau}^D(t) = \boldsymbol{\tau}_0^D(t) + \text{SYM} \int_0^t \frac{\dot{G}(s)}{G_0} \mathbf{F}_t^{-1}(t-s) \boldsymbol{\tau}_0^D(t-s) \mathbf{F}_t(t-s) ds, \quad (4.6)$$

$$\boldsymbol{\tau}^H(t) = \boldsymbol{\tau}_0^H(t) + \int_0^t \frac{\dot{K}(s)}{K_0} \boldsymbol{\tau}_0^H(t-s) ds. \quad (4.7)$$

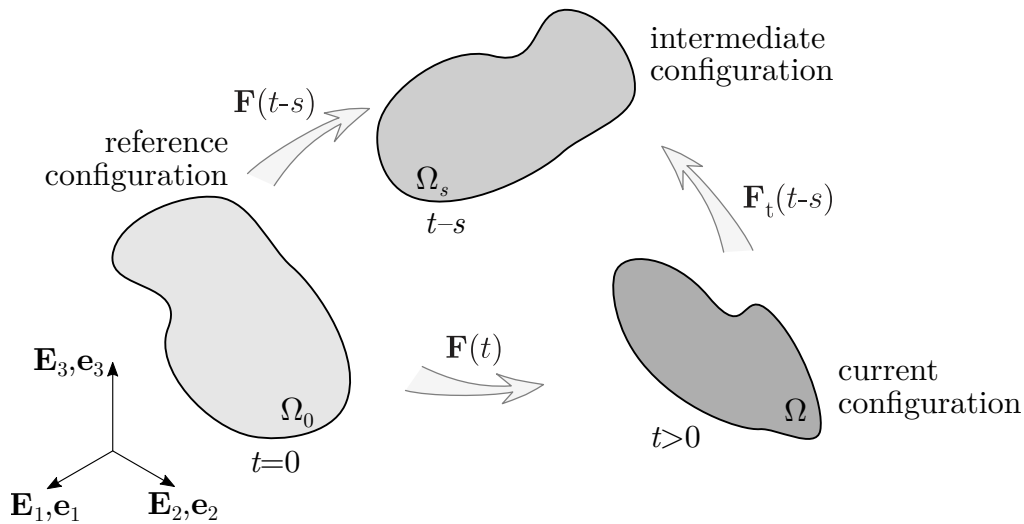


Figure 4.4: The representation of the $\mathbf{F}_t(t-s)$ relative deformation gradient

The hereditary integral of the deviatoric part is performed via the so-called pull-back $\mathbf{F}_t(t-s)$ and push-forward $\mathbf{F}_t^{-1}(t-s)$ operators. In order to ensure objectivity (see Section 2.2.4), the system is transformed firstly back into the state corresponding to time $t-s$, where the convolution integral can be performed and then transformed back into the spatial configuration. Finally, the symmetric part of the solution is obtained by using the SYM operator. The pull-back operator (illustrated in Fig. 4.4) is practically a relative deformation gradient defined between the time instants $t-s$ and t , thus

$$\mathbf{F}_t(t-s) = \mathbf{F}(t-s)\mathbf{F}^{-1}(t). \quad (4.8)$$

In the governing constitutive law in (4.6)-(4.7) G_0 and K_0 are the instantaneous shear and bulk moduli, respectively. Similarly to (4.1), the rate-dependent mechanical moduli are provided in Prony-series representation as

$$G(t) = G_0 \left(g_\infty + \sum_{k=1}^{P_g} g_k e^{-t/\tau_k^G} \right), \quad (4.9)$$

$$K(t) = K_0 \left(k_\infty + \sum_{k=1}^{P_k} k_k e^{-t/\tau_k^K} \right), \quad (4.10)$$

where g_k and k_k are the relative, while g_∞ and k_∞ are the long-term moduli, respectively. For the so-called relaxation moduli the following condition holds:

$$g_\infty + \sum_{k=1}^{PG} g_k = k_\infty + \sum_{k=1}^{PK} k_k = 1. \quad (4.11)$$

The substitution of (4.9)-(4.10) into the convolution integrals in (4.6) and (4.7) defines the constitutive equation of the material model as

$$\boldsymbol{\tau}^D(t) = \boldsymbol{\tau}_0^D(t) - \text{SYM} \left[\sum_{k=1}^{P_g} \frac{g_k}{\tau_k^G} \int_0^t \mathbf{F}_t^{-1}(t-s) \boldsymbol{\tau}_0^D(t-s) \mathbf{F}_t(t-s) e^{-s/\tau_k^G} ds \right], \quad (4.12)$$

$$\boldsymbol{\tau}^H(t) = \boldsymbol{\tau}_0^H(t) - \sum_{k=1}^{P_k} \frac{k_k}{\tau_k^K} \int_0^t \boldsymbol{\tau}_0^H(t-s) e^{-s/\tau_k^K} ds. \quad (4.13)$$

Based on the literature suggestions it is assumed that the number of parameters in the deviatoric and the hydrostatic parts are equal, letting $P_g = P_k = P$ [9, 15]. In addition, the expression above can also be simplified by letting $g_k = k_k$ and $\tau_k^G = \tau_k^K = \tau_k$ [9, 15, 27]. Applying the previous assumptions, the visco-hyperelastic extension of the Hyperfoam model becomes

$$\boldsymbol{\tau}^D(t) = \boldsymbol{\tau}_0^D(t) - \text{SYM} \left[\sum_{k=1}^P \frac{g_k}{\tau_k} \int_0^t \mathbf{F}_t^{-1}(t-s) \boldsymbol{\tau}_0^D(t-s) \mathbf{F}_t(t-s) e^{-s/\tau_k} ds \right], \quad (4.14)$$

$$\boldsymbol{\tau}^H(t) = \boldsymbol{\tau}_0^H(t) - \sum_{k=1}^P \frac{g_k}{\tau_k} \int_0^t \boldsymbol{\tau}_0^H(t-s) e^{-s/\tau_k} ds, \quad (4.15)$$

where the instantaneous stress responses, $\boldsymbol{\tau}_0^D(t)$ and $\boldsymbol{\tau}_0^H(t)$ are adopted from the Hyperfoam material model defined in (3.13).

4.2.3 Numerical solution

The stress solution for visco-hyperelastic materials can be obtained as the solution of the derived constitutive equation in (4.14) and (4.15), where the prescribed $\lambda(t)$ stretch-history in the instantaneous stress response characterise the loading path. During the finite element analysis, it is required to solve the integrals efficiently. Therefore, a numerical integration scheme is also provided [15], where solution is integrated forward in time.

Firstly, let us introduce $\boldsymbol{\tau}_k^D(t)$ and $\boldsymbol{\tau}_k^H(t)$ internal deviatoric and hydrostatic stresses, which are defined as

$$\boldsymbol{\tau}_k^D(t) = \text{SYM} \left[\frac{g_k}{\tau_k} \int_0^t \mathbf{F}_t^{-1}(t-s) \boldsymbol{\tau}_0^D(t-s) \mathbf{F}_t(t-s) \exp \left[\frac{-s}{\tau_k} \right] ds \right], \quad (4.16)$$

$$\boldsymbol{\tau}_k^H(t) = \frac{g_k}{\tau_k} \int_0^t \boldsymbol{\tau}_0^H(t-s) \exp \left[\frac{-s}{\tau_k} \right] ds. \quad (4.17)$$

For the deviatoric stresses, the pull-back, the push-forward and the SYM operators should also be considered, thus a modified deviatoric stresses should be obtained as

$$\hat{\boldsymbol{\tau}}_0^D(t) = \text{SYM} \left[\Delta \mathbf{F} \boldsymbol{\tau}_0^D(t) \Delta \mathbf{F}^{-1} \right], \quad (4.18)$$

$$\hat{\boldsymbol{\tau}}_k^D(t) = \text{SYM} \left[\Delta \mathbf{F} \boldsymbol{\tau}_k^D(t) \Delta \mathbf{F}^{-1} \right], \quad (4.19)$$

where $\Delta \mathbf{F} = \mathbf{F}_t(t + \Delta t)$. Assuming first-order approximation for all the quantities within a step, the stress solution at time $t + \Delta t$ can be provided as

$$\begin{aligned} \boldsymbol{\tau}(t + \Delta t) = & \left(1 - \sum_{k=1}^P a_i g_k \right) \boldsymbol{\tau}_0^D(t + \Delta t) + \sum_{k=1}^P b_i g_k \hat{\boldsymbol{\tau}}_0^D(t) + \sum_{k=1}^P c_i \hat{\boldsymbol{\tau}}_k^D(t) + \\ & \left(1 - \sum_{k=1}^P a_i g_k \right) \boldsymbol{\tau}_0^H(t + \Delta t) + \sum_{k=1}^P b_i g_k \boldsymbol{\tau}_0^H(t) + \sum_{k=1}^P c_i \boldsymbol{\tau}_k^H(t), \end{aligned} \quad (4.20)$$

with

$$a_i = 1 - \frac{\tau_k}{\Delta t} (1 - c_i); \quad b_i = \frac{\tau_k}{\Delta t} (1 - c_i) - c_i; \quad c_i = \exp \left[\frac{-\Delta t}{\tau_k} \right]. \quad (4.21)$$

Therefore, the stress solution at time $t + \Delta t$ can be derived from the instantaneous and internal stress values at time instant t and $t + \Delta t$. The detailed derivation of the integration scheme is provided in Appendix C.

4.3 Closed-form stress solutions

The visco-hyperelastic material parameters could be obtained directly from the relaxation test, if the closed-form stress solution for such loading history is available. This stress solution can be obtained by solving the hereditary integrals in (4.14)-(4.15) [SzB1], [SzB4]. The analytical solvability of the convolution integrals strongly depends on the loading history. The stretch history corresponding to the ramp loading in compression, as shown in Fig. 4.5, is given by

$$\lambda(t) = \begin{cases} 1 + \dot{\epsilon} t & t \leq T \\ 1 + \dot{\epsilon} T & t > T \end{cases}, \quad (4.22)$$

which means that firstly, the body is compressed with constant $\dot{\epsilon} < 0$ strain rate in a finite T time, then the strain is kept constant.

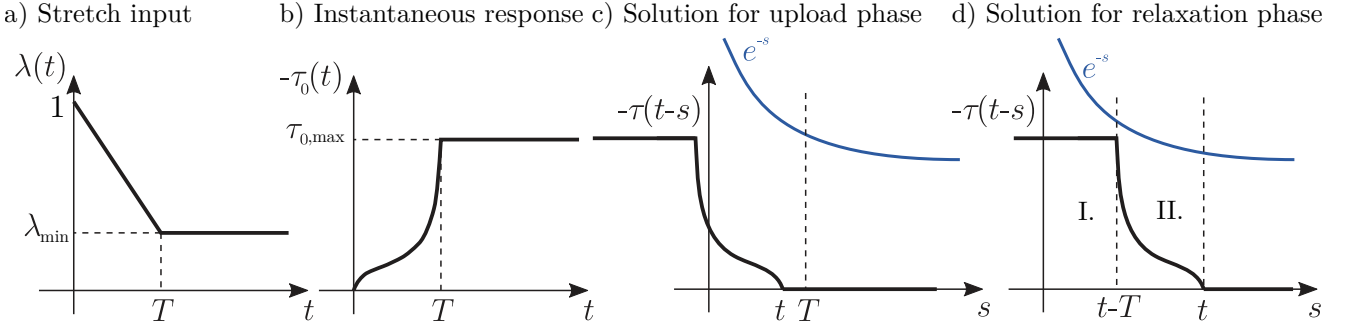


Figure 4.5: The a) stretch input $\lambda(t)$, where $\lambda_{\min} = 1 + \varepsilon T$ and the corresponding b) instantaneous stress function $\tau_0(t)$ and c)-d) the steps of the convolution integral for the uploading and the relaxation parts

Integrals (4.14)-(4.15) could not be performed in one step, because $\lambda(t)$ and the instantaneous Kirchhoff stress $\tau_0(t)$ is a piecewise function containing two-phases: the uploading and the relaxation regimes (see Fig. 4.5). Therefore, the hereditary integral is performed also in two steps and the exact stress solution is provided as separated functions for the uploading and the relaxation phases, respectively.

4.3.1 Homogeneous confined compression

The exact stress-solutions for homogeneous confined compression loading cases (uniaxial, equibiaxial and volumetric) have the same structure, therefore let us introduce the parameter M [SzB1], which indicates the applied loading case, namely

$$M = \begin{cases} 1 & \text{for uniaxial (CU)} \\ 2 & \text{for equibiaxial (CB)} \\ 3 & \text{for volumetric (VOL)} \end{cases} . \quad (4.23)$$

In all cases the body is compressed uniformly in M directions and the corresponding so-called longitudinal stretch is denoted by λ_L . In the other $(3 - M)$ directions, the transverse stretches, denoted by λ_T , are kept constant, letting $\lambda_T \equiv 1$. In order to simplify the presentation the notation (t) will be omitted in the following expressions. Based on (3.19),(3.22) and (3.30), the deformation gradient and the instantaneous Kirchhoff stress tensors for the three loading cases become

$$\mathbf{F}^{\text{CU}} = \begin{bmatrix} \lambda_L & 0 & 0 \\ 0 & \lambda_T & 0 \\ 0 & 0 & \lambda_T \end{bmatrix} = \begin{bmatrix} \lambda_L & 0 & 0 \\ 0 & 1 & 0 \\ 0 & 0 & 1 \end{bmatrix}, \quad \boldsymbol{\tau}_0^{\text{CU}} = \begin{bmatrix} \tau_{L0} & 0 & 0 \\ 0 & \tau_{T0} & 0 \\ 0 & 0 & \tau_{T0} \end{bmatrix}, \quad (4.24)$$

$$\mathbf{F}^{\text{CB}} = \begin{bmatrix} \lambda_L & 0 & 0 \\ 0 & \lambda_L & 0 \\ 0 & 0 & \lambda_T \end{bmatrix} = \begin{bmatrix} \lambda_L & 0 & 0 \\ 0 & \lambda_L & 0 \\ 0 & 0 & 1 \end{bmatrix}, \quad \boldsymbol{\tau}_0^{\text{CB}} = \begin{bmatrix} \tau_{L0} & 0 & 0 \\ 0 & \tau_{L0} & 0 \\ 0 & 0 & \tau_{T0} \end{bmatrix}, \quad (4.25)$$

$$\mathbf{F}^{\text{VOL}} = \begin{bmatrix} \lambda_L & 0 & 0 \\ 0 & \lambda_L & 0 \\ 0 & 0 & \lambda_L \end{bmatrix}, \quad \boldsymbol{\tau}_0^{\text{VOL}} = \begin{bmatrix} \tau_{L0} & 0 & 0 \\ 0 & \tau_{L0} & 0 \\ 0 & 0 & \tau_{L0} \end{bmatrix}. \quad (4.26)$$

The corresponding volume ratio becomes $J = (\lambda_L)^M$. For the hereditary integrals in (4.14)-(4.15) the instantaneous Kirchhoff stress tensor $\boldsymbol{\tau}_0$ is obtained by substituting the stretch input into the

pure hyperelastic stress solution using (3.20),(3.28),(3.31) and Table 2.1. The expressions for the instantaneous longitudinal $\tau_{L0}(t)$ and the transverse $\tau_{T0}(t)$ stress components can be obtained as

$$\tau_{L0}(t) = \sum_{i=1}^N \frac{2\mu_i}{\alpha_i} \left([\lambda(t)]^{\alpha_i} - [\lambda(t)]^{-M\alpha_i\beta_i} \right), \quad (4.27)$$

$$\tau_{T0}(t) = \sum_{i=1}^N \frac{2\mu_i}{\alpha_i} \left(1 - [\lambda(t)]^{-M\alpha_i\beta_i} \right). \quad (4.28)$$

After performing the integrals the stress solutions can be expressed as [SzB1]

$$\tau_L(t) = \begin{cases} \tau_{L0}(t) - \sum_{k=1}^P g_k \left(\sum_{i=1}^N \frac{2\mu_i}{\alpha_i} \eta_{ik} \right) & t \leq T, \\ \tau_{L0}(T) \left(1 - \sum_{k=1}^P g_k \left(1 - e^{-\frac{T-t}{\tau_k}} \right) \right) - \sum_{k=1}^P g_k \left(\sum_{i=1}^N \frac{2\mu_i}{\alpha_i} \vartheta_{ik} \right) & t > T, \end{cases} \quad (4.29)$$

$$\tau_T(t) = \begin{cases} \tau_{T0}(t) - \sum_{k=1}^P g_k \left(\sum_{i=1}^N \frac{2\mu_i}{\alpha_i} \hat{\eta}_{ik} \right) & t \leq T, \\ \tau_{T0}(T) \left(1 - \sum_{k=1}^P g_k \left(1 - e^{-\frac{T-t}{\tau_k}} \right) \right) - \sum_{k=1}^P g_k \left(\sum_{i=1}^N \frac{2\mu_i}{\alpha_i} \hat{\vartheta}_{ik} \right) & t > T, \end{cases} \quad (4.30)$$

where the quantities $\eta_{ik}, \vartheta_{ik}, \hat{\eta}_{ik}, \hat{\vartheta}_{ik}$ are the second-order parameter tensors, defined using the loading case parameter M as

$$\begin{aligned} \eta_{ik} = & e^{-\frac{t-1/\dot{\epsilon}}{\tau_k}} \left(\frac{-1}{\dot{\epsilon}\tau_k} \right)^{M\alpha_i\beta_i} \left(\Gamma \left[1 - M\alpha_i\beta_i, \frac{-1}{\tau_k\dot{\epsilon}} \right] - \Gamma \left[1 - M\alpha_i\beta_i, \frac{-1-t\dot{\epsilon}}{\tau_k\dot{\epsilon}} \right] \right) \\ & + e^{-\frac{t+1/\dot{\epsilon}}{\tau_k}} \left(\frac{-1}{\dot{\epsilon}\tau_k} \right)^{-\alpha_i} \left(\Gamma \left[1 + \alpha_i, -\frac{1+t\dot{\epsilon}}{\tau_k\dot{\epsilon}} \right] - \Gamma \left[1 + \alpha_i, -\frac{1}{\tau_k\dot{\epsilon}} \right] \right), \end{aligned} \quad (4.31)$$

$$\begin{aligned} \vartheta_{ik} = & e^{-\frac{t-1/\dot{\epsilon}}{\tau_k}} \left(\frac{-1}{\dot{\epsilon}\tau_k} \right)^{M\alpha_i\beta_i} \left(\Gamma \left[1 - M\alpha_i\beta_i, \frac{-1}{\tau_k\dot{\epsilon}} \right] - \Gamma \left[1 - M\alpha_i\beta_i, \frac{-1-T\dot{\epsilon}}{\tau_k\dot{\epsilon}} \right] \right) + \\ & + e^{-\frac{1-\dot{\epsilon}t}{\dot{\epsilon}\tau_k}} \left(\frac{-1}{\dot{\epsilon}\tau_k} \right)^{-\alpha_i} \left(\Gamma \left[1 + \alpha_i, \frac{-1-T\dot{\epsilon}}{\tau_k\dot{\epsilon}} \right] - \Gamma \left[1 + \alpha_i, \frac{-1}{\tau_k\dot{\epsilon}} \right] \right), \end{aligned} \quad (4.32)$$

$$\begin{aligned} \hat{\eta}_{ik} = & e^{-\frac{t-1/\dot{\epsilon}}{\tau_k}} \left(\frac{-1}{\dot{\epsilon}\tau_k} \right)^{M\alpha_i\beta_i} \left(\Gamma \left[1 - M\alpha_i\beta_i, \frac{-1}{\tau_k\dot{\epsilon}} \right] - \Gamma \left[1 - M\alpha_i\beta_i, \frac{-1-t\dot{\epsilon}}{\tau_k\dot{\epsilon}} \right] \right) \\ & + 1 - e^{-\frac{t}{\tau_k}}, \end{aligned} \quad (4.33)$$

$$\begin{aligned} \hat{\vartheta}_{ik} = & e^{-\frac{t-1/\dot{\epsilon}}{\tau_k}} \left(\frac{-1}{\dot{\epsilon}\tau_k} \right)^{M\alpha_i\beta_i} \left(\Gamma \left[1 - M\alpha_i\beta_i, \frac{-1}{\tau_k\dot{\epsilon}} \right] - \Gamma \left[1 - M\alpha_i\beta_i, \frac{-1-t\dot{\epsilon}}{\tau_k\dot{\epsilon}} \right] \right) \\ & + e^{-\frac{t-T}{\tau_k}} - e^{-\frac{t}{\tau_k}}. \end{aligned} \quad (4.34)$$

In the parameters above, $\Gamma[a, z]$ represents the incomplete upper gamma function [105, 106], which is defined as

$$\Gamma[\nu, x] = \int_x^{\infty} t^{\nu-1} e^{-t} dt. \quad (4.35)$$

Using the above-introduced expressions the exact Kirchhoff stress solution can be obtained as

$$\boldsymbol{\tau}^{\text{UN}}(t) = \begin{bmatrix} \tau_L(t) & 0 & 0 \\ 0 & \tau_T(t) & 0 \\ 0 & 0 & \tau_T(t) \end{bmatrix} \text{ with } M = 1, \quad (4.36)$$

$$\boldsymbol{\tau}^{\text{EB}}(t) = \begin{bmatrix} \tau_L(t) & 0 & 0 \\ 0 & \tau_L(t) & 0 \\ 0 & 0 & \tau_T(t) \end{bmatrix} \text{ with } M = 2, \quad (4.37)$$

$$\boldsymbol{\tau}^{\text{VOL}}(t) = \begin{bmatrix} \tau_L(t) & 0 & 0 \\ 0 & \tau_L(t) & 0 \\ 0 & 0 & \tau_L(t) \end{bmatrix} \text{ with } M = 3. \quad (4.38)$$

The Cauchy stress solutions can be also obtained using the identity $\boldsymbol{\sigma}(t) = \boldsymbol{\tau}(t)/J(t)$. This yields, that the instantaneous Cauchy stresses become

$$\sigma_{L0}(t) = \frac{\tau_{L0}(t)}{J(t)}, \quad \sigma_{T0}(t) = \frac{\tau_{T0}(t)}{J(t)}, \quad (4.39)$$

where

$$J(t) = \begin{cases} (1 + \dot{\varepsilon}t)^M & t \leq T, \\ (1 + \dot{\varepsilon}T)^M & t > T. \end{cases} \quad (4.40)$$

For simplicity let $J(T) \equiv (1 + \dot{\varepsilon}T)^M$. Substituting (4.40) and (4.29)-(4.30) into (4.39) leads to the solutions

$$\sigma_L(t) = \begin{cases} \sigma_{L0}(t) - \sum_{k=1}^P g_k \left(\sum_{i=1}^N \frac{2\mu_i}{\alpha_i} \eta_{ik} \right) (1 + \dot{\varepsilon}t)^{-M} & t \leq T, \\ \sigma_{L0}(T) \left(1 - \sum_{k=1}^P g_k \left(1 - e^{-\frac{T-t}{\tau_k}} \right) \right) - \frac{1}{J(T)} \sum_{k=1}^P g_k \left(\sum_{i=1}^N \frac{2\mu_i}{\alpha_i} \vartheta_{ik} \right) & t > T, \end{cases} \quad (4.41)$$

$$\sigma_T(t) = \begin{cases} \sigma_{T0}(t) - \sum_{k=1}^P g_k \left(\sum_{i=1}^N \frac{2\mu_i}{\alpha_i} \hat{\eta}_{ik} \right) (1 + \dot{\varepsilon}t)^{-M} & t \leq T, \\ \sigma_{T0}(T) \left(1 - \sum_{k=1}^P g_k \left(1 - e^{-\frac{T-t}{\tau_k}} \right) \right) - \frac{1}{J(T)} \sum_{k=1}^P g_k \left(\sum_{i=1}^N \frac{2\mu_i}{\alpha_i} \hat{\vartheta}_{ik} \right) & t > T. \end{cases} \quad (4.42)$$

4.3.2 Homogeneous compression with $\beta_i = 0$

In the case, when the hyperelastic material parameters β_i are zero, e.g. for open-cell foams (see Section 3.1) [SzB4], the longitudinal loads have no effect in the transverse directions, therefore $\lambda_T \equiv 1$ and the transverse stress is identically zero, thus $\tau_T(t) \equiv 0$. Consequently, the deformation gradients for the uniaxial, biaxial and volumetric loading cases will be the same as in (4.24)-(4.26). In order to distinguish from the previous loading case, index B will be applied for the longitudinal direction, when $\beta_i = 0$ holds. The instantaneous longitudinal $\tau_{B0}(t)$ Kirchhoff stress and the corresponding Cauchy stress components simplify to

$$\tau_{B0}(t) = \sum_{i=1}^N \frac{2\mu_i}{\alpha_i} ([\lambda(t)]^{\alpha_i} - 1), \quad \sigma_{B0}(t) = \frac{\tau_{B0}(t)}{J(t)}. \quad (4.43)$$

This yields, that the solutions should be derived only for $\tau_{B0}(t)$. After performing the hereditary integral, the solution becomes [SzB4]

$$\tau_B(t) = \begin{cases} \tau_{B0}(t) - \sum_{k=1}^P g_k \left(\sum_{i=1}^N \frac{2\mu_i}{\alpha_i} \tilde{\eta}_{ik} \right) & t \leq T, \\ \tau_{B0}(T) \left(1 - \sum_{k=1}^P g_k \left(1 - e^{-\frac{T-t}{\tau_k}} \right) \right) - \sum_{k=1}^P g_k \left(\sum_{i=1}^N \frac{2\mu_i}{\alpha_i} \tilde{\vartheta}_{ik} \right) & t > T, \end{cases} \quad (4.44)$$

in which

$$\tilde{\eta}_{ik} = -e^{-\frac{-t-1/\dot{\epsilon}}{\tau_k}} \left(\frac{-1}{\dot{\epsilon}\tau_k} \right)^{-\alpha_i} \left(\Gamma \left[1 + \alpha_i, \frac{-1}{\tau_k \dot{\epsilon}} \right] - \Gamma \left[1 + \alpha_i, \frac{-1 - t\dot{\epsilon}}{\tau_k \dot{\epsilon}} \right] \right) + e^{-\frac{t}{\tau_k}} - 1, \quad (4.45)$$

$$\tilde{\vartheta}_{ik} = -e^{-\frac{-1-\dot{\epsilon}t}{\dot{\epsilon}\tau_k}} \left(\frac{-1}{\dot{\epsilon}\tau_k} \right)^{-\alpha_i} \left(\Gamma \left[1 + \alpha_i, \frac{-1}{\tau_k \dot{\epsilon}} \right] - \Gamma \left[1 + \alpha_i, \frac{-1 - T\dot{\epsilon}}{\tau_k \dot{\epsilon}} \right] \right) + e^{-\frac{t}{\tau_k}} - e^{-\frac{-t+T}{\tau_k}}. \quad (4.46)$$

This means that the Kirchhoff stress tensor solutions can be written as

$$\boldsymbol{\tau}_B^{\text{UN}}(t) = \begin{bmatrix} \tau_B(t) & 0 & 0 \\ 0 & 0 & 0 \\ 0 & 0 & 0 \end{bmatrix}, \quad (4.47)$$

$$\boldsymbol{\tau}_B^{\text{EB}}(t) = \begin{bmatrix} \tau_B(t) & 0 & 0 \\ 0 & \tau_B(t) & 0 \\ 0 & 0 & 0 \end{bmatrix}, \quad (4.48)$$

$$\boldsymbol{\tau}_B^{\text{VOL}}(t) = \begin{bmatrix} \tau_B(t) & 0 & 0 \\ 0 & \tau_B(t) & 0 \\ 0 & 0 & \tau_B(t) \end{bmatrix}. \quad (4.49)$$

Similarly to (4.41)-(4.42), the Cauchy stress solution can be obtained as

$$\sigma_B(t) = \begin{cases} \sigma_{B0}(t) - \sum_{k=1}^P g_k \left(\sum_{i=1}^N \frac{2\mu_i}{\alpha_i} \tilde{\eta}_{ik} \right) (1 + \dot{\epsilon}t)^{-M} & t \leq T, \\ \sigma_{B0}(T) \left(1 - \sum_{k=1}^P g_k \left(1 - e^{-\frac{T-t}{\tau_k}} \right) \right) - \frac{1}{J(T)} \sum_{k=1}^P g_k \left(\sum_{i=1}^N \frac{2\mu_i}{\alpha_i} \tilde{\vartheta}_{ik} \right) & t > T. \end{cases} \quad (4.50)$$

4.3.3 Comparison with numerical integration (FEA)

In the previous section, the exact stress solutions for the ramp loading have been derived via the analytical solution of the hereditary integrals. The validation of the analytical integration was performed using the numerical integration in ABAQUS.

The goal of the analysis is to compare the model prediction of the proposed closed-form stress solution and the numerical scheme for ramp loading prescribed by $\lambda(t)$ in (4.22). Furthermore, the analysis also aims to highlight that with properly chosen time increments, the numerical scheme with first-order approximation (see the numerical integration in Subsection 4.2.3 and Appendix C) results in accurate stress-solution.

The FEA was performed in ABAQUS [15]. The geometry is a unit cube ($1 \times 1 \times 1$ mm), the mesh contains only one eight-node brick element with reduced integration (C3D8R), in order to fully characterize homogeneous deformations. As boundary condition zero displacement was applied on plane 1-2-3-4 in direction \mathbf{E}_1 , on plane 3-4-8-7 in direction \mathbf{E}_2 and on plane 1-5-8-4 in direction \mathbf{E}_3 , respectively. Additionally, the homogeneous deformation was ensured by the displacements U_1, U_2, U_3 on planes 5-6-7-8, 1-2-6-5 and 2-3-7-6, respectively as indicated in Fig. 4.6. The prescribed displacement values for the different load cases are listed in Table 4.1.

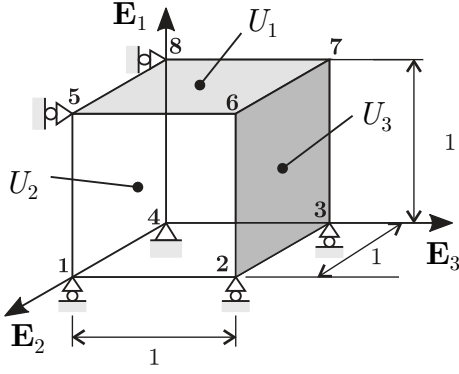


Figure 4.6: The FE model and the applied U_1, U_2, U_3 displacements

Table 4.1: Prescribed displacement values for FE validation

Load case	M	U_1 [mm]	U_2 [mm]	U_3 [mm]
Confined uniaxial	1	-0.8	0	0
Confined biaxial	2	-0.6	-0.6	0
Volumetric	3	-0.8	0	0
Uniaxial with $\beta_i = 0$	-	-0.8	-0.8	-0.8

The FE calculations have been divided into two steps. In the first step, the body is compressed with a constant strain rate up to the prescribed displacement in $T = 2$ s, while in the second step, the strain was kept constant. The steps were computed in numerous increments in order to provide an accurate numerical solution for the nonlinear material law. The parameters of the steps applied in the FEA are listed in Table 4.2. Note, that further step-refinement has completely negligible effect on the results. Hence, this solution is considered to be the exact one.

Table 4.2: The step parameters and number of increments in FE validation

Step	Start	End	Increment	Number of Increments
1	0 s	2 s	0.01 s	200
2	2 s	100 s	0.2 s	490

4.3.3.1 Material parameters

In order to adopt the stress solution, all $3N$ hyperelastic (α_i, μ_i, β_i) and $2P$ Prony-parameters (g_i, τ_i) have to be provided. During the FE calculations a 3rd-order Prony-series (i.e. $P = 3$)

was applied, while the order of the hyperelastic model was also $N = 3$. The hyperelastic and Prony-parameters, presented in Table 4.3, were chosen arbitrarily for illustrative purposes.

Table 4.3: The material parameters applied in FEA validation

Hyperfoam parameters $N = 3$								
α_1 [-]	μ_1 [MPa]	β_1 [-]	α_2 [-]	μ_2 [MPa]	β_2 [-]	α_3 [-]	μ_3 [MPa]	β_3 [-]
2.63	0.00064	1.214	4.78	0.084	0.0072	0.0058	0.0085	0.6
Prony-parameters $P = 3$								
g_1 [-]	g_2 [-]	g_3 [-]	τ_1 [s]	τ_2 [s]	τ_3 [s]			
0.12	0.74	0.05	0.2	2	20			

4.3.3.2 Comparison of results

The comparison the FE results and the prediction using the closed-form stress solutions are presented in Fig. 4.7. Furthermore, the accuracy of the solution was also implemented using the numerical scheme presented in Section 4.2.3. The result clearly shows that the analytical solution provides the same stress solution as the FEA and the numerical scheme, which confirms the correctness of the analytical integration and the adequate accuracy of the first-order approximation in the numerical scheme.

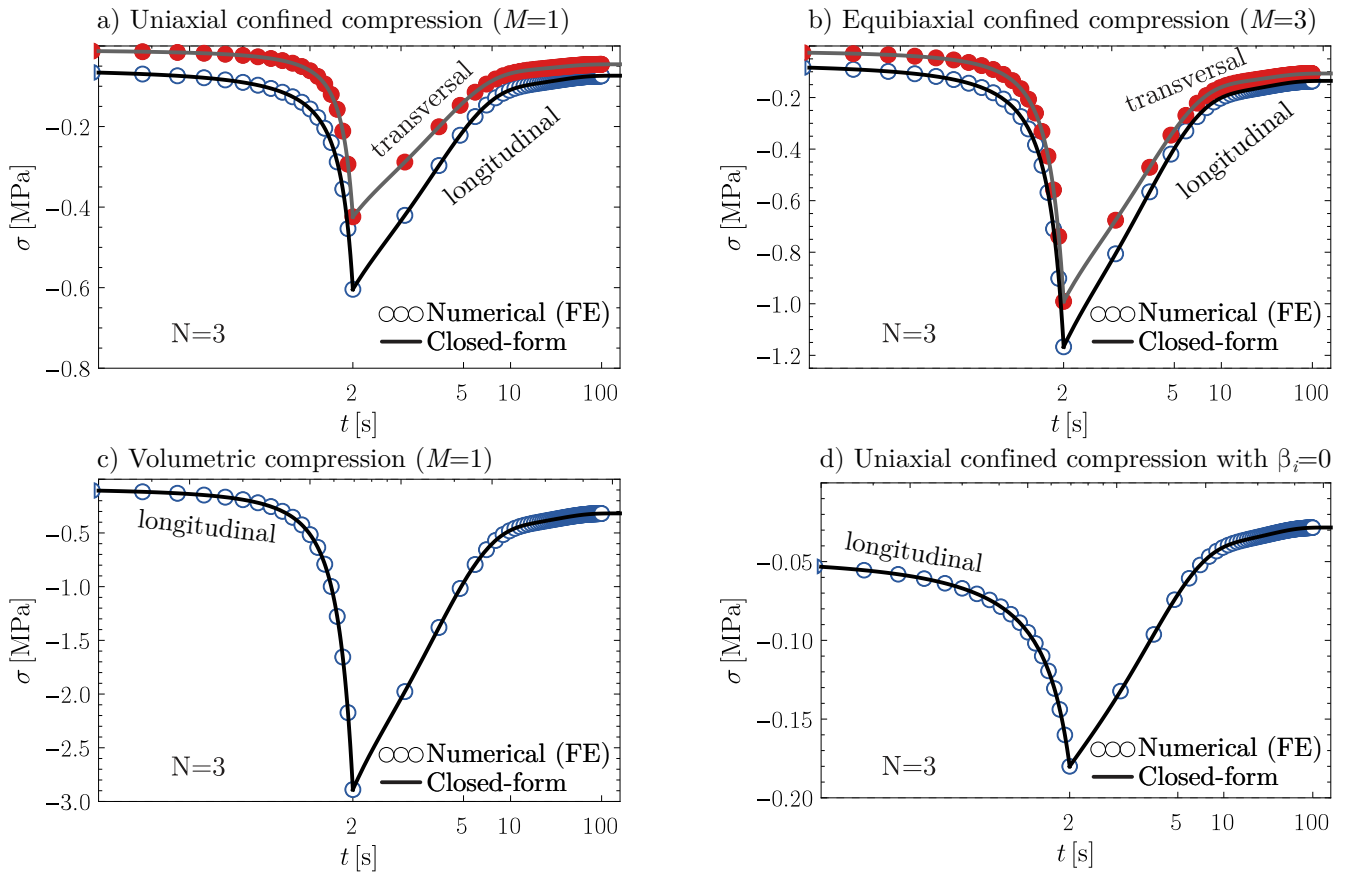


Figure 4.7: Comparison of the closed-form stress-solutions with numerical integration in ABAQUS in case of a) confined uniaxial, b) confined equibiaxial, c) volumetric and d) confined uniaxial compression with $\beta_i = 0$

4.4 Case-study: Polyurethane memory foam

In order to present the benefits of the novel closed-form stress solutions during the parameter identification process, mechanical tests were carried out on a particular open-cell polymer foam material. Based on the obtained measurement data, the performance of the different parameter-fitting approaches (separated and closed-form) were compared. The investigated material is a commercial so-called “memory foam”, which is an open-cell polyurethane foam applied in mattresses and medical products. The microstructure of the material is presented in Fig. 4.8.

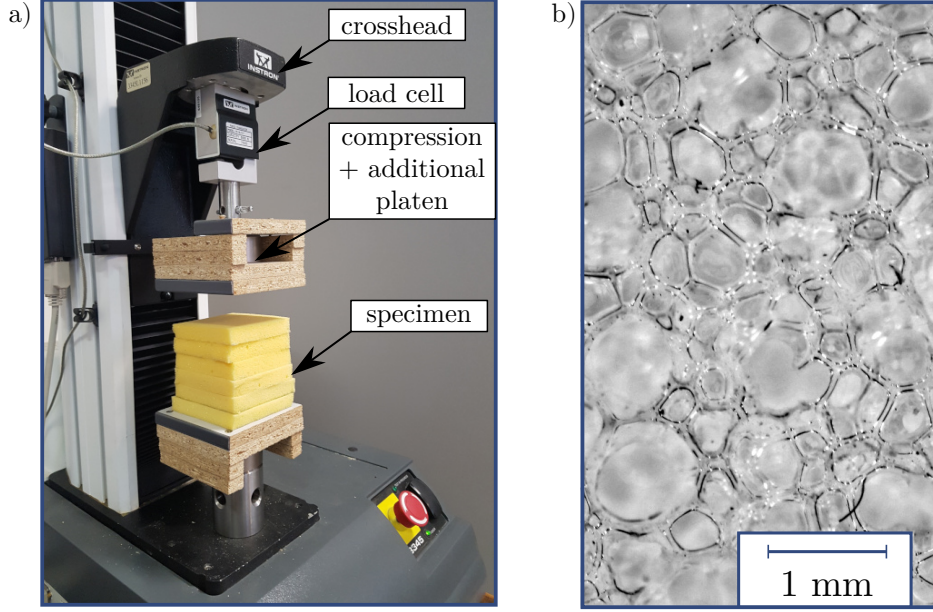


Figure 4.8: The a) measurement layout and b) the microstructure of the investigated polyurethane memory foam

4.4.1 Measurement results

Since the investigated material is open-cell foam, for simplicity its Poisson’s ratio is approximated with $\nu \approx 0$ [9, 27], which yields that the hyperelastic parameter $\beta_i = 0$. Therefore, the material parameters could be fitted using uniaxial compression test data. The measurements were performed with an Instron 3345 Single Column Universal Testing System, while the load was measured by an Instron model 2519-107 5kN load cell. From the raw material, homogeneous specimens were cut with the size of $8 \times 8 \times 8$ cm and piled together accordingly to ISO 3386 [73]. In order to provide the required measurement data for the fitting process, displacement-controlled relaxation and cyclic tests were performed. During the measurement, in every sampling point the load (F) and the displacement (u) values were recorded, from which the longitudinal stretch and the engineering stress data can be obtained as

$$\lambda_1 = 1 + \frac{u}{L_0}, \quad P_1 = \sigma_1 = \frac{F}{A_0}, \quad (4.51)$$

where the initial cross-section is $A_0 = 6400 \text{ mm}^2$ and specimens’ height is $L_0 = 80 \text{ mm}$. Additionally, the Cauchy (σ_1) and the first Piola–Kirchhoff (P_1) stresses are identical, since the transversal strains can be neglected, i.e. $\lambda_T = 1$ and $J = \lambda_1$.

4.4.1.1 Relaxation test

During this test, the specimen was compressed with a constant strain rate in a finite time T , and then the strain was kept constant, while the stress relaxes. In order to have significant relaxation, the uploading strain rate ($\dot{\epsilon}$) should be as high as possible. The applied test parameters are presented in Table 4.4, while Fig. 4.9 shows the $\sigma(t)$ stress response for stress relaxation.

Table 4.4: Relaxation test parameters

Time of uploading, T	4.57 s
Minimal longitudinal stretch, λ_{\min}	0.24
Strain rate, $\dot{\epsilon}$	-0.1662 1/s
Time of relaxation, t_r	600 s

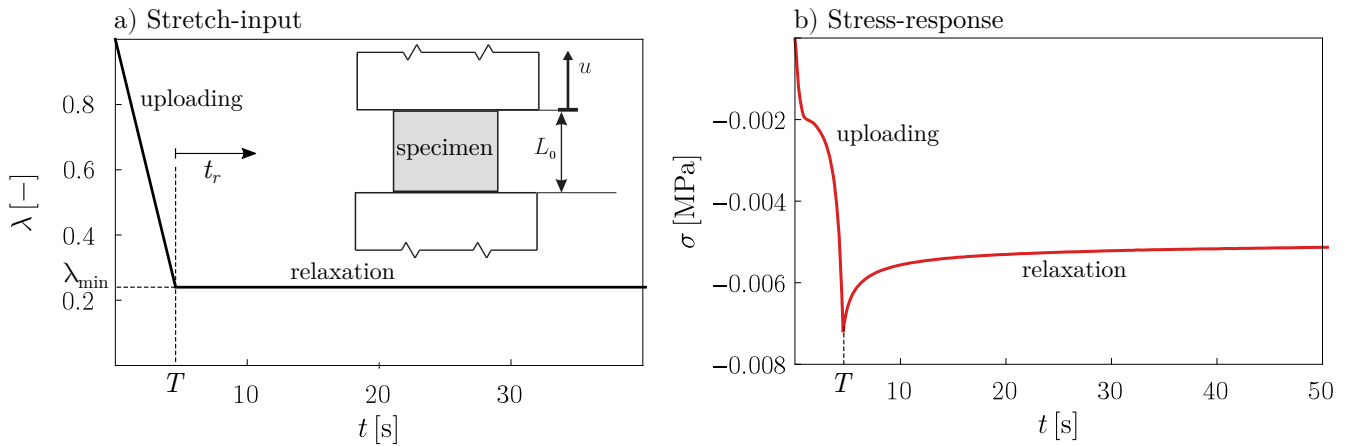


Figure 4.9: The a) stretch-input and b) the stress response of the relaxation test for $t \in [0, 50]$ s

4.4.1.2 Cyclic test

In the case of the cyclic test, the specimen was compressed incrementally, and the strain was kept constant after each step to ensure stress relaxation. Similarly, the unload process was also performed incrementally. Due to the viscoelastic properties, the uploading and the unloading process follows different paths due to the energy dissipation in the material. During the relaxation sessions, the stress values tend to the long-term (rate-independent) stress response. Hence, the results of the cyclic test can be applied in the parameter-fitting of the rate-independent hyperelastic material model. The uploading and the unloading phases were performed with $n = 10$ increments using a lower strain rate than in the previous case. The test parameters are presented in Table 4.5, while the $\sigma(t)$ stress response curve is illustrated in Fig. 4.10.

Table 4.5: The parameters of the cyclic test

Time of uploading, T	1.6 s
Minimal longitudinal stretch, λ_{\min}	0.24
Strain rate, $\dot{\epsilon}$	-0.015 1/s
Stretch increment, $\Delta\lambda$	0.024
Time of relaxation, t_r	30 s

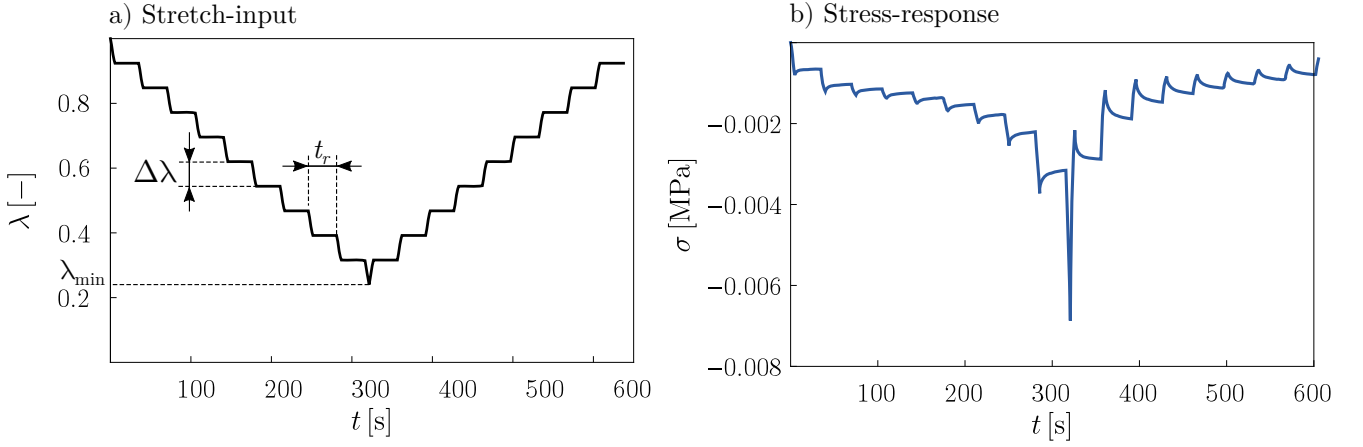


Figure 4.10: The a) stretch-input and b) the stress response of the cyclic test

4.4.1.3 Summary of results

The results can be summarised on a common $\sigma - \lambda$ stress-stretch diagram (see Fig. 4.11). These characteristics show that the stress values in case of the relaxation test are higher than the stress values obtained by cyclic test, since the strain rate were also higher in case of the relaxation test. Additionally, it can be clearly seen, that in the relaxation regions of both tests the stress values tend to the long-term (rate-independent) stress response values, which lay in between the up- and unloading parts of the cyclic test.

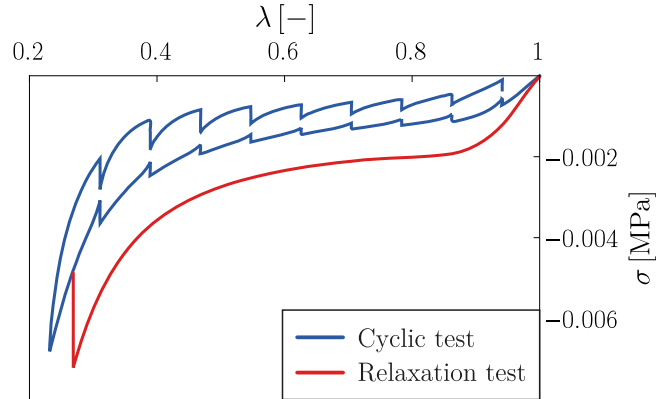


Figure 4.11: The measured $\sigma - \lambda$ stress-stretch characteristics

4.4.2 Parameter-fitting

The goal of the parameter fitting method is to determine both the viscoelastic and the hyperelastic parameters based on the measurement data. Since for open-cell foams $\beta_i = 0$ is assumed, the number of material parameters included in the corresponding visco-hyperelastic model are: $2N$ ($\alpha_1, \alpha_2 \dots \alpha_N; \mu_1, \mu_2 \dots \mu_N$) parameters for the rate-independent hyperelastic model and $2P$ ($g_1, g_2 \dots g_P; \tau_1, \tau_2 \dots \tau_P$) parameters for the rate-dependent viscoelastic model. It means that altogether $2(N + P)$ parameters should be fitted to the measurement data in order to describe the visco-hyperelastic material behaviour. For the investigated memory foam a fourth-order viscoelastic ($P = 4$) and a second-order hyperelastic model ($N = 2$) was fitted using two different approaches: the commonly applied separated method and the closed-form fitting based on the corresponding stress response.

4.4.2.1 Separated fitting - Hyperfoam parameters

In this approach, the hyperelastic model is fitted to the long-term stress response, while the viscoelastic parameters are fitted to the stress relaxation behaviour. The long-term behaviour is determined from cyclic compression-relaxation loading, where the data points for the i^{th} step ($\lambda_i^{\text{long}} - \sigma_i^{\text{long}}$) corresponding to the long-term behaviour appears between the uploading and unloading curves [9].

On the measured stress-stretch curve, the start and end point of each relaxation phase were detected for the upload and for the unload curves corresponding to the $\lambda_i^{\text{long}} = i \cdot \Delta\lambda$ stretch value after the i^{th} step. The detected points are denoted as $\sigma_{i,\text{max}}^{\text{up}}, \sigma_{i,\text{min}}^{\text{up}}, \sigma_{i,\text{max}}^{\text{un}}, \sigma_{i,\text{min}}^{\text{un}}$ as illustrated in Fig. 4.12. The most convenient way to approximate the long-term stress point is to assume that σ_i^{long} lays in the middle of the distance between the upload and unload curves. However, a novel approach is proposed in order to compensate the different relaxation lengths for uploading and unloading. For this, let us introduce the ratio of relaxation sections as

$$\xi_i = \frac{|\sigma_{i,\text{max}}^{\text{up}} - \sigma_{i,\text{min}}^{\text{up}}|}{|\sigma_{i,\text{max}}^{\text{un}} - \sigma_{i,\text{min}}^{\text{un}}|}. \quad (4.52)$$

Assuming, that the long-term stress point divide the distance between the upload and unload curves by the ratio ξ_i of the degree of relaxation at each step, namely

$$\xi_i = \frac{|\sigma_{i,\text{max}}^{\text{up}} - \sigma_i^{\text{long}}|}{|\sigma_i^{\text{long}} - \sigma_{i,\text{min}}^{\text{un}}|}. \quad (4.53)$$

Therefore, the long-term stress points can be expressed as

$$\sigma_i^{\text{long}} = \frac{\sigma_{i,\text{max}}^{\text{up}} + \xi_i \sigma_{i,\text{min}}^{\text{un}}}{1 + \xi_i}. \quad (4.54)$$

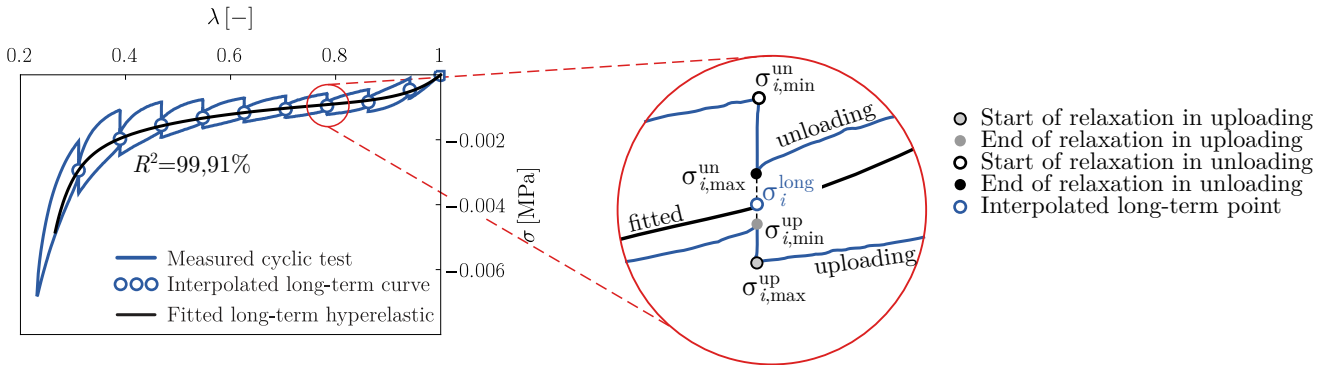


Figure 4.12: The fitted long-term hyperelastic model using separated fitting approach and the process of interpolation

The material parameters of the long-term hyperelastic material model denoted as $(\tilde{\alpha}_i, \tilde{\mu}_i)$, while the stress relaxation is characterised using the Prony-parameters (g_k, τ_k) . It should be noted, that the long-term hyperelastic parameters $(\tilde{\alpha}_i, \tilde{\mu}_i)$, are not equal with the hyperelastic parameters (α_i, μ_i) in the visco-hyperelastic constitutive equation in ((4.14)-(4.15)), which were related to the instantaneous stress response. However, the long-term and the instantaneous stress responses can be related as

$$\tau_0(t) = \frac{1}{g_\infty} \tau_\infty(t), \quad (4.55)$$

where $g_\infty = 1 - \sum g_k$ can be obtained from the g_k Prony-parameters. Note, that in ABAQUS [15] the hyperelastic parameters can be defined both for the long-term and the instantaneous stress responses, thus it does not induce any further error during the material modelling.

Based on (4.43), the long-term hyperelastic model to be fitted becomes

$$\tau_1 = \frac{2\tilde{\mu}_1}{\tilde{\alpha}_1} \left(\lambda_1^{\tilde{\alpha}_1} - 1 \right) + \frac{2\tilde{\mu}_2}{\tilde{\alpha}_2} \left(\lambda_1^{\tilde{\alpha}_2} - 1 \right), \quad (4.56)$$

which contains four material parameters, namely $\tilde{\alpha}_1, \tilde{\alpha}_2, \tilde{\mu}_1, \tilde{\mu}_2$. As it was derived previously in (3.8), the parameters should satisfy the following criteria $\tilde{\mu}_1 + \tilde{\mu}_2 > 0$ and to ensure Drucker-stable solution, accordingly to (3.52): $\mu_1 \lambda^{\alpha_1} + \mu_2 \lambda^{\alpha_2} > 0$ for $0 < \lambda \leq 1$. The parameter fitting was performed in Wolfram Mathematica using NMinimize algorithm [107], while corresponding error function was obtained as the sum of squared differences, namely

$$e^{\text{long}} = \sum_{i=1}^n \left[\left(\frac{2\tilde{\mu}_1}{\tilde{\alpha}_1} \left((\lambda_i^{\text{long}})^{\tilde{\alpha}_1} - 1 \right) + \frac{2\tilde{\mu}_2}{\tilde{\alpha}_2} \left((\lambda_i^{\text{long}})^{\tilde{\alpha}_2} - 1 \right) \right) - \sigma_i^{\text{long}} \right]^2, \quad (4.57)$$

where $n = 10$ is the number of measurement data points and $(\lambda_i^{\text{long}}; \sigma_i^{\text{long}})$ the measured values. The fitting results are presented in Fig. 4.12, while the fitted parameters are listed in Table 4.6. The result shows, that the pure hyperelastic parameters could be fitted with excellent accuracy ($R^2 = 99.91\%$).

Table 4.6: The hyperelastic parameters using separated fitting method

$\tilde{\alpha}_1$ [-]	$\tilde{\alpha}_2$ [-]	$\tilde{\mu}_1$ [MPa]	$\tilde{\mu}_2$ [MPa]	R^2 [%]
-7.14	18.225	$1.575 \cdot 10^{-7}$	0.00663	99.91

4.4.2.2 Separated fitting - Prony parameters

The viscoelastic behaviour is characterised by the Prony-parameters (see 4.9), which can be fitted to the relaxation test results (see Fig. 4.9). The measurement results are considered to be ideal relaxation response corresponding to step loading, in this case the stress solution using small strain formulation is

$$\sigma(t) = \sigma_0 \left(e_\infty + \sum_{k=1}^P e_k e^{-t/\tau_k} \right), \quad (4.58)$$

where σ_0 is the instantaneous stress response for the applied stretch λ_0 . Obviously, σ_0 is unknown, and in fact it is impossible to determine from measurements, because infinite strain-rate loading would be needed, which is technically impossible to achieve. Consequently, σ_0 should be eliminated from the equation above in order to fit the Prony-parameters. The instantaneous (σ_0) and the long-term (σ_∞) stresses are related as

$$\sigma_\infty = e_\infty \sigma_0. \quad (4.59)$$

Consequently, by expressing e_∞ based on (4.11), the stress relaxation in (4.58) can be written as

$$\sigma(t) = \frac{\sigma_\infty}{e_\infty} \left(e_\infty + \sum_{k=1}^P e_k e^{-t/\tau_k} \right) = \frac{\sigma_\infty}{1 - \sum_{k=1}^P e_k} \left(1 - \sum_{k=1}^P e_k + \sum_{k=1}^P e_k e^{-t/\tau_k} \right). \quad (4.60)$$

Dividing both sides with σ_∞ and applying the assumption of $e_k = g_k = k_k$ [9, 15] gives [SzB4]

$$\bar{\sigma}(t) = \frac{\sigma(t)}{\sigma_\infty} = \frac{1}{1 - \sum_{k=1}^P g_k} \left(1 - \sum_{k=1}^P g_k + \sum_{k=1}^P g_k e^{-t/\tau_k} \right). \quad (4.61)$$

The right-hand side contains only the Prony-parameters, whereas the modified data $\bar{\sigma}(t)$ is simply determined by dividing the experimental stress values with the long-term response σ_∞ , which can be easily obtained. Finally, σ_0 is eliminated and the new function $\bar{\sigma}(t)$ can be fitted to the modified experimental data. For the chosen Prony-series ($P = 4$) the fitting criteria are

$$\tau_k > 0, \quad g_k > 0, \quad g_1 + g_2 + g_3 + g_4 < 1. \quad (4.62)$$

In the literature, there are several methods, which reduces the error resulting from the ramp loading by modifying the experimental data (e.g. by time-shifting) [108]. According to the Factor-of-ten method [109], relaxation modulus $E(t)$ can be obtained from the step-strain case only for $t > 10T$, this yields that

$$\bar{\sigma}^{10T}(t) = \bar{\sigma}(t), \quad t \geq 10T. \quad (4.63)$$

The method of Zapas and Philips [110] shifts the relaxation curve by $T/2$, thus

$$\bar{\sigma}^{ZP}(t) = \bar{\sigma}(t + T/2), \quad t \geq T/2. \quad (4.64)$$

The iterative method proposed by Solvari and Malinen [108] is based on the two point trapezoidal rule of integration is applied, yielding

$$\bar{\sigma}^{SM}(t - T) = \bar{\sigma}(t) - \frac{\dot{\bar{\sigma}}(t)}{2\dot{\epsilon}_0}(1 + \lambda_0), \quad t \geq T; \quad \text{with} \quad \dot{\bar{\sigma}}(t) = \frac{\bar{\sigma}(t + h) - \bar{\sigma}(t - h)}{2h}, \quad (4.65)$$

where h is an arbitrarily chosen step time.

After performing the parameter fitting for all cases, the fitted parameters were substituted back into (4.61) and compared with the measurement data, in which $\sigma_\infty = -0.00489$ MPa. The result of the parameter fitting is presented in Fig. 4.13, while the corresponding material parameters are listed in Table 4.7.

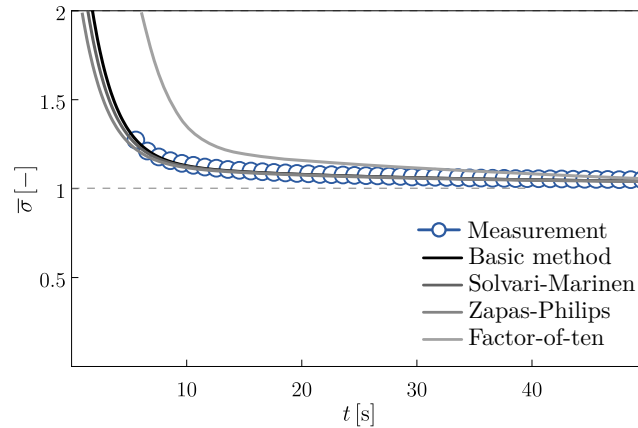


Figure 4.13: The measured $\bar{\sigma}(t)$ function and the fitted ideal relaxation $\bar{\sigma}(t)$ model using Prony-series using Basic, 10T, ZP and SM methods

Table 4.7: The fitted Prony-parameters using separated fitting method

Method	g_1 [-]	g_2 [-]	g_3 [-]	g_4 [-]	τ_1 [s]	τ_2 [s]	τ_3 [s]	τ_4 [s]	R^2 [%]
Basic	0.0147	0.00204	0.0385	0.6114	249.134	100.259	18.939	2.149	94.05
10T	0.0784	0.759	0.000051	0.1474	2.1	8.285	3.142	93.91	65.42
ZP	0.0332	0.00204	0.00484	0.00819	2.592	7.231	2.182	87.15	94.75
SM	0.00324	0.00126	0.861	0.012	16.42	7.253	4.227	66.39	93.87

4.4.2.3 Closed-form parameter fitting

Since the closed-form stress response $\tau(t)$ is obtained in (4.44)-(4.46), the material model can be fitted directly to the stress relaxation data (see Fig. 4.9). The parameters of the loading case were the strain rate $\dot{\epsilon} = -0.1662$ 1/s and the time of uploading $T = 4.57$ s. The parameter fitting was performed again in Mathematica using the `NMinimize` global minimizer algorithm, where the error function (*SSD*) was defined as

$$e^{\text{closed}} = \frac{1}{L_1} \sum_{i=1}^{L_1} [\tau(t_i^{M_1}) - \sigma_i^{M_1}]^2 + \frac{1}{L_2} \sum_{i=1}^{L_2} [\tau(t_i^{M_2}) - \sigma_i^{M_2}]^2, \quad (4.66)$$

where L_1 and L_2 denotes the number of measurement points in the uploading and the stress relaxation parts, respectively. The applied material model contains a second-order hyperelastic ($N = 2$) and a fourth-order Prony-series ($P = 4$). Based on the conditions in (3.8), the criteria for the parameters were defined as

$$\mu_1 + \mu_2 > 0, \quad \tau_k > 0, \quad g_k > 0, \quad g_1 + g_2 + g_3 + g_4 < 1. \quad (4.67)$$

The identified visco-hyperelastic material parameters are presented in Table 4.8.

Table 4.8: The material parameters in case of closed-form parameter fitting method

Hyperfoam parameters	α_1 [-]	α_2 [-]	μ_1 [MPa]	μ_2 [MPa]
	-3.1473	6.227	0.00001706	0.01265

Prony's parameters	g_1 [-]	g_2 [-]	g_3 [-]	g_4 [-]	τ_1 [s]	τ_2 [s]	τ_3 [s]	τ_4 [s]
	0.136	0.6202	0.000012	$1.05 \cdot 10^{-7}$	2.44	0.486	1.434	0.836

4.4.3 Evaluation of results

In the previous subsections, all the material parameters were identified for the visco-hyperelastic material model in case of uniaxial compression with $\beta_i = 0$. The fitted mechanical model can be validated using FEA as it was described in Section 4.3.3. The goal of the analysis is to investigate the accuracy of the fitted model compared to the measured stress relaxation data. The results are also presented in Fig. 4.14, while the corresponding R^2 values are listed in Table 4.9.

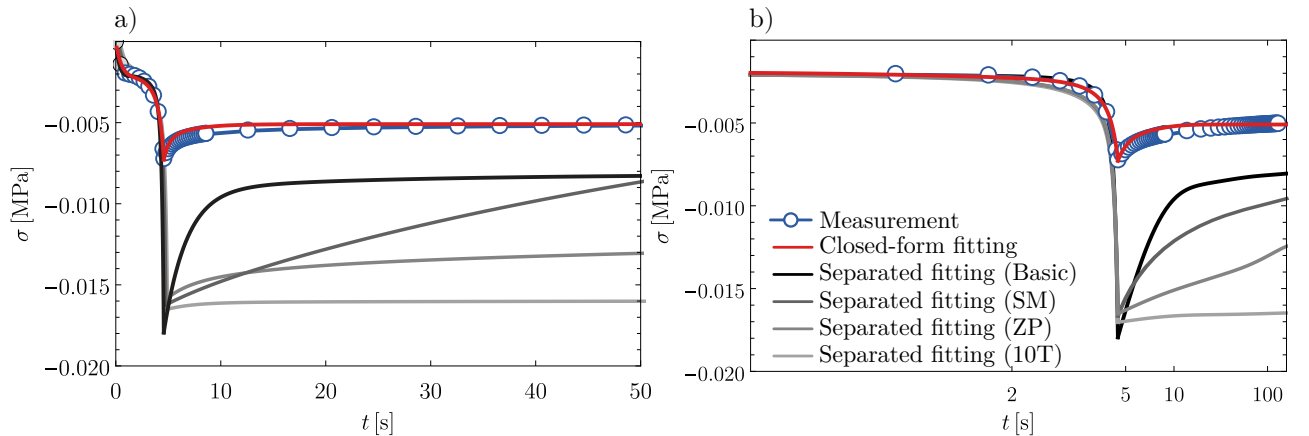


Figure 4.14: The comparison of the performance of the separated and the closed-form fitting methods a) for $t \in [0, 50]$ s and b) for $t \in [0, 120]$ s on logarithmic scale

Table 4.9: Comparison of R^2 values for closed-form and separated fitting methods

Method	Uploading R^2 [%]	Relaxation R^2 [%]	Overall R^2 [%]
Closed-form	99.78	92.35	96.89
Separated (basic)	80.35	27.45	54.04
Separated (10T)	82.78	4.24	41.12
Separated (ZP)	81.14	11.24	39.22
Separated (SM)	83.78	13.57	40.29

As the result shows, all models are close to the real measured data in the uploading part, while in case of the stress relaxation part the error of the separated approach is significant. Compared to the separated fitting method, the error of the closed-form approach is negligible, and it describes the material behaviour with excellent precision.

4.5 Main results

I have investigated the large-strain viscoelastic behaviour of polymer foams (memory foams) based on the visco-hyperelastic extension of the generalised Standard Solid Model in combination with Hyperfoam model. I have derived closed-form stress solution for ramp loading for confined homogeneous deformation and for open-cell foams, where the transverse effect is negligible. I have demonstrated, that the closed-form stress solution can be effectively utilised in the material characterisation process via the detailed experimental case study of an open-cell memory foam. By comparing the results with the separated fitting approaches in the literature, I have obtained the following results.

Thesis statement 2

Consider ABAQUS's finite strain visco-hyperelastic constitutive model in the form of

$$\boldsymbol{\tau}^D(t) = \boldsymbol{\tau}_0^D(t) - \text{SYM} \left[\sum_{k=1}^P \frac{g_k}{\tau_k} \int_0^t \mathbf{F}_t^{-1}(t-s) \boldsymbol{\tau}_0^D(t-s) \mathbf{F}_t(t-s) e^{-s/\tau_k} ds \right],$$

$$\boldsymbol{\tau}^H(t) = \boldsymbol{\tau}_0^H(t) - \sum_{k=1}^P \frac{g_k}{\tau_k} \int_0^t \boldsymbol{\tau}_0^H(t-s) e^{-s/\tau_k} ds,$$

where $\boldsymbol{\tau}^D$ and $\boldsymbol{\tau}^H$ are the deviatoric and hydrostatic Kirchhoff stresses, while g_k , τ_k are the Prony-parameters characterizing linear stress relaxation. When the instantaneous stress response $(\boldsymbol{\tau}_0^D, \boldsymbol{\tau}_0^H)$ is modelled using the Ogden–Hill's hyperelastic model, the τ_L longitudinal and τ_T transversal stress solutions for homogeneous confined compression ramp tests are expressed in closed-form as

$$\tau_L(t) = \begin{cases} \tau_{L0}(t) - \sum_{k=1}^P g_k \left(\sum_{i=1}^N \frac{2\mu_i}{\alpha_i} \eta_{ik} \right) & t \leq T, \\ \tau_{L0}(T) \left(1 - \sum_{k=1}^P g_k \left(1 - e^{-\frac{T-t}{\tau_k}} \right) \right) - \sum_{k=1}^P g_k \left(\sum_{i=1}^N \frac{2\mu_i}{\alpha_i} \vartheta_{ik} \right) & t > T, \end{cases}$$

$$\tau_T(t) = \begin{cases} \tau_{T0}(t) - \sum_{k=1}^P g_k \left(\sum_{i=1}^N \frac{2\mu_i}{\alpha_i} \hat{\eta}_{ik} \right) & t \leq T, \\ \tau_{T0}(T) \left(1 - \sum_{k=1}^P g_k \left(1 - e^{-\frac{T-t}{\tau_k}} \right) \right) - \sum_{k=1}^P g_k \left(\sum_{i=1}^N \frac{2\mu_i}{\alpha_i} \hat{\vartheta}_{ik} \right) & t > T, \end{cases}$$

where N and P denote the order of the Hyperfoam model and the Prony-series, T is the upload time, while $\Gamma[\nu, x]$ stands for the upper-incomplete Gamma-function. The quantities η_{ik} , ϑ_{ik} , $\hat{\eta}_{ik}$, $\hat{\vartheta}_{ik}$ are the second-order parameter tensors, defined using the loading case parameter M as

$$\eta_{ik} = e^{-\frac{t-1/\dot{\epsilon}}{\tau_k}} \left(\frac{-1}{\dot{\epsilon}\tau_k} \right)^{M\alpha_i\beta_i} \left(\Gamma \left[1 - M\alpha_i\beta_i, \frac{-1}{\tau_k\dot{\epsilon}} \right] - \Gamma \left[1 - M\alpha_i\beta_i, \frac{-1-t\dot{\epsilon}}{\tau_k\dot{\epsilon}} \right] \right) \\ + e^{-\frac{t+1/\dot{\epsilon}}{\tau_k}} \left(\frac{-1}{\dot{\epsilon}\tau_k} \right)^{-\alpha_i} \left(\Gamma \left[1 + \alpha_i, -\frac{1+t\dot{\epsilon}}{\tau_k\dot{\epsilon}} \right] - \Gamma \left[1 + \alpha_i, -\frac{1}{\tau_k\dot{\epsilon}} \right] \right),$$

$$\vartheta_{ik} = e^{\frac{-t-1/\dot{\epsilon}}{\tau_k}} \left(\frac{-1}{\dot{\epsilon}\tau_k} \right)^{M\alpha_i\beta_i} \left(\Gamma \left[1 - M\alpha_i\beta_i, \frac{-1}{\tau_k\dot{\epsilon}} \right] - \Gamma \left[1 - M\alpha_i\beta_i, \frac{-1 - T\dot{\epsilon}}{\tau_k\dot{\epsilon}} \right] \right) + e^{\frac{-1-\dot{\epsilon}t}{\dot{\epsilon}\tau_k}} \left(\frac{-1}{\dot{\epsilon}\tau_k} \right)^{-\alpha_i} \left(\Gamma \left[1 + \alpha_i, \frac{-1 - T\dot{\epsilon}}{\tau_k\dot{\epsilon}} \right] - \Gamma \left[1 + \alpha_i, \frac{-1}{\tau_k\dot{\epsilon}} \right] \right),$$

$$\hat{\eta}_{ik} = e^{\frac{-t-1/\dot{\epsilon}}{\tau_k}} \left(\frac{-1}{\dot{\epsilon}\tau_k} \right)^{M\alpha_i\beta_i} \left(\Gamma \left[1 - M\alpha_i\beta_i, \frac{-1}{\tau_k\dot{\epsilon}} \right] - \Gamma \left[1 - M\alpha_i\beta_i, \frac{-1 - t\dot{\epsilon}}{\tau_k\dot{\epsilon}} \right] \right) + 1 - e^{\frac{-t}{\tau_k}},$$

$$\hat{\vartheta}_{ik} = e^{\frac{-t-1/\dot{\epsilon}}{\tau_k}} \left(\frac{-1}{\dot{\epsilon}\tau_k} \right)^{M\alpha_i\beta_i} \left(\Gamma \left[1 - M\alpha_i\beta_i, \frac{-1}{\tau_k\dot{\epsilon}} \right] - \Gamma \left[1 - M\alpha_i\beta_i, \frac{-1 - t\dot{\epsilon}}{\tau_k\dot{\epsilon}} \right] \right) + e^{\frac{-t-T}{\tau_k}} - e^{\frac{-t}{\tau_k}}.$$

Related publications: [SzB1],[SzB4],[SzB5],[SzB6]

Thesis statement 3

Consider the parameter fitting of open-cell polyethylene memory foams with significant viscoelastic effects and negligible transverse deformation (i.e. $\beta_i = 0$) using ABAQUS's finite strain visco-hyperelastic constitutive model in combination with the Ogden–Hill's hyperelastic model. In this fitting process, the 2N Hyperfoam and 2P Prony-parameter of can be fitted in one step to the uniaxial stress relaxation test (ramp test) with excellent accuracy ($R^2 > 0.98$) using the closed-form stress solution for ramp test, compared to the separated fitting approaches (e.g. Zapas-Phillips, Factor-of-ten, Solvari-Malinen methods), which contain significant error due to the idealisation of ramp test.

Related publications: [SzB1],[SzB4],[SzB5],[SzB6]

5

Viscoelastic-viscoplastic model for microcellular foams

This chapter is devoted to the mechanical characterisation of a particular thermoplastic foam material, the so-called microcellular polyethylene-terephthalate (MC-PET) foam. Compared to conventional foam materials (presented in Chapters 3 and 4), the mechanical behaviour of MC-PET foams are mostly characterised by their thermoplastic PET skin layer, that shows significant viscoelastic-viscoplastic properties in combination with large strains and deformation, which fundamentally characterise the manufacturing process of MC-PET.

The usual manufacturing process of microcellular foams is thermoforming, which is one of the most widely applied manufacturing processes since the beginning of the polymer industry [23]. Using this process, a great variety of products can be manufactured with moderate costs, including extremely thin parts with complex geometries as well. During the process, the raw material sheet is heated up to the so-called forming temperature, where the forming process is applied (e.g. using vacuum, compressed air or mechanical contact), which is followed by cooling to room temperature. The final geometry of the part is strongly dependent on the technological parameters of process, e.g. temperature levels, rate of loading, holding times [24, 25]. Due to the high sensitivity of the material behaviour on the technical parameters, the setting of proper production parameters is usually achieved after several tries, which might be very time-consuming and costly. However, the final shape may be adequately modelled using finite element (FE) simulation as it is discussed by Guzman-Maldonado et al. [111], which could also reduce the time and costs of production design. Additionally, such simulations can also be applied to assess the long-term behaviour of the thermoformed parts, which is in high industrial demand due to the unreasonable amount of time required for the experimental investigations.

5.1 Literature overview and objectives

In order to perform FE simulation of the forming process adequately, the thermoplastic material should be characterised using an accurate constitutive model including all relevant deformation behaviours occurring during the entire forming process. As several studies in the literature have revealed, the thermoplastic materials undergo large strains and deformations which show signifi-

cant viscous, elastic and yielding characteristics with dominant temperature-dependent properties. Consequently, the constitutive model applied in FE simulations must be able to describe yielding properties with hardening, viscoelastic and elastic contributions. Nevertheless, the number of suitable models in the commercial finite element software (e.g. ABAQUS [15], ANSYS [16], MSC MARC [17]) is limited. Moreover, these models were mostly proposed for metals, not polymers. Therefore, the development of advanced material models for characterising the complex mechanical behaviours of thermoplastics is currently a highly investigated field of computational solid mechanics.

In addition to the available models in FE software, a commercially available model family for solid polymers is the PolyUMod Library provided by Bergström via Veryst Engineering [5]. This library includes the Three-Network Model (TNM) and the Parallel Network Model (PNM) proposed especially for modelling thermoplastics. These advanced models, however, contains a high number of material parameters without including explicit temperature dependence. Besides, recent studies have also proposed viscoelastic and viscoplastic models for modelling temperature-dependent behaviour of various thermoplastic materials (including PLA and PVA core-shell nanofibres, PMMA, PLA, PC and isotactic PP) using parallel and serial configurations of the well-known rheological models (see Section 2) combined with nonlinear viscoelastic-viscoplastic elements [112, 113, 114, 115, 116, 117, 118, 119, 120, 121]. Whereas, the novel constitutive model proposed for temperature-dependent structural relaxation by Das et al. [122] also includes multiple time-scales using statistical homogenization. Additionally, several studies investigated the yielding behaviour of thermoplastics based on cyclic tests utilizing kinematic hardening approach [123, 124, 125, 126].

Microcellular foaming technology was invented at Massachusetts Institute of Technology (MIT) by Martini et al. and patented in 1982 [127]. Microcellular foam materials show excellent insulation and diffuse reflection properties, which can be achieved by relatively low production prices [128, 129]. One of the possible fields of application of such foams is in lighting (e.g. as lamp shells), which are manufactured using thermoforming process at temperatures above 200 °C, for which the proper temperature-dependent modelling at all relevant temperature levels (as discussed above) is essential. However, there is a lack in the literature regarding the experimental and numerical investigations of such foam materials at wide temperature-regime, which was the main motivation of this study. Since the material behaviour changes significantly with increasing temperature, the objective was to apply a constitutive law such that characterise the material on the entire temperature domain with adequate accuracy. The proposed material model comprises of a Maxwell-type branch in parallel with an elastic-plastic model using isotropic hardening and associative flow rule with Mises yield function, while the nonlinear viscoelastic effect was modelled using strain- and time-hardening power-law creep models. This model-family is also commonly cited as two-layer viscoplastic model, abbreviated as TLVP [15, 130, 131]. Additionally, the goal was also to analyse performance and the sensitivity of the proposed model, which is also discussed further in details. Moreover, in this chapter, analytical functions are also proposed to describe the variation of viscous-elastic-plastic material parameters with temperature.

5.2 Mechanical behaviour of micro-cellular PET foam

The investigated material is a microcellular-polyethene-terephthalate (MC-PET) and currently under development at Furukawa Electric Technology Ltd. [132]. Compared to pure PET, the MC-PET material contains microcells which ensure excellent diffuse reflection quantities. The foam is mainly used as lamp shells in different places, including extraordinary circumstances (e.g. extreme cold, high UV-radiation, etc. . .), thus the material model is required to capture the

mechanical properties during the entire thermoforming process. The MC-PET foam is produced as sheets with thickness 0.94 mm. The microstructure of the foam consists of a thin PET skin-layer and a microcellular foam core, which is presented on the SEM image in Fig. 5.1/a. The skin-layer/foam core thickness ratio is approximately 1:5, while the size of the microcells is in the range of 5 – 10 μm . Due to the foam core and the various deformation mechanisms of cellular structures [41], the mechanical properties of the MC-PET foam significantly differ from the behaviour of the matrix PET material (e.g. reduced density, improved impact absorption, etc.). Therefore, during material modelling, one could not rely on the constitutive models and characteristics of single PET material.

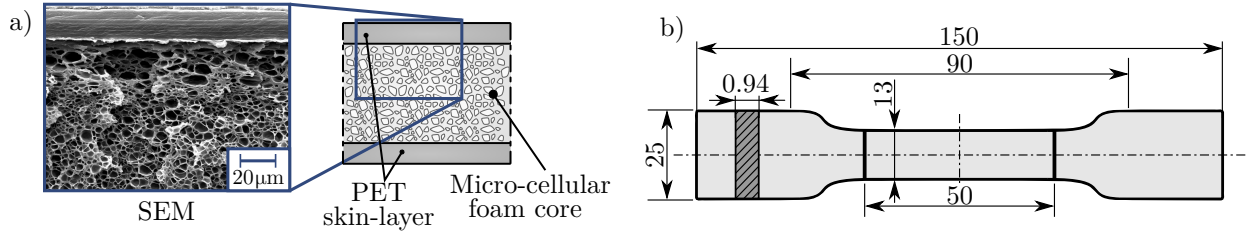


Figure 5.1: The a) SEM image of microstructure of the investigated MC-PET foam and b) the specimen geometry for uniaxial tests with the markers for video extensometer

5.2.1 Preliminary material tests

In order to get preliminary information about the temperature-dependent behaviour of the material, the raw material was tested using sweep DMA test (dynamic mechanical analysis) in order to investigate the viscoelastic and the temperature-dependent properties [7, 8]. The measurement was performed in the laboratory of the Department of Polymer Technology at BME. The measured quantities are the storage modulus E' representing the stored elastic energy and the loss modulus E'' quantifying the energy dissipated as heat. The results of the DMA tests (see Fig. 5.2) shows that the mechanical properties significantly change at elevated temperatures. Based on the DMA curves, the glass-transition temperature T_g can be obtained using the inflection of $E'(T)$ or the maxima of $E''(T)$, namely $T_g = 90^\circ\text{C}$ according to [133].

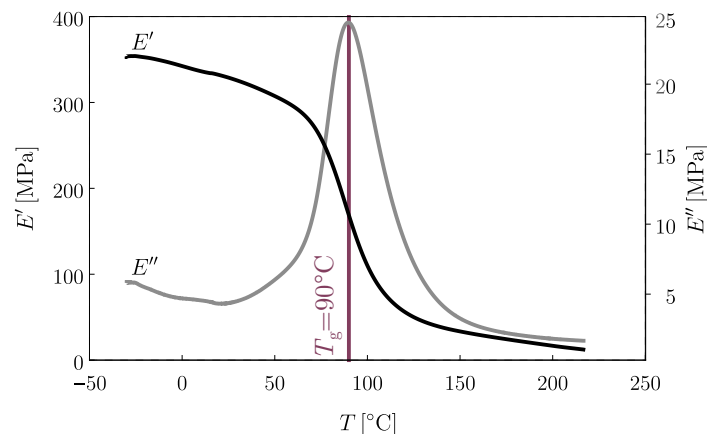


Figure 5.2: The results of the DMA tests: the variation of the storage modulus E' and the loss modulus E'' against temperature

Beside the DMA tests, preliminary uniaxial tensile cyclic tests were also performed on the specimens in order to reveal and identify the deformation characteristics in the investigated temperature domain. The uniaxial tests were performed using a Zwick Roell Z010 Testing System with

Zwick Xforce P load-cell with a maximal load capacity of 1 kN. Additionally, for the temperature-dependent measurements, an air-feed-based Zwick heat chamber was applied, which ensures uniform temperature distribution in the chamber. Note, that after reaching the required temperature, the specimen was laying in the chamber for 2 min to ensure that the whole volume of the specimen is heated up. During the heating-up period, the speed of temperature changing was approximately 12 K/min as it is provided in the heat chamber specification. The heat chamber and the applied specimen conditioning procedure ensure reliable test results according to standards ISO 527-1 [134], ASTM D618 [135] and D638 [136]. The preliminary uniaxial cyclic tests consist of several loading-unloading cycles with increasing displacements in the temperature range of 21 – 210 °C, which is the usual regime of the thermoforming production process of this particular material in order to avoid the degradation of the microstructure which occurs at around 220 – 240 °C. From the measured force-displacement curves the engineering stress P and the engineering strain ε^{eng} were computed from the measured force F and displacement value u as

$$P = \frac{F}{A_0} \quad \text{and} \quad \varepsilon^{\text{eng}} = \frac{u}{L_0}, \quad (5.1)$$

where $A_0 = 12.24 \text{ mm}^2$ and $L_0 = 50 \text{ mm}$ are the initial cross-section and the initial gauge length. The measured curves (data points) are illustrated in Fig. 5.3. The results at all temperatures show that the material behaviour exhibits stress relaxation properties and the permanent deformation after each cycle is also significant [SzB7].

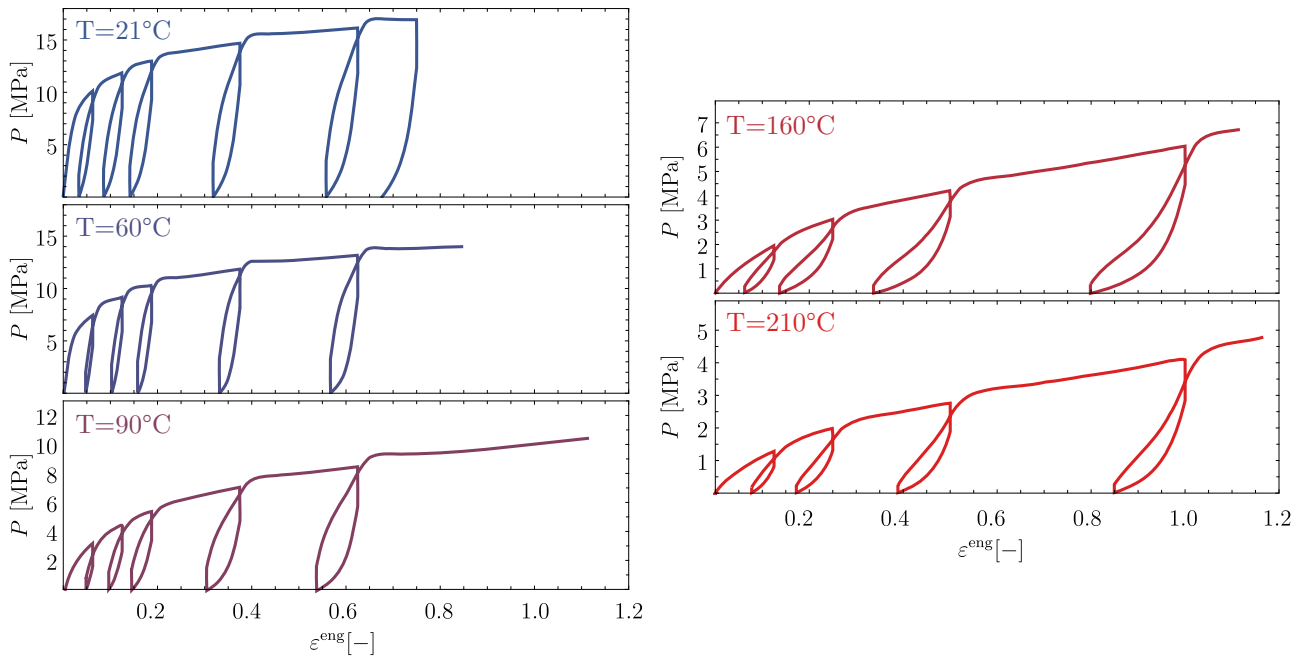


Figure 5.3: The measured engineering stress – engineering strain curves in case of the preliminary cyclic uniaxial tensile tests at temperatures of 21 °C, 60 °C, 90 °C, 160 °C and 210 °C

5.2.2 Uniaxial tensile tests

As the preliminary tests (DMA and cyclic) revealed, deformation of the MC-PET foam shows significant elastic, plastic and viscous properties with significant temperature dependency. During the constitutive modelling, in order to reduce the computational time of the parameter fitting, the simplest test should be applied, which is also expected to involve both viscoelastic and viscoplastic properties. Therefore, uniaxial tensile tests have been performed using a single cycle with three

loading steps [SzB8], which is illustrated in Fig. 5.4. Firstly, displacement-controlled uploading to u_{\max} with cross-head speed v_c , then relaxation by holding the strain for $t_r = t_2 - t_1 = 60$ s and finally displacement-controlled unloading with v_c until zero load is reached, namely $F = 0$ N. The test parameters are summarised in Table 5.1.

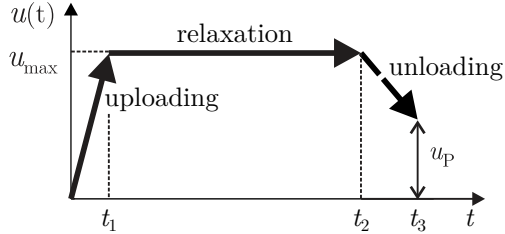


Figure 5.4: The prescribed displacement history during uniaxial test

Table 5.1: The uniaxial test parameters

upload time, t_1	25 s
maximal displacement, u_{\max}	37.5 mm
relaxation time, t_r	60 s
crosshead speed, v_c	1.5 mm/s

As the DMA results indicated, the material behaviour significantly changes at around 90°C , therefore the investigated temperature values were not uniformly distributed in the regime of $21\text{--}210^\circ\text{C}$ as smaller temperature increments were applied around the glass transition temperature according to [137]. Consequently, the tests were performed at ten different temperature levels, namely 21°C , 60°C , 75°C , 83°C , 90°C , 97°C , 106°C , 120°C , 160°C and 210°C [SzB7].

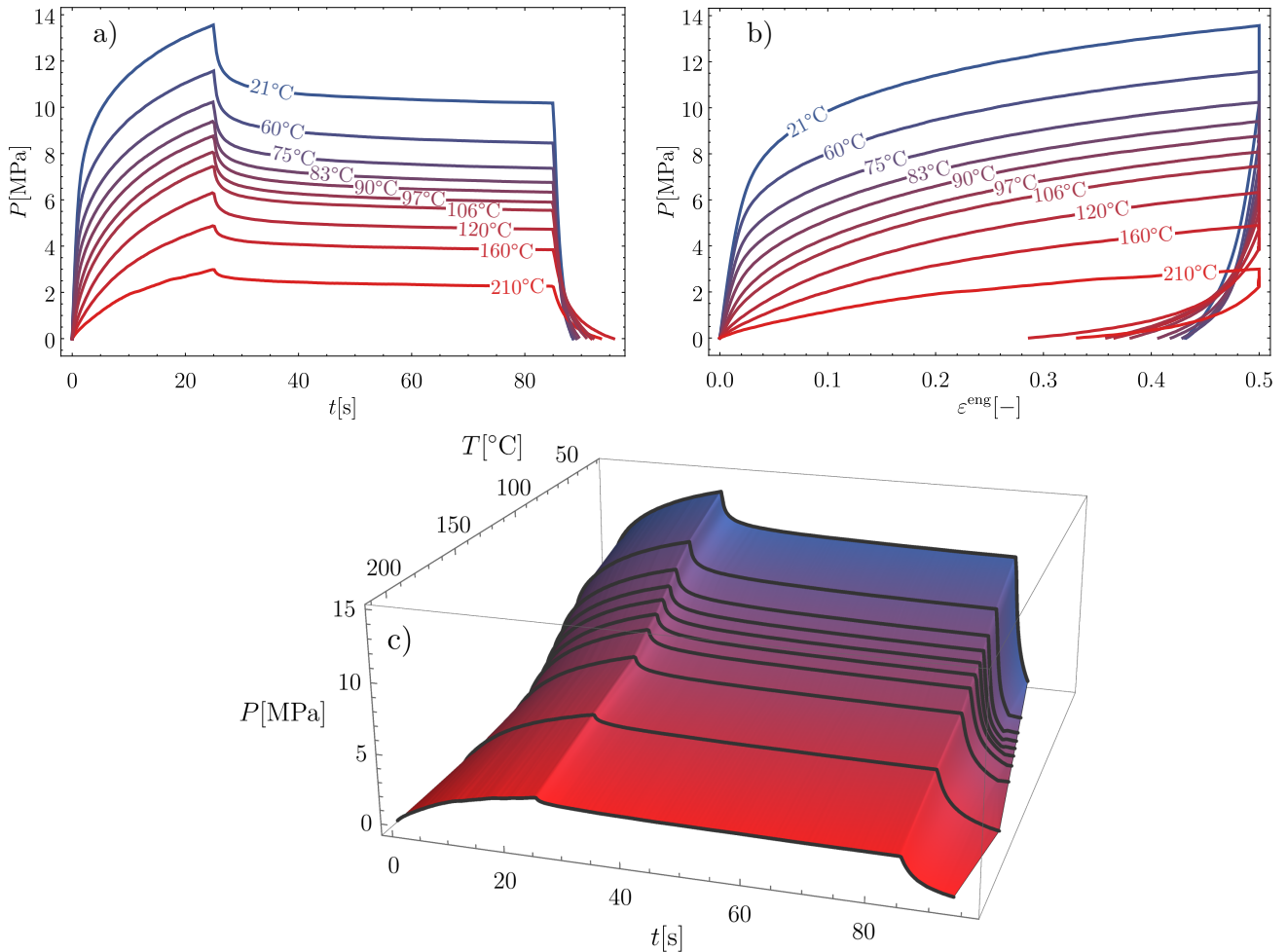


Figure 5.5: The measured uniaxial a) $P - t$ and b) $P - \varepsilon^{\text{eng}}$ curves and the corresponding c) 3D surface in the temperature domain of $21\text{--}210^\circ\text{C}$

The measured engineering-stress against time curves and the stress-strain curves are summarised in Fig. 5.5, respectively. The results show that temperature has a significant softening effect on overall mechanical behaviour. Furthermore, it can also be stated that the above glass transition temperature, due to the microstructural changes, significantly different behaviour occurs while the permanent deformation at the end of the cycle, which can be quantified by u_P (as indicated in Fig. 5.4), also increases.

5.3 Parallel viscoelastic-viscoplastic constitutive models

The constitutive model proposed for the characterisation of the investigated MC-PET material at all temperature levels is a particular parallel viscoelastic-viscoplastic model [SzB7], [SzB8], that is commonly cited as two-layer viscoplastic model (TLVP) [4, 15]. The TLVP model one of the simplest parallel viscoelastic-viscoplastic model, which is comprised of a Maxwell-type nonlinear viscoelastic branch and an elastic-plastic network, respectively. This model is mainly applied for high-temperature modelling of metals [138, 139, 140, 141], although, originally it was proposed for polymers [130, 131] and can also be efficiently applied for other materials [142, 143]. Among parallel viscoelastic-viscoplastic models, the TLVP model is beneficial thanks to its simple structure and the relatively small number of parameters, whereas it is also implemented in the commercial FE software ABAQUS [15]. The 1D representation of the TLVP model is depicted in Fig. 5.6. Due to the parallel configuration, the total stress can be expressed additively as

$$\sigma = \sigma_V + \sigma_P, \quad \text{while} \quad \varepsilon_V = \varepsilon_P = \varepsilon, \quad (5.2)$$

where σ_V denotes the stress acting on the viscoelastic branch, whereas σ_P on the elastic-plastic network, respectively

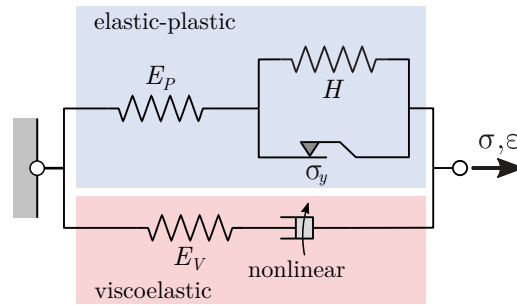


Figure 5.6: The 1D representation of the two-layer viscoplastic model

5.3.1 Elastic behaviour

The elastic behaviour of the material is modelled using linear isotropic elasticity, which is represented by the elastic moduli E_V and E_P in the viscoelastic and the elastoplastic networks, respectively. Therefore, the total elastic modulus can be expressed as $E = E_V + E_P$. The ratio of E_V and E is introduced as a new parameter f_e , the so-called fraction of elasticity (or elastic-ratio) for convenience as

$$f_e = \frac{E_V}{E}. \quad (5.3)$$

Furthermore, as isotropic behaviour is assumed, the Poisson's ratio in both networks is identical, namely $\nu = \nu_V = \nu_P$.

Moreover, due to the large strains and deformations that the material behaviour shows, the linear isotropic elastic behaviour is modelled using finite strain approach, namely by the so-called hypoelastic model using the formulation for solid elements in ABAQUS [6, 11, 15], where the governing differential equation is expressed as

$$\dot{\boldsymbol{\sigma}}^J = \mathcal{D}^e : \mathbf{d}. \quad (5.4)$$

In which $\dot{\boldsymbol{\sigma}}^J$ represents the Jaumann stress-rate of the Cauchy stress tensor, \mathbf{d} is the rate of deformation tensor and \mathcal{D}^e is the Hooke-operator. Assuming that the stretch varies linearly in time, namely $\lambda(t) = 1 + \dot{\varepsilon}^{\text{eng}} t$, the integration of (5.4) for uniaxial extension simplifies for the Cauchy-stress as

$$\sigma(t) = E \ln(\lambda(t)) = E \varepsilon^{\text{true}}(t) \quad (5.5)$$

where $\varepsilon^{\text{true}}$ denotes the true strain.

5.3.2 Nonlinear creep laws

In the proposed TLVP model, the nonlinear viscous behaviour is modelled through nonlinear creep laws [14]. Among several available creep laws, the so-called power-law models are the most widely used models, thanks to their simplicity. The models only consider deviatoric creep, therefore the governing differential equations are expressed using the Mises equivalent stress q , defined as

$$q = \sqrt{\frac{3}{2} \mathbf{s} : \mathbf{s}}, \quad (5.6)$$

where $\mathbf{s} = \text{dev}(\boldsymbol{\sigma})$ is the deviatoric stress tensor. In this study time-hardening and strain-hardening power-law models are investigated in detail [SzB7], [SzB8]. Note, that the time-hardening power-law model is mainly recommended for slightly varying stress states, whereas the strain-hardening model can be applied also for varying stress states as well. Additionally, both models assume that the stresses are low [14, 15]. The governing equation of the equivalent creep strain ε^{cr} for the time-hardening power-law is expressed for tension as

$$\dot{\varepsilon}^{\text{cr}} = A q^n t^m, \quad (5.7)$$

while in case of strain-hardening power-law, the expression for tension becomes

$$\dot{\varepsilon}^{\text{cr}} = (A q^n [(m+1)\varepsilon^{\text{cr}}]^m)^{\frac{1}{m+1}}, \quad (5.8)$$

where A , n and m are parameters, while the equivalent creep strain is defined as

$$\varepsilon^{\text{cr}} = \sqrt{\frac{2}{3} \boldsymbol{\varepsilon}^{\text{cr}} : \boldsymbol{\varepsilon}^{\text{cr}}}. \quad (5.9)$$

It should be noted, that for $m = 0$ both models reduce to the Norton–Hoff creep law, which is defined as

$$\dot{\varepsilon}^{\text{cr}} = A q^n. \quad (5.10)$$

Beside the power-law creep models, there also exist more complex nonlinear creep laws (e.g. Anand, Darveaux and Double power). In these models, however, the number of material parameters are also higher, which makes the parameter-fitting even more difficult and uncertain, thus in the following, only the power-law models are discussed. During the numerical solution of the TLVP model using FEA in ABAQUS, the accuracy of creep integration was controlled by the so-called creep strain error tolerance, for which value of $5 \cdot 10^{-5}$ was prescribed according to the ABAQUS suggestion [15]. This error tolerance determines the time increment so that the creep strain increment is always smaller than the elastic strain increment [15].

5.3.3 Yielding behaviour

Due to the lack of proper volumetric measurements, only deviatoric effects were taken into account in the characterization of yielding behaviour. The elastic-plastic network was modelled using associative flow rule with Mises yield criterion (see Chapter 2). Additionally, isotropic hardening rule is assumed [SzB8]. In order to obtain proper hardening curve, the cyclic tests were analysed in the true stress – true strain curve (see Fig. 5.7/a), where $\sigma = P(\varepsilon^{\text{eng}} + 1)$ and $\varepsilon^{\text{true}} = \ln(\varepsilon^{\text{eng}} + 1)$ using the volumetric incompressibility assumption. It should be noted that the elastic contribution in the strain involves volumetric strain, but it is negligible compared to the viscous and plastic strains. Furthermore, the endpoints of each load steps were also detected, namely the endpoint of uploading/unloading and each relaxation steps as indicated by dot markers in Fig. 5.7/a.

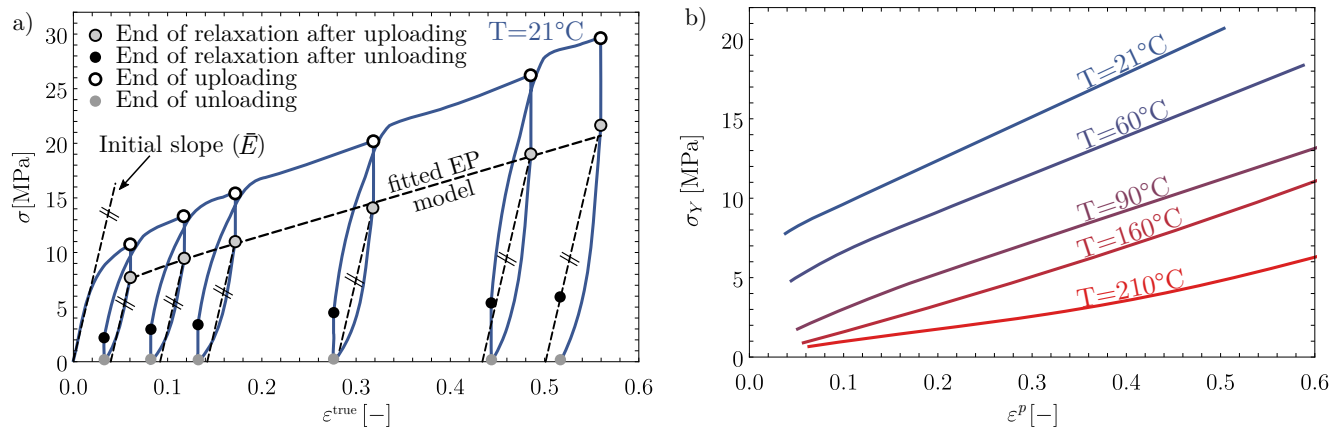


Figure 5.7: The a) method for estimation of long-term behaviour and hardening law at 21 °C and b) the linear hardening curves at all investigated temperatures

In order to eliminate the viscoelastic-viscoplastic effects, it was assumed that the endpoints of each relaxation phase after uploading steps correspond to the long-term, pure elastic-plastic behaviour [SzB7]. Therefore, the hardening curve can be approximated by a polynomial on the $\sigma - \varepsilon^{\text{true}}$ curves. Furthermore, the initial elastic modulus \bar{E} was obtained as the initial slope of the true stress – true strain curve, which is listed in Table 5.2.

Table 5.2: Estimation of the elastic modulus as the initial slope of the cyclic tests

Temperature [° C]	\bar{E} [MPa]
21	369.78
60	347.53
90	130.94
160	45.80
210	38.42

Using the decomposition of the total stress as in (2.68), the plastic strain values can be obtained (see Fig. 5.7/a) as

$$\varepsilon^p = \left(\varepsilon^{\text{true}} - \frac{\sigma}{\bar{E}} \right). \quad (5.11)$$

Moreover, using the same steps, the fitted polynomial yield function against the true plastic strain can also be obtained, which defines the hardening curve. As the results in Fig. 5.7/b show, the hardening curves can be approximated with linear functions with reasonable accuracy. Thus,

in the proposed model, linear isotropic hardening was applied [SzB7], [SzB8], where the hardening rule is defined accordingly to (2.79).

5.4 Fitting strategy and results

Having chosen the viscous and elastic-plastic elements of the TLVP model, the material parameters should be fitted to the uniaxial tests with uploading, relaxation and unloading phases as presented in Fig. 5.5. According to the generally applied parameter fitting strategy, the error between the model prediction and the measurement data is minimized [9].

The proposed TLVP model contains altogether eight material parameters. The elastic behaviour is characterised by the elastic modulus E , the Poisson's ratio ν and the fraction of elasticity f_e . The nonlinear viscous elements contain the power-law exponent m and power-law coefficients A and n , whereas the yield function is characterised by the initial yield stress σ_{y0} and plastic hardening modulus H . The parameters should also fulfil the following constraints to ensure physically admissible results:

$$E, A, n, H, \sigma_{y0} > 0, \quad (5.12)$$

$$0 < f_e < 1, \quad (5.13)$$

$$-1 < m < 0. \quad (5.14)$$

Since the fitting was performed using uniaxial tensile tests, the Poisson's ratio has a negligible effect on the stress result. Therefore, for minimizing the parameters to be fitted, the Poisson's ratio is considered to be constant, namely $\nu = 0.4$ [132, 144].

In contrast to the visco-hyperelastic model (in Chapter 4), the closed-form stress solution cannot be expressed analytically, thus a FE-based parameter-fitting method is proposed [SzB7], [SzB8]. In each iteration step a complete FE simulation of the problem was performed [143]. The procedure was performed on a single, eight-node brick element with reduced integration. The boundary conditions were set similarly as in Section 4.3.3, while displacement U_1 was set according to the simplified uniaxial measurement data presented in Section 5.2.2 and the resultant engineering stress values were obtained in each iteration step.

The fitting process, which is represented via its flowchart in Fig. 5.8, was defined to minimize the error function, which can be calculated as the sum of squared differences (SSD) between the simulation results and the measured data as

$$e^{\text{TLVP}} = \sum_{i=1}^M \left(P_i^{\text{meas}} - P^{\text{FE}}(t_i^{\text{meas}}) \right)^2, \quad (5.15)$$

where $P_i^{\text{meas}} - t_i^{\text{meas}}$ are the measured stress-time value data pairs, P^{FE} is the stress values obtained from FE simulation, while M stands for the number of data points.

5.4.1 Numerical optimization scheme

This parameter fitting method is extremely time-consuming since a single iteration step lasts 20-25 s using a CPU with 3.1 GHz for the loading history used in the simulation. In order to reduce the fitting time, three numerical optimization algorithms were compared (see Fig. 5.9): Hooke–Jeeves (HJ), Downhill simplex (DS) and Adaptive Simulated Annealing (ASA).

The DS method finds the local minima after simplex-operations based on function evaluations at the simplexes [145, 146]. The HJ algorithm searches the optima by simultaneously performed optimization using several trial solutions in the parameter-space [147], whereas the strategy of

ASA method is based on a random search with adaptive parameter control using temperature schedules mimicking heat treatment of metals [148].

After several trial-runs, the HJ method was found to perform the best concerning optimization time. As the example in Fig. 5.9 shows the convergence of the elastic modulus at $T = 120^\circ\text{C}$ required 532, 2017 and 4035 iteration steps for the HJ, DS and ASA algorithms, respectively. Note, that since the ASA method based on a random search, the convergence can only be declared after a given number of unsuccessful tries in order to guarantee that no better solution can be obtained.

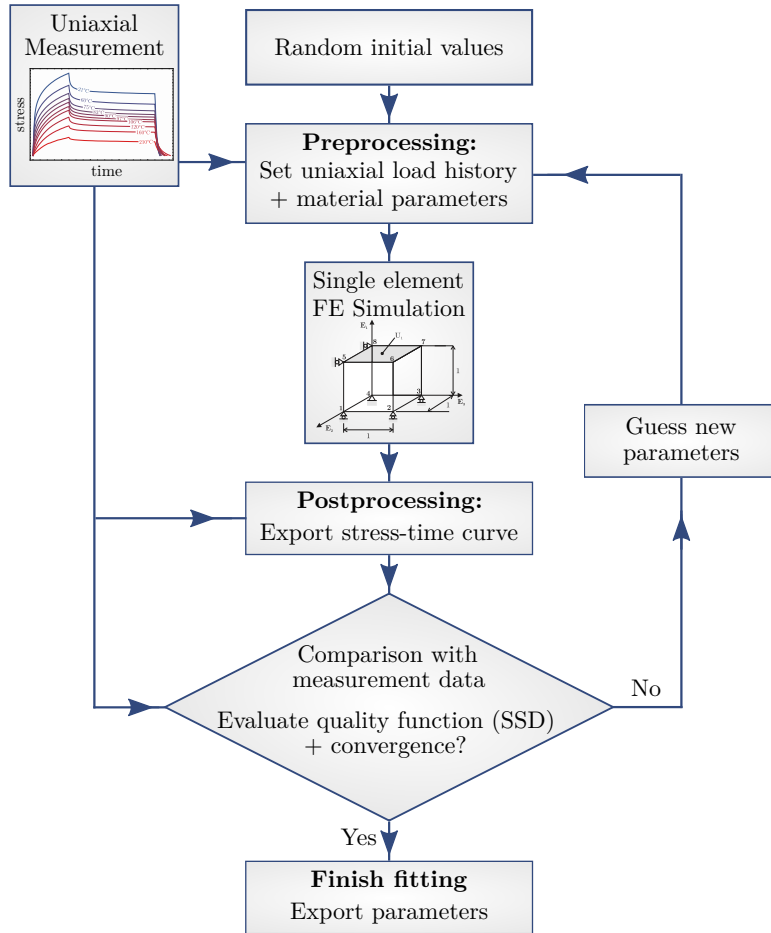


Figure 5.8: The flowchart of the proposed fitting method

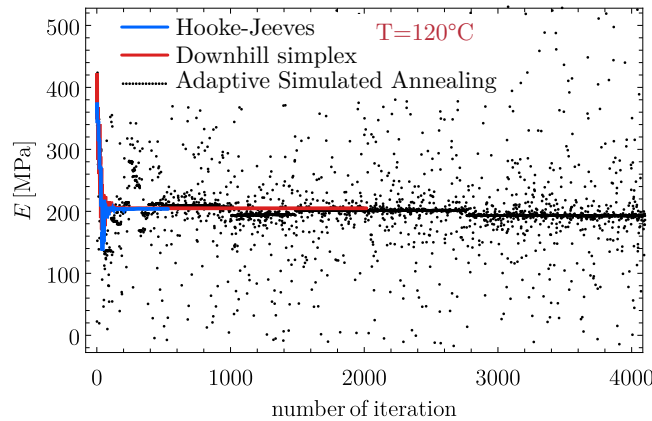


Figure 5.9: The comparison of numerical algorithms (HJ, DS, ASA) for the convergence of the elastic modulus at $T = 120^\circ\text{C}$

5.4.2 Fitting results: strain-hardening creep law

In case of the applied TLVP model using strain-hardening power-law creep model, the fitted material parameters are listed in Table 5.3, whereas Fig. 5.10 shows the fitted engineering stress-time curves at all investigated temperature levels.

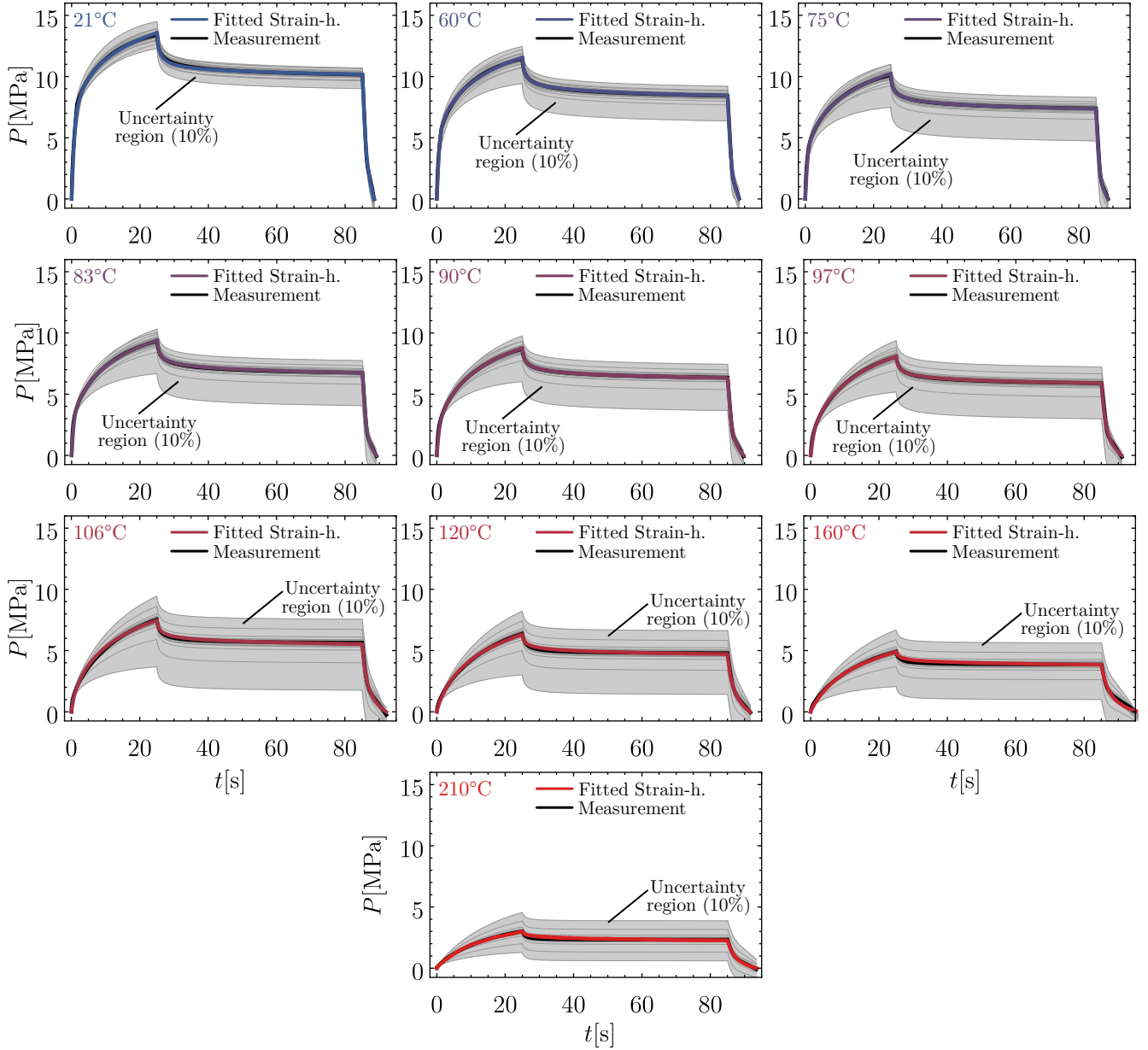


Figure 5.10: The comparison of the uniaxial measurement data and the fitted TLVP model using strain-hardening power-law creep model including the uncertainty region for at least 10% relative error for each parameter

Furthermore, the sensitivity of the model was also investigated using Monte-Carlo simulation, where a relative parameter error of $\delta_p = \pm 0 - 10\%$ was introduced for each fitted parameter [SzB7]. After performing the FE simulation of the simplified uniaxial extension problem for each combination of parameters with errors of $\pm 1\% \pm 2\% \pm 5\% \pm 10\%$, the so-called uncertainty region could be introduced as the envelope of the resultant engineering stress – time curves (see the grey shaded areas in Fig. 5.10). The results show that the TLVP model can characterise the viscous-elastic-plastic behaviour of the investigated MC-PET material with excellent accuracy. However,

at elevated temperatures (temperatures above the glass-transition temperature of $T_g = 90^\circ\text{C}$) the sensitivity of the model indicated by the uncertainty region, significantly increases.

Table 5.3: The fitted material parameters of the investigated microcellular foam using strain-hardening power-law creep model

Temp. [$^\circ\text{C}$]	E [MPa]	σ_{y0} [MPa]	H [MPa]	$A \cdot 10^3$ [-]	n [-]	m [-]	f_e [-]
21	685.08	4.099	29.51	0.446	2.500	-0.553	0.817
60	566.25	2.213	29.78	0.403	2.610	-0.541	0.858
75	520.06	1.325	29.37	0.538	2.610	-0.544	0.877
83	448.29	0.558	31.22	0.827	2.483	-0.521	0.877
90	384.41	0.000535	33.16	1.009	2.497	-0.522	0.876
97	302.83	0.000200	36.60	3.038	1.987	-0.588	0.879
106	267.59	0.000227	38.10	4.941	1.833	-0.623	0.882
120	206.00	0.000098	37.08	10.949	1.405	-0.710	0.884
160	135.81	0.000194	40.50	16.870	1.486	-0.761	0.880
210	80.01	0.000050	36.05	35.845	1.013	-0.770	0.890

5.4.3 Fitting results: time-hardening creep law

Similarly, the results in case of time-hardening power-law creep model can be summarised via the parameter Table 5.4 and by the comparison of measured engineering stress-time curves with the model prediction using the fitted parameters in Fig. 5.11. In the latter case, the sensitivity of the model is quantified by the uncertainty-region obtained by Monte-Carlo simulations as introduced previously. As the results show, this model is also able to characterise the material behaviour with adequate accuracy at all temperature levels. Additionally, the sensitivity analysis also shows similar results to the case of the TLVP model with strain-hardening creep law.

Table 5.4: The fitted material parameters of the investigated microcellular foam using time-hardening power-law creep model

Temp. [$^\circ\text{C}$]	E [MPa]	σ_{y0} [MPa]	H [MPa]	$A \cdot 10^3$ [-]	n [-]	m [-]	f_e [-]
21	753.37	4.935	30.99	0.528	3.389	-0.837	0.814
60	659.96	3.129	29.48	0.410	3.600	-0.797	0.843
75	576.57	2.211	29.33	0.725	3.513	-0.831	0.867
83	497.61	1.255	32.35	0.825	3.500	-0.795	0.881
90	409.29	0.832	35.86	1.476	3.403	-0.847	0.887
97	333.35	0.778	42.93	5.257	3.036	-0.938	0.895
106	297.08	0.404	45.96	9.743	2.866	-0.936	0.894
120	229.60	0.000383	46.98	35.037	2.388	-0.999	0.889
160	168.22	0.000279	48.00	98.019	2.295	-0.993	0.890
210	108.44	0.000051	43.23	309.744	1.753	-1.000	0.908

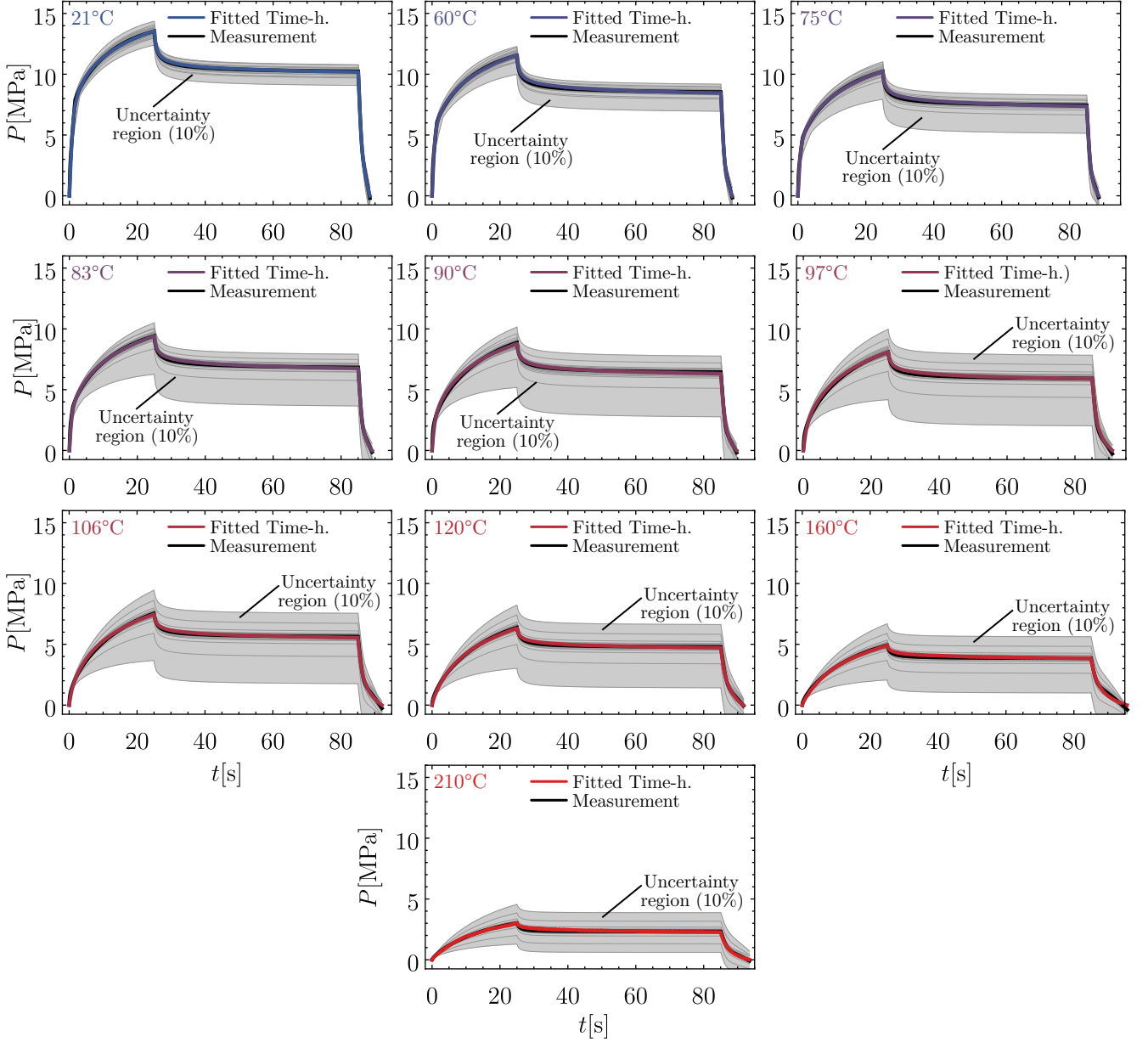


Figure 5.11: The comparison of the uniaxial measurement data and the fitted TLVP model using time-hardening power-law creep model including the uncertainty region for at least 10% relative error for each parameter

5.4.4 Comparison of models

The performance of the fitted models can also be analysed by the coefficient of determination R^2 , which is defined according to (3.68). This quantity, however, can give accurate result only if the curve is monotonously increasing, therefore for such curves, another quantity, namely the standard error of regression S (see (3.68)) is recommended [149][150].

The calculated values characterising the goodness of the fitting are listed in Table 5.5. It should be noted that values of SSD and S are not normalized, therefore the temperature-dependent tendency can only be obtained from the variation of R^2 . According to Fig. 5.12 the accuracy of the model prediction slightly decreases at the highest temperatures. Although, the R^2 values are always above 98.9%, which means that both models can be applied for characterising the material with good accuracy. The goodness of fitting also indicates that the strain-hardening power-law

creep model shows better accuracy compared to the time-hardening one, nearly all temperatures, but especially at the highest ones.

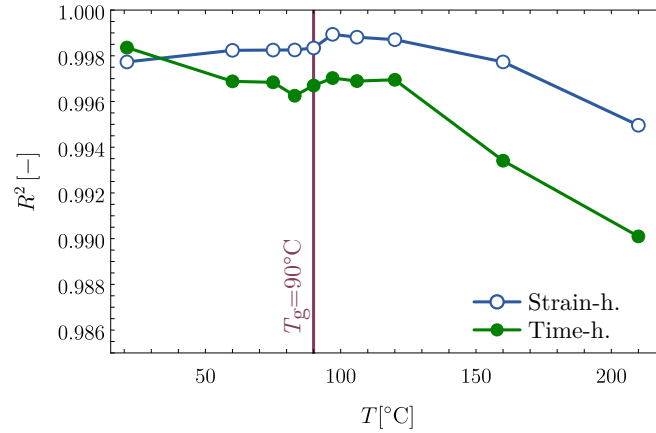


Figure 5.12: Variation of R^2 against temperature for strain- and time-hardening creep laws

Table 5.5: Comparison the performance of strain-hardening (Strain-h.) and time-hardening (Time-h.) TLVP models using fitting quality values of SSD , R^2 and S

Temp. [° C]	SSD [MPa ²]		R^2 [%]		S [MPa]	
	Strain-h.	Time-h.	Strain-h.	Time-h.	Strain-h.	Time-h.
21	12.94	10.18	99.78	99.83	0.0927	0.0823
60	7.23	14.71	99.84	99.67	0.0694	0.0991
75	6.13	12.51	99.83	99.67	0.0638	0.0912
83	6.91	14.33	99.81	99.61	0.0676	0.0973
90	5.47	15.47	99.84	99.57	0.0599	0.1008
97	4.12	20.92	99.88	99.43	0.0517	0.1163
106	4.71	12.02	99.86	99.67	0.0549	0.0877
120	3.22	8.25	99.87	99.68	0.0455	0.0728
160	4.76	16.94	99.78	99.21	0.0541	0.1021
210	2.84	7.39	99.61	98.94	0.0423	0.0681

5.4.5 Sensitivity of parameters

Besides the analysis of global sensitivity using uncertainty regions, the sensitivity of each parameter can also be obtained using the Monte-Carlo simulation method again [SzB7]. This case, only a single parameter was perturbed with δ_p relative parameter error of $\pm 1\% \pm 2\% \pm 5\% \pm 10\%$, and the resulted curves were compared using standard error of regression as in (5.15). The resultant curves are presented in Figs. 5.13-5.14, from which the effect of each parameter can be obtained.

5.4. FITTING STRATEGY AND RESULTS

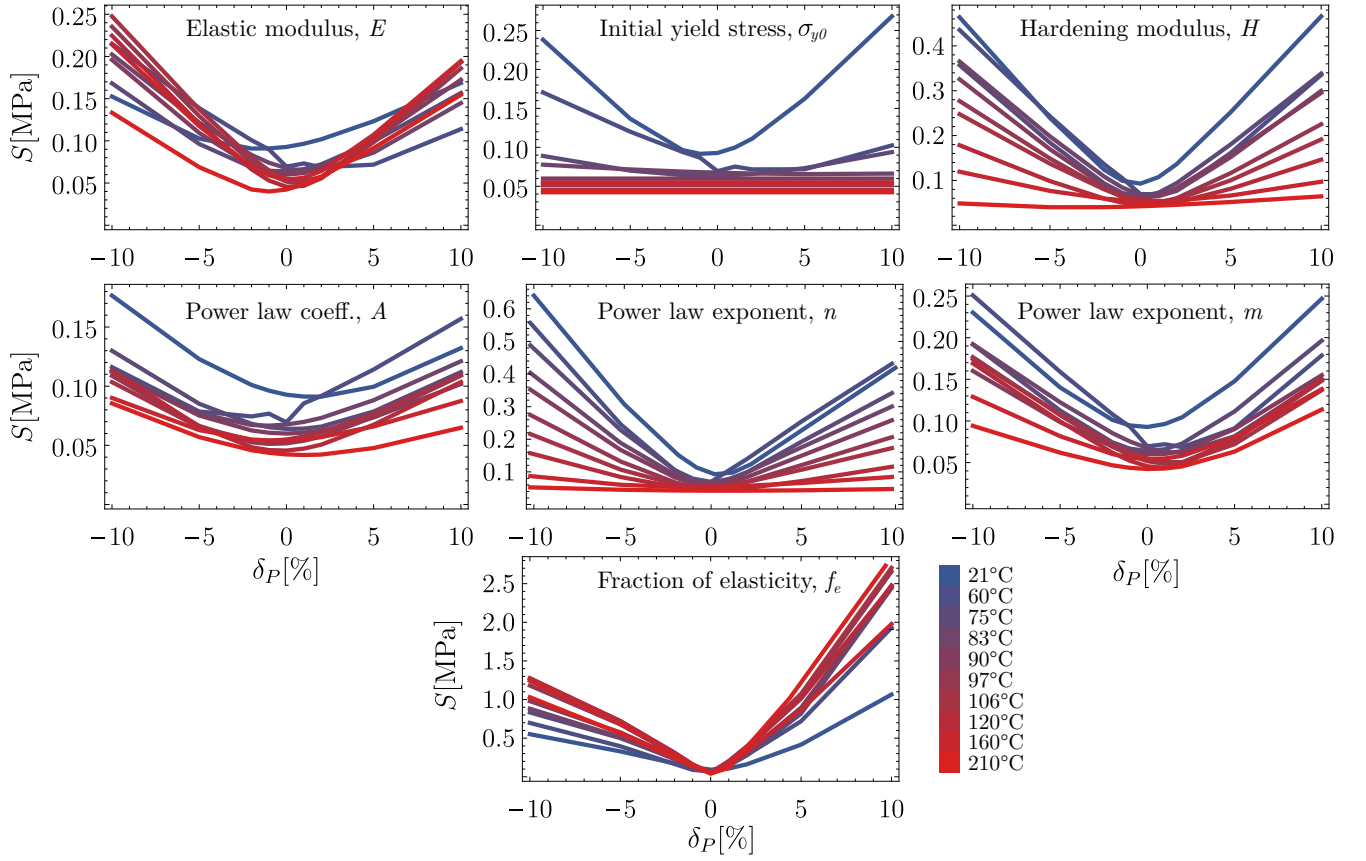


Figure 5.13: Sensitivity of the fitted parameters in case of TLVP model with strain-hardening creep

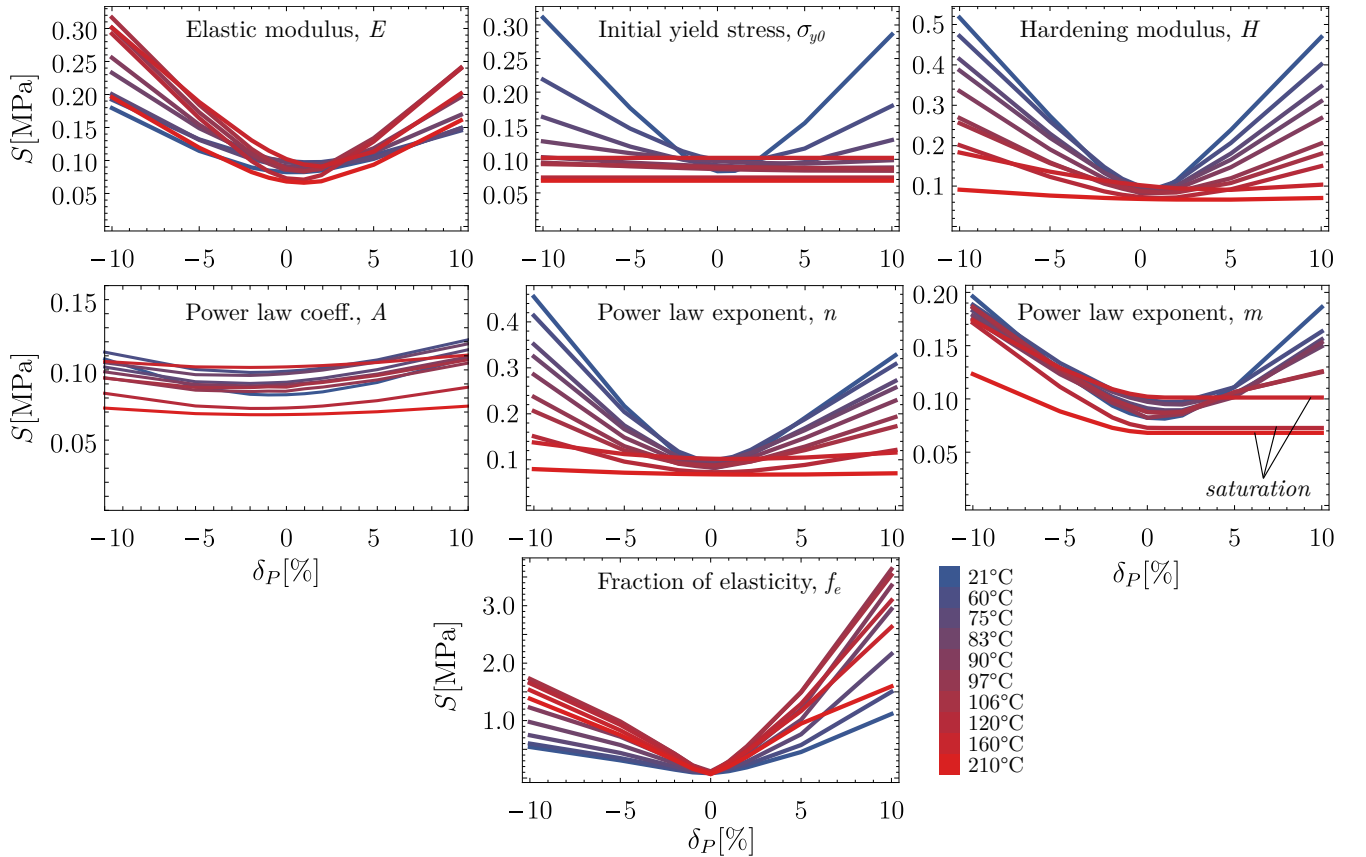


Figure 5.14: Sensitivity of the fitted parameters in case of TLVP model with time-hardening creep

As the results show, the parameter f_e (fraction of elasticity) has the largest effect on global sensitivity. It should be emphasized that the initial yield stress decreases approximately to zero, therefore it does not affect on the global error above the glass transition temperature. In case of the viscous parameters, the error varies on the same scale for all three viscous parameters (A , n and m). Note, that in case of the time-hardening power-law at temperatures 106-210° C the fitted value for the power-law exponent m lays close to the boundary of the possible parameter range as in (5.14), Consequently, the effect of positive relative errors ($\delta_p > 0$) cannot be analysed. Thus, the error considered to be saturated, which is indicated in Fig. 5.14.

5.5 Temperature-dependency of parameters

The result of the parameter fitting provides information about the temperature-dependence of the material parameters. This can be utilized as a validation method of the fitting by comparing the variation of elastic modulus with the DMA results. The long-term and instantaneous boundary models can be introduced for the TLVP model by substituting the nonlinear dashpot element with breakage and short-circuit, respectively [SzB7]. As it is discussed in [21, 151], the long-term behaviour is defined with $\dot{\epsilon} \rightarrow 0$, when the dashpot element deforms without any stress merging, thus the dashpot can be substituted with a breakage (see Fig. 5.15). Moreover, in case of instantaneous behaviour, namely $\dot{\epsilon} \rightarrow \infty$, the viscous element becomes infinitely stiff, thus only the elastic element deforms in the viscoelastic branch. Consequently, both cases can be represented with pure elastic-plastic models.

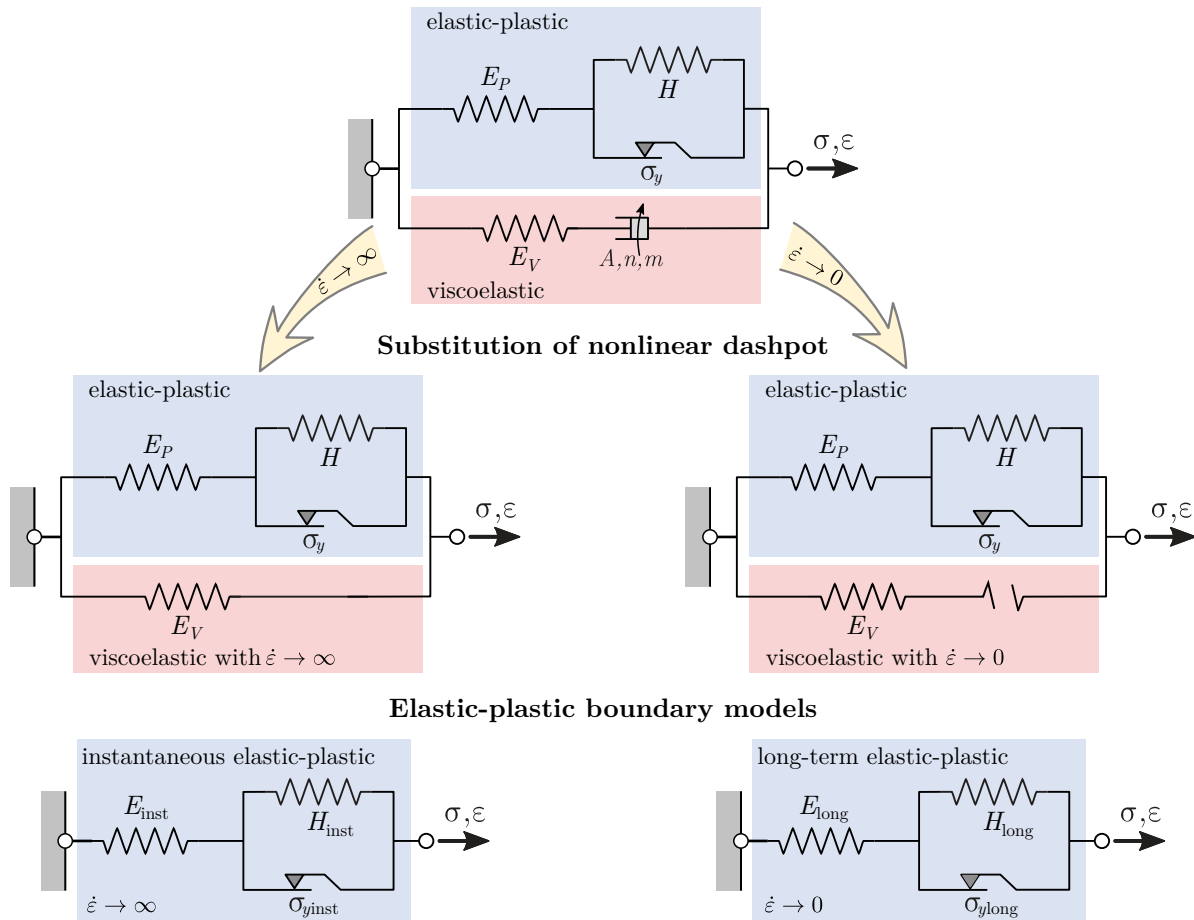


Figure 5.15: The introduction of the elastic-plastic boundary models for the TLVP model representing the long-term and instantaneous behaviour

The corresponding material parameters in the elastic-plastic boundary models in case of the applied TLVP model can be obtained as

$$E_{\text{inst}} = E_P + E_V = E, \quad \text{and} \quad E_{\text{long}} = E_P = (1 - f_e)E, \quad (5.16)$$

$$\sigma_{y0\text{inst}} = \frac{1}{1 - f} \sigma_{Y0}, \quad \text{and} \quad \sigma_{y0\text{long}} = \sigma_{y0}, \quad (5.17)$$

$$H_{\text{inst}} = \frac{f_e (1 - f_e) E + H}{(1 - f_e)^2}, \quad \text{and} \quad H_{\text{long}} = H, \quad (5.18)$$

where subscript ‘‘inst’’ refers to the instantaneous boundary model, whereas ‘‘long’’ for the long-term, respectively [SzB7].

Using the previously introduced models, the long-term and instantaneous elastic moduli can be obtained for all temperatures using both creep models, respectively. By comparing the variation of these curve against the temperature with the DMA results (see Fig. 5.16), it can be clearly seen that the DMA measurement always lays in between the long-term and instantaneous responses, since the DMA measurement was performed with finite deformation speed. For the boundary models, the glass transition temperature was also determined as the inflexion of the curves [133]. As a result of the numerical interpolation and derivation, the glass transition temperature was found to be $T_g^{\text{strain}} = 91.3^\circ\text{C}$ and $T_g^{\text{time}} = 87.7^\circ\text{C}$ respectively. This means that the parameter fitting and the DMA measurement are in excellent agreement.

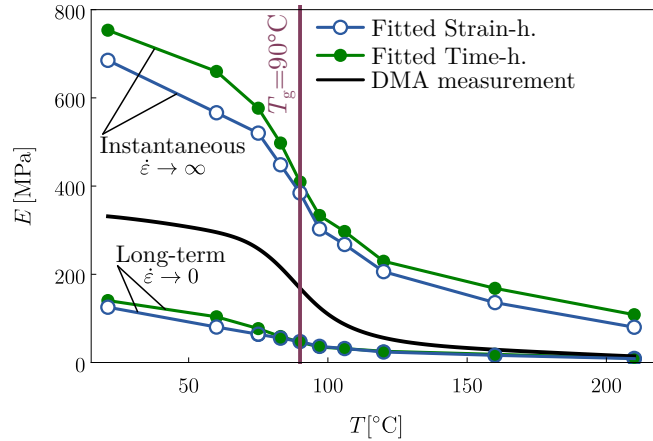


Figure 5.16: Comparison of the DMA results and the boundary models for the fitted strain- and time-hardening power-law TLVP models

5.5.1 Analytical parameter functions

Besides the elastic modulus, all other material parameters, which characterise yielding and creeping, could also be analysed as a function of the temperature. The characteristics in Fig. 5.17 show clear tendencies only with moderate numerical noise. In the literature, a possible solution to describe the temperature dependency of material parameters is by introducing closed-form functions, usually in polynomial form [117].

Although, it can also be seen, that in the vicinity of the glass transition temperature, there is a significant change in all parameter value. Consequently, it is preferable to include T_g as internal parameter in the analytical temperature-dependent parameter functions as applied in [137, 152]. In the approach to finding suitable functions several possibilities were tried; the chosen functions

have the form [SzB7]:

$$E(T) = E_1 \arctan(E_2(T - T_g)) + E_3 \tag{5.19}$$

$$H(T) = H_1 \arctan(H_2(T - T_g)) + H_3 \tag{5.20}$$

$$n(T) = n_1 \arctan(n_2(T - T_g + n_3)) + n_4 \tag{5.21}$$

$$m(T) = m_1 \arctan(m_2(T - T_g + m_3)) + m_4 \tag{5.22}$$

$$\sigma_{y0}(T) = \begin{cases} Y_2(T - T_g)^2 + Y_1(T - T_g) + Y_0, & T \leq T_g \\ Y_3(T - T_g) + Y_0, & T > T_g \end{cases} \tag{5.23}$$

$$A(T) = \begin{cases} A_1(T - T_g) + A_0, & T \leq T_g \\ A_3(T - T_g)^2 + A_2(T - T_g) + A_0, & T > T_g \end{cases} \tag{5.24}$$

$$f_e(T) = \begin{cases} f_{e1}(T - T_g) + f_{e0}, & T \leq T_g \\ f_{e2}(T - T_g) + f_{e0}, & T > T_g \end{cases} \tag{5.25}$$

As the functions show, the elastic modulus E , the hardening modulus H , the power-law exponent n and m show a similar tendency according to the arctangent function. Whereas, the initial yield stress σ_{y0} , the power-law coefficient A and the fraction of elasticity f_e can be described using piecewise polynomials. The numerical values of the parameters in (5.19)-(5.25) are listed in Table 5.6. The variation of material parameters shows a excellent agreement with the change of material behaviour of thermoplastics around the glass transition temperature as summarised in [5, 7, 8]. Above T_g large segmental motions are activated, and the polymer starts to behave more fluid-like, as indicated by increasing A and f_e parameters, while the elastic modulus and the initial yield stress significantly drops.

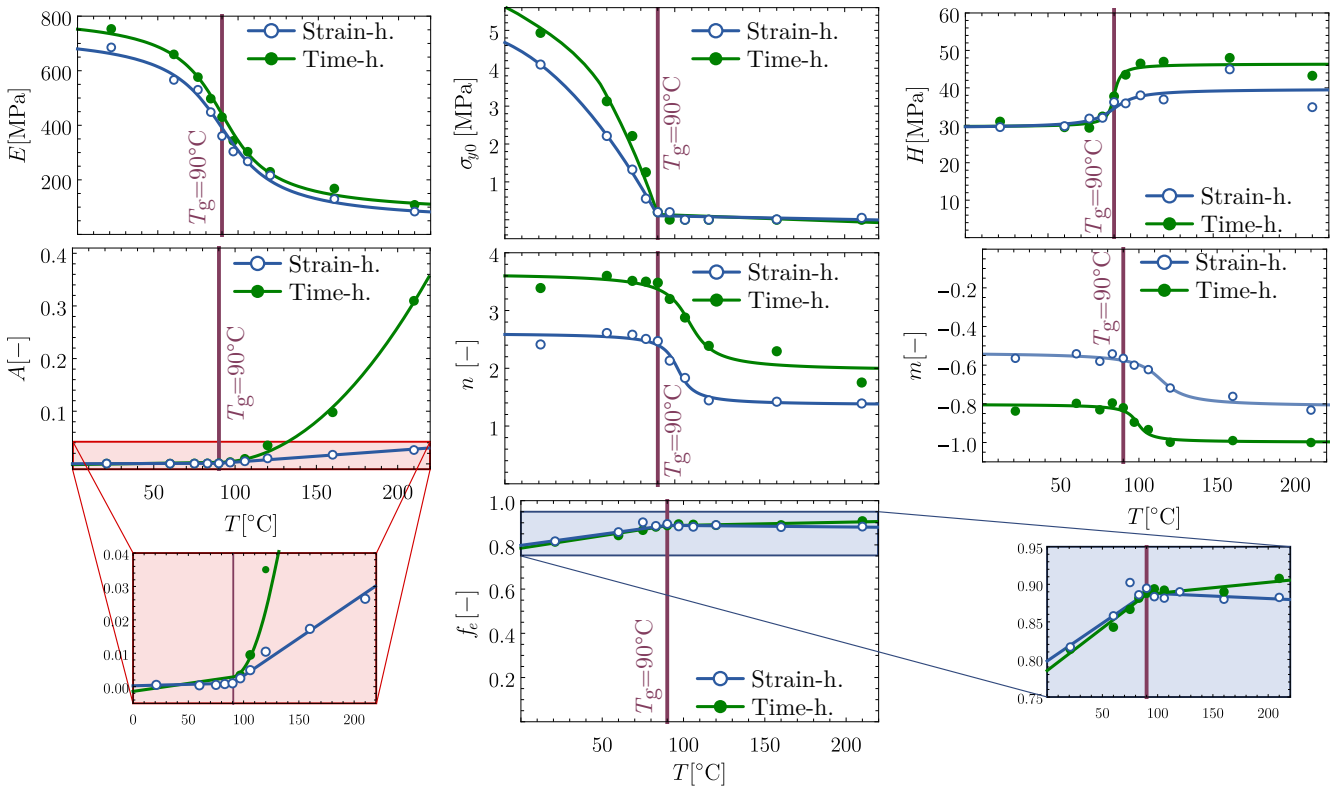


Figure 5.17: The temperature-dependency of material parameters and the fitted analytical functions for strain- and time-hardening power-law TLVP models

Table 5.6: Parameters of the analytical temperature-dependent parameter functions for TLVP with strain-hardening and time-hardening creeping

Parameter	Strain-h.	Time-h.	Parameter	Strain-h.	Time-h.
E_1 [MPa]	223.7	236.2	A_0 [-]	0.0013	0.0034
E_2 [MPa]	-0.039	-0.043	A_1 [-]	0.000018	0.0000585
E_3 [MPa]	390.4	440.4	A_2 [-]	0.000211	0.0000293
Y_0 [MPa]	0.1506	0.1403	A_3 [-]	0	0.0000208
Y_1 [MPa]	-0.0809	-0.1372	n_1 [-]	-0.4895	-0.5613
Y_2 [MPa]	-0.000334	-0.000988	n_3 [-]	0.0943	0.0740
Y_3 [MPa]	-0.000849	-0.00165	n_3 [-]	1.9418	2.7969
H_1 [MPa]	-2.856	-5.434	n_4 [-]	-11.909	-17.621
H_2 [MPa]	-0.239	-0.983	m_1 [-]	-0.0794	-0.0584
H_3 [MPa]	33.67	37.67	m_2 [-]	0.1226	0.280
f_{e0} []	0.888	0.887	m_3 [-]	-0.646	-0.898
f_{e1} [-]	0.00101	0.00113	m_4 [-]	-18.98	-4.72
f_{e2} [-]	0.00066	0.0014			

5.5.2 Improved fitting with analytical functions

The previously introduced analytical functions not only express the relation of temperature and the parameter values but also can be utilized for initializing the fitting process. As it was discussed above, the FE-based parameter fitting procedure could be extremely time-consuming and also very sensitive to the initial set of parameter values. The proposed analytical functions contain only 2-4 parameters, therefore based on approximately 3 fittings (e.g. at room temperature, at 60 °C and at the maximum temperature), the analytical function parameters in (5.19)-(5.25) can be fitted. This approach was motivated by the model of Dupaix, where temperature-dependent shear modulus function is fitted to measurements below and above glass transition temperature [137, 152]. After evaluating the function at all other temperature levels, this could give a possible guess for the initial parameters and ensures significantly faster fitting. This flowchart of this fitting algorithm is illustrated in Fig. 5.18.

The benefit of this method is presented via a case study of elastic modulus fitting at 120 °C using TLVP with strain-hardening power-law. As the fitting is performed for 21 °C, 60 °C and 210 °C using the originally proposed method, the analytical function in (5.19) can be fitted to E_{21} , E_{60} and E_{210} values (see Table 5.4) and hence, the numerical estimation function becomes

$$E^* = 255.36 \cdot \arctan(-0.0356(T - 90)) + 450.89, \quad (5.26)$$

from which the initial value for the fitting at 120 °C becomes

$$E_{\text{init},120} = 241.82 \text{ MPa}. \quad (5.27)$$

As Fig. 5.19 shows, the fitting process started with this value needs only 514 iteration steps, while the same fitting started from the room-temperature result of $E_{21} = 753.37$ MPa needed 1487 iterations. Therefore, the time needed to finalize fitting could be reduced to its third by properly chosen initial values based on the analytical parameter functions proposed above.

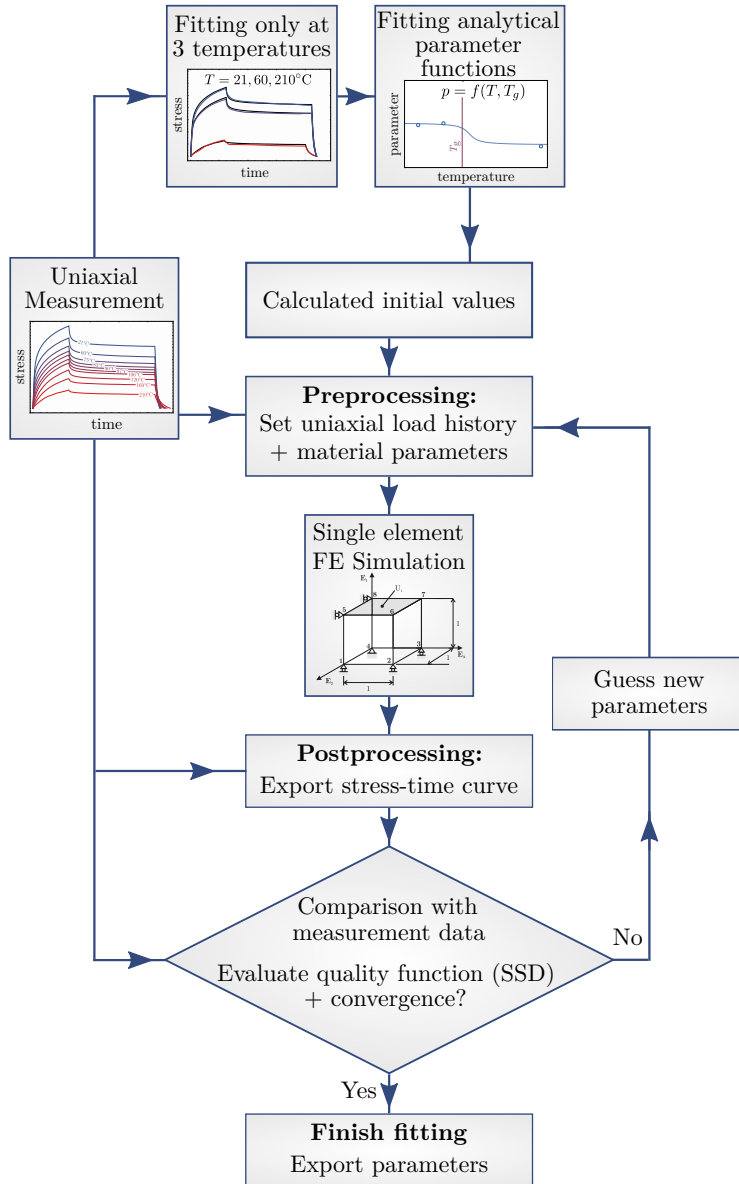


Figure 5.18: The flowchart of the fitting method utilizing the analytical parameter functions for initializing numerical parameter values

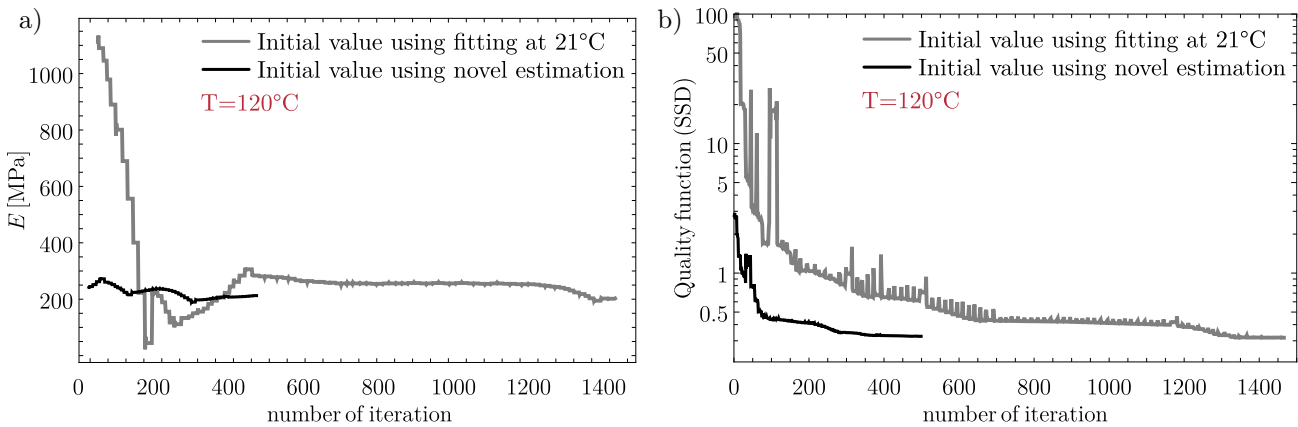


Figure 5.19: Comparison of the parameter fitting at 120°C with strain-hardening TLVP model using initial values from original room-temperature fitting and novel analytical estimations

5.6 Punch-test based validation procedure

The previously discussed material characterisation process was usually based on uniaxial measurements including creep, relaxation and cyclic tests performed at several temperatures. For such nonlinear constitutive models, a perfectly fitted model to uniaxial tests may lead to extreme deviation during the prediction of the material behaviour for different load cases [66].

During thermoforming, the dominant loading is biaxial, therefore one cannot rely on the fitted model to uniaxial data without validation for biaxial load case. In the literature, a commonly applied method for performing such biaxial loading with single-column testing systems is punch-test measurements [153, 9, 143, 154].

In the proposed method for thermoplastic MC-PET material, punch-tests are combined with laser scanning measurements in order to obtain not only the force-displacement characteristic but also the final shape and thickness variation along of the specimen [SzB9]. The measured punch-test data can further be utilized during the validation process by comparing with the FE simulation result of the punch-test applying the fitted material model. The proposed validation method contains the following four main steps, which are also illustrated in Fig. 5.20.

1. Experimental punch-tests with spherical head geometry
2. 3D surface laser scanning of top and bottom surfaces
3. FE simulation of the punch-test
4. Comparison of the thickness variation, final shape and force-time curves

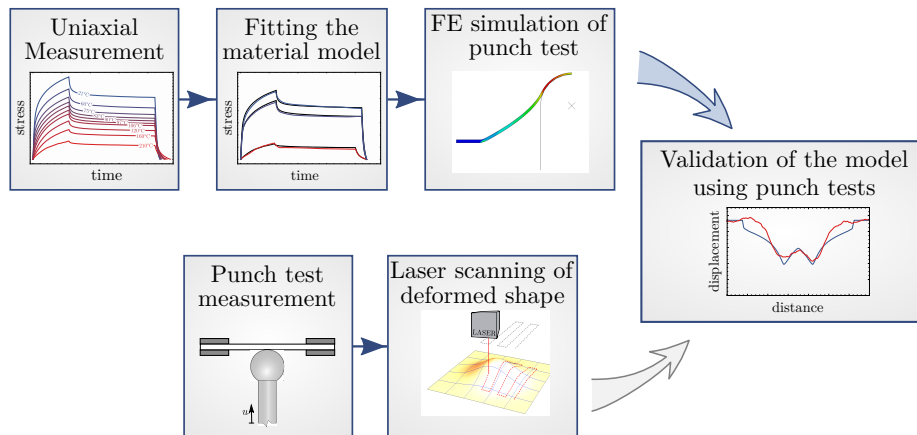


Figure 5.20: The workflow of the validation strategy for thickness variation using punch-tests

5.6.1 Punch-tests

The schematics of the axisymmetric punch-test measurement is presented in Fig. 5.21/a. A piece of a raw MC-PET material sheet with dimensions of 75×75 mm was placed in a special fixture mounted in Zwick Z010 Testing System equipped with temperature chamber and the punch-test was performed with stainless steel spherical punch with diameter of 19 mm. The displacement-based loading consists of three parts: uploading with $v_c = 500$ mm/min, relaxation for $t_r = 30$ s and unloading with $v_c = 100$ mm/min until $F = 0$ N is reached. Figure 5.21/b illustrates the experimental punch-test force-displacement $F - u$ data at same temperatures levels as in Section 5.2.2.

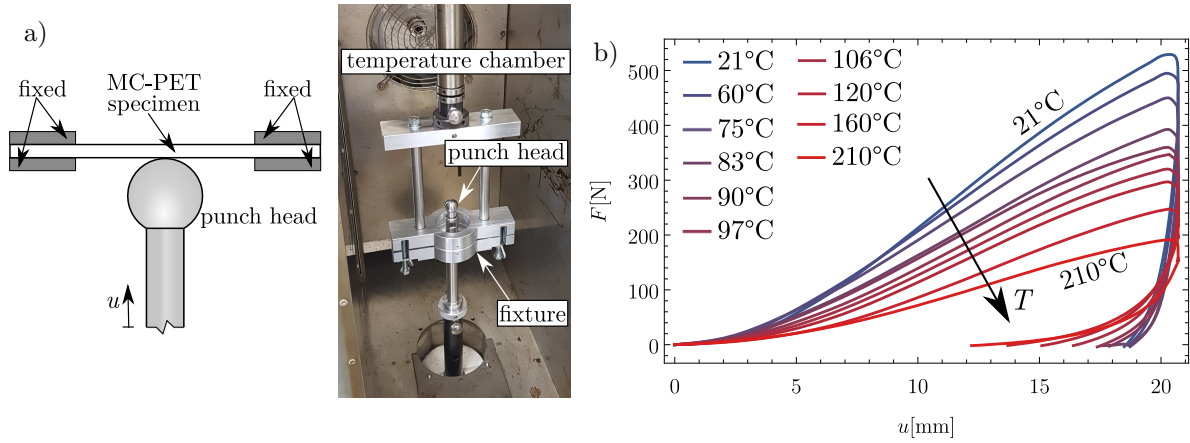


Figure 5.21: The a) layout of the punch-test measurement in heat chamber and b) the measured force-displacement characteristics

5.6.2 Laser scanning

After punch-tests, the deformed specimens were placed in an NCT EmR-610Ms CNC milling machine, where the top and the bottom surfaces were scanned using a KEYENCE IL-030 Laser Differentiation Displacement Sensor following a predefined “zig-zag”-like path as shown in Fig. 5.22/a (for further details of the laser system see [155]).

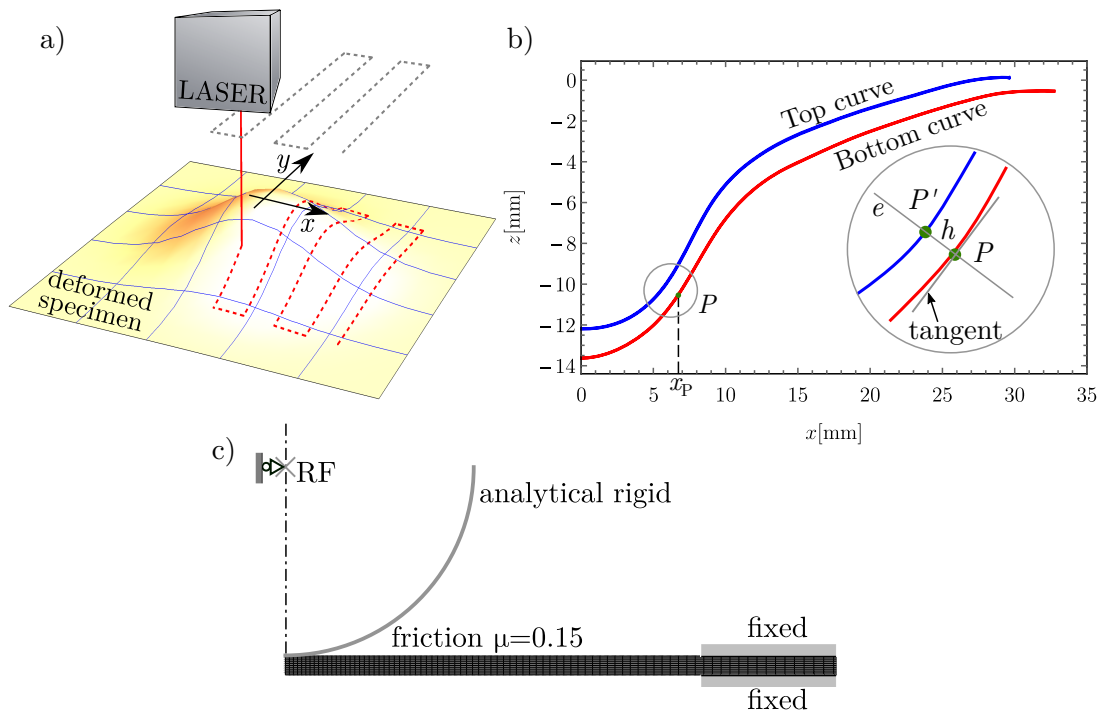


Figure 5.22: The a) schematics of the deformed surface detection using laser scanner and b) the determination of local thickness from top and bottom curves and c) the applied FE model

After synchronization of the time signal of the distance variation recorded by the laser sensor and the position data provided by the CNC machine, the point clouds corresponding to both top and bottom surfaces of the deformed shape were obtained. Based on the scanned surfaces the thickness variation was determined along the surface and evaluated along the x -axis by searching point P' on the top curve (see Fig. 5.22/b) to the corresponding point on the bottom curve

(denoted by P). For this purpose, the perpendicular line e to the tangent at $P(x_P, y_P)$ was determined and then P' was obtained as the closest point on the top curve on the line. Finally, the thickness h at each x_P along the x-axis was obtained as

$$h(x_P) = |\overline{PP'}|. \quad (5.28)$$

5.6.3 Simulation of punch-test

As a next step, the FE simulation of the punch-test was performed using the commercial software ABAQUS [15]. The applied axisymmetric FE-model is illustrated in Fig. 5.22/c. In order to reduce the computational time, the punch head was modelled as an analytical rigid surface, while the contact between the rigid punch and the MC-PET was modelled with Coulomb-friction with the coefficient of $\mu = 0.15$ [144]. Furthermore, the model was meshed with CAX4R elements with reduced integration.

5.6.4 Validation results

The comparison of the measured punch-test force-time ($F-t$) data and the FE simulation results are presented in Fig. 5.23. The comparison of the force-time curves shows that in case of 21 °C the discrepancy between the simulation result and the measurement is remarkable. However, at elevated temperatures, this deviation becomes moderate, especially in case of TLVP model with time-hardening creeping.

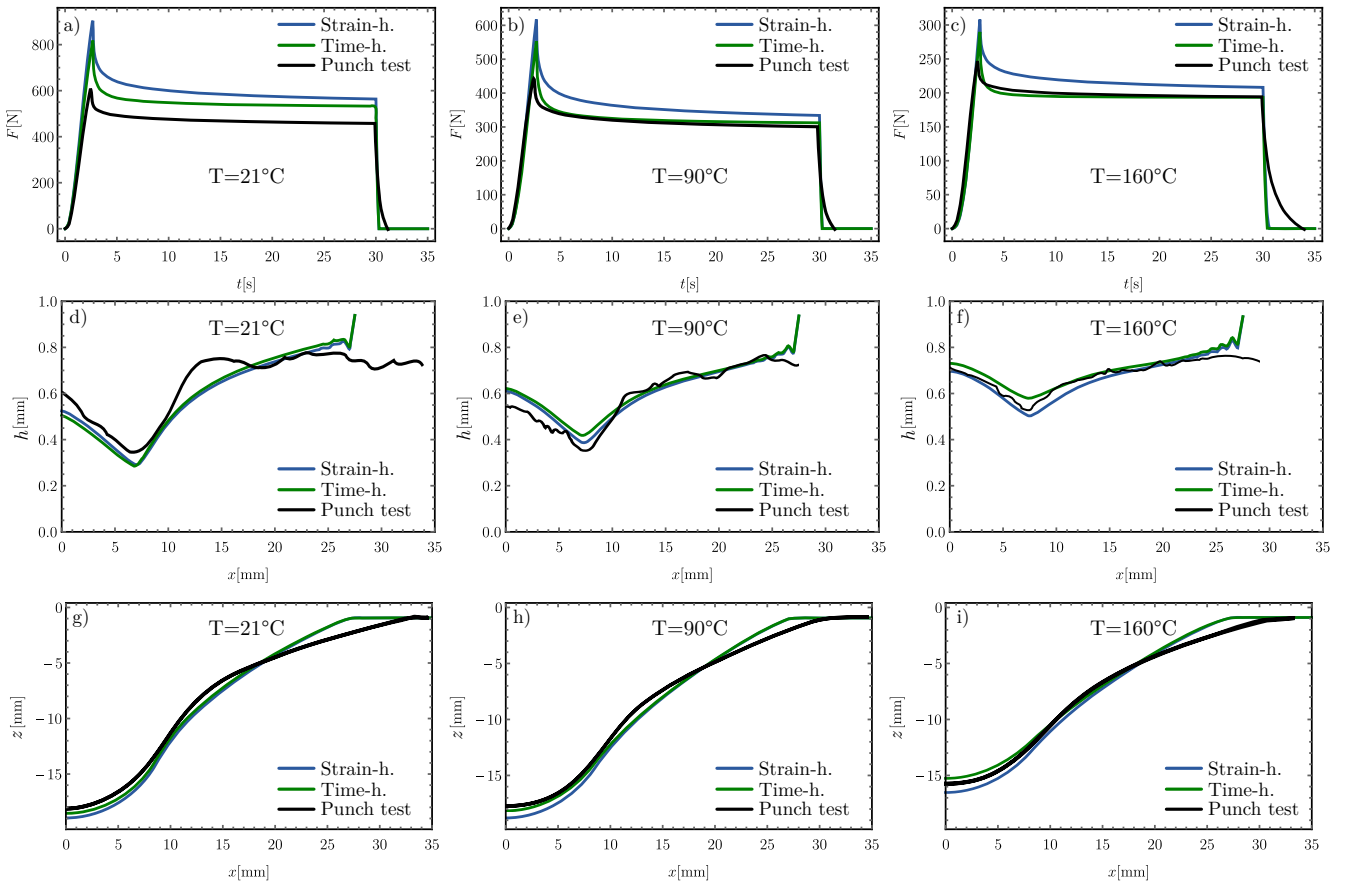


Figure 5.23: The comparison of the experimental results and the FE simulation using TLVP with strain- and time-hardening power-law models at 21 °C, 90 °C and 160 °C based on a)-c) force-time data from punch test, d)-f) thickness variation and g)-i) the deformed shape of the specimen by laser scanning technique

The variation of the thickness h along the x -axis shows good agreement with the results of the laser scanning measurement. Note, that in Fig. 5.23/d-f numerical noise is observable in the neighbourhood of the fixed support, which could be eliminated with mesh-refinement or by using full integration, however, its effect on the simulation results is negligible. The local minima on the thickness variation also indicate the contact region between the punch-head and the specimen. Finally, the excellent accuracy between the deformed geometries (represented with the position in z -direction) also confirms that the TLVP-model can be applied for describing the material behaviour and the permanent deformation for complex geometries and non-homogeneous deformations as well.

In order to characterise the model accuracy with the temperature, the relative error of the maximal force and the minimal thickness values were compared using the measurement data as a reference value. The variation of the relative errors δ_{rel} is illustrated in Fig. 5.24. The relative error of the maximal force varies between 5–30% and significantly decreases at elevated temperatures, while the error of the minimal thickness is always less than 10%. The comparison of the thickness variation obtained by FE prediction and the laser scanning method are in good agreement. The relative error of the maximal force varies between 5–30% and significantly decreases at elevated temperatures, while the error of the minimal thickness is always less than 10%.

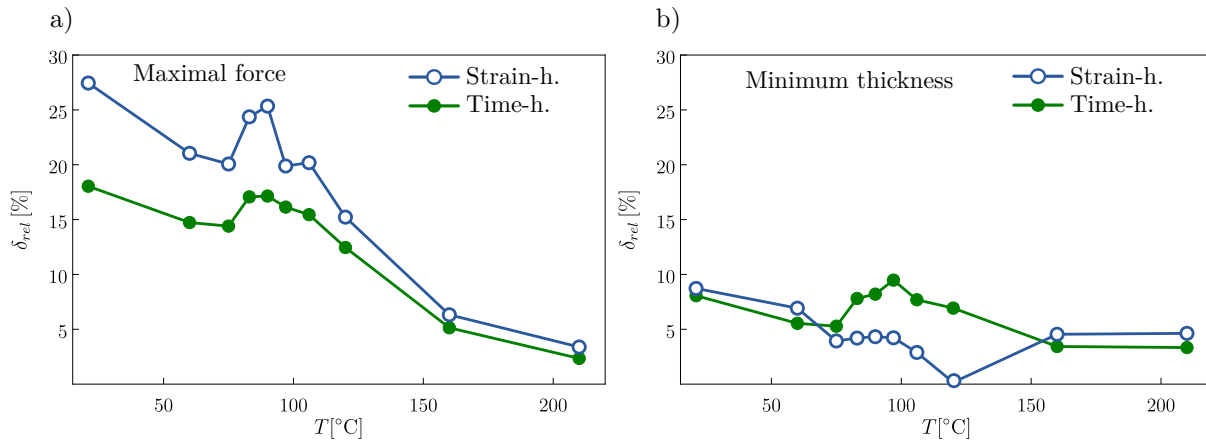


Figure 5.24: Comparison of the error of the applied TLVP models with strain- and time-hardening power-law models

The higher relative error of the maximal force values at low temperatures indicates that at these temperatures it is harder to extrapolate from uniaxial test data to biaxial load case, while at elevated temperatures the biaxial stress state can be approximated from the uniaxial test with reasonable accuracy. The reason behind this fact is that under the glass transition temperature the material behaviour is mostly characterised by nonlinear elastic and yielding properties, while above this temperature the behaviour of the material becomes more fluid-like [5, 7, 8]. It can also be concluded that the TLVP model can characterise the material behaviour in biaxial stress-state with adequate accuracy, even if only uniaxial tests were used during the fitting process. The results also revealed that the prediction of the TLVP model with time-hardening power-law creeping law is more accurate than TLVP model utilizing strain-hardening creeping law.

5.7 Main results

I have performed detailed experimental study on the mechanical behaviour of a particular microcellular polyethene-therephthalate foam material on wide temperature range. I have proposed a parallel viscoelastic-viscoplastic model, that is able to characterise the material on the entire temperature regime with excellent accuracy. Using a FE-based fitting procedure I have determined the temperature dependent material parameters. By means of the analysis of the parameters I have proposed analytical functions, that describe the variation of parameters with the temperature. Furthermore, I have also proposed a punch-test based validation technique for the validation of the fitted model non-homogeneous deformation with complex geometry. By analysing the performance of the proposed models, I have obtained the following results.

Thesis statement 4

The mechanical behaviour of thermoplastic microcellular polyethene-therephthalate foam material shows significant elastic, rate-dependent and permanent deformations on the temperature domain of 21–210°C, which is relevant for its thermoforming applications.

The captured mechanical behaviour can be effectively modelled on the entire temperature domain using a parallel viscoelastic-viscoplastic constitutive model with finite strain approach, where the viscoelastic properties modelled via a Maxwell-element with nonlinear power-law creeping law with strain- and time-hardening, while the yielding behaviour is modelled with associative flow rule based on the von Mises yield criterion with linear isotropic hardening. At high temperatures, however, the sensitivity of the model increases significantly.

The accuracy of time- and strain-hardening power-law creep laws shows only minor discrepancy in uniaxial case, and furthermore the constitutive model also predicts the force-displacement characteristic of punch-tests within reasonable errors.

Related publications: [\[SzB7\]](#),[\[SzB8\]](#),[\[SzB9\]](#),[\[SzB10\]](#)

Thesis statement 5

Consider the temperature-dependent mechanical behaviour of the microcellular polyethene-terephthalate foam to be modelled using the parallel viscoelastic-viscoplastic constitutive model as a combination of an elastic-plastic network based on von Mises yield criterion with linear isotropic hardening and a Maxwell-element with nonlinear strain and time hardening power-law creeping. The temperature-dependency of the material parameters, namely the elastic modulus (E), initial yield stress (σ_{y0}), hardening modulus (H), fraction of elasticity (f_e), creep-law coefficient (A) and exponents (m, n), can be characterized with monotonous, continuous functions of the T actual temperature and T_g glass-transition temperature in the form of

$$\begin{aligned}
 E(T) &= E_1 \arctan(E_2(T - T_g)) + E_3, \\
 H(T) &= H_1 \arctan(H_2(T - T_g)) + H_3, \\
 n(T) &= n_1 \arctan(n_2(T - T_g + n_3)) + n_4, \\
 m(T) &= m_1 \arctan(m_2(T - T_g + m_3)) + m_4, \\
 \sigma_{y0}(T) &= \begin{cases} Y_2(T - T_g)^2 + Y_1(T - T_g) + Y_0, & T \leq T_g \\ Y_3(T - T_g) + Y_0, & T > T_g \end{cases}, \\
 A(T) &= \begin{cases} A_1(T - T_g) + A_0, & T \leq T_g \\ A_3(T - T_g)^2 + A_2(T - T_g) + A_0, & T > T_g \end{cases}, \quad \text{and} \\
 f_e(T) &= \begin{cases} f_{e1}(T - T_g) + f_{e0}, & T \leq T_g \\ f_{e2}(T - T_g) + f_{e0}, & T > T_g \end{cases}.
 \end{aligned}$$

Related publications: [SzB7],[SzB8],[SzB10]

6

Pellet impacts for impulse excitation

In this chapter, the benefits of the previously introduced parallel viscoelastic-viscoplastic model with the proposed parameter-fitting strategy is presented via the case study of airsoft pellet impacts applied for impulse excitation.

In the research field of machine tool vibrations, the frequency response function (FRF) of cutting tools with large length/diameter ratio and blade-type workpieces plays significant role [156]. In modal testing, the FRF can be measured as the response for impulse excitation performed by a modal hammer. However, during the hammer impact, the so-called multiple-hitting phenomena might occur (see Fig. 6.1) resulting in non-ideal input force signal, which should be avoided. The natural frequencies of machine tools are usually high, which yields that the time of impact (T_{imp}) should be decreased to ensure wider relevant frequency range of the Fourier-transform of the force signal, yielding that the FRF of the tool could also be obtained on a wider frequency domain. Therefore, smaller hammers (e.g. micro-hammers) should be applied, however, the signal-to-noise ratio is typically worse due to the small energy transfer during the impacts. In addition, due to the dynamical properties of the spindle bearings, the FRF can change during rotation, and the hammer excitation of high-speed rotating tools also poses safety risks, implying a significant need for an alternative impulse excitation method.

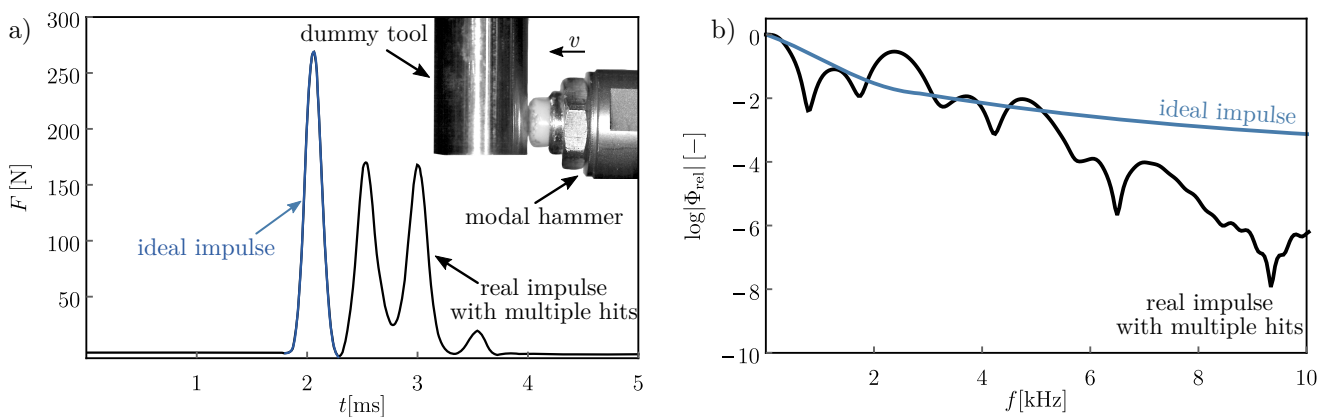


Figure 6.1: The a) phenomena of multiple-hitting during hammer excitation of a dummy tool and b) the comparison of the frequency spectra of ideal and real hammer excitation

6.1 Impulse excitation of high-speed rotating machine tools

In modal analysis, two main approaches can be distinguished: experimental and operational modal analysis. In case of experimental modal analysis, the calculation of the FRF is based on the direct measurements of both input and output signals during artificial excitation (e.g. impulse excitation with modal hammer). However, during operational modal analysis only the structural responses are measured, while the knowledge of the input is replaced by the assumption that the input is a realisation of a stochastic process [157, 158, 159, 160].

In the novel experimental modal approach provided by SIREN ERC research group at the Department of Applied Mechanics (siren.mm.bme.hu), the impulse excitation of the machine tool is provided by shots of spherical airsoft pellets using a custom-designed pneumatic gun [161]. The drawback of this technique is the lack of measurable excitation force (i.e. the input signal), which yields that the FRF of the investigated mechanical system cannot be obtained directly. However, on the relevant frequency domain, where the Fourier transform of the excitation (contact force) signal is mostly constant, the FRF is assumed to be identical to the fast Fourier transformation (FFT) of the output signal except for a constant multiplier. As the FRF of the machining system is discovered, its modal parameters (e.g. eigenfrequencies, damping factors) can also be calculated, which has key role in the prediction of stability of turning operations, milling operations, and other machining processes, where the self-excited vibrations are major problems limiting the productivity [162, 163, 164, 165, 166, 167, 168].

The relevant frequency range can be estimated based on the Fourier transform of the contact force signal, which can be obtained using FE simulations. The proper estimation of the contact characteristics (e.g. contact time, maximal force, dissipated energy) and the contact force signal requires the accurate constitutive modelling of the pellet materials including experimental work, constitutive modelling and FE simulations.

The numerical and experimental analysis of pellet impacts has been provided in several discussions in the literature. In the work of Gustafsson et al. the fracture properties of iron pellets are investigated using a strain-rate dependent fracture model [169]. The dynamic FE simulation of the impact of an elastic sphere using axisymmetric elements has also been proposed [170, 171]. At the same time the same problem was also investigated, assuming elastic-plastic properties for both the sphere and the half-space using semi-analytical methods [172, 173]. Jayadeep [174] also discussed the loss of kinetic energy and the variation of the coefficient of restitution in case of the adhesive impact of an elastic sphere and a rigid body. Additionally, there are also recent papers regarding the numerical methods with different contact formulations and algorithms such as dimensionality reduction and artificial neural networks in which the numerical solution of the sphere-plane contact problem also occurs, and its contact properties are investigated [175, 176, 177, 178, 179].

The dependence of the maximal contact force (F_{\max}) and the impact time (T_{imp}) on the impact velocity (v_0) during contact of an elastic sphere and rigid walls are also discussed [180, 181, 182]. This could be utilised for obtaining the necessary impact velocity to ensure the maximal impact force and the necessary relevant frequency bandwidth.

One of the main motivations of this chapter is to investigate the applicability of the pellet shot excitation. This goal requires the accurate mechanical modelling of the material response. The proposed technique is essential for the experimental investigation of high-speed machining, which would certainly help to understand better the dynamics of machine-tool vibrations.

6.2 Material characterisation

The investigated samples of the commercial airsoft pellet (Madbull Precision Ultimate Heavy Sniper BB) are spherical balls with diameter $d = 5.95 \pm 0.01$ mm and average mass $m = 0.43$ g (see Fig. 6.2). Regarding the material and the manufacturing of the pellet, there is limited information available, namely that the raw material is likely a polymer blend of high impact polystyrene (HIPS), while the pellets have undergone precision lapping and polishing processes.

6.2.1 Compression tests

Due to the lack of the raw material, the mechanical behaviour of the pellet can be investigated by mechanical compression tests performed on the pellet itself. Based on the experiences on the viscous-elastic-plastic behaviour of polymers, the same three-step compression tests were performed as in Section 5.2.2: uploading ($u_{\max} = 0.24$ mm, $T_1 = 14.3$ s), holding (relaxation) ($T_2 = 314.3$ s) and unloading ($T_3 = 318.3$ s). The tests were performed on Instron 3345 one-column testing system with Instron 2519-107 load cell with limit load of 5 kN. Due to its small range (see Fig. 6.2/a), the measured displacement values using the dedicated Instron extensometer were verified using high-resolution camera recordings and image detection, which showed perfect agreement. The measurement was performed on several specimens and a typical measured force-displacement ($F - u$) characteristics and the permanent deformation is presented in Fig. 6.2/a.

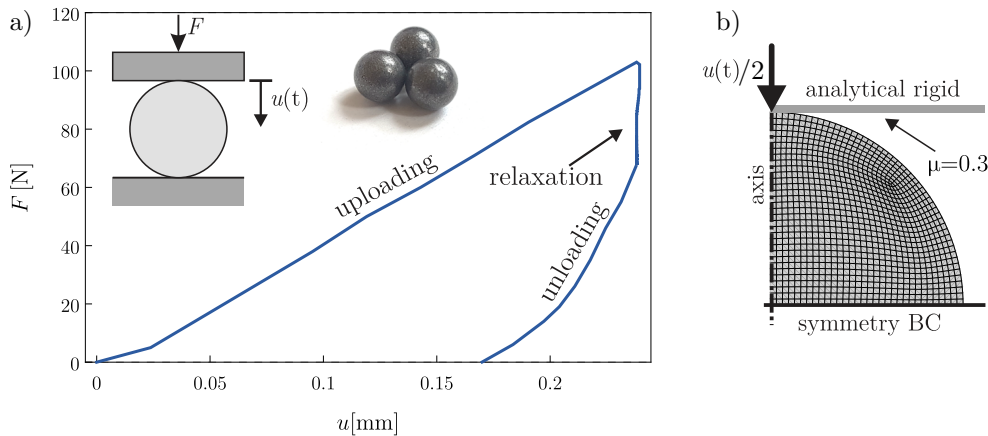


Figure 6.2: The a) measured force-displacement characteristics on the airsoft pellet and b) the applied FE model of the uniaxial compression test during the FE-based parameter fitting

6.2.2 Constitutive model and fitting

The measured force-displacement curve for this non-homogeneous stress state and complex geometry is qualitatively similar to the one measured for the microcellular foam material (see Fig. 5.5) for uniaxial homogeneous extension. Therefore, the material behaviour was modelled similarly: using the parallel viscoelastic-viscoplastic (the TLVP) constitutive model with nonlinear strain hardening power-law creeping in combination with linear isotropic hardening yield properties [SzB11],[SzB12] as discussed in Section 5.3.

Consequently, in this case, the parameter fitting strategy in Fig. 5.8 was adopted, where the comparison of the measurement data and the simulation results are evaluated using the *SSD* between the experimental and simulated data.

Due to symmetry, the geometry of the FE model during the iteration is an axisymmetric quarter model (see Fig. 6.2/b) meshed with eight-noded *CAX8* elements with full integration. The

friction coefficient between the wall and the pellet is set to $\mu = 0.3$ [183]. It is noted here, that the friction coefficient has a very minor effect on the force-displacement curve. The microstructure of the airsoft pellet is granular, thus the Poisson’s ratio is definitely lower than 0.5. As an approximation $\nu = 0.25$ was applied, which was kept constant during the fitting. However, its effect on the mechanical behaviour is negligible.

It should also be noted that in case of rate-dependent behaviour the material parameters are usually fitted to various measurement results at different loading rates, especially when such high rates like impacts occur. Due to the small size of the pellet and the limitations of the testing system, such measurements could not be performed with good accuracy. However, the viscoelastic-viscoplastic material parameters can also be fitted to relaxation test results as it is presented in several case studies in the literature [9, 98].

The accuracy of the fitted model is demonstrated in Fig. 6.3, whereas the obtained material parameters are collected in Table 6.1. The result shows that the proposed material model characterise the material behaviour with excellent accuracy [SzB11].

Table 6.1: The fitted material parameters of the airsoft pellet using the two-layer viscoplastic model

	Elastic		Viscous		Plastic
E [MPa]	2309.4	A [-]	0.00242	σ_y [MPa]	14.24 MPa
ν [-]	0.25	n [-]	0.48255	H [MPa]	45.7 MPa
f_e [-]	0.39943	m [-]	-0.55108		

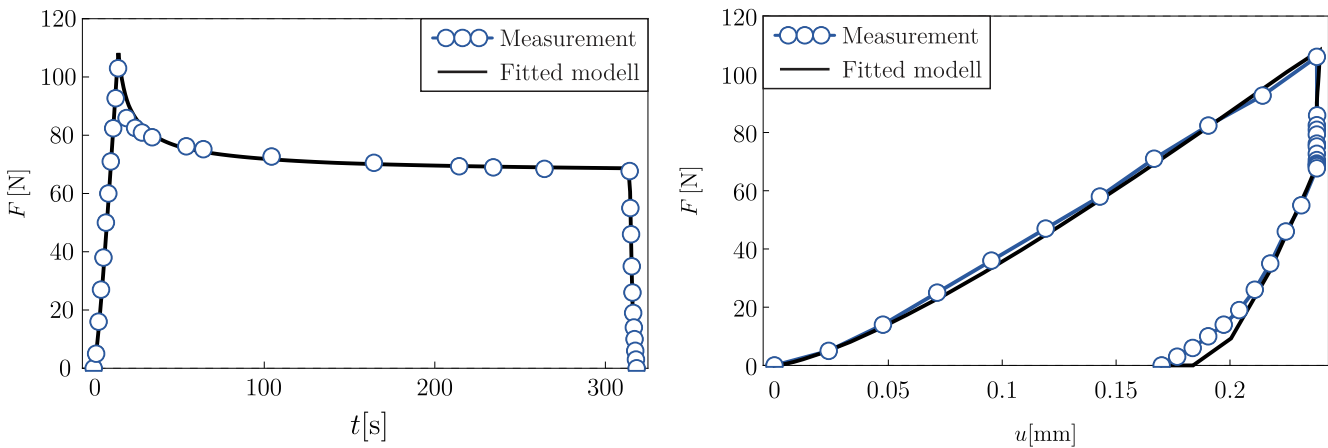


Figure 6.3: The comparison of the fitted TLVP model prediction and the measured a) force-time b) force-displacement characteristics

6.2.3 Elastic-plastic boundary models

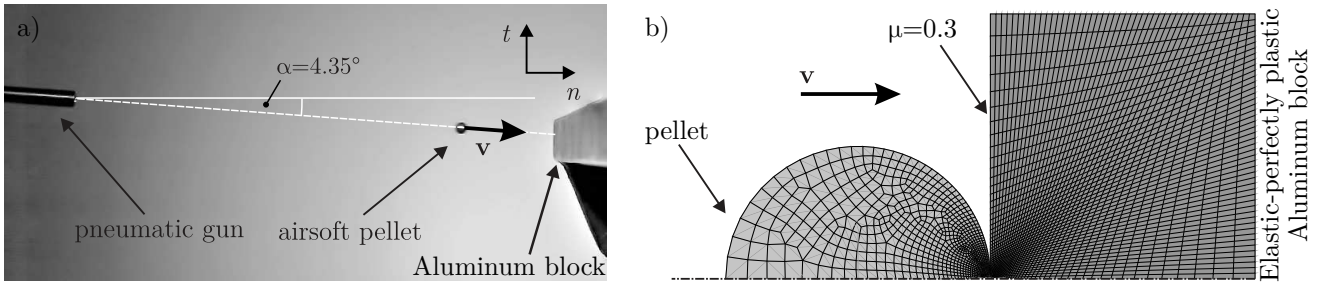
Having determined the model parameters, the dynamical simulation could be performed. Nevertheless, the proposed TLVP is not implemented for explicit solvers, whereas using implicit solver, non-realistic results were experienced regarding the behaviour of the viscous model. Therefore, the impact characteristics were approximated by the boundary elastic-plastic models substituting the nonlinear viscous element with its two extremes: instantaneous and long-term cases (see. Fig. 5.15 and (5.16)-(5.18)), letting the real material behaviour lay in between the prediction of implicit FE simulations using the instantaneous and long-term models, respectively. The obtained elastic-plastic material parameters of the airsoft pellet are listed in Table 6.2.

Table 6.2: The material parameters for the airsoft pellet using elastic-plastic boundary models

Instantaneous		Long-term	
E_{inst} [MPa]	2309.4	E_{long} [MPa]	1387.02
ν_{inst} [-]	0.25	ν_{long} [-]	0.25
$\sigma_{y\text{inst}}$ [MPa]	23.71	$\sigma_{y\text{long}}$ [MPa]	14.24
H_{inst} [MPa]	1659.72	H_{long} [MPa]	45.7

6.3 FE simulation of pellet impacts

After determining the material parameters of the airsoft pellet using the equivalent elastic-plastic model of the TLVP constitutive equation, the impact of the pellet can be investigated using FE simulations. The goal of the simulations is to obtain the contact force signal of the airsoft shots in order to estimate the frequency bandwidth where it ensures adequate excitation. Therefore, the impact process was investigated using Photron FASTCAM SA5 high-speed camera system with frame rate of 40000 fps, which is illustrated in Fig. 6.4/a.


Figure 6.4: The a) measurement layout of airsoft shooting using high-speed camera and b) the applied FE model for impact simulations

During the measurement the pellet was shot towards a heavy aluminum wall and its motion was detected using image processing algorithms, from which the velocity of the pellet before the impact in the coordinate system (n, t) was provided from one typical case, namely

$$\mathbf{v} = \begin{bmatrix} v_n \\ v_t \end{bmatrix} = \begin{bmatrix} 28.14 \\ 2.14 \end{bmatrix} \text{ m/s.} \quad (6.1)$$

6.3.1 FE model

The applied FE model (see. Fig. 6.4/b) is an axisymmetric model of the impact with structured mesh of **CAX8** elements. According to the fitted material parameters and the high-speed camera recordings, the stiffness of the airsoft pellet (HIPS with $\rho_{\text{HIPS}} = 3900 \text{ kg/m}^3$) and is small compared to the aluminum wall ($E_{\text{inst}} = 2.31 \text{ GPa}$ or $E_{\text{long}} = 1.38 \text{ GPa}$). However, according to the Hertz-theory [184, 185], the stresses at the contact point are infinite and thus, elastic-plastic deformation is assumed for the wall itself using elastic-perfectly plastic constitutive model. The corresponding material parameters are $\rho_{\text{Al}} = 2780 \text{ kg/m}^3$, $E_{\text{Al}} = 73.1 \text{ GPa}$, $\nu_{\text{Al}} = 0.33$ and $\sigma_{y\text{Al}} = 324 \text{ MPa}$ [144]. During the impulse excitation, only the amplitude of the contact force plays significant role, therefore the impact is considered to be oblique during the simulations with impact velocity of $|\mathbf{v}| = 28.22 \text{ m/s}$ according to (6.1). The friction between the bodies were modelled using a friction coefficient of $\mu = 0.3$ based on literature suggestion [183, 144].

6.3.2 Impact characteristics

As the result of the FE simulation of the pellet impact, the contact forces are provided for both the instantaneous and the long-term substitute models. Fig. 6.5/a shows the comparison of the two models regarding the contact force characteristics.

In the FE simulations, the impact was perfectly oblique, although a slight obliqueness that can be characterised by the angle α (as in Fig. 6.4), might affect on the contact force curves. Thus, further 3D FE simulations (complete geometry, structured mesh and C3D8R elements) were performed with different angles, namely $\alpha = 5^\circ, 10^\circ$ and 15° , using both the instantaneous and the long-term models. The comparison of the force-time functions (see Fig. 6.5/b-c) shows that obliqueness has a minor effect on the contact time and the contact force curve, thus the effect of obliqueness is neglected in further investigations and the axisymmetric model could be applied. Similarly, the effect of the friction coefficient of μ was also investigated, and its effect was also considered to be negligible.

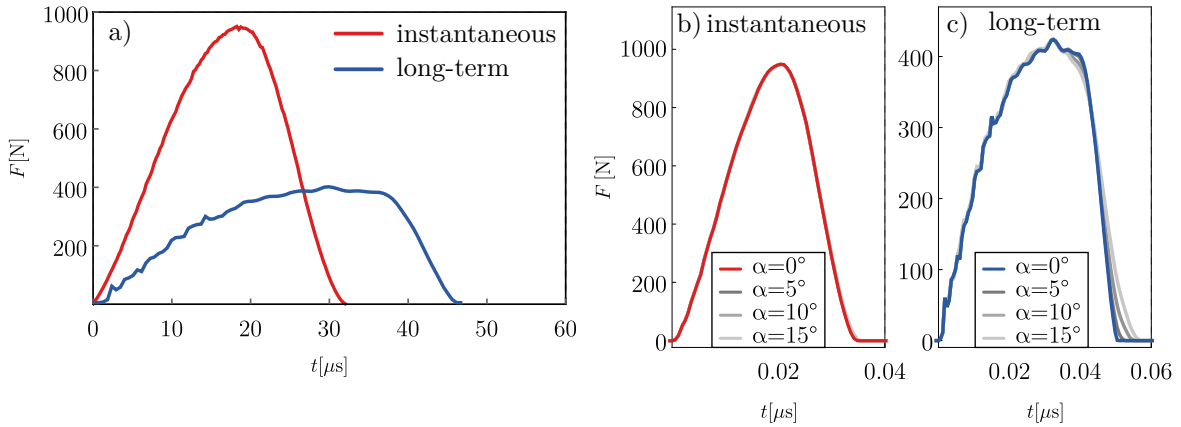


Figure 6.5: Comparison of the a) impact characteristics in case of instantaneous and long-term boundary elastic-plastic models and b)-c) the effect of obliqueness

6.3.3 Relevant excitation frequency bandwidth

The contact forces can also be compared by introducing the relevant force F_{rel} as

$$F_{rel}(t) = \frac{F(t)}{F_{\max}}. \quad (6.2)$$

Similarly let us introduce the relevant spectrum Φ_{rel} [SzB11] by

$$\Phi_{rel}(\omega) = \frac{|\Phi(\omega)|}{\max_{\omega \geq 0} |\Phi(\omega)|}, \quad (6.3)$$

where $\Phi(\omega) = \mathcal{F}(F(t))$ is the Fourier-transform of the force signal obtained by Fast Fourier Transform (FFT). Let us introduce, the relevant frequency ^{rel}f as the highest frequency f , for which

$$\log |\Phi_{rel}(\omega)| > -1.5, \quad (6.4)$$

holds for all $\omega \in [0, 2\pi f]$ [SzB11],[SzB12]. The force spectra and the estimated frequencies are summarised in Fig. 6.6 and Table 6.3.

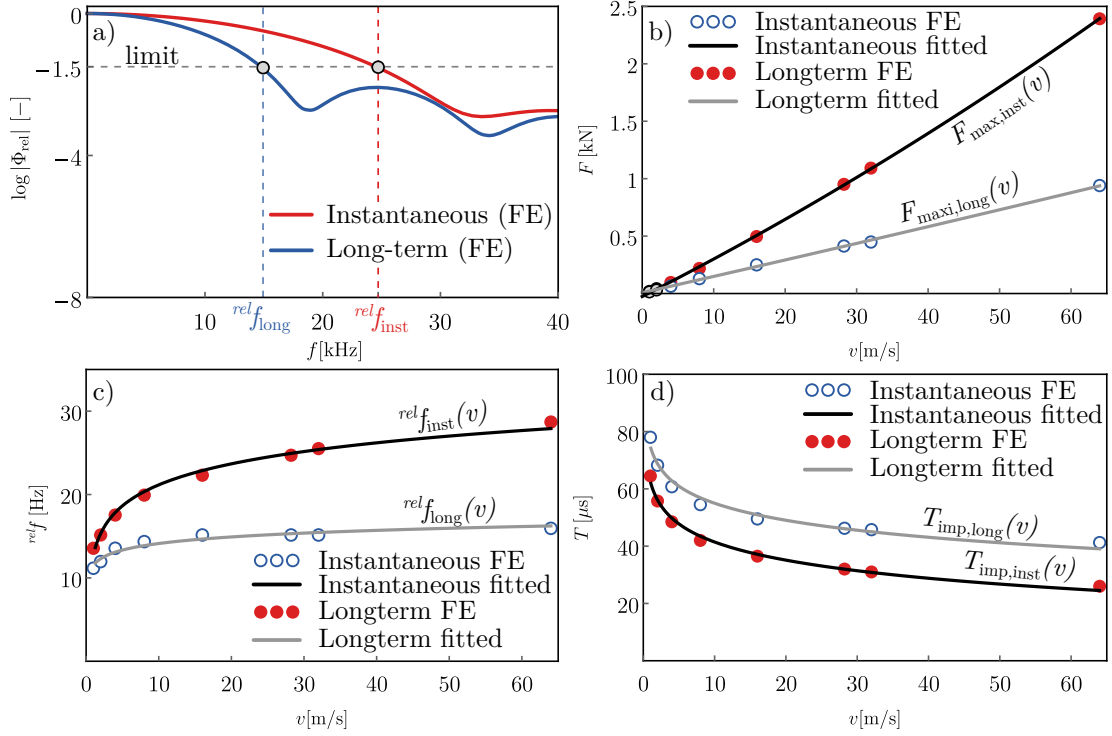


Figure 6.6: The a) estimated force spectra and the relevant frequencies using instantaneous and long-term models and the variation of b) maximal impact force, c) relevant frequency and d) impact time as a function of the impact velocity and the corresponding analytical functions.

The results show that the airsoft impact can be applied as impulse excitation for frequencies $f \leq 15.15 - 24.71$ kHz. However, by comparing the high-speed camera recordings (see Fig. 6.7) with the instantaneous 3D simulation results plotted on the high-speed camera recordings, only a slight difference is observed. This confirms that due to the high-speed impact the behaviour of the airsoft pellet can be approximated with the instantaneous elastic-plastic boundary model, thus $rel f_{\text{pellet}} = 24.71$ Hz.

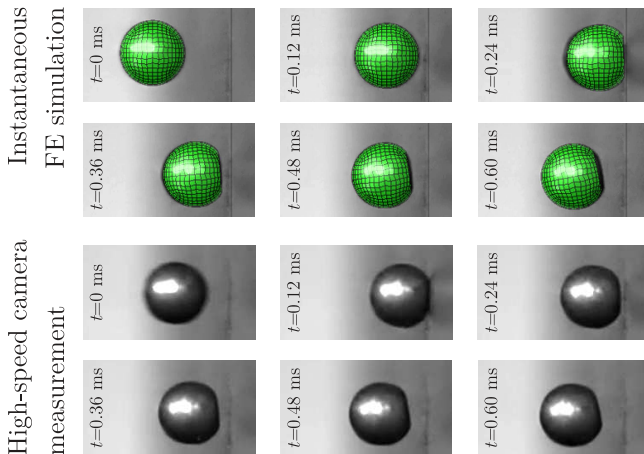


Figure 6.7: Comparison of high-speed camera recordings and the FE model prediction (plotted together with the camera recordings) using the instantaneous elastic-plastic boundary model

Table 6.3: The impact parameters using elastic-plastic boundary models

	Instantaneous	Long-term
F_{max} [N]	950.706	413.508
T_{imp} [μs]	32.013	42.625
$rel f$ [kHz]	24.71	15.15

6.3.4 Prediction of the contact characteristics

The relation of the contact characteristics and the velocity magnitude before the impact could help us to choose the adequate velocity to ensure the necessary relevant frequency range. Using the FE simulations of the pellet, the prediction of the maximal force (F_{\max}) and the time of impact (T_{imp}) were obtained for impact velocities of $v = 1, 2, 4, 8, 16, 32$ and 64 m/s [SzB12]. The resultant characteristics are presented in Fig. 6.6. After normalization with the measured reference value corresponding to $v = 28.22$ m/s the relations can be expressed using logarithmic and quadratic functions of

$$F_{\max}(v) = a_2 v^2 + a_1 v + a_0, \tag{6.5}$$

$$T_{\text{imp}}(v) = b_0 + b_1 \ln b_2 v, \tag{6.6}$$

$${}^{rel} f(v) = c_2 v + c_1 \sqrt{v} + c_0, \tag{6.7}$$

while the fitted parameters are listed in Table 6.4 [SzB12].

Table 6.4: The coefficients of the fitted closed-form functions characterizing the velocity-dependent impact parameters

Model	a_0	a_1	a_2	b_0	b_1	b_2	c_0	c_1	c_2
Instantaneous	-25.98	31.66	0.0964	85.49	-9.11	12.55	10.33	3.75	-0.185
Long-term	-7.18	14.11	0.0067	105.1	-8.56	34.66	10.02	1.72	-0.127

6.4 Experimental validation

In order to present the applicability and the benefits of the pellet shot excitation method, modal analyses were carried out on particular aluminum block (see Fig. 6.8/a). Beside the pellet shots, the impulse excitations were also performed using Modal Hammer 2302-10 with different tips (metal, polymer and rubber) and a B&K Type 8203 micro hammer with B&K 2647-A charge amplifier. During the modal hammer excitation, an additional mass was not used since its effect on the impact time is negligible compared to the type of different tips. As a response for the $F(t)$ input force excitation, the $a(t)$ accelerations were recorded at three different locations of the workpieces using PCB 352C23 accelerometers and National Instruments data acquisition system NI cDAQ-9178 with NI 9234 module with sampling rate of 51 kHz. During the measurement no additional filtering was applied except for the natural high-pass filter of the accelerometer with cut-off frequency $f_c \approx 2$ Hz.

The investigated workpiece is an aluminum (AL2024-T351) block with size of $180 \times 80 \times 40$ mm. The workpiece was hanged on rubber stripes, thus the vibration can be approximated as constraint-free. The measurement layout of the aluminum workpiece is illustrated in Fig. 6.8. In addition to the different hammers, the excitation was also performed in point E (see Fig. 6.8) using the previously introduced airsoft pellet.

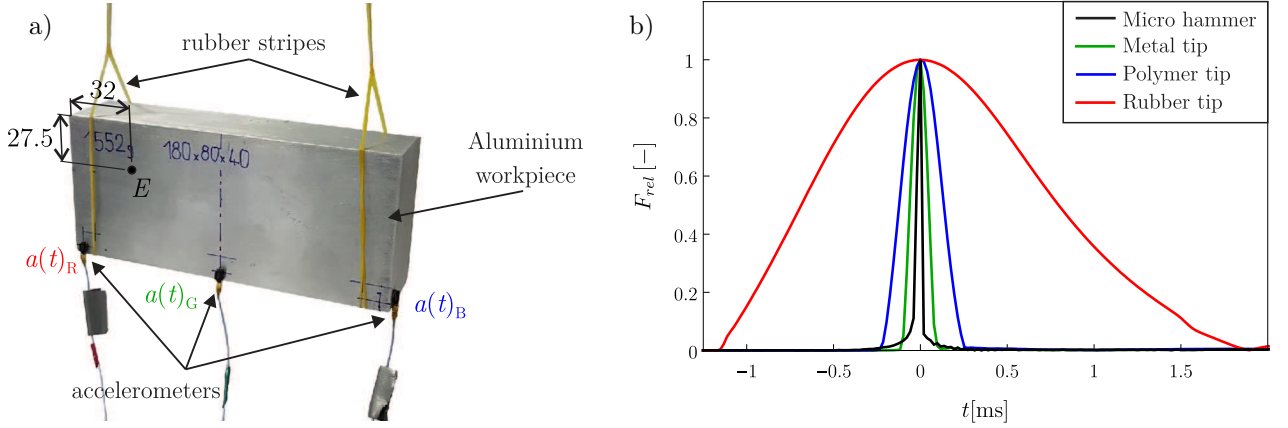


Figure 6.8: The measurement layout and positions of PCB accelerometers and the location of the excitation point E in case of modal analysis of aluminum workpiece; and b) the comparison of the relative force spectra and the estimated relevant frequency ranges for different modal hammers

6.4.1 Experimental results

The different hammer excitation methods are compared by the F_{rel} relevant force and Φ_{rel} relevant spectra, which are presented in Fig. 6.9.

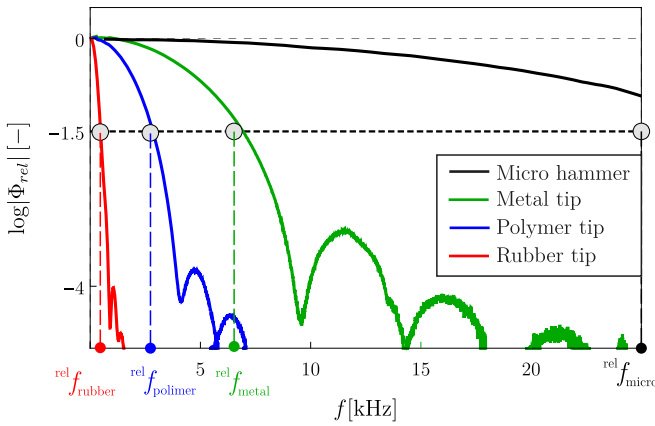


Figure 6.9: Comparison of the Φ_{rel} relevant force spectra and the estimated relevant frequency ranges for different modal hammer tips

Table 6.5: The maximal forces and the estimated relevant frequencies using impulse force signals and the FE prediction of the airsoft impact in case of aluminum workpiece

Excitation	F_{max} [N]	$rel f$ [kHz]
Rubber tip	121.66	0.45
Polymer tip	404.54	2.71
Metal tip	390.29	6.52
Micro hammer	144.36	25
Pellet (inst.)	950.706	24.71

Based on the relevant spectra, the $rel f$ relevant frequencies can be estimated using the condition in (6.4). The maximal forces and the relevant frequencies are listed in Table 6.5. Note, that by decreasing the time of impact the $rel f$ increases. In case of the rubber and the polymer hammers, where the time of impact is larger (see Fig. 6.10), noisy signals are expected at high frequencies. Additionally, the FRF of the workpiece between the excitation point E and sensing points R-G-B can be obtained formally as

$$FRF(\omega) = \frac{\alpha(\omega)}{\Phi(\omega)}. \quad (6.8)$$

The comparison of the FFT of the acceleration signals $\alpha(\omega) = \mathcal{F}(a(t))$ and the calculated FRF of the aluminum workpiece is presented in Fig. 6.10, where the red, green and blue lines represent the FFT and the FRF of the different accelerometers.

The results show that the airsoft pellet shots provide smoother signals even at high-frequency range and all the peaks corresponding to the natural frequencies are well-detectable. Moreover, the estimation for the relevant frequencies illustrated with green shaded domain in Fig. 6.10 show good correspondence with the frequencies presented in Table 6.5. Above this frequency domain, the noise level increases significantly, especially in case of the rubber and the polymer hammers due to insufficient excitation (e.g. long impact time and small relevant frequency). It should be noted that the micro-hammer is designed for excitation of high-frequencies, therefore some noise at lower frequencies might occur.

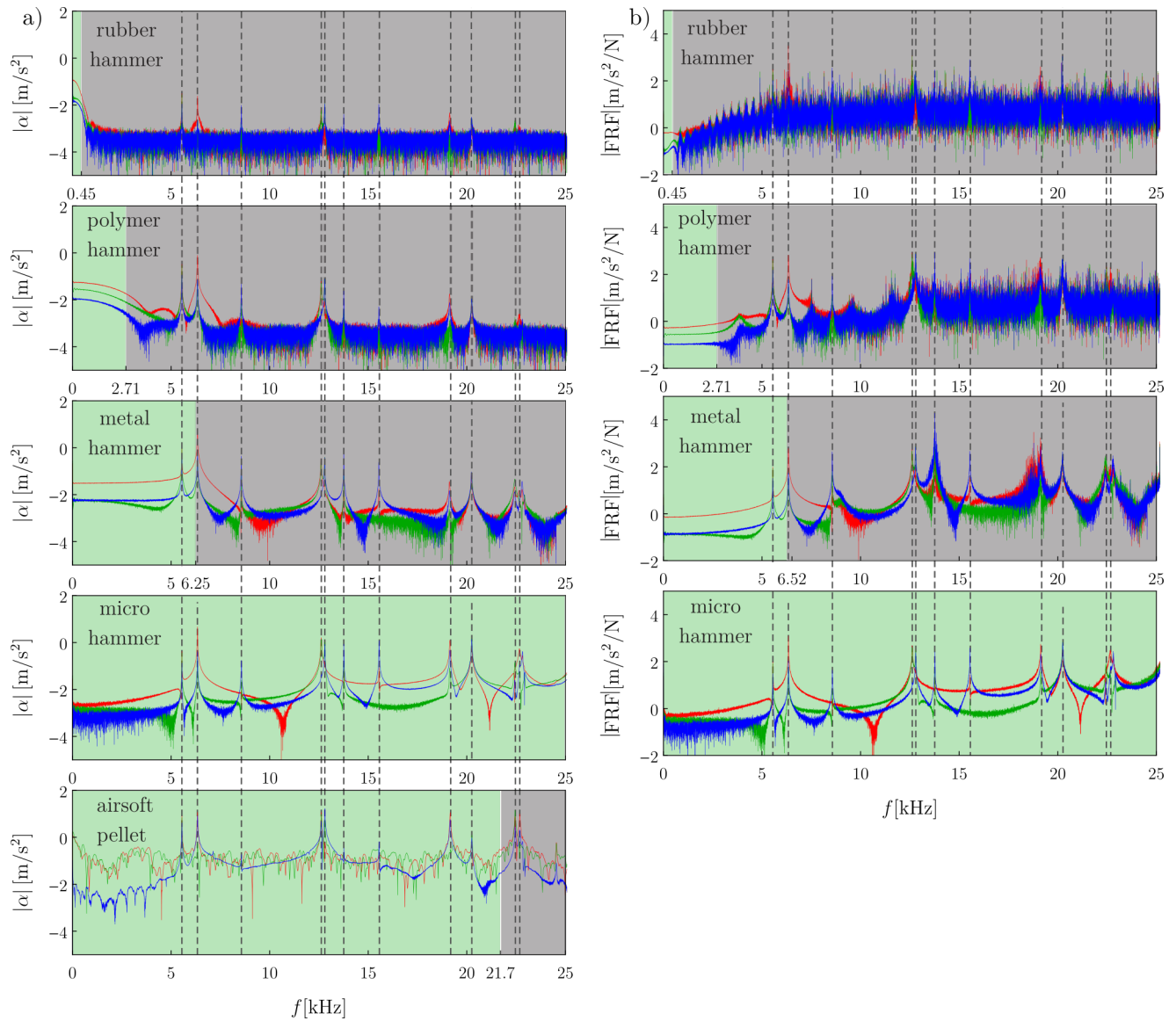


Figure 6.10: The comparison of a) $\alpha(\omega)$, the FFT of the acceleration signals (red, green and blue) and b) the calculated FRF for different types of modal hammers

6.4.2 Modal parameters

The goal of the modal analysis is to determine the modal parameters of the workpieces, namely the natural frequencies (f_N) and the damping-factors (D_N). A widely-applied method is the so-called 3 dB method, from which the parameters can be calculated directly from the FRF if there are separated peaks. In this case the modal parameters were determined from the FRF of the micro

hammer and the FFT of airsoft pellet (see Fig. 6.10) and additionally the natural frequencies are also compared with FE calculations of the natural frequencies. The mean values of the parameters (\bar{f}_N and \bar{D}_N) are determined from 5 measurements. Tables 6.6 and 6.7 present the mean values, their variance and the error between the micro hammer and the airsoft excitation. The eigenmodes of the corresponding natural frequencies are also obtained using FE simulation of the workpiece, which are presented in Fig. 6.11. It should be noted that some of the eigenfrequencies and corresponding damping factors could not be detected since the accelerometers might have been placed at nodes or the direction of the excitation was perpendicular to the corresponding mode, so some peaks could not be identified. Despite measuring the accelerations in multiple directions, the hammer excitation cannot excite all of the mode shapes if they have no displacement in the direction of excitation (see, for example the 6th mode in Fig. 6.11 and Tables 6.6 and 6.7).

Table 6.6: The obtained natural frequencies (f_N) of the aluminum workpiece using micro hammer excitation and airsoft pellet shot

N	FEA	Airsoft pellet		Micro hammer		δ_{abs} [Hz]
	f_N [Hz]	\bar{f}_N [Hz]	$\text{Var}(f_N)$ [Hz]	\bar{f}_N [Hz]	$\text{Var}(f_N)$ [Hz]	
1	5532	5549	0.00	5550	0.00	0.93
2	6322	6343	0.18	6343	0.02	0.27
3	8616	8616	0.21	8570	0.35	45.73
4	12608	12622	1.11	12623	0.55	0.59
5	12654	12803	0.22	12802	0.86	0.72
6	13860	No data		13773.3	0.06	-
7	15502	15551	0.15	15553	4.66	1.73
8	19040	19157	0.17	19146	0.04	10.37
9	19934	20257	3.46	20255	0.77	2.20

Table 6.7: The obtained damping factors (D_N) of the aluminum workpiece using micro hammer excitation and airsoft pellet shot

N	Airsoft pellet		Micro hammer		δ_{rel} [-]
	\bar{D}_N [-]	$\text{Var}(D_N)$ [-]	\bar{D}_N [-]	$\text{Var}(D_N)$ [-]	
1	0.000526	6.61E-12	0.000316	2.51E-10	39.99%
2	0.001111	1.10E-09	0.000432	4.11E-09	61.09%
3	0.002311	1.48E-05	0.000483	2.58E-09	79.12%
4	0.000618	3.81E-11	0.000691	9.47E-09	11.72%
5	0.000628	8.80E-10	0.000439	5.58E-09	30.06%
6	No data		0.000158	1.79E-10	-
7	0.000270	1.78E-10	0.000243	2.87E-09	9.85%
8	0.000571	1.17E-11	0.000556	9.16E-11	2.49%
9	0.000490	5.02E-10	0.000360	1.95E-09	26.62%

The results show that using the airsoft excitation, modal parameters can be obtained with good accuracy, especially the natural frequencies. The variance of the measurements also indicates that the airsoft method has good repeatability.

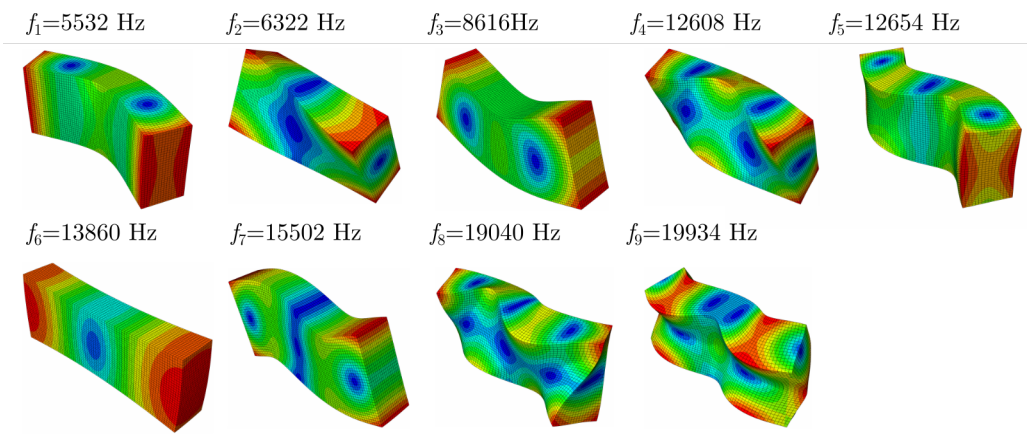


Figure 6.11: The first 9 eigenmodes of the aluminum workpiece

6.5 Main results

I have investigated the material behaviour of airsoft pellets using quasi-static experimental work and I have revealed that the material shows viscous-elastic-plastic properties. For the explicit dynamic simulation of pellet impacts I have introduced the elastic-plastic boundary models corresponding to instantaneous and long-term loadings. For the validation of the material model I have performed high-speed camera measurements and a case study of impulse excitation. By comparing the performance of the airsoft pellet impact with modal hammer excitations, I have drawn the following conclusions.

Thesis statement 6

During the impact of polymer airsoft pellets applied for impulse excitation, the mechanical behaviour exhibits viscous-elastic-plastic properties, which can effectively be modelled by the parallel viscoelastic-viscoplastic constitutive model. The contact characteristics can be determined by explicit dynamic finite element simulations using the elastic-plastic boundary models of the constitutive equation, corresponding to the instantaneous and long-term limit cases. The applicability limit of the airsoft pellet as an impulse excitation can be determined by the relevant frequency ${}^{rel}f$ introduced as the highest frequency f , for which

$$\log |\Phi_{rel}(\omega)| > -1.5,$$

holds for all $\omega \in [0, 2\pi f]$, in which

$$\Phi_{rel}(\omega) = \frac{|\Phi(\omega)|}{\max_{\omega \geq 0} |\Phi(\omega)|},$$

is the impact force spectra. This method ensured optimal excitation up to 24 kHz for HIPS pellet, which is significantly better than the limit of classical modal hammer excitation with rubber, polymer or metal hammer tips. By increasing the impact speed v , the relevant frequency bandwidth shows monotonously increasing characteristic according to

$${}^{rel}f(v) = c_2 v + c_1 \sqrt{v} + c_0,$$

where constants c_0 , c_1 and c_2 can be determined experimentally for different pellets.

Related publications: [\[SzB11\]](#), [\[SzB12\]](#), [\[SzB13\]](#), [\[SzB14\]](#)

Appendix



Linearization of Hyperfoam model and its relation to Hooke's law

The parameters in the Ogden–Hill's compressible hyperelastic (Hyperfoam) material model cannot be chosen freely, because certain physical conditions have to be satisfied during the parameter fitting process. One of these conditions states that the linearised form of the nonlinear material model should be equal with the Hooke's law in case of small strains. The linearisation is performed around the undeformed state, i.e. when $\lambda_i = 1$. Firstly, let us introduce a modified stretch-measure (λ_i^*) [71, 18] as

$$\lambda_i^* = \lambda_i J^{-1/3}. \quad (\text{A.1})$$

Based on this stretch-measure, the originally applied strain energy function $W(\lambda_1, \lambda_2, \lambda_3)$ can be rewritten as

$$W(\lambda_1, \lambda_2, \lambda_3) = W^*(\lambda_1^*, \lambda_2^*, \lambda_3^*, J), \quad (\text{A.2})$$

where λ_3^* can be expressed as the function of λ_1^* and λ_2^* using the relation $\lambda_3^* = (\lambda_1^* \lambda_2^*)^{-1}$. Substituting this into (A.2) the simplified strain energy function \hat{W}^* becomes

$$\hat{W}^*(\lambda_1^*, \lambda_2^*, J) = W^*(\lambda_1^*, \lambda_2^*, (\lambda_1^* \lambda_2^*)^{-1}, J). \quad (\text{A.3})$$

Based on this formulation, the initial moduli of the material model can be related to the partial derivatives of the strain energy function in (A.3), which are evaluated at the undeformed state, i.e. $\lambda_1^* = 1, \lambda_2^* = 1$ and $J = 1$ [71, 18]. Thus

$$K_0 = \frac{\partial^2 \hat{W}^*}{\partial J^2}(1, 1, 1), \quad (\text{A.4})$$

$$\mu_0 = \frac{\partial^2 \hat{W}^*}{\partial \lambda_1^{*2}}(1, 1, 1) = \frac{\partial^2 \hat{W}^*}{\partial \lambda_2^{*2}}(1, 1, 1) = 2 \frac{\partial^2 \hat{W}^*}{\partial \lambda_1^* \partial \lambda_2^*}(1, 1, 1), \quad (\text{A.5})$$

where K_0 is the initial bulk modulus and μ_0 the initial shear modulus.

APPENDIX A. LINEARIZATION OF HYPERFOAM MODEL AND ITS RELATION TO HOOKE'S LAW

In the Ogden–Hill's hyperelastic constitutive equation according to the ABAQUS [15] formulation the corresponding strain energy function can be written as

$$W = \sum_{i=1}^N \frac{2\mu_i}{\alpha_i^2} \left(\lambda_1^{\alpha_i} + \lambda_2^{\alpha_i} + \lambda_3^{\alpha_i} - 3 + \frac{1}{\beta_i} (J^{-\alpha_i\beta_i} - 1) \right), \quad (\text{A.6})$$

which, after substituting the relations in (A.1) back, leads that the \hat{W}^* function becomes

$$\hat{W}^*(\lambda_1^*, \lambda_2^*, J) = \sum_{i=1}^N \frac{2\mu_i}{\alpha_i^2} \left((\lambda_1^* J^{1/3})^{\alpha_i} + (\lambda_2^* J^{1/3})^{\alpha_i} + \left(\frac{J^{1/3}}{\lambda_1^* \lambda_2^*} \right)^{\alpha_i} - 3 + \frac{1}{\beta_i} (J^{-\alpha_i\beta_i} - 1) \right). \quad (\text{A.7})$$

After expressing and evaluating the partial derivatives in (A.4) and (A.5), the initial moduli can be expressed as

$$\mu_0 = \sum_{i=1}^N \mu_i, \quad \text{and} \quad K_0 = \sum_{i=1}^N 2\mu_i \left(\frac{1}{3} \beta_i \right). \quad (\text{A.8})$$

In the Hooke's law the conditions for the shear and the bulk moduli are $\mu_0 > 0$ and $K > 0$, respectively. Using the derived expressions in (A.8) leads that

$$\mu_0 = \sum_{i=1}^N \mu_i > 0, \quad K = \sum_{i=1}^N 2\mu_i \left(\frac{1}{3} + \beta_i \right) > 0, \quad (\text{A.9})$$

from which the conditions of the material parameters in the Ogden–Hill's Hyperfoam material model becomes

$$\sum_{i=1}^N \mu_i > 0, \quad \beta_i > -\frac{1}{3}. \quad (\text{A.10})$$

It should be noted that the condition $\beta_i > -1/3$ is stricter than the necessary condition for the β_i parameters, which significantly limits the possible domain of parameters. Although, this condition is applied in the literature and in ABAQUS as well [15].

B

Incomplete Gamma-function

The following summary of the upper incomplete gamma function $\Gamma(\nu, x)$, which occurred in the calculations, is based on Spanier and Oldham: An atlas of functions [105] and the documentations provided by [106].

B.1 The (complete) gamma function

The (complete) gamma function $\Gamma(n)$ is defined to be an extension of the factorial to complex and real number arguments, which is related to the factorial in case of natural numbers as

$$\Gamma(n) = (n - 1)!. \quad (\text{B.1})$$

Generally, the (complete) gamma function is defined as a definite integral for all $\text{Re}(z) > 0$. A possible formulation of this function is called as Euler's integral form, in which

$$\Gamma(z) = \int_0^{\infty} t^{z-1} e^{-t} dt, \quad (\text{B.2})$$

which can be alternatively given as

$$\Gamma(z) = \int_0^1 \left[\ln \left(\frac{1}{t} \right) \right]^{z-1} dt. \quad (\text{B.3})$$

The complete gamma function can be further generalized using the so-called incomplete gamma functions, which by definition satisfy

$$\Gamma(\nu) = \Gamma(\nu, x) + \gamma(\nu, x), \quad (\text{B.4})$$

where $\Gamma(\nu, x)$ is the so-called upper incomplete gamma function and $\gamma(\nu, x)$ the lower incomplete gamma function. The functions contain two variables: ν is called as the parameter, while x is the argument in both incomplete gamma functions. The adjective “incomplete” reflects the restricted ranges of the definite integral compared to the complete gamma function in (B.2). The adjectives “upper” and “lower” specifies that the particular incomplete gamma function is defined on which range of the $x > 0$ domain.

B.2 The upper incomplete gamma function

The upper incomplete gamma function is defined via an improper integral as

$$\Gamma(\nu, x) = \int_x^\infty t^{\nu-1} e^{-t} dt, \quad (\text{B.5})$$

for all $\text{Re}(\nu) > 0$ and $x > 0$. Using the above introduced notation, the (complete) gamma function $\Gamma(\nu)$ can be related to the upper incomplete gamma function as

$$\Gamma(\nu) = \Gamma(\nu, 0). \quad (\text{B.6})$$

When the parameter (ν) is a natural number, then the function can also be expressed using the exponential sum as

$$\Gamma(n, x) = (n-1)! e^{-x} \sum_{k=0}^{n-1} \frac{x^k}{k!}. \quad (\text{B.7})$$

The definition of the function in (B.5) can be extended to $\text{Re}(z) < 0$ by utilizing the recursion formula. Therefore

$$\Gamma(\nu, x) = \frac{x^\nu e^{-x}}{\Gamma(1-\nu)} \int_0^\infty \frac{t^{-\nu} e^{-t}}{t+x} dt. \quad (\text{B.8})$$

B.3 Special cases

For some special values of ν and x , the upper incomplete gamma function reduces to other well-known functions, like

$$\Gamma\left(\frac{1}{2}, x\right) = \sqrt{\pi} \text{erfc}(\sqrt{x}), \quad (\text{B.9})$$

where $\text{erfc}(x)$ denotes the complementer Gauss error function, or

$$\Gamma(0, x) = \begin{cases} -\text{Ei}(-x) - i\pi, & \text{if } x < 0 \\ -\text{Ei}(-x), & \text{if } x > 0 \end{cases}. \quad (\text{B.10})$$

where $\text{Ei}(x)$ is the so-called exponential integral function. Furthermore

$$\Gamma(\nu + 1, x) = \nu \Gamma(\nu, x) + x^\nu e^{-x}. \quad (\text{B.11})$$

C

Numerical integration scheme for finite strain viscoelastic model

The following derivation steps are the summary the detailed derivation available in the Theory Guide of ABAQUS [15]. Based on the definition of the visco-hyperelastic constitutive equation in ABAQUS, the Kirchhoff stress solutions can be obtained as

$$\boldsymbol{\tau}^D(t) = \boldsymbol{\tau}_0^D(t) - \text{SYM} \left[\sum_{k=1}^P \frac{g_k}{\tau_k} \int_0^t \mathbf{F}_t^{-1}(t-s) \boldsymbol{\tau}_0^D(t-s) \mathbf{F}_t(t-s) \exp \left[\frac{-s}{\tau_k} \right] ds \right], \quad (\text{C.1})$$

$$\boldsymbol{\tau}^H(t) = \boldsymbol{\tau}_0^H(t) - \sum_{k=1}^P \frac{g_k}{\tau_k} \int_0^t \boldsymbol{\tau}_0^H(t-s) \exp \left[\frac{-s}{\tau_k} \right] ds, \quad (\text{C.2})$$

where $\boldsymbol{\tau}^D(t)$ is the deviatoric and $\boldsymbol{\tau}^H(t)$ the hydrostatic part of the Kirchhoff stress tensor ($\boldsymbol{\tau}$). Let us introduce the so-called internal stresses, associated with each term of the series

$$\boldsymbol{\tau}_k^D(t) = \text{SYM} \left[\frac{g_k}{\tau_k} \int_0^t \mathbf{F}_t^{-1}(t-s) \boldsymbol{\tau}_0^D(t-s) \mathbf{F}_t(t-s) \exp \left[\frac{-s}{\tau_k} \right] ds \right], \quad (\text{C.3})$$

$$\boldsymbol{\tau}_k^H(t) = \frac{g_k}{\tau_k} \int_0^t \boldsymbol{\tau}_0^H(t-s) \exp \left[\frac{-s}{\tau_k} \right] ds. \quad (\text{C.4})$$

The above introduced stresses are stored in each material point and integrated forward in time. Let us assume, that the stress solution at time t is known and the solution at time $t + \Delta t$ should be defined. The numerical integration of the convolution integrals in (C.1) and (C.2) are performed separately for the deviatoric and the hydrostatic parts.

C.1 Integration of the hydrostatic stress

The internal hydrostatic stress values at time $t + \Delta t$ can be obtained from

$$\boldsymbol{\tau}_k^H(t + \Delta t) = \frac{g_k}{\tau_k} \int_0^{t+\Delta t} \boldsymbol{\tau}_0^H(t + \Delta t - s) \exp \left[\frac{-s}{\tau_k} \right] ds. \quad (\text{C.5})$$

Introducing $\hat{t} = s - \Delta t$ it follows that

$$\boldsymbol{\tau}_k^H(t + \Delta t) = \frac{g_k}{\tau_k} \exp\left[\frac{-\Delta t}{\tau_k}\right] \int_{-\Delta t}^0 \boldsymbol{\tau}_0^H(t - \hat{t}) \exp\left[\frac{-\hat{t}}{\tau_k}\right] d\hat{t} + \exp\left[\frac{-\Delta t}{\tau_k}\right] \boldsymbol{\tau}_k^H(t) \quad (\text{C.6})$$

To perform the integral, assume that $\boldsymbol{\tau}_0^H(t - \hat{t})$ is a linear function over the increment, therefore

$$\boldsymbol{\tau}_0^H(t - \hat{t}) = \left(1 + \frac{\hat{t}}{\tau_k}\right) \boldsymbol{\tau}_0^H(t) - \frac{\hat{t}}{\tau_k} \boldsymbol{\tau}_0^H(t + \Delta t), \quad -\Delta t \leq \hat{t} \leq 0. \quad (\text{C.7})$$

Substitution back into (C.6) yields

$$\begin{aligned} \boldsymbol{\tau}_k^H(t + \Delta t) &= \frac{g_k}{\tau_k} \exp\left[\frac{-\Delta t}{\tau_k}\right] \int_{-\Delta t}^0 \left[\left(1 + \frac{\hat{t}}{\tau_k}\right) \boldsymbol{\tau}_0^H(t) - \frac{\hat{t}}{\tau_k} \boldsymbol{\tau}_0^H(t + \Delta t) \right] \exp\left[\frac{-\hat{t}}{\tau_k}\right] d\hat{t} \\ &\quad + \exp\left[\frac{-\Delta t}{\tau_k}\right] \boldsymbol{\tau}_k^H(t). \end{aligned} \quad (\text{C.8})$$

After expressing the integrals, the solution at the end of the increment becomes

$$\begin{aligned} \boldsymbol{\tau}_k^H(t + \Delta t) &= \left[1 - \frac{\tau_k}{\Delta t} \left(1 - \exp\left[\frac{-\Delta t}{\tau_k}\right] \right) \right] g_k \boldsymbol{\tau}_0^H(t + \Delta t) + \\ &\quad \left[\frac{\tau_k}{\Delta t} \left(1 - \exp\left[\frac{-\Delta t}{\tau_k}\right] \right) - \exp\left[\frac{-\Delta t}{\tau_k}\right] \right] g_k \boldsymbol{\tau}_0^H(t) + \exp\left[\frac{-\Delta t}{\tau_k}\right] \boldsymbol{\tau}_k^H(t), \end{aligned} \quad (\text{C.9})$$

which can be written in a simplified form as

$$\boldsymbol{\tau}_k^H(t + \Delta t) = a_i g_k \boldsymbol{\tau}_0^H(t + \Delta t) + b_i g_k \boldsymbol{\tau}_0^H(t) + c_i \boldsymbol{\tau}_k^H(t), \quad (\text{C.10})$$

where

$$a_i = 1 - \frac{\tau_k}{\Delta t} (1 - c_i); \quad b_i = \frac{\tau_k}{\Delta t} (1 - c_i) - c_i; \quad c_i = \exp\left[\frac{-\Delta t}{\tau_k}\right]. \quad (\text{C.11})$$

C.2 Integration of the deviatoric stress

The internal deviatoric stress values at time $t + \Delta t$ can be obtained from

$$\boldsymbol{\tau}_k^D(t + \Delta t) = \text{SYM} \left[\frac{g_k}{\tau_k} \int_0^{t+\Delta t} \mathbf{F}_{t+\Delta t}^{-1}(t + \Delta t - s) \boldsymbol{\tau}_0^D(t + \Delta t - s) \mathbf{F}_{t+\Delta t}(t + \Delta t - s) \exp\left[\frac{-s}{\tau_k}\right] ds \right]. \quad (\text{C.12})$$

Where the push-back operator related between time t and $t + \Delta t$ becomes

$$\mathbf{F}_{t+\Delta t}(t - s) = \mathbf{F}_t(t - s) \mathbf{F}_{t+\Delta t}(s). \quad (\text{C.13})$$

Introducing $\hat{t} = s - \Delta t$, $\Delta \mathbf{F} = \mathbf{F}_t(t + \Delta t)$ and a new variable $\hat{\boldsymbol{\tau}}^D$ for which

$$\hat{\boldsymbol{\tau}}_0^D(t) = \text{SYM} \left[\Delta \mathbf{F} \boldsymbol{\tau}_0^D(t) \Delta \mathbf{F}^{-1} \right], \quad (\text{C.14})$$

$$\hat{\boldsymbol{\tau}}_0^D(t + \Delta t) = \boldsymbol{\tau}_0^D(t + \Delta t), \quad (\text{C.15})$$

$$\hat{\boldsymbol{\tau}}_k^D(t) = \text{SYM} \left[\Delta \mathbf{F} \boldsymbol{\tau}_k^D(t) \Delta \mathbf{F}^{-1} \right], \quad (\text{C.16})$$

relation hold, the integral simplifies to

$$\boldsymbol{\tau}_k^D(t + \Delta t) = \frac{g_k}{\tau_k} \exp\left[\frac{-\Delta t}{\tau_k}\right] \int_{-\Delta t}^0 \hat{\boldsymbol{\tau}}_0^D(t - \hat{t}) \exp\left[\frac{-\hat{t}}{\tau_k}\right] d\hat{t} + \exp\left[\frac{-\Delta t}{\tau_k}\right] \hat{\boldsymbol{\tau}}_k^D(t). \quad (\text{C.17})$$

To perform the integral, assume that $\hat{\boldsymbol{\tau}}_0^D(t - \hat{t})$ is a linear function over the increment, therefore

$$\boldsymbol{\tau}_0^D(t - \hat{t}) = \left(1 + \frac{\hat{t}}{\tau_k}\right) \hat{\boldsymbol{\tau}}_0^D(t) - \frac{\hat{t}}{\tau_k} \hat{\boldsymbol{\tau}}_0^D(t + \Delta t), \quad -\Delta t \leq \hat{t} \leq 0. \quad (\text{C.18})$$

Substituting back into (C.17), and performing the integration, exactly the same form of the stress solution as in (C.10) and (C.11) is given, thus

$$\boldsymbol{\tau}_k^D(t + \Delta t) = a_i g_k \boldsymbol{\tau}_0^D(t + \Delta t) + b_i g_k \hat{\boldsymbol{\tau}}_0^D(t) + c_i \hat{\boldsymbol{\tau}}_k^D(t), \quad (\text{C.19})$$

where

$$a_i = 1 - \frac{\tau_k}{\Delta t}(1 - c_i); \quad b_i = \frac{\tau_k}{\Delta t}(1 - c_i) - c_i, \quad c_i = \exp\left[\frac{-\Delta t}{\tau_k}\right]. \quad (\text{C.20})$$

C.3 Total stress solution

From the previously derived hydrostatic and deviatoric internal stress solutions in (C.10) and (C.19), respectively, the total stress at time $t + \Delta t$ can be expressed as

$$\boldsymbol{\tau}(t + \Delta t) = \boldsymbol{\tau}_0(t - s) - \sum_{k=1}^P \boldsymbol{\tau}_k^D(t + \Delta t) - \sum_{k=1}^P \boldsymbol{\tau}_k^H(t + \Delta t) \quad (\text{C.21})$$

which with equations (C.10) and (C.19) can also be written as

$$\begin{aligned} \boldsymbol{\tau}(t + \Delta t) = & \left(1 - \sum_{k=1}^P a_i g_k\right) \boldsymbol{\tau}_0^D(t + \Delta t) + \sum_{k=1}^P b_i g_k \hat{\boldsymbol{\tau}}_0^D(t) + \sum_{k=1}^P c_i \hat{\boldsymbol{\tau}}_k^D(t) + \\ & \left(1 - \sum_{k=1}^P a_i g_k\right) \boldsymbol{\tau}_0^H(t + \Delta t) + \sum_{k=1}^P b_i g_k \boldsymbol{\tau}_0^H(t) + \sum_{k=1}^P c_i \boldsymbol{\tau}_k^H(t), \end{aligned} \quad (\text{C.22})$$

with

$$a_i = 1 - \frac{\tau_k}{\Delta t}(1 - c_i), \quad b_i = \frac{\tau_k}{\Delta t}(1 - c_i) - c_i, \quad c_i = \exp\left[\frac{-\Delta t}{\tau_k}\right]. \quad (\text{C.23})$$

D

Biaxial compression fixture

During the mechanical tests of closed-cell polymer foams in Chapter 3, equibiaxial tests were performed using the fixture proposed by Kossa. In the followings the details fixture are summarized based on the paper of Kossa [66].

The equibiaxial fixture (see Fig. D.1/a-c) consist of two comb-like steel parts, which can slide into each other. Thanks to the perpendicular forks, the equibiaxial compression force F^{EB} and the equibiaxial extension u^{EB} become

$$F^{\text{EB}} = F/\sqrt{2} \quad \text{and} \quad u^{\text{EB}} = u/\sqrt{2}, \quad (\text{D.1})$$

where F is the loading force on the fixture, while u stands for the crosshead's displacement.

Figure D.1/d illustrates the equibiaxial compression of a cube specimen with edge length L_0 . In such case the equibiaxial nominal stress and stretch values are obtained as

$$P^{\text{EB}} = \frac{F^{\text{EB}}}{L_0^2} \quad \text{and} \quad \lambda^{\text{EB}} = 1 + \varepsilon^{\text{EB}} = 1 - \frac{u^{\text{EB}}}{L_0}. \quad (\text{D.2})$$

After substituting back the relations in (D.1), the equibiaxial stress and stretch values can be expressed from the loading force and the crosshead's displacement as

$$P^{\text{EB}} = \frac{F}{\sqrt{2}L_0^2} \quad \text{and} \quad \lambda^{\text{EB}} = 1 + \varepsilon^{\text{EB}} = 1 - \frac{u}{\sqrt{2}L_0}. \quad (\text{D.3})$$

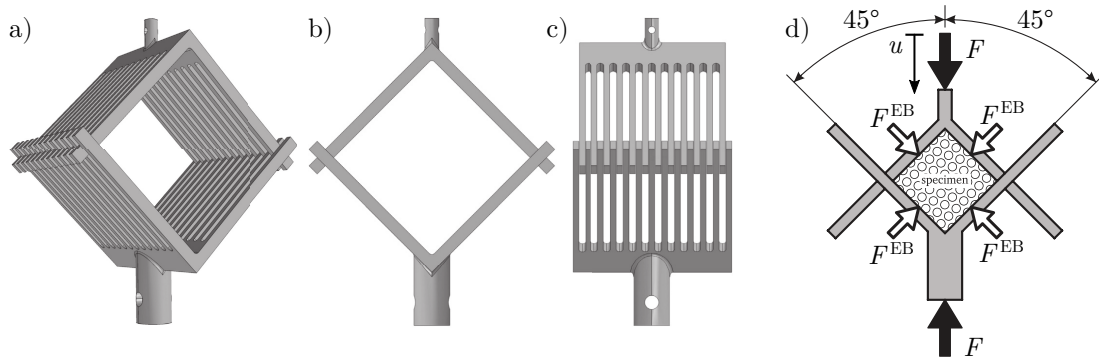


Figure D.1: The a)-c) the CAD drawing of the Kossa-type biaxial fixture and d) the forces acting on the specimen in equibiaxial loading (based on [66])

Bibliography

- [1] A. F. Bower. *Applied Mechanics of Solids*. Taylor & Francis Inc, 2009.
- [2] I. Doghri. *Mechanics of Deformable Solids*. Springer Berlin Heidelberg, 2010.
- [3] M. F. Ashby, H. Shercliff, and D. Cebon. *Materials*. Elsevier LTD, Oxford, 2013.
- [4] H. Altenbach and A. Öchsner. *State of the Art and Future Trends in Material Modeling*. Springer International Publishing, 2019.
- [5] J. S. Bergstrom. *Mechanics of Solid Polymers*. William Andrew Publishing, 2015.
- [6] G. Holzapfel. *Nonlinear Solid Mechanics*. John Wiley & Sons, 2000.
- [7] G. Bodor and L. Vas. *Polimer anyagtudomány*. Budapesti Műszaki és Gazdaságtudományi Egyetem, 1999.
- [8] G. Bodor and L. Vas. *Polimer anyagszerkezettan*. Műegyetemi Kiadó, 2000.
- [9] G. Silber and C. Then. *Preventive Biomechanics*. Springer Berlin Heidelberg, 2013.
- [10] A. D. Drozdov. *Finite Elasticity and Viscoelasticity*. WSPC, 1996.
- [11] E. A. de Souza Neto, D. Peric, and D. R. J. Owen. *Computational Methods for Plasticity*. John Wiley & Sons, Ltd, 2008.
- [12] M. A. Crisfield. *Non-linear finite element analysis of solids and structures*. Wiley, Chichester New York, 2000.
- [13] M. A. Crisfield, J. J. C. Remmers, C. V. Verhoosel, and R. de Borst. *Nonlinear Finite Element Analysis of Solids and Structures*. John Wiley & Sons Inc, 2012.
- [14] J. Betten. *Creep Mechanics*. Springer-Verlag GmbH, 2008.
- [15] Dassault Systèmes. Abaqus, version 2019.
- [16] ANSYS Inc. Mechanical, version 19.2, 2020.
- [17] MSC Softwares. Marc, 2020.
- [18] R. W. Ogden. Recent advances in the phenomenological theory of rubber elasticity. *Rubber Chemistry and Technology*, 59(3):361–383, 1986.
- [19] R. W. Ogden, G. Saccomandi, and I. Sgura. Fitting hyperelastic models to experimental data. *Computational Mechanics*, 34(6):484–502, 2004.
- [20] J. Bonet. *Nonlinear continuum mechanics for finite element analysis*. Cambridge University Press, Cambridge, UK New York, 2008.

- [21] W. M. Lai, E. Krempl, and D. H. Rubin. *Introduction to Continuum Mechanics*. Elsevier Science & Technology, 2009.
- [22] B. Cottrell and T. J. R. H. Hughes. *Isogeometric Analysis*. John Wiley & Sons, 2009.
- [23] P. Klein. *Fundamentals of Plastics Thermoforming*. Number 1. Morgan & Claypool Publishers LLC, 2009.
- [24] J. L. Throne. *Understanding Thermoforming*. Carl Hanser Verlag GmbH & Co. KG, 2008.
- [25] P. Schwarzmann. *Thermoforming*. Carl Hanser Verlag GmbH & Co. KG, 2018.
- [26] F. Thamm. *Műanyagok szilárdságtana I*. Budapesti Műszaki Egyetem, 1983.
- [27] S. P. C. Marques and G. J. Creus. *Computational Viscoelasticity*. Springer Berlin Heidelberg, 2012.
- [28] R. G. Albrecht Bertram. *Solid Mechanics*. Springer-Verlag GmbH, 2015.
- [29] N. Mills. *Polymer Foams Handbook*. Elsevier Science & Technology, 2007.
- [30] M. Itskov. *Tensor Algebra and Tensor Analysis for Engineers*. Springer International Publishing, 2016.
- [31] G. Béda. *Kontinuum mechanika*. Műegyetemi Kiadó, 1992.
- [32] G. Béda, I. Kozák, and J. Verhás. *Continuum mechanics*. Akadémiai Kiadó, Budapest, 1995.
- [33] I. Kozák and G. Szeidl. *Tenzorszámítás indexes jelölésmódban*. Miskolci Egyetem, Mechanikai Tanszék, 2013.
- [34] T. Hughes and J. C. Simo. *Computational Inelasticity*. Springer New York, 2000.
- [35] A. Kossa. *Exact stress integration schemes for elastoplasticity*. PhD thesis, Budapest University of Technology and Economics, 2012.
- [36] W.-F. Chen and D.-J. Han. *Plasticity for Structural Engineers*. J ROSS PUB INC, 2007.
- [37] W.-F. Chen. *Plasticity for structural engineers*. Springer-Verlag, New York, 1988.
- [38] R. E. von Mises. Mechanik der festen körper im plastisch- deformablen zustand, mathematisch-physikalische klasse. *Nachrichten von der Gesellschaft der Wissenschaften zu Göttingen*, 1:582–592., 1913.
- [39] L. Prandtl. Spannungsverteilung in plastischen körpern. *Proceedings of the 1st International Congress on Applied Mechanics*, page 43–54, 1925.
- [40] E. Reuss. Berücksichtigung der elastischen formänderung in der plastizitätstheorie,. *Zeitschrift für angewandte Mathematik und Mechanik*, 10:266–274, 1930.
- [41] L. J. Gibson and M. F. Ashby. *Cellular Solids*. Cambridge University Press, 1997.
- [42] N. Mills. Polymer foams for personal protection: cushions, shoes and helmets. *Composites Science and Technology*, 63(16):2389–2400, 2003.

-
- [43] L. Gibson. *Cellular materials in nature and medicine*. Cambridge University Press, Cambridge New York, 2010.
- [44] F. S. Gerhard Silber. *Bauteilberechnung und Optimierung mit der FEM*. Teubner B.G. GmbH, 2005.
- [45] A. Drozdov and J. deClaville Christiansen. Modeling the elastic response of polymer foams at finite deformations. *International Journal of Mechanical Sciences*, 171:105398, 2020.
- [46] H.-Y. Mi, X. Jing, and L.-S. Turng. Fabrication of porous synthetic polymer scaffolds for tissue engineering. *Journal of Cellular Plastics*, 51(2):165–196, 2014.
- [47] J. Wang, J. Luo, R. Kunkel, M. Saha, B. N. Bohnstedt, C.-H. Lee, and Y. Liu. Development of shape memory polymer nanocomposite foam for treatment of intracranial aneurysms. *Materials Letters*, 250:38–41, 2019.
- [48] A. K. Singh, A. Shishkin, T. Koppel, and N. Gupta. A review of porous lightweight composite materials for electromagnetic interference shielding. *Composites Part B: Engineering*, 149:188–197, 2018.
- [49] Y. Ma, X. Su, R. Pyrz, and J. C. Rauhe. A novel theory of effective mechanical properties of closed-cell foam materials. *Acta Mechanica Solida Sinica*, 26(6):559–569, 2013.
- [50] R. Widdle, A. Bajaj, and P. Davies. Measurement of the Poisson’s ratio of flexible polyurethane foam and its influence on a uniaxial compression model. *International Journal of Engineering Science*, 46(1):31–49, 2008.
- [51] N. Mills and A. Gilchrist. Modelling the indentation of low density polymer foams. *Cellular Polymers*, 19(6):389–412, 2000.
- [52] W. H. El-Ratal and P. K. Mallick. Elastic response of flexible polyurethane foams in uniaxial tension. *Journal of Engineering Materials and Technology*, 118(2):157–161, 1996.
- [53] J. Ciambella and G. Saccomandi. A continuum hyperelastic model for auxetic materials. *Proceedings of the Royal Society A: Mathematical, Physical and Engineering Sciences*, 470(2163):20130691, 2014.
- [54] J. Ciambella, A. Bezazi, G. Saccomandi, and F. Scarpa. Nonlinear elasticity of auxetic open cell foams modeled as continuum solids. *Journal of Applied Physics*, 117(18):184902, 2015.
- [55] Y. Li and C. Zeng. On the successful fabrication of auxetic polyurethane foams: Materials requirement, processing strategy and conversion mechanism. *Polymer*, 87:98–107, 2016.
- [56] A. B. F. Scarpa. Mechanical behaviour of conventional and negative poisson’s ratio thermo-plastic polyurethane foams under compressive cyclic loading. *International Journal of Fatigue*, 29(5):922–930, 2007.
- [57] C. Briody, B. Duignan, and S. Jerrams. Testing, modelling and validation of numerical model capable of predicting stress fields throughout polyurethane foam. *Constitutive Models for Rubber VII*, pages 143–148, 2012.
- [58] S. Kim, H. Shin, S. Rhim, and K. Y. Rhee. Calibration of hyperelastic and hyperfoam constitutive models for an indentation event of rigid polyurethane foam. *Composites Part B: Engineering*, 163:297–302, 2019.
-

- [59] N. Mills, R. Stämpfli, F. Marone, and P. Brühwiler. Finite element micromechanics model of impact compression of closed-cell polymer foams. *International Journal of Solids and Structures*, 46(3-4):677–697, 2009.
- [60] K. M. Moerman, B. Fereidoonzhad, and P. McGarry. Novel hyperelastic models for large volumetric deformations. *International Journal of Solids and Structures*, 2020.
- [61] S. Demiray, W. Becker, and J. Hohe. Analysis of two- and three-dimensional hyperelastic model foams under complex loading conditions. *Mechanics of Materials*, 38(11):985–1000, 2006.
- [62] A. K. Landauer, X. Li, C. Franck, and D. L. Henann. Experimental characterization and hyperelastic constitutive modeling of open-cell elastomeric foams. *Journal of the Mechanics and Physics of Solids*, 133:103701, 2019.
- [63] M. Sasso, G. Palmieri, G. Chiappini, and D. Amodio. Characterization of hyperelastic rubber-like materials by biaxial and uniaxial stretching tests based on optical methods. *Polymer Testing*, 27(8):995–1004, 2008.
- [64] M. Petre, A. Erdemir, and P. Cavanagh. Determination of elastomeric foam parameters for simulations of complex loading. *Computer Methods in Biomechanics and Biomedical Engineering*, 9(4):231–242, 2006.
- [65] A. A. Farag and J. S. Suri. *Deformable Models II*. Springer-Verlag GmbH, 2007.
- [66] A. Kossa. A new biaxial compression fixture for polymeric foams. *Polymer Testing*, 45:47–51, 2015.
- [67] P. Steinmann, M. Hossain, and G. Possart. Hyperelastic models for rubber-like materials: consistent tangent operators and suitability for treloar’s data. *Archive of Applied Mechanics*, 82(9):1183–1217, 2012.
- [68] R. W. Ogden. Large deformation isotropic elasticity: on the correlation of theory and experiment for compressible rubberlike solids. *Proceedings of the Royal Society of London. A. Mathematical and Physical Sciences*, 328(1575):567–583, 1972.
- [69] R. Hill. Aspects of invariance in solid mechanics. In *Advances in Applied Mechanics*, pages 1–75. Elsevier, 1979.
- [70] B. Storåkers. On material representation and constitutive branching in finite compressible elasticity. *Journal of the Mechanics and Physics of Solids*, 34(2):125–145, 1986.
- [71] R. W. Ogden. *Elastic Deformations of Rubberlike Solids*. Elsevier, 1982.
- [72] D. Drucker. On the postulate of stability of material in the mechanics of continua. *Journal de Mécanique*, 3:235–249, 1964.
- [73] International Organization for Standardization. ISO 3386: Flexible cellular polymeric materials – determination of stress-strain characteristics in compression.
- [74] M. Schrodts, G. Benderoth, A. Kuhhorn, and G. Silber. Hyperelastic description of polymer soft foams at finite deformations. *Technische Mechanik*, 25:162–173, 2005.
- [75] P. J. Blatz and W. L. Ko. Application of finite elastic theory to the deformation of rubbery materials. *Transactions of the Society of Rheology*, 6(1):223–252, 1962.

-
- [76] C. Briody, B. Duignan, S. Jerrams, and J. Tiernan. The implementation of a visco-hyperelastic numerical material model for simulating the behaviour of polymer foam materials. *Computational Materials Science*, 64:47–51, 2012.
- [77] M. Grujicic, B. Pandurangan, G. Arakere, W. Bell, T. He, and X. Xie. Seat-cushion and soft-tissue material modeling and a finite element investigation of the seating comfort for passenger-vehicle occupants. *Materials & Design*, 30(10):4273–4285, 2009.
- [78] W. Shen and I. A. R. Galer. Development of a pressure related assessment model of seating discomfort. *Proceedings of the Human Factors and Ergonomics Society Annual Meeting*, 37(10):831–835, 1993.
- [79] J. Wu, H. Yuan, and X. Li. A novel method for comfort assessment in a supine sleep position using three-dimensional scanning technology. *International Journal of Industrial Ergonomics*, 67:104–113, 2018.
- [80] D. Y. Kim, J. H. Bang, C. A. Lee, H. Y. Kim, K. Y. Choi, and B. G. Lim. Numerical evaluation of time-dependent sagging for low density polyurethane foams to apply the long-term driving comfort on the seat cushion design. *International Journal of Industrial Ergonomics*, 64:178–187, 2018.
- [81] NASA Scientific and Technical Information. Forty-year-old foam springs back with new benefits consumer/home/recreation, 2005.
- [82] Fagerdala Singapore PTE. Ltd. <http://www.fagerdalagroup.com/>.
- [83] H. Weber, T. Wolf, and U. Duenger. Determination of relaxation moduli and poisson’s ratio in uniaxially loaded solid polyethylene foam specimens as part of full material characterization. *Mechanics of Time-Dependent Materials*, 1(2):195–208, 1997.
- [84] K. Bekkour and O. Scrivener. Time-dependent and flow properties of foams. *Mechanics of Time-Dependent Materials*, 2(2):171–193, 1998.
- [85] A. Aili, M. Vandamme, J.-M. Torrenti, and B. Masson. Theoretical and practical differences between creep and relaxation poisson’s ratios in linear viscoelasticity. *Mechanics of Time-Dependent Materials*, 19(4):537–555, 2015.
- [86] T. Sakai, T. Tao, and S. Somiya. Estimation of creep and recovery behavior of a shape memory polymer. *Mechanics of Time-Dependent Materials*, 19(4):569–579, 2015.
- [87] H. Khajehsaeid, J. Arghavani, R. Naghdabadi, and S. Sohrabpour. A visco-hyperelastic constitutive model for rubber-like materials: A rate-dependent relaxation time scheme. *International Journal of Engineering Science*, 79:44–58, 2014.
- [88] Y. Anani and Y. Alizadeh. Visco-hyperelastic constitutive law for modeling of foam’s behavior. *Materials & Design*, 32(5):2940–2948, 2011.
- [89] M. Pawlikowski. Non-linear approach in visco-hyperelastic constitutive modelling of polyurethane nanocomposite. *Mechanics of Time-Dependent Materials*, 18(1):1–20, 2013.
- [90] L. Yang and V. Shim. A visco-hyperelastic constitutive description of elastomeric foam. *International Journal of Impact Engineering*, 30(8-9):1099–1110, 2004.
-

- [91] M. Elfarhani, A. Jarraya, S. Abid, and M. Haddar. Fractional derivative and hereditary combined model for memory effects on flexible polyurethane foam. *Mechanics of Time-Dependent Materials*, 20(2):197–217, 2016.
- [92] A. S. Khan and R. Liang. Behaviors of three BCC metal over a wide range of strain rates and temperatures: experiments and modeling. *International Journal of Plasticity*, 15(10):1089–1109, 1999.
- [93] S. Lee and W. Knauss. A note on the determination of relaxation and creep data from ramp tests. *Mechanics of Time-Dependent Materials*, 4(1):1–7, 2000.
- [94] A. Bula, M. Kozłowski, J. Hulimka, and B. Chmielnicki. Analysis of methyl methacrylate adhesive (MMA) relaxation with non-linear stress–strain dependence. *International Journal of Adhesion and Adhesives*, 94:40–46, 2019.
- [95] R. Moran, J. H. Smith, and J. J. García. Fitted hyperelastic parameters for human brain tissue from reported tension, compression, and shear tests. *Journal of Biomechanics*, 47(15):3762–3766, 2014.
- [96] P. Areias, A. Rodrigues, T. Rabczuk, J. Garção, and A. Carvalho. Analysis of experimentally assessed EVA foams with mixed solid-shell elements capable of very large strains. *Finite Elements in Analysis and Design*, 128:19–31, 2017.
- [97] M. Hosseini-Farid, M. Ramzanpour, M. Ziejewski, and G. Karami. A compressible hyper-viscoelastic material constitutive model for human brain tissue and the identification of its parameters. *International Journal of Non-Linear Mechanics*, 116:147–154, 2019.
- [98] W. G. Knauss, I. Emri, and H. Lu. Mechanics of polymers: Viscoelasticity. In *Springer Handbook of Experimental Solid Mechanics*, pages 49–96. Springer US, 2008.
- [99] S. Goh, M. Charalambides, and J. Williams. Determination of the constitutive constants of non-linear viscoelastic materials. *Mechanics of Time-Dependent Materials*, 8(3):255–268, 2004.
- [100] R. Prony. Essai expérimental et analytique: sur les lois de la dilatabilité de uides élastique et sur celles de la force expansive de la vapeur del’alkool, à diérentes températures. *Journal de l’École Polytechnique Floréal et Plairial*, 1(22):24–76, 1795.
- [101] J. Y. Hristov. Linear viscoelastic responses: The prony decomposition naturally leads into the caputo-fabrizio fractional operator. *Frontiers in Physics*, 6, 2018.
- [102] J. Hristov. Linear viscoelastic responses and constitutive equations in terms of fractional operators with non-singular kernels. *The European Physical Journal Plus*, 134(6), 2019.
- [103] J. Ciambella, M. Destrade, and R. W. Ogden. On the ABAQUS FEA model of finite viscoelasticity. *Rubber Chemistry and Technology*, 82(2):184–193, 2009.
- [104] J. Ciambella. *Experimental Testing and Nonlinear Viscoelastic Modeling of Filled Rubber*. PhD thesis, SAPIENZA Università di Roma, 2010.
- [105] K. B. Oldham, J. Myland, and J. Spanier. *An Atlas of Functions*. Springer-Verlag New York Inc., 2008.
- [106] Wolfram. Mathword: Incomplete gamma function, 2016.

- [107] Wolfram Research. Mathematica, version 10.3, 2016.
- [108] J. Sorvari and M. Malinen. Determination of the relaxation modulus of a linearly viscoelastic material. *Mechanics of Time-Dependent Materials*, 10(2):125–133, 2006.
- [109] J. Meissner. Combined constant strain rate and stress relaxation test for linear viscoelastic studies. *Journal of Polymer Science: Polymer Physics Edition*, 16(5):915–919, 1978.
- [110] L. J. Zapas and J. C. Phillips. Simple shearing flows in polyisobutylene solutions. *Journal of Research of the National Bureau of Standards- A. Physics and Chemistry*, 75(1):33–41, 1971.
- [111] E. Guzman-Maldonado, N. Hamila, N. Naouar, G. Moulin, and P. Boisse. Simulation of thermoplastic prepreg thermoforming based on a visco-hyperelastic model and a thermal homogenization. *Materials & Design*, 93:431–442, 2016.
- [112] H. F. Alharbi, M. Luqman, H. Fouad, K. A. Khalil, and N. H. Alharthi. Viscoelastic behavior of core-shell structured nanofibers of PLA and PVA produced by coaxial electrospinning. *Polymer Testing*, 67:136–143, 2018.
- [113] P. Yu, X. Yao, Q. Han, S. Zang, and Y. Gu. A visco-elastoplastic constitutive model for large deformation response of polycarbonate over a wide range of strain rates and temperatures. *Polymer*, 55(25):6577–6593, 2014.
- [114] F. Shen, G. Kang, Y. C. Lam, Y. Liu, and K. Zhou. Thermo-elastic-viscoplastic-damage model for self-heating and mechanical behavior of thermoplastic polymers. *International Journal of Plasticity*, 121:227–243, 2019.
- [115] M. R. Adibeig, S. Hassanifard, and F. Vakili-Tahami. Optimum creep lifetime of polymethyl methacrylate (PMMA) tube using rheological creep constitutive models based on experimental data. *Polymer Testing*, 75:107–116, 2019.
- [116] P. Gelineau, S. Weigand, L. Cauvin, and F. Bédoui. Compatibility effects of modified montmorillonite on elastic and visco-elastic properties of nano-reinforced poly(lactic acid): Experimental and modeling study. *Polymer Testing*, 70:441–448, 2018.
- [117] B. Chang, X. Wang, Z. Long, Z. Li, J. Gu, S. Ruan, and C. Shen. Constitutive modeling for the accurate characterization of the tension behavior of PEEK under small strain. *Polymer Testing*, 69:514–521, 2018.
- [118] J. G. Lee and R. W. Flumerfelt. A refined approach to bubble nucleation and polymer foaming process: Dissolved gas and cluster size effects. *Journal of Colloid and Interface Science*, 184(2):335–348, 1996.
- [119] F. Luo, X. Liu, C. Yan, H. Liu, M. Dong, X. Mai, C. Shen, C. Liu, J. Zhang, N. Wang, and Z. Guo. Molecular orientation dependent dynamic viscoelasticity in uni-axially drawn polycarbonate. *Polymer Testing*, 69:528–535, 2018.
- [120] X. Wang, Y. Pan, Y. Qin, M. Voigt, X. Liu, G. Zheng, Q. Chen, D. W. Schubert, C. Liu, and C. Shen. Creep and recovery behavior of injection-molded isotactic polypropylene with controllable skin-core structure. *Polymer Testing*, 69:478–484, 2018.
- [121] J. Jiang, X. Liu, M. Lian, Y. Pan, Q. Chen, H. Liu, G. Zheng, Z. Guo, D. W. Schubert, C. Shen, and C. Liu. Self-reinforcing and toughening isotactic polypropylene via melt sequential injection molding. *Polymer Testing*, 67:183–189, 2018.

- [122] S. Das, S. R. Chowdhury, and D. Roy. A constitutive model for thermoplastics based on two temperatures. *European Journal of Mechanics - A/Solids*, 72:440–451, 2018.
- [123] H. da Costa Mattos, J. Reis, L. de Medeiros, A. Monteiro, S. Teixeira, and E. Chaves. Analysis of the cyclic tensile behaviour of an elasto-viscoplastic polyamide. *Polymer Testing*, 58:40–47, 2017.
- [124] E. Motta, J. Reis, and H. da Costa Mattos. Analysis of the cyclic tensile behaviour of an elasto-viscoplastic polyvinylidene fluoride (PVDF). *Polymer Testing*, 67:503–512, 2018.
- [125] J. Chaboche and O. Jung. Application of a kinematic hardening viscoplasticity model with thresholds to the residual stress relaxation. *International Journal of Plasticity*, 13(10):785–807, 1997.
- [126] D. L. McDowell. A nonlinear kinematic hardening theory for cyclic thermoplasticity and thermoviscoplasticity. *International Journal of Plasticity*, 8(6):695–728, 1992.
- [127] J. E. Martini-Vvedensky, N. P. Suh, and F. A. Waldman. Microcellular closed cell foams and their method of manufacture, 1982.
- [128] R. Guan, B. Xiang, Z. Xiao, Y. Li, D. Lu, and G. Song. The processing–structure relationships in thin microcellular PET sheet prepared by compression molding. *European Polymer Journal*, 42(5):1022–1032, 2006.
- [129] G. Lu, W. van Driel, X. Fan, M. Y. Mehr, J. Fan, K. Jansen, and G. Zhang. Degradation of microcellular PET reflective materials used in LED-based products. *Optical Materials*, 49:79–84, 2015.
- [130] J. Kichenin. *Comportement Thermomécanique du Polyéthylène – application aux structures gazières*. PhD thesis, Ecole Polytechnique, Paris, 1992.
- [131] J. Kichenin, K. V. Dang, and K. Boytard. Finite-element simulation of a new two-dissipative mechanisms model for bulk medium-density polyethylene. *Journal of Materials Science*, 31(6):1653–1661, 1996.
- [132] Furukawa Electric Co., Ltd. Micro-cellular foamed light reflective sheet, 2020.
- [133] International Organization for Standardization. ISO 6721: Plastics — determination of dynamic mechanical properties.
- [134] International Organization for Standardization. ISO 527: Plastics — determination of tensile properties — part 1: General principles.
- [135] American Society for Testing and Materials. ASTM D618: Standard practice for conditioning plastics for testing.
- [136] American Society for Testing and Materials. ASTM D638: Standard test method for tensile properties of plastics.
- [137] R. B. Dupaix and M. C. Boyce. Constitutive modeling of the finite strain behavior of amorphous polymers in and above the glass transition. *Mechanics of Materials*, 39(1):39–52, 2007.

- [138] E. Charkaluk, A. Bignonnet, A. Constantinescu, and K. D. Van. Fatigue design of structures under thermomechanical loadings. *Fatigue & Fracture of Engineering Materials and Structures*, 25(12):1199–1206, 2002.
- [139] S. B. Leen, A. Deshpande, and T. H. Hyde. Experimental and numerical characterization of the cyclic thermomechanical behavior of a high temperature forming tool alloy. *Journal of Manufacturing Science and Engineering*, 132(5), 2010.
- [140] T. P. Farragher, S. Scully, N. P. O’Dowd, and S. B. Leen. Thermomechanical analysis of a pressurized pipe under plant conditions. *Journal of Pressure Vessel Technology*, 135(1), 2012.
- [141] T. P. Farragher, S. Scully, N. P. O’Dowd, C. J. Hyde, and S. B. Leen. High temperature low cycle fatigue characterization of p91 weld and heat affected zone material. *Journal of Pressure Vessel Technology*, 136(2), 2014.
- [142] R. Solasi, Y. Zou, X. Huang, and K. Reifsnider. A time and hydration dependent viscoplastic model for polyelectrolyte membranes in fuel cells. *Mechanics of Time-Dependent Materials*, 12(1):15–30, 2007.
- [143] J. Kang, A. Becker, and W. Sun. Determination of elastic and viscoplastic material properties obtained from indentation tests using a combined finite element analysis and optimization approach. *Proceedings of the Institution of Mechanical Engineers, Part L: Journal of Materials: Design and Applications*, 229(3):175–188, 2013.
- [144] I. S. Grigoriev, E. Z. Meilikhov, and A. A. Radzig. *Handbook of Physical Quantities*. CRC Press, 1996.
- [145] W. Spendley, G. R. Hext, and F. R. Himsworth. Sequential application of simplex designs in optimisation and evolutionary operation. *Technometrics*, 4(4):441–461, 1962.
- [146] J. A. Nelder and R. Mead. A simplex method for function minimization. *The Computer Journal*, 7(4):308–313, 1965.
- [147] R. Hooke and T. A. Jeeves. "direct search" solution of numerical and statistical problems. *Journal of the ACM*, 8(2):212–229, 1961.
- [148] L. Ingber. Adaptive simulated annealing (asa): Lessons learned. *Control and Cybernetics*, 25(1):33–54, 1996.
- [149] T. O. Kvalseth. Note on the r2 measure of goodness of fit for nonlinear models. *Bulletin of the Psychonomic Society*, 21(1):79–80, 1983.
- [150] A.-N. Spiess and N. Neumeyer. An evaluation of r2 as an inadequate measure for nonlinear models in pharmacological and biochemical research: a monte carlo approach. *BMC Pharmacology*, 10(1), 2010.
- [151] R. M. Guedes. *Creep and Fatigue in Polymer Matrix Composites*. Elsevier Science & Technology, 2019.
- [152] P. Hempel. *Constitutive modeling of amorphous thermoplastic polymers with special emphasis on manufacturing processes*. PhD thesis, Karlsruher Institut für Technologie, 2016.
- [153] O. Jacobs, P. Wolf-Regett, and W. Dalock. A test system for punching of thermoplastic foils. *Polymer Testing*, 21(4):403–410, 2002.

- [154] M. Kaliske and H. Rothert. Formulation and implementation of three-dimensional viscoelasticity at small and finite strains. *Computational Mechanics*, 19(3):228–239, 1997.
- [155] A. K. Kiss, D. Bachrathy, and G. Stepan. Laser scanned patterns of machined surfaces. *Procedia CIRP*, 77:355–358, 2018.
- [156] Y. Altintas. *Manufacturing Automation - Metal Cutting Mechanics, Machine Tool Vibrations and CNC Design*. Cambridge University Press, Cambridge, 2012.
- [157] D. J. Ewins. *Modal testing : theory and practice*. Research Studies Press Wiley, Letchworth, Hertfordshire, England New York, 1984.
- [158] P. L. Gatti. *Applied Structural and Mechanical Vibrations*. Taylor & Francis Ltd, 2017.
- [159] E. Orlowitz and A. Brandt. Comparison of experimental and operational modal analysis on a laboratory test plate. *Measurement*, 102:121–130, 2017.
- [160] F. Magalhães and Á. Cunha. Explaining operational modal analysis with data from an arch bridge. *Mechanical Systems and Signal Processing*, 25(5):1431–1450, 2011.
- [161] D. Takács, R. Wohlfart, Á. Miklós, G. Krajnyák, A. Tóth, and G. Stépán. Ball shooting tests for identification of modal parameter variation in rotating main spindles. *Procedia CIRP*, 77:481–484, 2018.
- [162] D. Hajdu, T. Insperger, and G. Stepan. The effect of non-symmetric frf on machining: A case study. *Proceedings of the ASME 2015 International Design Engineering Technical Conferences & Computers and Information in Engineering Conference, 2015.08.02-2015.08.05, Boston, USA*, 2015.
- [163] D. Hajdu, T. Insperger, and G. Stepan. Robust stability analysis of machining operations. *The International Journal of Advanced Manufacturing Technology*, 88(1-4):45–54, 2016.
- [164] A. K. Kiss, D. Bachrathy, and G. Stepan. Cumulative surface location error for milling processes based on tool-tip frequency response function. *Procedia CIRP*, 46, 2016.
- [165] H. T. Sykora, D. Bachrathy, and G. Stepan. A theoretical investigation of the effect of the stochasticity in the material properties on the chatter detection during turning. *Volume 8: 29th Conference on Mechanical Vibration and Noise*. American Society of Mechanical Engineers, 2017.
- [166] H. T. Sykora, D. Bachrathy, and G. Stepan. Gaussian noise process as cutting force model for turning. *Procedia CIRP*, 77:94–97, 2018.
- [167] G. Stepan, B. Beri, A. Miklos, R. Wohlfart, D. Bachrathy, G. Porempovics, A. Toth, and D. Takacs. On stability of emulated turning processes in HIL environment. *CIRP Annals*, 68(1):405–408, 2019.
- [168] D. Hajdu, F. Borgioli, W. Michiels, T. Insperger, and G. Stepan. Robust stability of milling operations based on pseudospectral approach. *International Journal of Machine Tools and Manufacture*, 149:103516, 2020.
- [169] G. Gustafsson, H. Haggblad, M. Nishida, S. Larsson, and P. Jonsén. Fracture probability modelling of impact-loaded iron ore pellets. *International Journal of Impact Engineering*, 102:180–186, 2017.

- [170] G. J. Huh and B. M. Kwak. Constrained variational approach for dynamic analysis of elastic contact problems. *Finite Elements in Analysis and Design*, 10(2):125–136, 1991.
- [171] H. Minamoto and S. Kawamura. Moderately high speed impact of two identical spheres. *International Journal of Impact Engineering*, 38:123–129, 2011.
- [172] C. Wu, C. Thornton, and L. Li. A semi-analytical model for oblique impacts of elastoplastic spheres. *Proceedings of the Royal Society*, 465:937–960, 2009.
- [173] C. Wu, L. Li, and C. Thornton. Energy dissipation during normal impact of elastic and elastic–plastic spheres. *International Journal of Impact Engineering*, 32:593–604, 2005.
- [174] U. Jayadeep and M. Bobji. Energy loss due to adhesion during the impact of elastic spheres. *Procedia Engineering*, 173:238–243, 2017.
- [175] S. H. Ko and B. M. Kwak. Frictional dynamic contact analysis in deformable multibody systems. *Finite Elements in Analysis and Design*, 12(1):27–40, 1992.
- [176] E. Willert and V. L. Popov. Impact of an elastic sphere with an elastic half space with a constant coefficient of friction: Numerical analysis based on the method of dimensionality reduction. *Zeitschrift für Angewandte Mathematik und Mechanik*, pages 1–7, 2016.
- [177] I. A. Lyashenko and V. L. Popov. Impact of an elastic sphere with an elastic half space revisited: Numerical analysis based on the method of dimensionality reduction. *Scientific Reports*, 5(8479), 2015.
- [178] G. Hattori and A. L. Serpa. Contact stiffness estimation in ANSYS using simplified models and artificial neural networks. *Finite Elements in Analysis and Design*, 97:43–53, 2015.
- [179] B. G. Compton, E. A. Gamble, and F. W. Zok. Failure initiation during impact of metal spheres onto ceramic targets. *International Journal of Impact Engineering*, 55:11–23, 2013.
- [180] H. Conway, P. Engel, and H. Lee. Force-time investigations for the elastic impact between a rigid sphere and a thin layer. *International Journal of Mechanical Sciences*, 14(8):523–529, 1972.
- [181] S. MansoorBaghaei and A. M. Sadegh. Elastic spherical shell impacted with an elastic barrier: A closed form solution. *International Journal of Solids and Structures*, 48(22-23):3257–3266, 2011.
- [182] N. Maw. The oblique impact of elastic spheres. *Wear*, 38(1):101–114, 1976.
- [183] H. Unal, U. Sen, and A. Mimaroglu. Dry sliding wear characteristics of some industrial polymers against steel counterface. *Tribology International*, 37(9):727–732, 2004.
- [184] H. Hertz. Ueber die berührung fester elastischer körper. *Journal für die Reine und Angewandte Mathematik*, 92:156–171, 1881.
- [185] J. Reed. Energy losses due to elastic wave propagation during an elastic impact. *Journal of Physics D*, 18(12):2329–2337, 1985.

Publications by the Author

- [SzB1] Sz. Berezvai and A. Kossa. Closed-form solution of the Ogden–Hill’s compressible hyperelastic model for ramp loading. *Mechanics of Time-Dependent Materials*, 21(2):263–286, 2016.
- [SzB2] Sz. Berezvai and A. Kossa. Effect of the skin layer on the overall behavior of closed-cell polyethylene foam sheets. *Journal of Cellular Plastics*, 52(2):215–229, 2015.
- [SzB3] A. Kossa and Sz. Berezvai. Novel strategy for the hyperelastic parameter fitting procedure of polymer foam materials. *Polymer Testing*, 53:149–155, 2016.
- [SzB4] A. Kossa and Sz. Berezvai. Visco-hyperelastic characterization of polymeric foam materials. *Materials Today: Proceedings*, 3(4):1003–1008, 2016.
- [SzB5] Sz. Berezvai and A. Kossa. Memóriahabok mechanikai modellezése. In *XXIV. Nemzetközi Gépészeti Találkozó, Déva, Románia*, pages 47–50, 2006.
- [SzB6] Sz. Berezvai and A. Kossa. Nonlinear viscoelastic characterization of polymeric foams. In *Proceedings of the VII European Congress on Computational Methods in Applied Sciences and Engineering*, 2016.
- [SzB7] Sz. Berezvai and A. Kossa. Performance of a parallel viscoelastic-viscoplastic model for a microcellular thermoplastic foam on wide temperature range. *Polymer Testing*, 84:106395, 2020.
- [SzB8] Sz. Berezvai and A. Kossa. Characterization of a thermoplastic foam material with the two-layer viscoplastic model. *Materials Today: Proceedings*, 4(5):5749–5754, 2017.
- [SzB9] Sz. Berezvai, A. Kossa, and A. K. Kiss. Validation method for thickness variation of thermoplastic microcellular foams using punch-tests. *Materials Today: Proceedings*, (online first) 2020.
- [SzB10] Sz. Berezvai and A. Kossa. Viszkózus-rugalmas-képlékeny anyagmodellek vizsgálata mikrocellás polimer hab hőformázása esetén. In *XIII. Magyar Mechanikai Konferencia, Miskolc*, 2019.
- [SzB11] Sz. Berezvai, A. Kossa, D. Bachrathy, and G. Stepan. Numerical and experimental investigation of the applicability of pellet impacts for impulse excitation. *International Journal of Impact Engineering*, 115:19–31, 2018.
- [SzB12] Sz. Berezvai, A. Kossa, and G. Stepan. Airsoft lövedék viszkózus-rugalmas-képlékeny ütközésének szimulációja és alkalmazása. In *XXVI. Nemzetközi Gépészeti Konferencia, Marosvásárhely, Románia*, pages 39–42, 2018.

PUBLICATIONS BY THE AUTHOR

- [SzB13] Sz. Berezhvai, A. Kossa, and G. Stepan. Nonlinear material modelling of an airsoft pellet applied for impulse excitation. In *European Nonlinear Oscillations Conference, Budapest, Hungary, 2017*.
- [SzB14] Sz. Berezhvai, A. Kossa, and G. Stepan. Investigation of the performance of the two-layer viscoplastic model applied for simulating airsoft ball impacts. In *Computational Plasticity Conference, Barcelona, Spain, 2017*.